1995

A study of Ag/Ag(100) thin film growth with scanning tunneling microscopy

Jianming Wen
Iowa State University

A study of Ag/Ag(100) thin film growth with scanning tunneling microscopy

by

Jianming Wen

A Dissertation Submitted to the

Graduate Faculty in Partial Fulfillment of the

Requirements for the Degree of

DOCTOR OF PHILOSOPHY

Department: Chemistry
Major: Physical Chemistry

Approved:

Signature was redacted for privacy.

In Charge of Major Work

Signature was redacted for privacy.

For the Major Department

Signature was redacted for privacy.

For the Graduate College

Iowa State University
Ames, Iowa

1995

A study of Ag/Ag(100) thin film growth with scanning tunneling microscopy

Jianming Wen

Major Professor: Patricia Thiel

Iowa State University

We used STM to study metal thin film growth processes. The following are main conclusions:

1. Large metal cluster diffuse on Ag(100) surface. The metal-metal system large adatom cluster diffusion is reported for the first time. The evaporation-condensation of adatoms dominating the vacancy cluster diffusion process is suggested. The diffusion coefficients is on the order of 10^{-18} cm^2s^{-1} .

2. Metal film evolution behaviors at different coverage regime are examined. At low coverage, cluster diffusion dominates the coarsening process. At high submonolayer coverage, vacancy cluster repining dominates the process. At moderate coverage, edge-running dominates the process.

3. The vacancy cluster diffusion is also observed. The vacancy were formed by controlling the deposition flux and film coverage. The method is simple and offers similar advantages of the sputtering method. The diffusion coefficients is on the order of 10^{-18} cm^2s^{-1}, is smaller than that of adatom clusters, and has a scaling factor α roughly close to 0.5 in $D \propto N^{-\alpha}$. The evaporation-condensation of vacancy monomers dominating the vacancy

cluster diffusion process is suggested.

4. We have presented a number of observations of dynamical phenomena of Ag cluster on Ag (100) with UHV-STM. Ag cluster on Ag (100) at room temperature are mobile. The interaction between clusters and between clusters and surface steps are mediated via 2D dilute adatom gas on the terrace and different adatom concentrations around clusters and steps. Background gases and impurities on cluster edges can strongly affect film coarsening process. The former can enhance clusters dissolution, but the latter can stabilize the local structure and geometry of the Ag film.

TABLE OF CONTENTS

CHAPTER 1: GENERAL INTRODUCTION	1
CHAPTER 2: DIFFUSION OF LARGE METAL CLUSTERS ON AG(100)	32
CHAPTER 3: COARSENING MECHANISMS IN A METAL FILM: FROM CLUSTER DIFFUSION TO VACANCY RIPENING	53
CHAPTER 4: DIFFUSION OF LARGE VACANCY CLUSTERS ON AG(100)	73
CHAPTER 5: SURFACE DYNAMICAL PHENOMENA	103
CHAPTER 6: CONCLUSION	185
REFERENCES	188
ACKNOWLEDGMENTS	192
APPENDIX I: THE CONSTRUCTION OF THE VACUUM CHAMBER	193
APPENDIX II: PREPARATION OF SCANNING TUNNELING MICROSCOPY TIP	197
APPENDIX III: THE MAJOR STM DATABASE	203
APPENDIX IV: SUMMARY OF VIBRATION ISOLATION MEASUREMENTS AND ESTIMATE OF VIBRATIONAL NOISE REACHING THE TIP-SAMPLE JUNCTION	205

CHAPTER 1

GENERAL INTRODUCTION

1. The importance of thin film growth kinetics

Thin films are attracting more and more attention in both the industrial and scientific communities. Many applications of thin films have been developed in industry. By using various growth methods, thin films can be used in optics, microelectronic devices, magnetic recording media, and as protective coatings. In order to improve existing applications and to find new ones, it is essential to understand what makes them so useful in applications and what factors affect their properties. Therefore, an understanding of film growth processes is necessary. Scientifically, many fundamental interactions, such as the interaction between the atoms that comprise the film and substrate, or the interaction between film atoms, are of great interest to surface scientists; studies of these interactions can provide dramatic insights into the nature of thin films and therefore, can further drive technology forward. In every application, the film structures, including morphology and microstructure, and adhesion between film and substrate are critical to the film's properties and therefore its performance. Studies of the mechanisms that control film morphology, microstructure and adhesion thus are important. Film growth kinetics can provide important information regarding the film structure and adhesion. Film growth is an atomistic process. The chemistry and physics of the system can be better understood if the information provided is at an atomic level.

The purpose of this chapter is to provide an overview of thin film growth kinetics. In this chapter, first, a general microscopic description of growth process is given. The focus is mainly on metal-on-metal systems, although the principles are applicable to other systems. Then, a short literature review of metal-on-metal growth with emphasis on diffusion and coarsening is introduced. Finally, a general introduction of scanning tunneling microscopy is given since it is the main technique employed in this study.

2. Overview of growth kinetics

a. What will happen during film growth

Thin films can be grown in many different ways. The growth process relevant to this study can be classified as vapor deposition. It is one of the most widely used deposition techniques. As the name implies, the technique consists of vaporization of the solid material by heating it to sufficiently high temperatures and condensing it onto a cooler substrate to form a film. The whole system needs to be placed in a vacuum chamber since in atmosphere evaporator cannot be functional and substrate and vapor source can be contaminated.

Most metal-on-metal systems are expected to have one of three classical growth modes in terms of thermodynamics, as shown in Figure 1: (1) sequential filling of layers, defined as Frank-van der Merwe mode; (2) after initial layer growth under critical thickness, agglomeration into three-dimensional clusters, defined as Stranski-Krastanov mode; and (3) agglomeration into three-dimensional (3D) clusters, defined as Volmer-Weber mode. The growth mode is predicted on the basis of the surface free energy calculations involving

Frank-van der Merwe

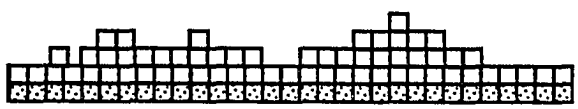

Stranski-Krastanov

Volmer-Weber

Figure 1. The three classical growth modes

□ Adatom

⊡ Substrate

substrate, film, and interface (γ_s, γ_f, and γ_i, respectively). For homoepitaxial systems, the system for which the substrate and deposition materials are the same, layer-growth is predicted for all film thickness. For heteropitaxial growth, where the substrate and deposition materials are not identical, 3D clustering is always the case. However, under certain deposition conditions, the growth may be far from equilibrium. Then the kinetic processes involved in film growth can be critical in terms of controlling film structure.

During film growth, adatoms are continuously deposited onto the substrate at a certain rate. The adatoms that land on the substrate will have a certain lifetime to migrate on the surface and interact with the surface atoms as well as with each other. In some cases, these interactions may cause growth of substrate steps, intermixing of deposited atoms and substrate atoms, and alteration of further film growth. These interactions result in nucleation on the surface, two-dimensional (2D) condensation of adatoms into islands and their subsequent growth, and the continuous growth from 2D to 3D clusters.

Growth kinetics depend on the fundamental surface processes of surface adsorption, desorption, and diffusion. Often the thermodynamically favored film states are 2D islands and 3D clusters on the substrate rather than a random distribution of adatoms. Film growth is a non-equilibrium process where surface phase separation occurs and growth kinetics play an essential role. As illustrated in Figure 2, there are two ways to make phase separation occur. In order to enter the two-phase coexistence regime from one phase state, one can quench the system. During quenching, the system is brought to a temperature-concentrate regime where the single phase state is no longer stable. This is the isoconcentration

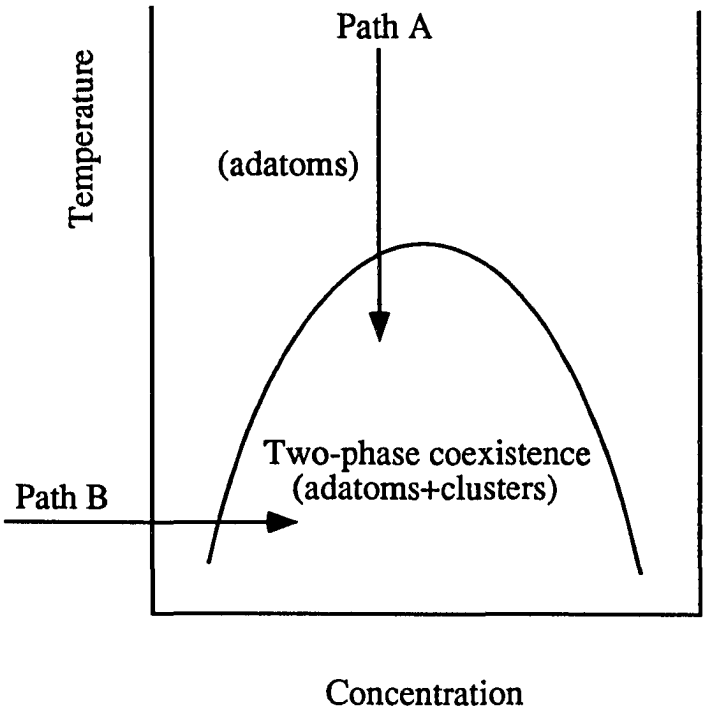

Figure 2. Phase Diagram of Surface with Film and Substrate

Path A and Path B can bring the system into two-phase coexistence regime. For explanation, see text

transition. This process is shown by Path A. The regime now consistents of two phases, a dense state phase (2D islands or 3D clusters) and a dilute adatom phase. The other way is to enter the two-phase coexistence regime isothermally, represented by Path B. Continuous deposition of adatoms onto a substrate at a constant temperature drives the system into a supersaturated state, i.e., it makes the 2D vapor pressure of the adatoms higher than that at equilibrium. The system tries to move back to equilibrium by forming a condensed phase, e.g. 2D islands or 3D clusters. The large decrease in molar entropy accompanying the process indicates that condensation is a thermodynamically favored process. The driving force for condensation comes from the lowering of the potential energy of the adatoms when they form bonds to each other. Since the adatoms are continuously being deposited, this relaxation toward equilibrium is taking place continuously.

There are three major stages in the formation of a condensed phase from a 2D vapor: nucleation, early stage growth, and late stage growth. Arriving adatoms make a random walk on the surface and, upon meeting each other, form nuclei. This is the nucleation process. In this stage, the nuclei are generated in large number but with a narrow size distribution. Random nucleation and spinodal decomposition are the dominant processes in nucleation. In random nucleation, the 2D adatoms are in a metastable state. This means that an energy barrier exists to form the two-phase regime, i.e., to form nuclei. The system needs to overcome this barrier to relax. On the other hand, in spinodal decomposition, the 2D adatom adlayer is unstable and forms nuclei spontaneously without a barrier to overcome. While nucleation continues the existing nuclei start to grow by

capturing more adatoms. The nucleation rate slows down when supersaturation is reduced. In the early growth stage, nucleation may still occur. However, the growth of 2D clusters is more pronounced. In this stage, depending on the deposition parameters, coalescence may occur, although this process mainly takes place in later growth process. This stage is a transition stage between nucleation and the later growth stage.

In the later growth stage, also called the coarsening process, the islands continue to grow by capturing free adatoms but other processes, i.e., combining two islands into a larger one upon impact, dominate. This process is favored since the surface free energy is reduced during the coalescence. When deposition is stopped and supersaturation is locally eliminated, island growth is usually thought to be dominated by Ostwald ripening. Ostwald ripening is characterized by large clusters growing at the expense of smaller clusters. Small clusters evaporate and their atoms diffuse on terraces and incorporate into larger clusters. The driving force for the ripening process is a concentration gradient of adatoms associated with the difference in vapor pressure over islands of different size. At this time, coalescence is also possible if the clusters are mobil. This stage is characterized by the dramatic reduction in cluster density.

This simple picture is applicable only in a binary system, when there are two different phases and no intermixing of adatoms and substrate atoms occurs. If the coverage is in the multiple layer regime, the process described will be complicated further, since interlayer diffusion and film roughness may occur. Therefore, the study of submonolayer deposition can eliminate some of these complications while providing valuable information

about growth.

Realistically, the other way to reduce and eliminate supersaturation in the 2D lattice gas is the incorporation of adatoms at surface steps. The surface by no means is flat. Steps always exist due to imperfect plane orientation. Steps are generally considered good places to trap adatoms because step atoms have higher coordination. Therefore when an adatom arrives on the surface, it diffuses on a terrace and takes one of the following ways to settle: colliding with another adatom or several other adatoms to form a new island (nucleation), exchanging with a surface atom (surface alloying), diffusing into the bulk of the substrate (interdiffusion), migrating into an existing island (growth), migrating into a substrate step (step incorporation), or leaving the surface and returning to the gas phase (reevaporation). Figure 3 shows these processes.

Island formation and incorporation at surface steps are two competing processes. The spatial distribution of islands formed after a submonolayer deposition reflects this competition. Near steps the island number density will be lower than that far from the steps because the adatoms that land near the surface steps are able to reach the steps before meeting other adatoms to form islands. From the atomistic point of view, the most important microscopic aspects underlying the above processes are the interaction of adatoms with steps (including substrate steps and island steps) and the surface migration of adatoms. The interaction between adatoms and surface steps includes 2D condensation and desorption from steps, step barriers for adatom to cross steps, and diffusion along steps.

The general expectation is that all surface steps are good adatom traps, i.e., all

Figure 3. The deposited atom can take these possible ways to settle.

1. Deposition
2. Nucleation
3. Diffusing into a cluster
4. Approaching and incorporating into an ascending step
5. Approaching and incorporating into a descending step
6. Diffusing into surface layer or into bulk
7. Leaving the surface

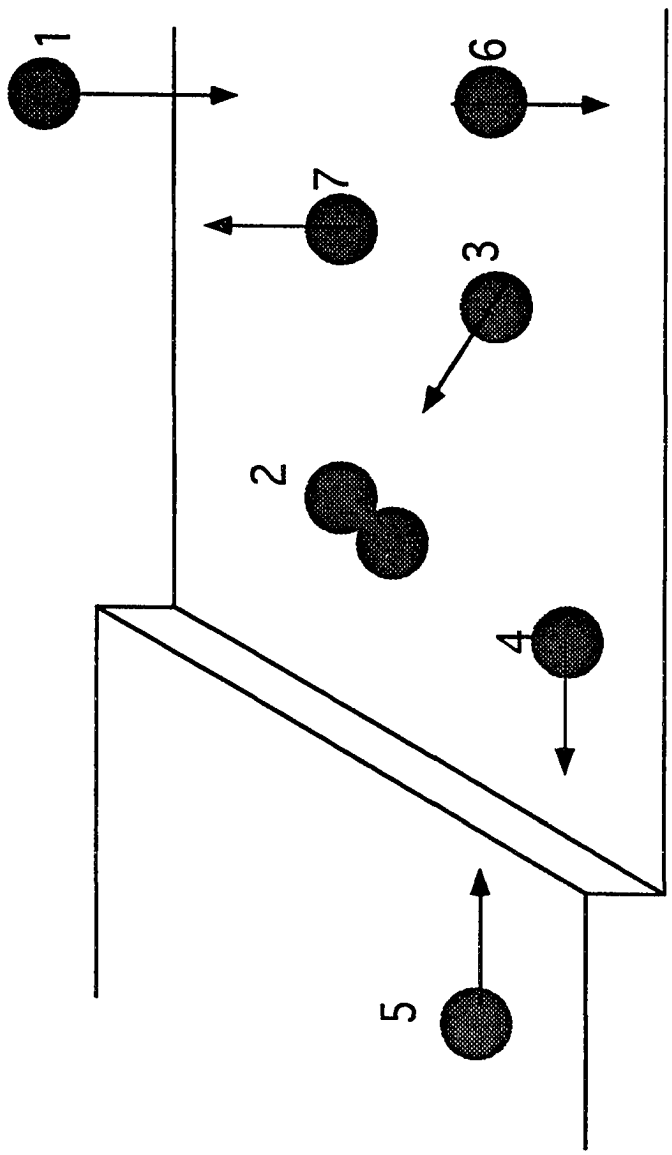
1
6
7
3
2
4
5

adatoms reaching a step from its down terrace (ascending) by surface diffusion will be trapped at the step to lower the total surface potential energy, since the surface steps are conceptually identical to 2D cluster edges. The existence of an energy barrier at a step for adatoms to cross downward is assumed for some systems, corresponding to an adatom being reflected back when it approaches a descending step. The physical picture to explain the existence of this barrier is that at the edge before an adatom is falling down over the step the adatom will have a lower coordination number and hence higher energy than on the flat terrace. In other words, the adatom would rather stay on the terrace than cross the step. This barrier also affects the smoothness of film growth. In the case where the step barrier is high, adatoms are not able to cross downward. Therefore, each adatom will be forced to stay on the terrace where it landed. Consequently, there is a difficulty to fill one layer completely, resulting in 3D growth. A knowledge of the existence of a possible barrier for downward flow is therefore of great importance for the understanding of the growth process. Since not all systems have step barriers, the physical picture mentioned above is not universal.

Once an adatom reaches to an edge, it may diffuse to find the edge site with lowest energy and then stay there. If its binding to the edge is not very strong or the temperature is high enough, the adatom may diffuse along or even desorb from the edge. The ease with which adatoms can move along the edge depends upon the atomic structure of the edge and the interaction between the adatoms and the edge. The diffusion barrier for edge migration is lower than that for laterally desorbing from the edge onto a terrace, but higher than that

for migrating on the flat terrace because of the extra bonding with edge atoms. Due to these possible interactions between adatoms and steps, the growth kinetics can change dramatically. Furthermore, the important role steps play in film growth can be described by a process known as step propagation. In this process the incorporation of adatoms to steps dominates over nucleation and growth on terraces. It can considered as a heterogeneous nucleation process at steps and the result is step growth. This process is more likely to occur on high step density surfaces.

b. General experimental methods

Physical and chemical properties of thin films are determined to a large extent by their structure and morphology, therefore by the growth mode. Studies on these subjects have revealed a variety of complex atomic surface structures and growth behaviors. Some of these studies have employed averaging techniques, such as scattering methods and diffraction methods, from which local atomic structures and film morphological information can only be obtained indirectly. The different growth modes have been investigated from the coverage dependence of spectroscopic intensities or from the intensities/widths of diffraction beams at different coverages. Other studies have involved high resolution tools to reveal detailed local information on the atomic scale directly. These methods include field emission and transmission electron microscopes, but due to experimental limitations, only limited systems have been studied under extreme conditions. Basically, these methods can track the system for a very long time. Surface structure and morphology changes as a

function of time can provide insight to the kinetics. These are direct measurements. A newer technique, scanning tunneling microscopy (STM) can provide, in real space, direct information on film dynamics with high resolution and large field, because of the local nature of the measurements. In particular the different aspects of the later growth stages can be studied and understood to a large extent from systematic STM observations. Thus, more and more studies have been carried out with this tool. In this chapter, section 4, a discussion of STM's principles of operation will be given.

3. Literature review

The purpose of this section is to provide a brief review on published experimental results regarding surface diffusion and coarsening.

From the aforementioned description of growth processes, the dynamics of adatoms and clusters are very important to film morphology and structure. In fact, surface diffusion is one of the most important fundamental interactions in the metal-on-metal thin film growth. In all stages of film growth, diffusion is the central step involved. As Doll and Voter have said, "*Diffusion plays the role in interfacial phenomena that gas-kinetic collisions do in gas-phase chemistry. An understanding of surface diffusion is a prerequisite for understanding the rate of a variety of interfacial phenomena, including surface chemical reactions, crystallization, annealing , and vapor deposition. Conversely, surface diffusion itself serves as a valuable microscopic probe of both surface topography and adsorbate/surface interactions*"[1]. Only under extreme conditions, such as when the

substrate temperature is low enough, or when the binding between adatom and substrate is very strong, are the adatoms fixed on the sites where they land. In this growth regime, diffusion is not operative and will not be discussed in this study. We will begin with single atom diffusion.

A substrate is not flat. From the microscopic view, there are steps, defects, and contamination. At the atomic level, the arrangements of surface atoms affect surface corrugation. For example, an fcc(111) surface is less corrugated than an fcc(110) surface. The moving of adatoms from one surface site to another is called surface diffusion. Surface diffusion encompasses a broad phenomena. The atomic motion on the surface can include that of individual atoms and clusters, diffusion of vacancies, rearrangement of clusters, and stability of clusters. The direct consequence of these
motions is changes in surface morphology and surface features.

The traditional picture of single atom diffusion on low-index surface is the hopping of the atom, i.e., the atom moves from one energy minimum site to another minimum site via a potential minimum pathway, a saddle point. A simple picture of atom hopping on surface can be viewed as a rigid spherical ball rolling on a rigid surface lattice consisting of a matrix of rigid balls. The activation energy for surface diffusion is the energy difference between the saddle point energy and the energy associated with the equilibrium binding position. One expectation would be that increasing the binding energy of the atom to the surface will make the atom more difficulty to migrate, i.e., higher activation energy. Another expectation would be that rougher surfaces will have a higher activation energy

due to higher saddle point. The diffusion of single metal atoms on metallic surface has been studied mainly by field ion microscope (FIM). FIM is capable of locating the position of an atom. An individual atom on a well defined low-index single crystal surface can increase local field strength, and therefore, enhance field ionization. A bright spot due to the higher emission is an indicator of the location of the atom. The locations of the atom as a function of time can provide diffusion information. Due to the nature of FIM, a limited number of surfaces have been used to study different problems. Wang and Ehrlich [2], and Bassett and Parsley [3] have measured diffusion barriers for various metal atoms (Pd, Ni, Rh, Ir, and Re) on W(211). They found that with increased bulk sublimation energies of the elements, the diffusion barriers were increased. This means that the surface diffusion barriers were higher for higher-melting-point metals. Tung and Graham [4] measured Ni on Ni(110). The row-and-trough surface of fcc(110) is a good choice to examine the anisotropic diffusion behavior. When the activation energies for in-channel and cross-channel diffusion were compared, they found in-channel diffusion had a barrier of 0.23 eV while the other was 0.32 eV. Ayrault and Ehrlich [5] conducted a systematic study of Rh on Rh surfaces with different atomic roughness. They found that the activation energy increased with increased atomic corrugation of the surface. For the more isotropic surfaces (111) and (100), with increased corrugation, the barriers were 0.16 eV and 0.88 eV, respectively. The isotropic surfaces are surfaces which have identical atom arrangement in both the x and y directions on the surface plane. The anisotopic surfaces are surfaces with different atom arrangement in x and y directions on surface plane. For anisotropic surfaces (311), (110), and (331), with

increased corrugation, the barriers were 0.54 eV, 0.60 eV, and 0.64 eV, respectively. Chen and Tsong [6] measured Ir self-diffusion on unreconstructed and reconstructed Ir(110) surfaces. They concluded that the higher diffusion barrier in reconstructed Ir(110) in-channel diffusion than that in unreconstructed was due to a slightly larger corrugation after reconstruction.

In addition to the traditional diffusion pattern, a second diffusion mechanism for single atoms is proposed, i.e., exchange-displacement, to interpret unexpected experimental results. Bassett and Webber [7] studied Pt self-diffusion on Pt(110). They reported that on this row-and-trough surface, instead of seeing the expected anisotropic motion of the atom, the atom had 2-dimensional migration and the diffusion barrier of in-channel diffusion was similar to the barrier of cross-channel motion. To explain this surprising experimental finding, they proposed the exchange-displacement theory, in which diffusion in the cross-channel direction results when an adatom pushes one atom in the channel wall onto the adjacent channel and then itself occupies the channel wall position. Because the atoms in the channel wall have less bonding than atoms on the terrace, these atoms are easier to replace energetically. Wrigley and Ehrlich combined FIM and time-of-flight mass spectrometry[8] to provide more experimental evidence to support the exchange-displacement mechanism by their study of W on Ir(110). This system is a heterogeneous system, and the chemical identity of adatom and wall atom can be detected. Mass spectrometry was used to identify the atoms monitored by FIM. More convincing results came from Pt on Ni(110) [9].

Since the exchange-displacement mechanism was proposed and confirmed

experimentally in 1978, all measurements were done on rough surfaces such as fcc(110). However, the theoretical work about self-diffusion on fcc(100) by Feibelman [10] indicated that the exchange-displacement process can take place on atomically-smooth surfaces since the activation energy of this process is less than that of hopping process. The exchange mechanism on an atomically-smooth surface is as follows: The adatom occupying the four-fold hollow site on a fcc(100) surface, for example, starts pushing down toward one of the four surface atoms forming a four-fold hollow site. The adatom is lowering its height while the surface atom is raising its position. At the saddle position of the process, these two are at same level above the surface, and the bonding configurations are the same. Then, the adatom starts to move into the vacancy left by the surface atom. At the same time, the surface atom moves to the diagonally opposite four-fold hollow site. That the exchange-displacement mechanism is favored over traditional hopping can be explained because the former allows less bond-breaking during the process than the latter. Kellogg and Feibelman [11] and Chen and Tsong [12] confirmed this mechanism by their studies of self-diffusion on Pt(100) and Ir(100), respectively. Ni on Pt(100) [13] and Pt on Ni(100) [14] also follow the same mechanism. It will be very interesting to see whether this mechanism can occur on the atomically-smoothest surfaces, fcc(111) or hcp(001). So far, there are no reports.

Metal cluster diffusion has also been investigated, mainly with FIM. Both the motion of individual atoms in the cluster and the motion of the center of the cluster attract a great deal of attention [15-18], since the relationship between individual atom displacement and the center of the entire cluster can provide information on the cluster diffusion mechanism.

The center of the cluster can diffuse because of the movement of atoms around the cluster periphery, and because of dissociation-reattachment of periphery atoms. The cluster may migrate under simultaneous movement of every atom in the cluster, i.e., the entire cluster gliding on the surface.

Dimers, the smallest possible cluster, have been studied extensively. For row-and-trough surfaces, two types of dimers exist. If the dimer is oriented perpendicular to the surface row, the dimer is called cross-channel dimer. When the two atoms are oriented in the same direction as the rows, the dimer is named an in-channel dimer. There are many studies about cross-channel dimer diffusion. All these studies show that individual atoms undergo a series of motion which causes the dimers' mobility. Studies of Re_2 on W(211) [15], W_2 on W(211) [16], W_2 on W(110) [17], Pt_2 on W(110) [18] all suggested that the displacement of the center of cluster was due to displacement of each atom, not due to the simultaneous movement of the whole cluster. Furthermore, the activation energies for dimers in many cases were found to be comparable to or smaller than that for single atom, such as W_2 on W(110) [19], Rh_2 on W(110) [20], Mo_2 on W(211), Re_2 on W(211) [15], Pt_2 on W(110) [18]. The possible explanation for this observation is that the dimer stays at a surface with less potential roughness than the monomer does [21]. This helps to reduce the diffusion barrier. The energies at saddle points will also be reduced due to interaction between atoms of cluster [15,22,23,24]. These observations show that cluster diffusion is as important as single atom diffusion during thin metal growth.

Experimental studies are also available for clusters larger than dimers, but the

number is limited and the clusters are general smaller than 20 atoms. A study of Pt on Rh(100) [25] indicated hexamers have a higher activation energy than trimers, tetramers, and pentamers which have the same activation energy. The observed cluster shapes may help to explain the results. The trimer, tetramer, and pentamer are most stable when they line up with a one-dimensional configuration. The same shape in clusters (n=3,4, and 5 respectively) may be responsible for the same activation energy if they have same rate-limiting step in the diffusion process. For the hexamer, the most stable configuration is a two-dimensional cluster. The different rate-limiting step with a higher barrier gives the hexamer lower mobility. A study of Ir self-diffusion on Ir(111) by Wang and Ehrlich [26] showed Ir atoms migrating on the edge of a 12-atom cluster and consequently the center of the cluster had a short displacement.

The general trend of the relationship of the cluster size with activation energy is that the activation energy increases as the cluster size increases for these small clusters. Pt on W(110) [18], Ir on Ir(111) [27], Rh on W(110) [20] all indicate this general trend. However, Kellogg [28] reported an interesting result for Rh cluster (2-12 atoms) diffusion on Rh (100). He found that clusters with a square or rectangular shape have higher activation energies than clusters with extra atoms at the cluster edges. Thus, the activation energy of diffusion exhibits an oscillatory behavior as a function of cluster size. This behavior rules out the gliding of the entire cluster as the diffusion mechanism. Instead, atom migration around cluster edges is more likely for these small clusters, since extra energy is needed to release an atom from an edge of the cluster.

Thus far cluster diffusion has been shown to include individual atoms in a cluster contributing to the entire cluster's motion via hopping. There is little experimental evidence showing that individual atoms can facilitate the cluster diffusion via exchange [29]. Kellogg and Voter showed the that Pt dimer on Pt(100) diffuses via an exchanging process in which one atom exchanges with a substrate atom in a similar manner as in the monomer case and the other atom in the dimer basically stays stationary. The results of the displacement are that the center of the dimer moves and the dimer changes orientation. The activation energy for this process is lower than that of the monomer. For Pt trimers, the exchange and hopping both contribute to the motion of Pt_3, and the activation energy is comparable to that of the monomer.

FIM has been proven to be a successful and mature method to measure adatom and cluster diffusion on surfaces. During the last three decades, FIM has been the main technique to provide understanding of the fundamental phenomena of diffusion of atoms and small clusters at the atomic-scale. Very detailed diffusion information is available only for atom/small cluster. However, this method has severe drawbacks, including that the substrate is limited to a very small size, generally around 100Å. In an FIM apparatus, the substrate is in the form of a tip. Therefore, the substrate materials are limited to those from which an emission tip can be made. The tip has surface structure other than an ordinary crystal surface. An FIM tip has a near circular shape with descending steps at the edge of the terrace in all directions. Coexistence of planes with different Miller indices may be the case. Under these conditions, therefore, the size of the cluster for a specific surface plane is

limited.

Compared with FIM, STM is a relatively new technique. It can view a larger area with atomic resolution than FIM. The intermediate length-scale of the observation it provides can be very useful for understanding thin film growth, since this is the area range between FIM and averaging techniques such as diffraction and scattering methods. One example of an averaging method was the characterization of diffusion of Cu on Cu(100) indirectly. Ernst [30] used He scattering to investigate the system over a wide range of coverage and temperature. They concluded that the diffusion of Cu adatoms on Cu(100) is via exchange.

STM has been used in studies of nucleation [31,32,33,34], island shape and size [35], growth mode [36,37], and interactions between adatoms and steps [32, 35]. A few measurements of diffusion with STM at an atomic level are available. Gane and coworkers[38], using STM, observed that isolated Pd adatoms can diffuse on Ge(111) at elevated temperatures via the exchange pathway. The same group also described concerted motion of an adatom row on Ge(111). Mo [39] and Stroscio [40] used STM to measure the average island density to obtain diffusion information with the modeling of the nucleation and growth processes. In another STM study, Sb on Si(001)[41], Mo usedSTM to study the Sb dimer diffusion. For metal-on-metal systems, no experimental literature is available on the mobility of large clusters.

Vacancy cluster diffusion can play an important role in film ordering kinetics. 3D vacancy clusters have been studied extensively in crystal growth processes and in metallic

alloys [42,43,44,45,46]. Recently the study of two-dimensional vacancies emerges. A two-dimensional vacancy cluster can be viewed as the inverse of a two-dimensional cluster. Thus, STM is an ideal tool to study this phenomenon also. One recent STM experiment by de la Figuera *et al.* [47] showed that artificially created (with STM tip) two-dimensional Cu vacancy clusters on clean Cu(111) are immobile, but on Co-modified Cu(111), Cu vacancy clusters undergo surface diffusion. The presence of Co on the Cu surface is needed to lower the surface diffusion barriers. Another example of 2D metal vacancy diffusion was shown by Comsa [48]. Ag vacancies were created by ion sputtering on a Ag(111) surface. Brownian motion described the diffusion of the vacancies. The relationship between cluster size and diffusion coefficient is also addressed. All these studies were carried out on a triangular substrate.

Once a film has been deposited, two processes are considered as main contributors to the evolution of the films: Ostwald ripening and dynamic cluster coalescence. The concept of Ostwald ripening was first developed by Ostwald [49], then later advanced by Lifshitz, Slyozov and Wagner [50,51]. This phenomenon has been studied extensively [52]. The idea of dynamic cluster coalescence was first used in thin film growth by Zinsmeister [53]. This term refers to the coalescence of clusters due to random motion. It has been found that cluster mobility can affect film growth in many aspects, such as the cluster size distribution [54]. Both Ostwald ripening and dynamic cluster coalescence will result in a decrease both in the number of clusters, and the size distribution as a function of time for these mechanisms. It is difficult to distinguish these two mechanisms by just looking at the

final results [55]. In experimental studies of later stage growth, the cluster size and shape are characterized with scattering methods [56], scanning electron microscopy (SEM) [57], scanning transmission electron microscopy (STEM) [58], low energy electron microscopy (LEEM) [59], and STM [60,61]. Futamoto, *et al* [57], by using SEM, showed Ga clusters on GaAs(001) underwent different coarsening processes under different conditions, i.e., at 833K cluster coalescence dominated, while at 758K Ostwald ripening dominated. SEM was also used to investigate systems involving metals: Ag on Mo(100) [62], Ag on W(110) [63], Ag on Si(111) [64]. However, the studies were limited by the low resolution of SEM. LEEM, with higher resolution (~20Å), was used by Bauer [59] to observe the cluster dynamics of Au on Si(111). STM was used on Si, Ge on Si(100) [60,65] to study cluster shape and size. On Fe/Fe(100), STM was used to analyze the cluster density in order to characterize the growth kinetics.

In this thesis, STM is used to investigate a metal-on-metal system, Ag on Ag(100). Both large adatom cluster diffusion and vacancy cluster diffusion are studied. The mechanisms involving diffusion are discussed. Diffusion coefficients are measured. Growthprocesses in the late stage are also investigated in detail with STM. Other dynamic processes, such as biased cluster motion, are studied as well.

4. Scanning tunneling microscopy

a. Introduction

Since its first successful operation with atomic resolution in 1982 [67], scanning tunneling microscopy (STM) has been widely used to study a great variety of problems, including many traditional surface science problems, as well as many new ones. This technique redefines the concept of microscopy because it allows us to see atoms and other small features on surfaces in a wide range of environments such as in air, liquid, and ultrahigh vacuum [68]. In this section, the general concepts of STM are discussed.

Because of its atomic resolution and the ability to scan large areas, STM is an ideal tool for studying surface kinetic processes at the atomistic level. Using STM, we are capable of achieving a more accurate and comprehensive understanding of growth processes microscopically. This technique is based on quantum mechanical tunneling, in which electrons penetrate with nonzero probability through an energy barrier higher than the electrons' total energy. In STM, an atomically sharp metal tip is brought within a few Å to a sample surface such that the wavefunctions of the tip electron states overlap with those of the sample. A tunneling current will flow between the tip and the sample when a bias voltage is applied between them. The tunneling current has exponential dependence on the distance between the tip and the sample, i.e., the thickness of the barrier. At a typical tunneling distance, a roughly one Å change in the gap spacing will cause the tunneling current to change by a factor of ten. In the operation of an STM, piezoelectric elements (orthogonal piezoelectric triple or piezoelectric tube) force the tip to move in three

orthogonal directions: X and Y parallel to the sample and Z perpendicular to the surface. As the tip scans across the surface, the width of the microscopic tunneling gap changes due to the surface corrugation in the electron density contours, resulting in a change in the tunneling current. If this changing tunneling current is plotted vs. the X and Y positions, it directly gives an image of the surface corrugation. Another way to scan is to control the tip in the z direction with a feedback voltage to maintain a constant tunneling current, then to plot current vs. the X and Y positions to reflect the surface corrugation. This latter mode is called the constant-current mode. This constant-current contour mapping is most widely used because the feedback circuit prevents the tip from crashing into the surface, which is particularly important for rough surface. Because of the sensitive dependence of the current on the gap spacing together with an atomically sharp tip, an STM has extremely high resolution: ~1Å laterally and ~0.1Å vertically, thus enabling us to resolve atomic features on the surface. Furthermore, there is no fundamental limit on the maximum scanning range of STM, and views of large areas with atomic resolution can be obtained.

b. Theory

It is a great challenge to interpret STM images theoretically, since a theoretical treatment needs to relate the constant-current contours to the variation of surface properties of the samples. Early analyses of the tunneling current and STM image were based on analogy with the one-dimensional tunneling problem [69]. The relationship between current I and bias V is obtained from the following equation at low voltage and temperature [69]:

$$I \propto \exp(-2kd)$$

where k is the decay constant of the wave function in the tunneling barrier, and d is the separation between sample and tip. The decay constant, k, is related to the effective local work function ϕ by $k=(h/2\pi)^{-1}(2m\phi)^{-0.5}$. The exponential dependence of the tunneling current on distance gives STM its high sensitivity.

However, when considering STM scanning on a surface it is necessary to solve the three-dimensional tunneling problem. This involves the electrodes' Fermi level states which have complex spatial structures, leading to complex electronic interactions between electrodes. Moreover, it is uncertain what the distance, d, actually rerpresents under this 3D scanning condition.

One of the most successful attempts to interpret STM images has been made by Tersoff and Hamann [69]. They considered that the tip-surface interaction was weak when the separation was about a few Å. These two weakly coupled electrodes allowed them to use first-order perturbation theory based on Bardeen's transfer Hamiltonian approach. This method requires explicit expressions for the wavefunctions of the tip and the sample surface. Since the actual atomic structure of the tip is generally not known, they started with the simplest possible model, a spherical symmetric wavefunction, for the tip. The size of the tip is not important as long as the spherical symmetric wavefunction is maintained. Their results state that the tunneling conductance is proportional to the local density of states of the sample, at tip position and at Fermi energy. The tip path maps out a contour of constant Fermi-level local density of states (LDOS) of the surface. This theory has clarified

many important questions such as the resolution of the microscope. This theory is used to explain the STM images of the reconstructed Au(111) surface, which has a larger surface unit cell than a normal metal surface lattice [69]. However, the theory is somewhat simplistic, since both geometric and electronic structures of the tip must play an important role in the formation of the image. Thus this theory can be considered as a "macroscopic" approach. The theory cannot provide an explanation of the STM atomic resolution on a close-packed metal surface.

Taking into account the atomic structure of the tip, Chen [70] further developed the theoretical treatment of STM theory. His theory enabled one to explain the atomic resolution STM image of Al(111), a close-packed metal surface without reconstruction. He used a d_z^2-tip. The microscopic view of STM introduced in detail by him is based on symmetry considerations of the electronic states of the tip and the sample surface and therefore emphasizes the atomic-level imaging of STM.

Lang [71] introduced a model incorporating the microscopic and macroscopic pictures of STM. He described the tip and sample by an atom adsorbed on a jellium model of the surface. This theory considers the total current due to real atoms on the sample and tip. In his work, a sodium tip was scanned over a surface with adsorbed sodium, sulfur, and helium atoms. Tip displacement versus lateral separation for constant current was plotted. This plot was compared to contour plots of constant Fermi level local density of states and constant total density for each of the three surfaces versus the sodium tip. This method successfully explained the STM images of single-atom adsorbates on metals.

A perturbative treatment of tunneling will break down if the tip-surface separation becomes extremely small, i.e., if the wavefunction overlap of tip and sample surface becomes significant. In this case, the perturbative method is no longer valid. Non-perturbative treatments of tunneling based on the Green's function method [72, 73], which goes beyond the perturbation approximation, is used to improve the approximation. These more intensive STM theories will not be reviewed here.

c. Instrumentation

(1) Scanning Mechanism

A very precise and very stable driver for controlling the tunneling tip in three orthogonal directions is necessary in STM, since the tip rasters in the X-Y plane while responding to the surface corrugation in the Z direction with a feed-back loop. Piezoelectric materials can generate mechanical strain under the influence of an electric field across them. The deformation of material can provide linear motion at the sub-angstrom level and up to a hundred micrometers [74]. This capability, as well as the simple relationship between the strength of applied field and mechanical deformation results in this type of material being used almost exclusively in STM scanners. High piezoelectric-constant piezoelectric materials are used for small scanners in order to have enough scan area.

Currently, scanners with two different configurations are widely used, tripod and single tube. In a tripod scanner, three piezoelectric material bars are mounted orthogonally to each other. Two electrodes are placed across the two ends of each other. A polarization

process is needed before the bar can be used. A high electric field is employed across the two electrodes to force the randomly oriented dipoles in the material to orient in the direction of field, and then the field is removed. The polarization of the material will remain unless it is annealed to its Curie temperature resulting in the loss of polarization. The Curie temperature is the temperature at which the material's dipoles will reorient randomly. Under the influence of an applied field with the same direction as the polarization direction, the polarized material will expand in the direction of applied field and contract in the direction perpendicular to the field direction.

The second type is a single tube scanner. The outside of the tube is sectioned into four electrically separated parts along the circumference. Electric fields with the same strength but opposite signs are applied to the two opposite quadrants. Therefore, one quadrant will expand and the other will contract. This bending will cause the lateral movement. The tunneling tip is mounted at one end of the tube. The tube is polarized radially with a field applied between the inner and outer walls of the tube.

(2) Approach Mechanism

In order to bring the tip to within a tunneling range, one must move the tip over a macroscopic distance (hundreds of microns) with a precision of several tens of nm without crashing the tip into sample. An approach device is designed to do this. Several schemes are possible. Some designs are based on purely mechanical means [74], using fine-thread screws or a level system that transforms a coarse motion into a very fine linear tip approaching

motion until the tunneling current is detected. The other type involves the expansion and contraction generated by large size piezoelectric materials with a variety of clamping mechanisms to provide step motion of the scanner.

(3) Vibration Isolation

Effective vibration isolation is one of the critical elements in achieving atomic resolution by STM. Because the tunneling current is very sensitive to the separation between the tip and the sample, any disturbance due to external vibration can cause large noise in STM signals. The typical atomic corrugation amplitude is about a few tenth of an Å. Thus, the fluctuation of the separation must be reduced to much less than 0.1Å in order to achieve a good atomic image.

To overcome the external vibration influence on the tip-sample junction, two approaches have been employed: (1) high rigidity of STM assembly, (2) a vibration isolation system [74]. In general the trend has been toward compactness and simplicity to improve rigidity. It has become clear that increasing the rigidity of STM can be more conveniently achieved than perfecting a vibration isolation system. If the gap spacing between tip and sample can be held constant against all external vibration by using a rigid STM design then no isolation system is needed. But in practice, there are some limitations in improving the rigidity of STM, for example, the approach device and sample itself need to be able to move. In addition, other factors, such as operational convenience and construction cost, should be considered. Therefore, a combination of both is widely used. To date, the suspension spring with eddy-current damping is the most efficient vibration isolation system

for a very rigid STM. However, this system is large. An elastomer system is also in use. This system uses a stack of metal plates which are separated by rubber pieces. By increasing the number of metal plates, reasonably good vibration isolation can be achieved in a modest space. If the STM is not rigid enough, oif it is maintained in an Ultrahigh Vacuum (UHV) or cryogenic environments more sophisticated vibration isolation systems are needed. Pneumatic systems, as a secondary vibration isolation stage, are often used to float the whole STM or the entire UHV-STM.

5. Dissertation organization

This thesis includes four papers. Paper 1: Diffusion of Large Two-Dimensional Ag Clusters on Ag(100), appears in Physical Review Letters Volume 73 on page 2591, 1994. Paper 2: Coarsening Mechanisms in a Metal Film: From Cluster Diffusion to Vacancy Ripening, has been submitted to Physical Review Letters. Paper 3: Large Ag Vacancy Cluster Diffusion on Ag(100), will be submitted to Surface Science. Paper 4: Surface Dynamical Phenomena, will be submitted to Surface Science. Following the last paper are general conclusions, references cited in Chapter 1, and appendices that describe the apparatus and data summary.

CHAPTER 2

DIFFUSION OF LARGE METAL CLUSTERS ON AG(100)

A paper published in the Physical Review Letters

J.-M. Wen, S.-L. Chang, J. W. Burnett, J. W. Evans and P. A. Thiel

Abstract

Scanning tunneling microscopy shows that large, two-dimensional Ag clusters on Ag(100) can diffuse. The value of the diffusion coefficient at room temperature is on the order of 10^{-17} cm^2 s^{-1} and varies little, if at all, with cluster size in the range studied, 100 to 720 atoms per cluster. This weak variation rules out periphery diffusion as the main mechanism of cluster diffusion, suggesting instead two-dimensional evaporation-condensation. This conclusion is compatible with the energetics of atomic-scale events within the cluster, and with the dissolution of small clusters observed at low coverages.

Text

Diffusion of metal clusters can be important in metal film growth kinetics [1] and in coarsening processes, such as sintering. While experimental and theoretical studies over the past 20 years have led to the general expectation that small, two-dimensional (2D) metal clusters can undergo diffusion on metal substrates [2], large 2D clusters are not generally expected to diffuse. However, in this paper we report that *very large*, two-dimensional Ag

clusters (containing ca. 10^2 to 10^3 atoms, N) undergo measurable diffusion on a Ag(100) surface. We also present estimates of the diffusion coefficient, D, of large Ag clusters, and analyze the variation of D with N. This, together with analysis of atomic-scale energetics, allows us to to infer the mechanism by which diffusion occurs.

Previous experimental and theoretical work has shown that the mobility of small clusters ($N < 20$) decreases with increasing size, although some sizes display anomalously high mobilities [3-7]. The mechanism of diffusion usually is proposed to be short-range motion of a single atom away from the periphery, followed by regrouping of the cluster around the departed atom [6, 8], with some evidence for concerted gliding also available [5]. For larger, 3D metal clusters, there exists a body of work concerning diffusion on non-metallic substrates such as alkali halides [9-11], and here it has been shown that lattice mismatch can be important in determining diffusion characteristics [9,12]. However, for large 2D metal clusters ($N > 50$) on *metallic* substrates, we know of no previous experimental observations of diffusion.

Our experimental data are acquired with an Omicron scanning tunneling microscope (STM) housed in an ultrahigh vacuum chamber, with base pressure of 6×10^{-11} to 3×10^{-10} Torr. The microscope can routinely resolve the atomic-scale unit cells within the (100) terraces. Silver is deposited on a Ag(100) crystal from a resistively-heated, liquid-nitrogen-shrouded source. Evaporation of submonolayer coverages with the crystal at room temperature results in compact, two-dimensional Ag structures, such as islands, whose position, size, and shape is followed quantitatively as a function of time over a period of

several hours. The interval between measurements is typically ten to fifteen minutes. In order to establish fixed points of spatial reference, we include in the images a step edge containing an impurity; the step edge is then assumed to be pinned in the vicinity of the impurity [13].

The Ag islands can be perturbed by the tunneling tip. For instance, efforts to obtain atomic-scale resolution on small islands ($N < 30$) invariably perturb the island. Therefore we limit examination to islands of $N \geq 100$; further, we sacrifice spatial resolution to minimize perturbation. The images are typically obtained in the constant-current mode, with 1.0-1.1 V bias voltage and 3.0-3.4 nA tunneling current. We further examine the effect of different raster frequencies. Between the minimum raster rate accessible (one image per 10-15 minute interval) and the maximum rate (ca. 7 images per interval), we find no effect on the quantitative results reported here. This suggests that the tip does not induce the motion of the clusters.

We begin with the basic experimental observation, illustrated in Figure 1. The bright spots in the image are Ag clusters in the middle of a large terrace; the larger, ill-defined white shape toward the upper right is a spot of contamination, probably carbon; the diagonal line which contains it is a monatomic step edge. The Ag islands adopt an approximately square shape, although irregularities such as rounded corners and crooked edges are common. The Ag clusters in Figure 1 range in size from 100 to 800 atoms (830 to 6640 $Å^2$). Comparison of Figure 1a with 1b clearly shows that the Ag clusters have moved in the interval between images, in this case 5.7 hours. The trajectories of two differently-

sized clusters are illustrated in Figure 2a-b. Over a period of several hours, the net displacement of the clusters is on the order of 10^2 Å. Qualitatively, the trajectories appear to be random (diffusive).

Diffusion coefficients are extracted from trajectories such as those of Figure 2. Trajectories are analyzed only for those intervals where the clusters remain constant in size, to within ±15%, and where the clusters remain at least 300 Å (and more typically, 500-600 Å) away from a step edge Figure 3 shows the quantity $\langle d^2/t \rangle$, where d is the displacement between the cluster's center-of-mass location, as a function of the mean time interval between observations, $\langle t \rangle$, for two differently-sized clusters. The diffusion coefficient, D, is then defined as $\lim_{\langle t \rangle \to \infty} D(t)$, where $D(t) = 1/4\langle d^2/t \rangle$. Thus, D is extracted from the value of the plateau in $\langle d^2/t \rangle$ at long $\langle t \rangle$. The fact that $\langle d^2/t \rangle$ does reach a plateau demonstrates that motion of the clusters, at long $\langle t \rangle$, is diffusive. However, the value of $\langle d^2/t \rangle$ *always* shows a sharp decline at small values of $\langle t \rangle$. This signifies a slight tendency for clusters to move opposite the direction of recent motion--a "back-correlation". Such an effect has not been observed in previous experimental studies, although it has been observed in simulations of cluster diffusion, where it was associated with the requirement of cluster "connectivity" [14].

Figure 4 shows the value of D as a function of cluster size, with the experimental data represented by crosses. For $100 \leq N \leq 720$, D varies from 5.3×10^{-18} to 2.7×10^{-17} $cm^2\ s^{-1}$. However, there is little--if any--systematic variation of D with N (a factor of two

Figure 1. STM images obtained following deposition of 0.007 monolayers (ML) Ag on Ag(100) at room temperature. Deposition rate is 4×10^{-3} ML/s.

(a) t = 0 hr. (b) t = 5.7 hr

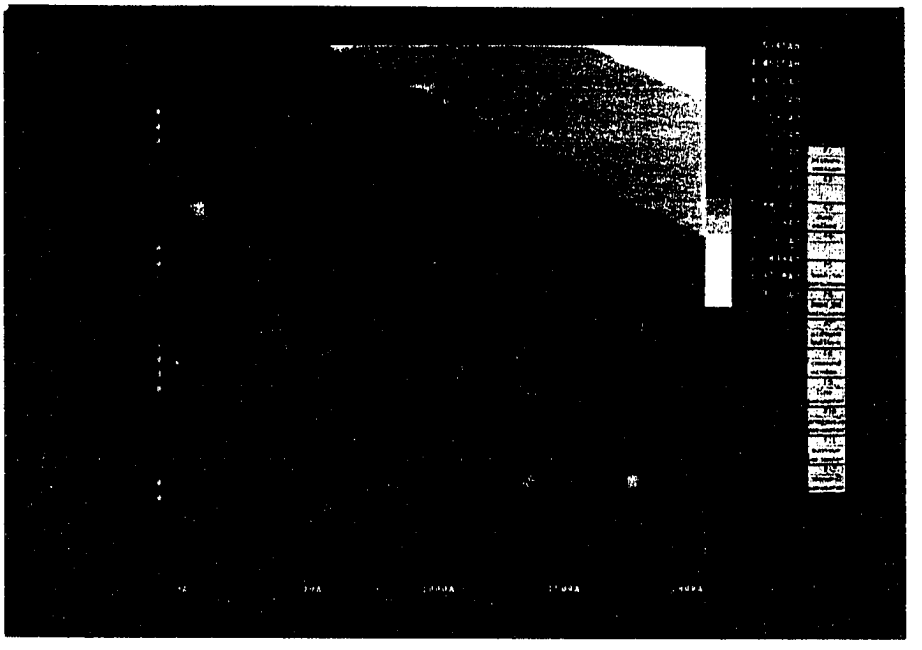

(a)

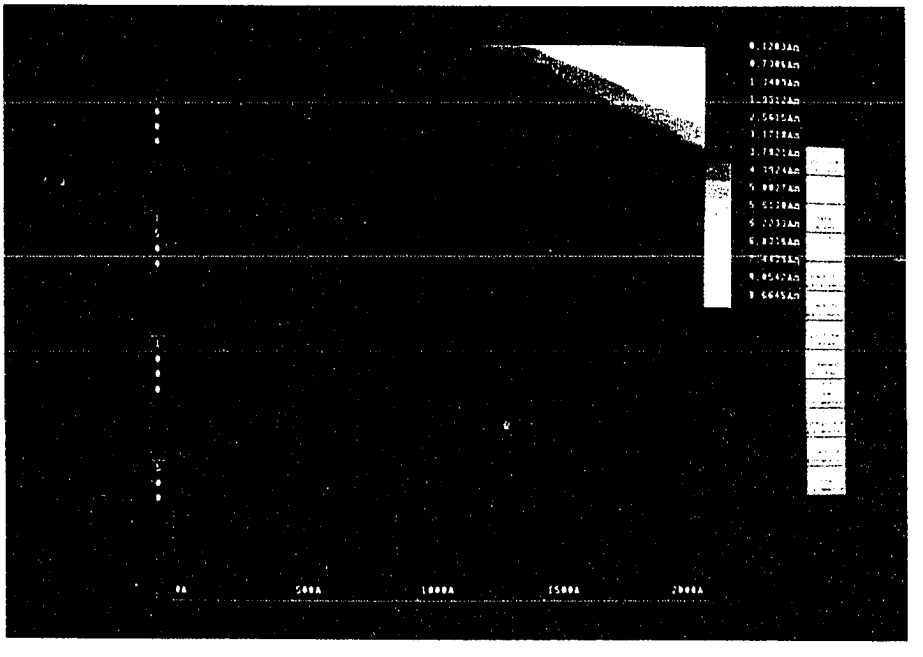

(b)

Figure 2. Trajectories for two differently-sized clusters. The starting and final locations are indicated by s and f, respectively. (A) N= 110. (B) N= 290.

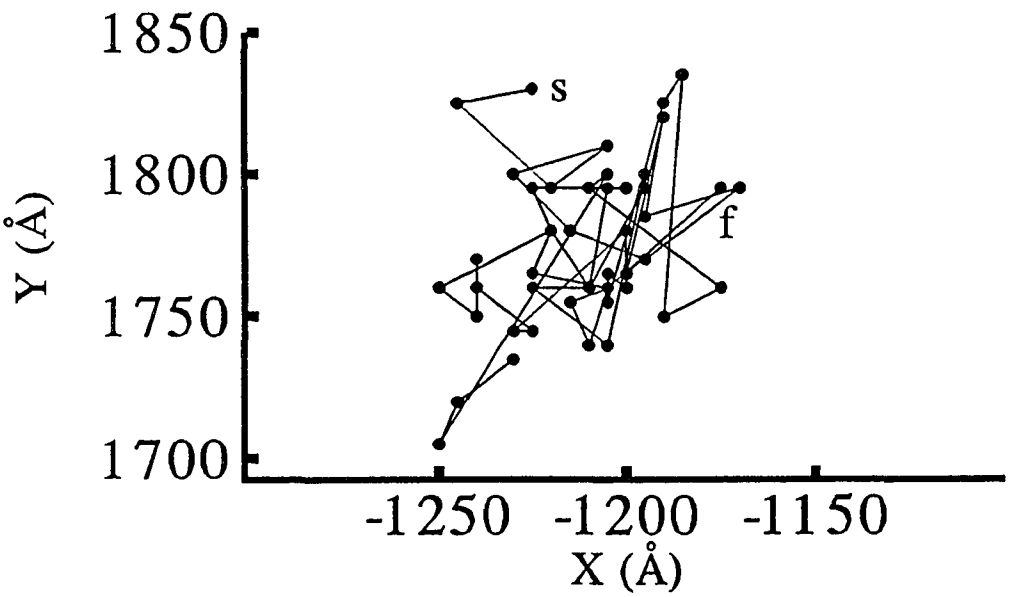
1850
1800
1750
1700
Y (Å)
s
f
-1250
-1200
-1150
X (Å)

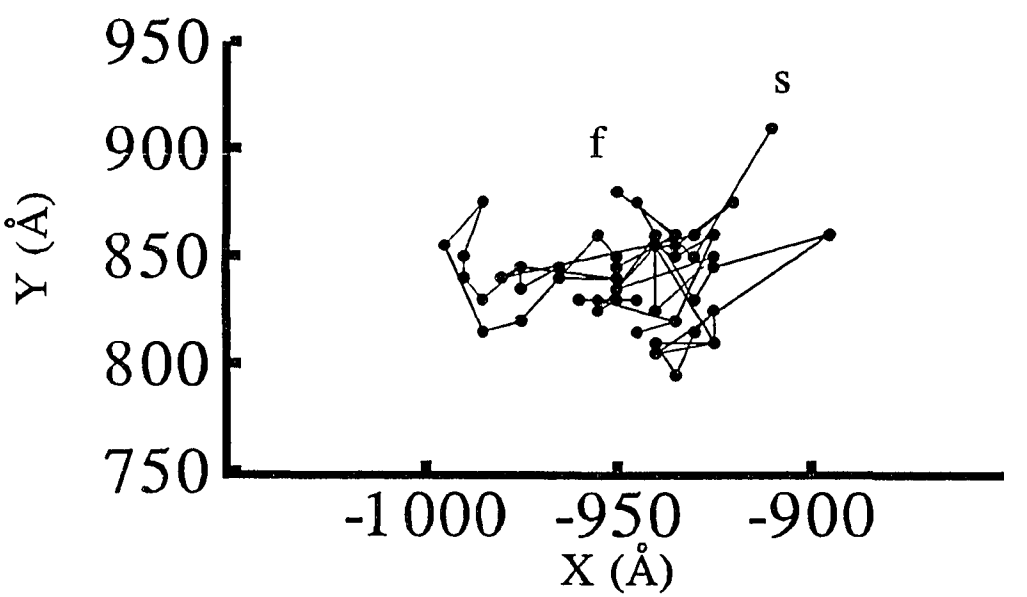
950
900
850
800
750
Y (Å)
s
f
-1000
-950
-900
X (Å)

Figure 3. <D2/t> vs. <T>, corresponding to the trajectories of Fig. 2. (A) N= 110. (B) N = 290.

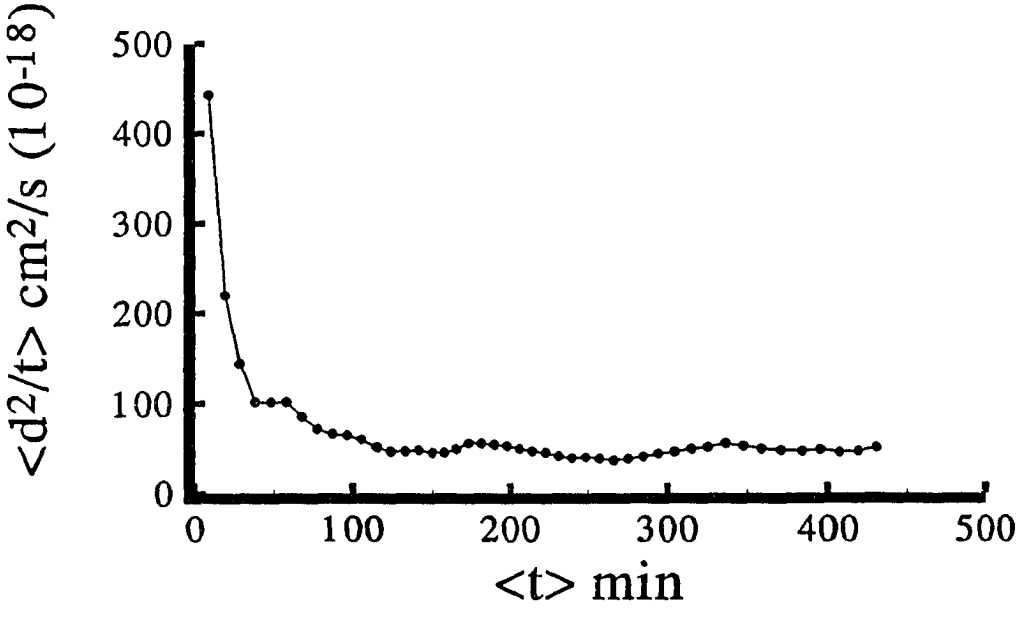
<d2/t> cm2/s (10-18)
500
400
300
200
100
0
0
100
200
300
400
500
<t> min

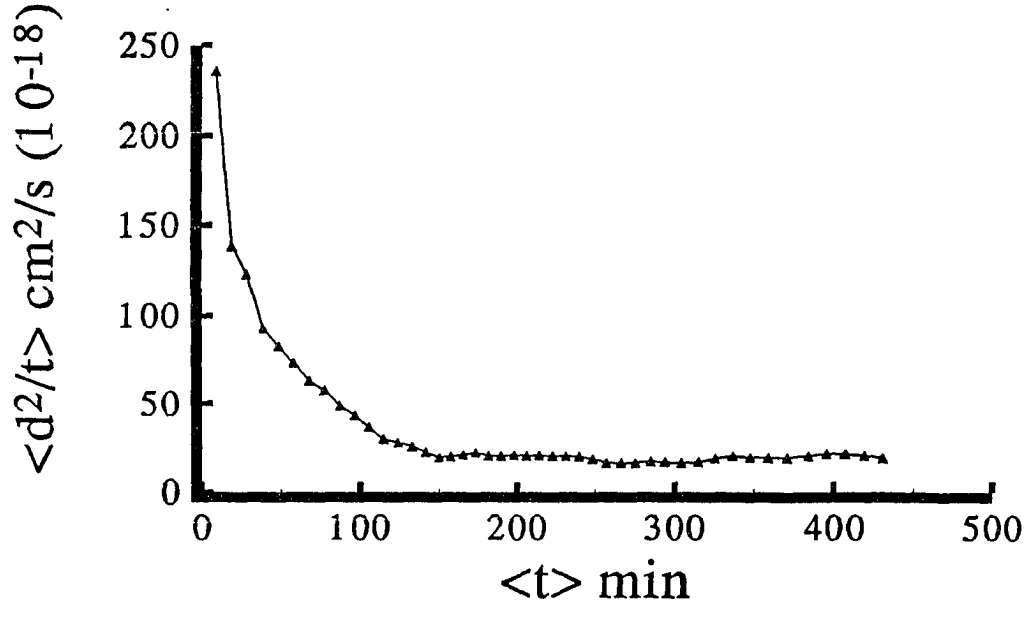
<d2/t> cm2/s (10-18)
250
200
150
100
50
0
0
100
200
300
400
500
<t> min

at most).

It is worth considering the possibility that adsorption of background gases plays some role in cluster diffusion, especially in light of the work by Cooper et al. showing that atmospheric contamination can strongly influence mass transport on Au [15, 16]. While adsorption of background gases can never be ruled out entirely, there are several factors which make the role of such contaminants unlikely here. First, in these experiments no static contaminants are imaged with the STM on the Ag(100) terraces; as noted above, the unit cells of the clean metal can be routinely resolved, and one would expect contamination at the surface to perturb such an image significantly--as it does at the steps. Second, Ag is inert toward most common gases at room temperature. Third, when the edges of the large clusters are imaged, they appear frizzy *(vide infra)*; in our experience, this frizziness is only obtained when foreign material is absent from the step edge [17]. Finally, the value of D we measure on an obviously-contaminated terrace is drastically lower than that which we report here. We consider two main, non-exclusive mechanisms which could facilitate cluster diffusion. The first is periphery diffusion (PD), i.e. atomic motion along the cluster periphery. The second is two-dimensional (2D) evaporation-condensation (EC), in which atoms leave and re-attach to cluster edges. In the EC mechanism, clusters are in a dynamic quasi-equilibrium with a dilute 2D gas of Ag atoms on the terrace. It might be anticipated that the PD mechanism would always dominate, since barriers for atoms to move along the edge are intuitively expected to be much lower than for atoms to leave (evaporate from) the cluster. Ultimately, we shall show that this is a false expectation. First, however, let us

assess which mechanism is most compatible with the experimental data.

Comparison of the EC and PD models with experimental data hinges upon predictions of D as a function of N. Specifically, we seek the exponent a which describes $D \sim N^{-a}$, for large N. For PD, Monte Carlo simulations are available which yield exact results, showing $a \sim 1.5$ to 2 [14, 18, 19]. Two of the simulations have even specifically modelled metal-on-metal systems, $Ag_N/A(100)$ v $Rh_N/Rh(100)$, and both yield $a \sim 1.75$ [18, 19]. The strong variation of D with N given by this value of a is shown by the solid line in Figure 4; it is clearly incompatible with the experimental results.

Unfortunately, there are no corresponding simulations available for the EC mechanism. In order to assess D(N) for EC, we can write [14, 20]

$$D \sim \langle H_N \rangle \langle \delta d_{CM}^2 \rangle. \qquad (1)$$

For EC, $dd_{CM} = 1/N$ is the center-of-mass (CM) displacement of the cluster in lattice constants, per edge-atom removal; and $\langle H_N \rangle$ is the total evaporation (or condensation) rate. If $\langle H_N \rangle \sim N^{0.5}$ for compact clusters, then $D \sim N^{-0.5}$. This relatively-weak dependence on N is shown by the dashed line in Fig. 4, and is roughly consistent with the experimental data. Note that for PD, $\delta d_{CM} = 1/N$ per edge-atom hop in Eq. (1) and $\langle H_N \rangle$ is the total rate of edge hops contributing to cluster diffusion [20], again assumed to vary as $N^{0.5}$. Hence, $D \sim N^{-1.5}$ for the PD mechanism from Eq. (1), in reasonable agreement with the Monte Carlo simulations. The main point, overall, is that the experimental data favor the

EC mechanism, based upon predictions of D(N) for both models.

In order to understand further the diffusion mechanisms and their ramifications, consider the atomic-scale processes which may occur at the edge of a cluster. Starting with the PD processes, they are shown by Figure 5a through c'. The activation energies calculated from the Embedded Atom Method (EAM) indicate that energy barriers are about equal for the processes represented by Figure 5b and b'. The same is true for Figure 5c and c' [19]. Using the EAM-based barriers, relative rates are also predictable, with the fastest processes represented by Figure 5a (ca. 10^{-8} s), next-fastest by Figure 5b,b' (ca. $10^{-3.5}$s), and slowest by Fig. 5c, c' (ca. 10^{2} s) [19]. Experimental data support the idea that one or more of the 'fast' processes does occur, on a time-scale which is at least shorter than the imaging process: with atomic-scale resolution, edges of large terraces and large islands appear frizzy in our STM images. In studies of other metal surfaces, this phenomenon has been attributed to escape of atoms from kink sites (Figure 5b) [21, 22]. Thus, one might expect that the fast, easy processes of Figure 5a, b, and b' dominate cluster diffusion, at least under the PD mechanism. However, this is not true because of a 'core breakup' requirement. At any moment in time, the cluster can be conceptually divided into a rough edge zone, and an inner, rectangular core. The core is outlined in Figure 5. If atomic-scale motion is limited to the edge zone, i.e. if only the fast processes occur, the inner core cannot move. With such a limitation, only slight displacements in the center-of-mass take place, due to fluctuations in atom distributions along the edges, and the cluster is effectively "tethered" by the core. Long-range motion, such as we observe, requires that atoms

Figure 4. Diffusion coefficient at room temperature as a function of cluster size. Each cross represents experimental error estimated for each data point, not a statistical variance. Solid line shows scaling relationship $D \sim N^{-1.75}$ [18], arbitrarily placed to coincide with experimental values at $N \sim 10^2$. Dashed line shows $D \sim N^{-0.5}$ as discussed in text, placed similarly.

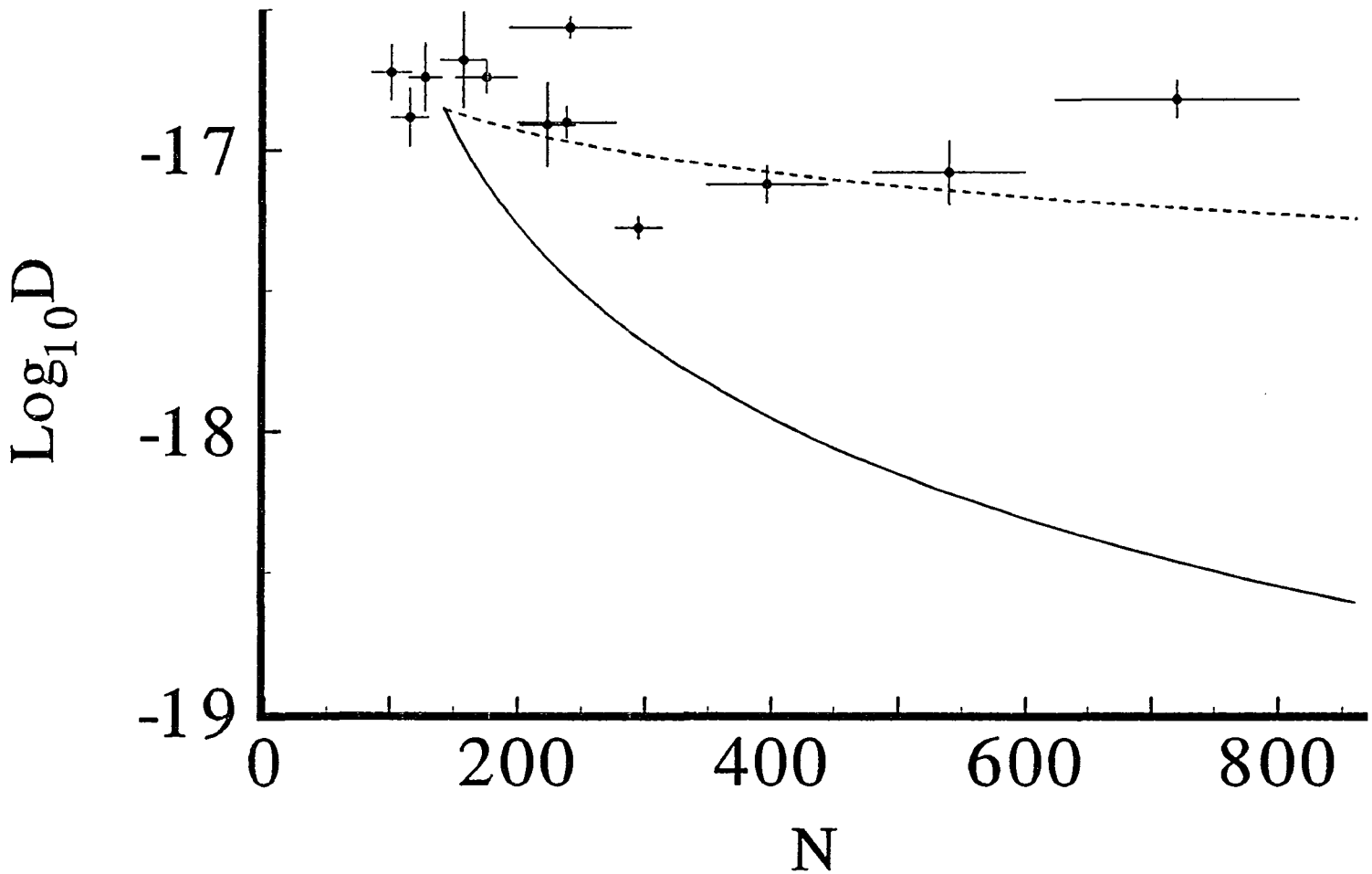
-17
-18
-19
$Log_{10}D$
0
200
400
600
800
N

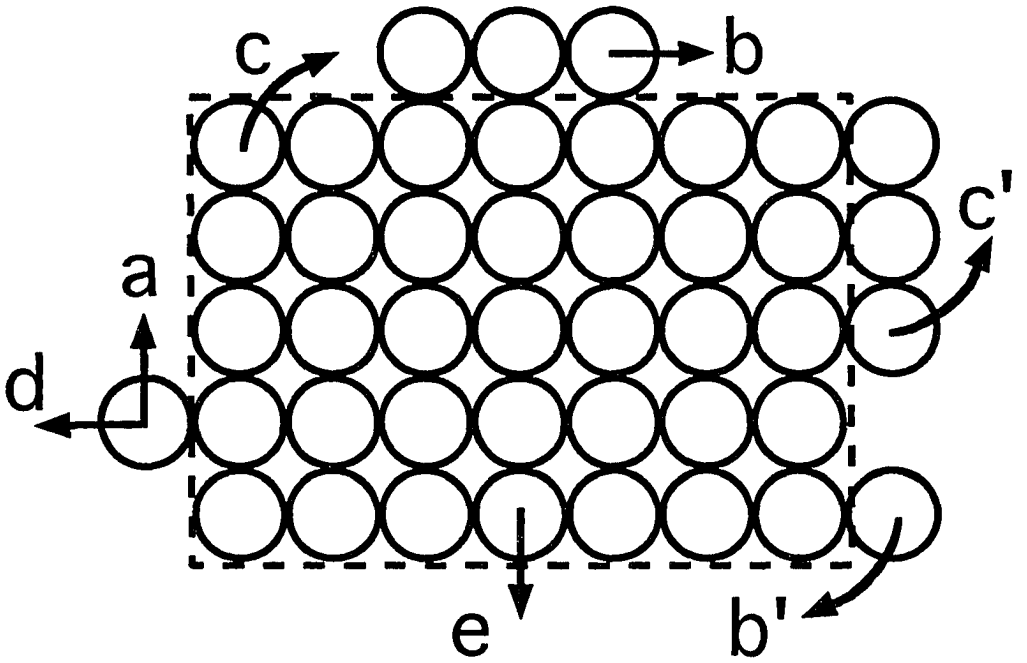

Figure 5. Schematic representation of atomic-scale processes. Rapid single-atom edge-diffusion (a). Less-rapid escape from kinds (b). And corner-rounding (b'). Slow core break-up (c), climbing onto a fresh edge (c'), or evaporation (d). Core break-up via (e) is effectively inoperative at 300 K. The dashed line shows the cluster "core".

exchange with the core itself. Hence, in PD, long-range diffusion is dominated by the slow processes of Figure 5c, wherein atoms leave the core.

Proof lies in EAM studies which show that, when clusters are constrained to diffuse via PD, i.e. when detachment is not allowed, core breakup is rate-determining [18, 19]. More specifically, Voter's EAM-based simulation of large Ag cluster diffusion via PD [19] yields a variation of D with N which can be fit by

$$D \sim 0.03N^{-1.75}\exp[(-0.82eV)/k_BT]\ cm^2s^{-1}. \qquad (2)$$

The barrier of 0.82 eV in Eq. (2) corresponds precisely to the EAM barrier for core breakup. Interestingly, Eq. (2) yields a value of D 1.6×10^{-19} cm^2s^{-1} for N = 100 at 300 K, which is two orders of magnitude below the experimental value. However, the experimental value of D can be recovered by retaining roughly the same barrier (vide infra) and prefactor in Eq. (2), but replacing the N-dependence by $N^{-0.5}$, as predicted by Eq. (1) for EC. This, plus Voter's observation that clusters tend to dissociate rather than move over distances > 10 Å [19], also supports EC rather than PD.

Core breakup is actually required for long-range diffusion under *both* of the mechanisms postulated here, PD and EC. The difference is that in PD, core breakup alone causes long-range diffusion, whereas in EC, core breakup must be followed by atom detachment (Figure 5d). In fact, EAM studies of metal systems show that the effective barrier for evaporation [23], and thus for EC, is comparable to that for core breakup [19].

Thus, if the barrier for core breakup can be surmounted, so too can that for evaporation. It follows that any intuitive expectation that PD dominates over EC, based on atomic-scale energetics, is false.

If core breakup and evaporation have comparable barriers, why then should either EC or PD prevail? The answer must lie in the weights associated with the rate-limiting events. For instance, in Eq. (1), the values of δd_{CM}^2 are N^{-1} and N^{-2} for EC and PD, respectively. In other words, each evaporation event in EC triggers a much larger change in the cluster's center-of-mass, than does each core breakup event in PD.

There is also *direct experimental evidence that evaporation and condensation occur at cluster edges in our system*. This is most clear at low coverages (below ca. 0.1 monolayers) from the long-term changes in island size: small islands tend to disappear; large islands tend to remain constant or (occasionally) grow larger. Such changes are evident in Figure 1. This phenomenon, known as Ostwald ripening, can occur *only* if a 2D gas is present to mediate exchange between the islands. Hence, the existence of a dilute 2D gas phase, which is required under the EC mechanism, is supported unequivocally by the experimental data.

Finally, cluster diffusion should not be regarded simply as an isolated, esoteric phenomenon; it can have important consequences for evolution of thin film structure. The long-term coarsening of 2D, homoepitaxial adlayers is traditionally regarded as being dominated by Ostwald ripening, and it is assumed also that the centers of mass of the clusters remain fixed [24]. However, cluster diffusion can lead to coalescence, a completely

different channel for coarsening. In fact, we have recently begun to study coarsening over long times for Ag/Ag(100), and find that diffusion-mediated coalescence plays a major role over a wide range of conditions. This leads to a radically different view of the coarsening process, which should be important in any system where cluster diffusion is significant. Details will be reported elsewhere.

Acknowledgments

We thank A. F. Voter and R. J. Behm for stimulating and informative discussions. This work is supported by NSF Grant No. CHE-9317660. One of us (P.A.T.) also acknowledges support of a National Science Foundation Faculty Award for Women in Science and Engineering. Some equipment and all facilities are provided by the Ames Laboratory. Ames Laboratory is operated for the U.S. Department of Energy by Iowa State University under contract No. W-7405-Eng-82.

References

1. J. A. Venables, G. D. T. Spiller and M. Hanbuecken, Rep. Prog. Phys. 47 (1984) 399; and references therein.

2. S.-L. Chang and P. A. Thiel, CRC Critical Reviews in Surface Chemistry 3 (1994) 239.

3. D. W. Bassett, J. Phys. C. (Solid State Phys.) 9 (1976) 2491.

4. T. T. Tsong and R. Casanova, Phys. Rev. B22 (1980) 4632.

5. H.-W. Fink and G. Ehrlich, Surf. Sci. 150 (1985) 419.

6. S. C. Wang and G. Ehrlich, Surface Sci. 239 (1990) 301.

7. G. L. Kellogg, Appl. Surface Sci. 67 (1993) 134.

8. C.-L. Liu and J. B. Adams, Surf. Sci. 268 (1992) 73.

9. A. Masson, J. J. Metois and R. Kern, Surface Sci. 27 (1971) 463.

10. C. R. Henry, C. Chapon and B. Mutaftschiev, Thin Solid Films 46 (1977) 157.

11. C. Chapon and C. R. Henry, Surface Science 106 (1981) 152.

12. R. Kern, A. Masson and J. J. Metois, Surface Science 27 (1971) 483.

13. J. S. Ozcomert, et al., Surface Sci. 293 (1993) 183.

14. H. C. Kang, P. A. Thiel and J. W. Evans, J. Chem. Phys. 93 (1990) 9018.

15. D. R. Peale and B. H. Cooper, J. Vac. Sci. Technol. A 10 (1992) 2210.

16. B. H. Cooper, et al., Mat. Res. Soc. Symp. Proc. 280 (1993) 37.

17. S.-L. Chang, et al., (1994) in preparation.

18. A. F. Voter, Phys. Rev. B34 (1986) 6819.

19. A. F. Voter, SPIE Modeling of Optical Thin Films 821 (1987) 214.

20. An exact treatment, for PD, replaces Eq. (1) with $D = C_N\langle T_N\rangle\langle \delta_{CM}^2\rangle$, where $\delta_{CM}=1/N$, $\langle T_N\rangle$ is the total hop rate, and $C_N < 1$ measures the back-correlation in the walk.[14] Microscopically, $C_N \ll 1$ since most hops are ineffective. Another perspective considers many-atom effective events, where core breakup is quickly followed by, e.g., removal of an entire edge. Here $\delta_{CM}(\text{eff}) = 1$ and the effective event rate decreases strongly with N for PD (but not for EC).

21. M. Giesen-Seibert, et al., Phys. Rev. Lett. 71 (1993) 3521.

22. L. Kuipers, M. S. Hoogeman and J. W. M. Frenken, Phys. Rev. Lett. 71 (1993) 3517.

23. The effective barrier for evaporation of a corner core atom is the maximum of the barriers for the individual steps (core breakup, Fig. 5c, and detachment from a straight [011] edge, Fig. 5d), and the collective barrier $E_d + E$, where E_d is the isolated atom

diffusion barrier, and E is the corner atom binding energy.

24. H.-J. Ernst, F. Fabre and J. Lapujoulade, Phys. Rev. Lett. 69 (1992) 458.

CHAPTER 3

COARSENING MECHANISMS IN A METAL FILM: FROM CLUSTER DIFFUSION TO VACANCY RIPENING

A paper submitted to Physical Review Letters

J.-M. Wen, J. W. Evans, M. C. Bartelt, J. W. Burnett, and P. A. Thiel

Abstract

Coarsening of Ag films on Ag(100) at room temperature occurs primarily via diffusion-mediated coalescence of two-dimensional adatom clusters, rather than by Ostwald ripening, up to a coverage of 0.65 monolayers. Above 0.8 monolayers, vacancy clusters coarsen primarily via Ostwald ripening, due to their much lower diffusivity. An asymmetric transition region separates these two regimes, characterized by a near-percolating structure which undergoes self-similar coarsening.

Text

The evolution and control of film morphology is of fundamental and technological interest. Typically, during deposition, a film is driven far-from-equilibrium, and thus can be potentially "trapped" in a variety of manifestly non-equilibrium configurations [1-3]. While this allows control of morphology by intelligent manipulation of deposition parameters, one

must recognize that a non-equilibrium structure is always prone to rearrangement. Understanding the mechanisms and kinetics of such rearrangement is necessary to predict film stability, and presents a key challenge in non-equilibrium physics.

Below a critical temperature for two-dimensional (2D) phase separation, the equilibrium structure of a partially-filled layer consists of a single large domain or "island" of a condensed phase coexisting with a dilute 2D gas phase [4]. Since nucleation and growth of islands during deposition produces a distribution of "smaller" islands [5, 6], *subsequent* temporal evolution toward the equilibrium state must involve coarsening, i.e., an increase in the length-scale characteristic of the dominant structure [7]. Current discussions of coarsening in adlayers primarily invoke Ostwald Ripening (OR) [7, 8], at least for low coverages, θ. During OR, atoms tend to detach from smaller islands and re-attach to larger islands, driven by a gradient in the vapor pressure of the surrounding 2D gas. This process results in asymptotically self-similar growth, with the characteristic linear dimension, L, increasing with time as $L \sim t^{1/3}$ (the Lifshitz-Slyozov law) [9]. It has also been recognized that another mechanism can control coarsening at moderate θ where the adlayer has an interconnected and interpenetrating structure [8]. This "edge running" mechanism involves long-range diffusion of adatoms along the domain boundary of the condensed phase.

We also note that there exists a substantial body of generic 2D lattice-gas modeling of coarsening phenomena [10], which might be expected to apply to adlayer evolution. However, it should be emphasized that, in the absence of information on activation barriers for adatom hopping rates in various configurations, these studies invariably use simple

Metropolis or Kawasaki rate choices [10]. While this approach might reasonably describe equilibrium behavior (for a suitably chosen Hamiltonian), it cannot correctly predict competition between different kinetic pathways during non-equilibrium coarsening.

The primary goal here is to determine the coarsening mechanism and kinetics for various θ, for the system Ag/Ag(100) at 300 K. This is the first comprehensive analysis of adlayer coarsening in such a system. We assess the relative contributions to coarsening of OR and a competing mechanism, cluster diffusion (CD) and subsequent coalescence, both for adatom clusters at low θ and for vacancy clusters at high θ. While CD was recognized in older studies of coarsening of 3D metal (adatom) clusters on non-metallic surfaces [11, 12], it has been overlooked in 2D metal-on-metal systems, presumably because of an expectation that diffusion of large 2D adatom or vacancy clusters is insignificant. Previously, the coarsening of vacancy islands has received only cursory attention [13, 14]. We find, unexpectedly, that CD of adatom islands dominates coarsening for low θ, and present detailed modeling of this behavior. A dramatic asymmetry between behavior at low and high θ is revealed. We also determine the transition region where interconnected domains, necessary to support edge-running, occur, and apply an appropriate correlated percolation theory to explain why this region occurs well above 0.5 monolayers (ML).

Scanning tunneling microscopy (STM) allows *direct* determination of the mechanism of coarsening (see Figure1). We use an Omicron STM housed in an ultrahigh vacuum chamber, as described previously [15]. Evaporation of submonolayer coverages, with the sample held at room temperature, generates the "initial" non-equilibrium 2D

structures, whose features are then monitored quantitatively as a function of time to observe coarsening, over a period of several hours. Precautions are taken to eliminate tip-induced effects [15].

The nucleation, growth, and subsequent coalescence of 2D islands during deposition is fairly well understood [5]. Nucleation of stable islands occurs only at very low θ, after which existing islands grow and the island density, N, remains constant until the onset of growth-induced coalescence around 0.4 ML. Percolation occurs much later, around 0.7-0.8 ML [6]. We can tailor the "initial" configuration created by deposition, simply by changing deposition flux, R: at fixed θ, and temperature, N decreases and the mean island size, $S_{av} \approx \theta/N$, increases with decreasing R. For the low θ (adatom island) regime, we label this initial configuration only with θ and S_{av} (or, equivalently, θ and N), although the full size and separation distributions provide a more complete description. A similar prescription applies to the high θ (vacancy cluster) regime. In the transition range of θ, where the film constitutes a near-percolating network, an appropriate measure of characteristic linear dimension is the chord length [6].

We now examine experimental data for coarsening in the three different θ regimes. The **low-θ (adatom-island) regime**, illustrated in Figure 1a, actually encompasses the majority of the first layer, since it extends up to about 0.65 ML. Here, we choose four initial configurations, labelled α-δ in Fig. 2a, and show N vs. time, t, for each point quantitatively in Figure 2b. In each case, the total (TOT) decrease in N is broken down into two components: one due to OR, and one due to CD (representing N-values that would occur if

only one of the coarsening mechanisms was active). The contribution of each is determined directly from the STM data. OR is taken to occur when a cluster disappears without an obvious collision, and also without marked increase in size of any single neighbor. This is often preceded by a gradual shrinkage. CD, on the other hand, can usually be discerned clearly by following the clusters' trajectories, and by confirming growth of a single neighbor when a cluster disappears. (A cluster which disappears via OR contributes to the miniscule growth of several neighbors.) Also, after collision, the overlapping, near-square shapes of the two original clusters sometimes remain visible for a time. Applying these criteria in examining the STM images, there is an ambiguity in determining the mechanism of disappearance in <5% of cases.

Surprisingly, in the entire low-θ region, coarsening is dominated by CD, rather than by the traditionally-pictured OR. Focussing on the part of this regime specified by Figure 2a, for instance, OR is insignificant at the two points, α and β, which are characterized by large S_{av} . It is measurable for both the lower-S_{av} points, γ and δ, but even there it only competes significantly with CD at δ. See Figure 2b.

These are reasonable observations, given the recent discovery [15] that large 2D adatom islands on Ag(100) undergo significant diffusion at 300 K on the time-scale of equilibration. Within a range of island sizes, S, of 100 to 700 atoms, the diffusion coefficient, $D \approx 10^{-17}$ cm^2 s^{-1} varies little with cluster size (a factor of two at most). Given the weak dependence of D on S, one expects that increasing the average initial island size (e.g., going from γ - δ to α - β in Figure 2a) does not diminish the effectiveness of the CD

Figure 1. STM images obtained following deposition of Ag on Ag(100) at room temperature. The upper frames show the starting points and the lower frames show the surface several hours later. Bright areas are the deposited film, one atom deep; dark areas are substrate. Each frame shows a single terrace of the substrate, except (b) where bunched steps are visible at the edges. Conditions are: (a) 0.11 ML, $N_o = 4.9 \times 10^{-5}$ Å^{-2}, $t_f = 520$ min; (b) 0.69 ML, $t_f = 400$ min; (c) 0.87 ML, $N_o = 1.5 \times 10^{-5}$ Å^{-2}, $t_f = 390$ min;

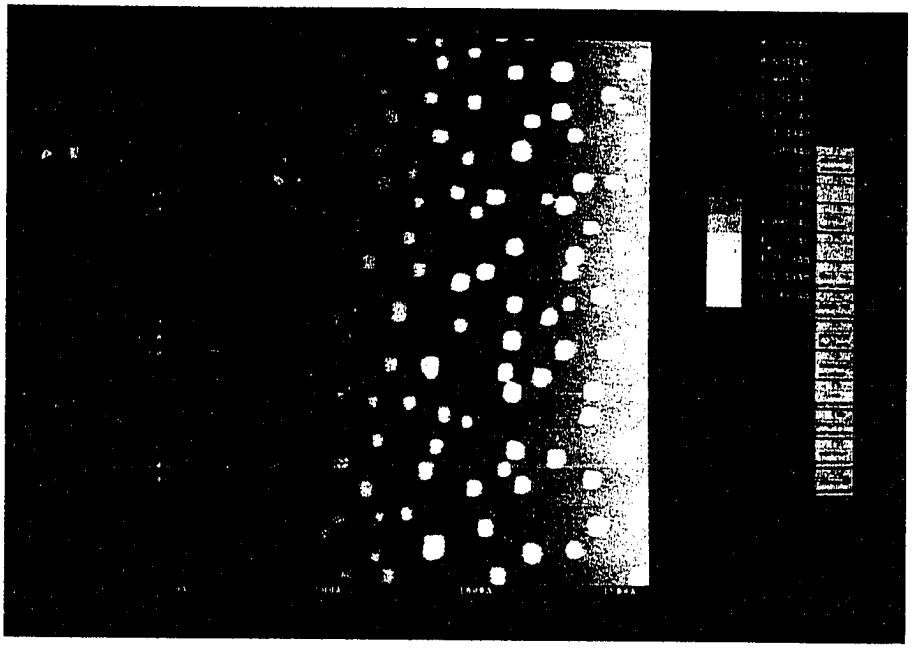

(a) t= 0

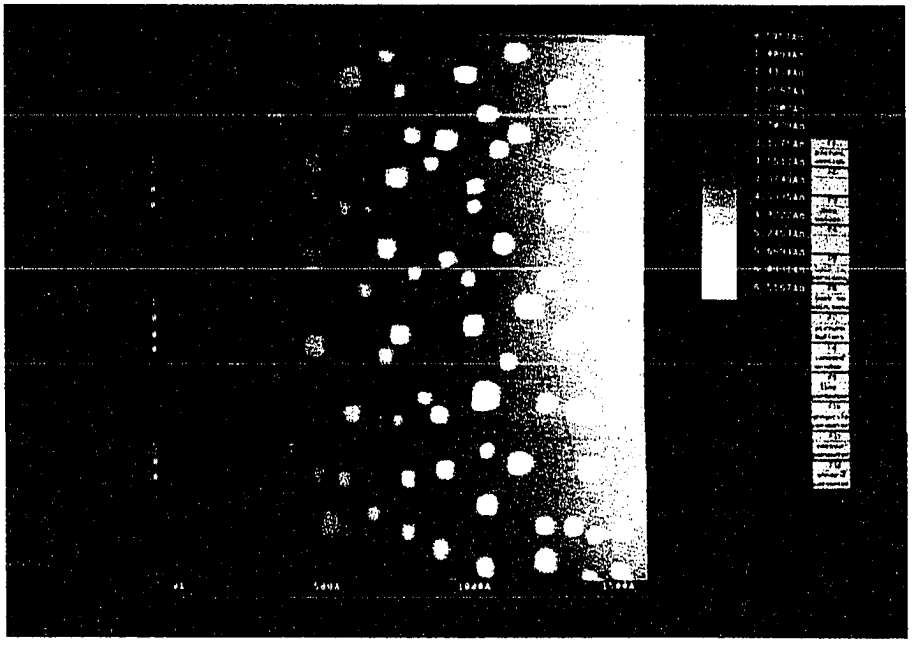

(a) $t=t_f$

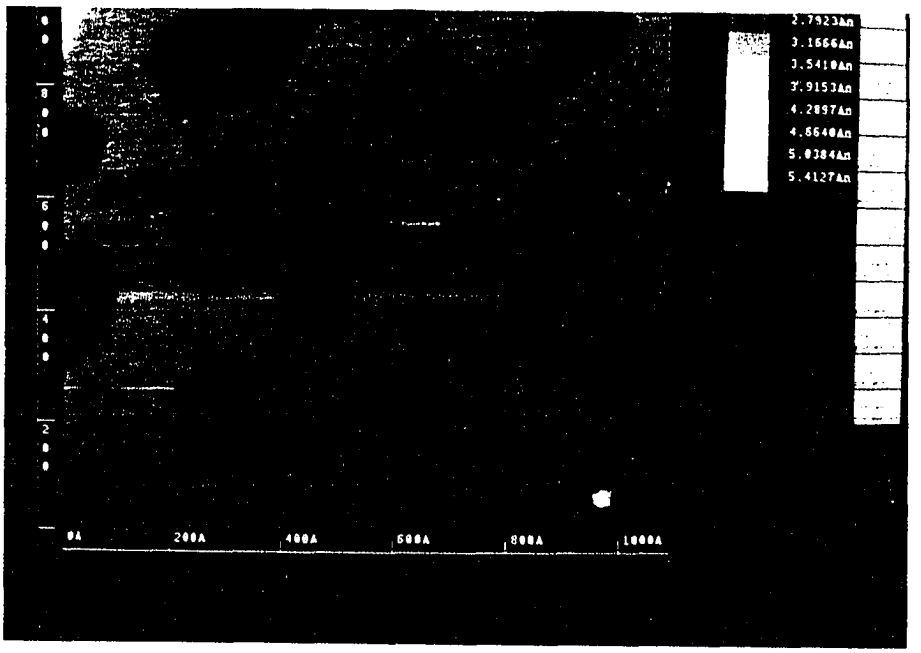

(b) t= 0

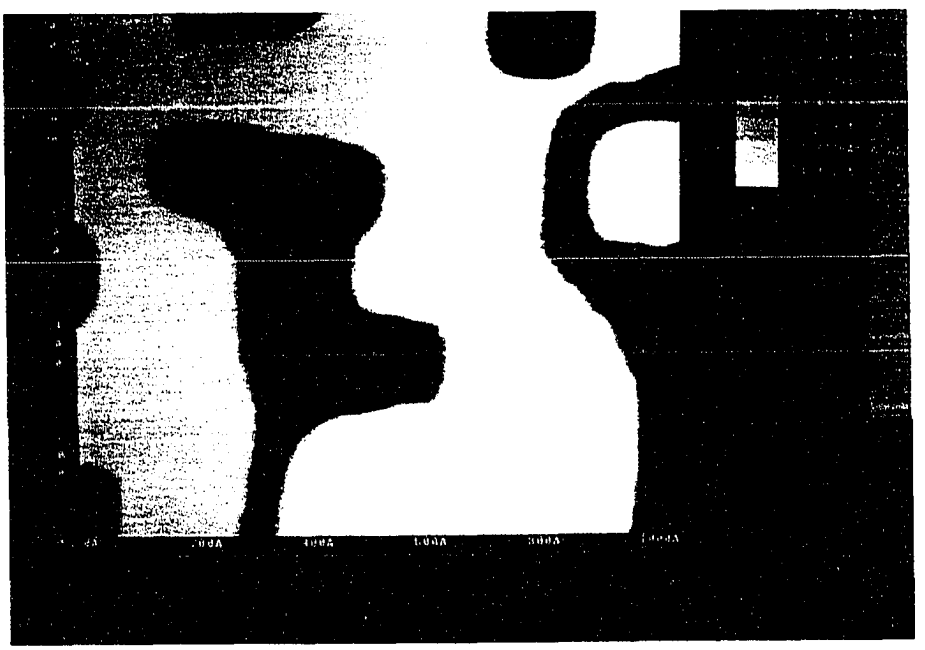

(b) $t=t_f$

Figure 1. cont.

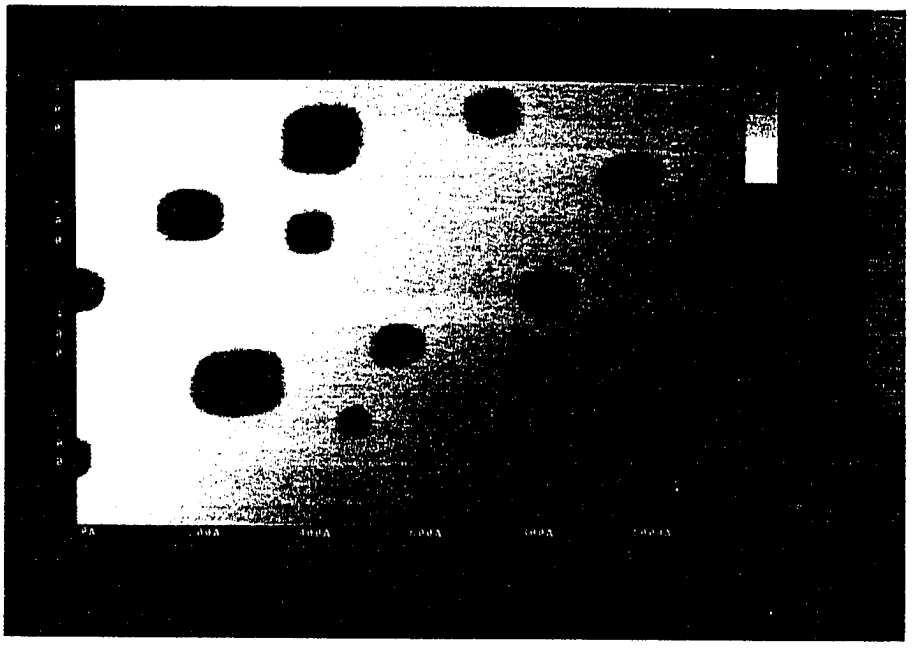

(c) t= 0

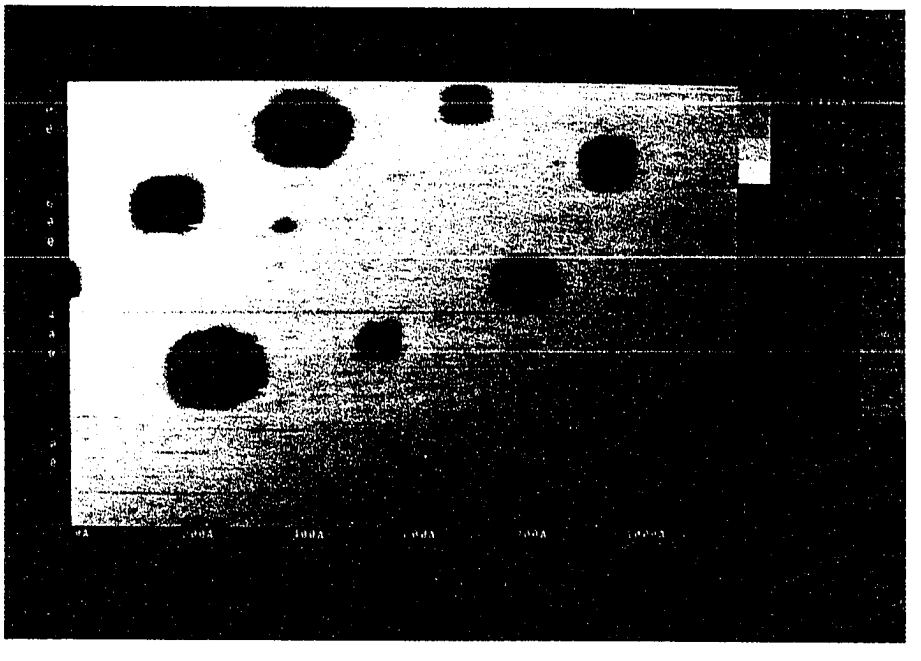

(c) $t=t_f$

Figure 1. cont.

process. However, absolute rates for island shrinkage or growth decrease as the mean curvature increases, and thus OR is inhibited for the larger S_{av} [7]. It might seem contradictory that the weak dependence of D on S also indicates that cluster diffusion is mediated by evaporation-condensation (EC) [15], the same mechanism which underlies OR. However, significant cluster motion via EC events could occur with little change in cluster size, if there is a high probability of re-condensation after each evaporation event.

A second factor, which also determines the propensity for CD, is the average separation between neighboring islands. This is the main quantity which varies within each pair of data points at roughly-constant S_{av}, α and β, or γ and δ, in Figure 2. The average separation between island *centers* is given by $L_{av} = N^{-1/2}$, and that between *edges* by $L_e = (1-\theta^{1/2})L_{av} = (\theta^{-1/2} -1)S_{av}^{1/2}$. For instance, in going from α to β, L_e increases from 60 Å to 145 Å. Since island edges are much closer in α, clusters need diffuse a shorter distance before they touch, and it is reasonable that CD is more efficient than at β. Similarly, for the two points at lower S_{av}, the value of L_e is smaller at γ (100 Å) than at δ (135 Å) which explains why CD is more significant at γ than at δ. In short, CD is the dominant coarsening mechanism in the entire low-θ regime, except in the extreme limits of low θ and large separation between islands.

More quantitative insight is provided by a rate equation analysis. Analyses of diffusion-mediated "coagulation" processes date back to the work of Smoluchowski [16], where evolution of the density, N_k, of islands of size k is described by the infinite coupled

Figure 2. Coarsening in the low-coverage regime. (a) The size-coverage space spanned by four specific points. Initial conditions are: (α) 0.27 ML, $N_o = 6.7 \times 10^{-5}$ Å^{-2}; (β) 0.07 ML, $N_o = 2.6 \times 10^{-5}$ Å^{-2}; (γ) 0.05 ML, $N_o = 5.8 \times 10^{-5}$ Å^{-2}; (δ) 0.03 ML, 0.11 ML, $N_o = 3.7 \times 10^{-5}$ Å^{-2}. (b) Island densities as functions of time, for the four data points in (a), normalized to the initial density. (c) Rate-equation simulation results (solid lines) for data corresponding to α and β.

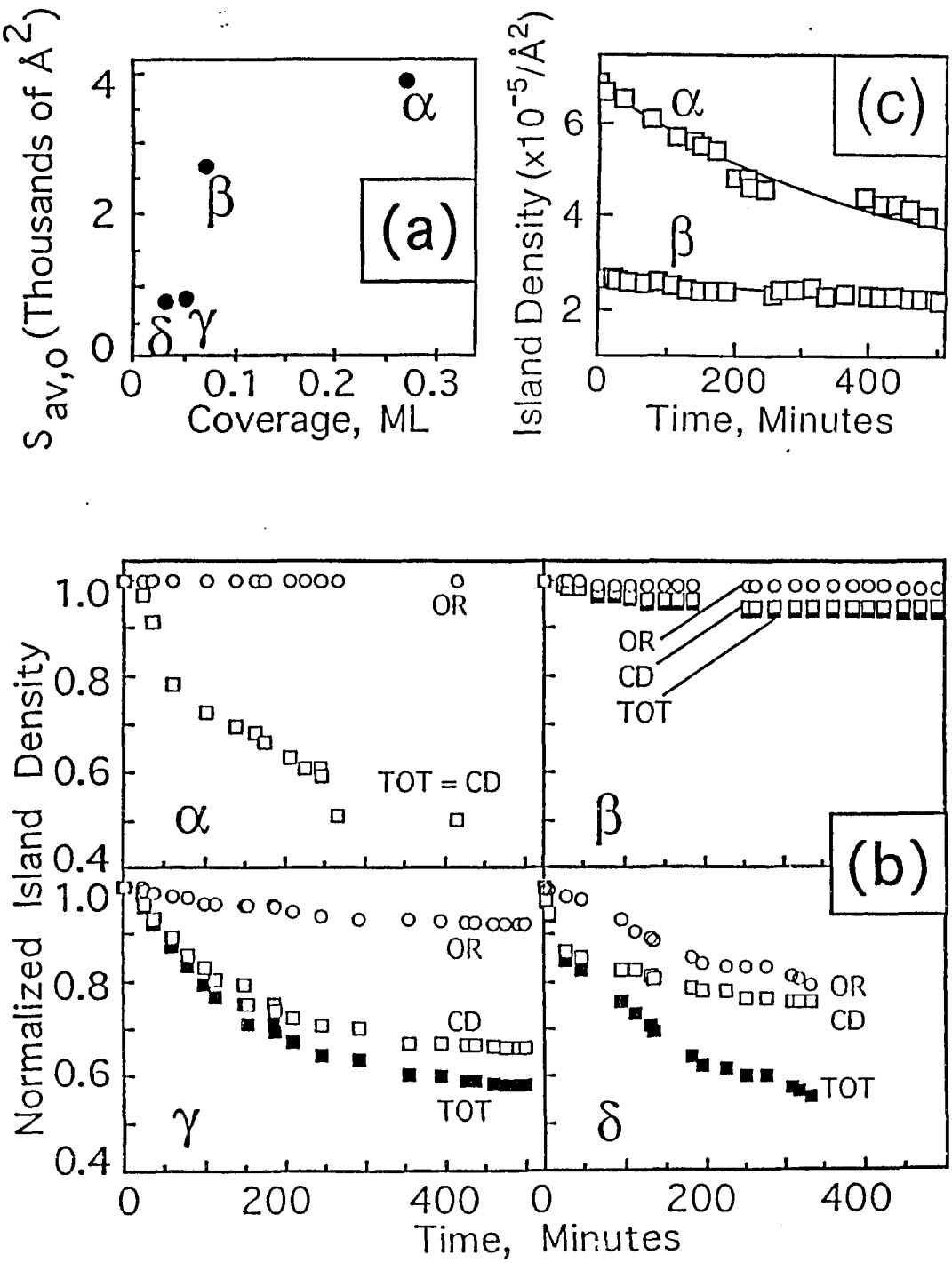
$S_{av,o}$ (Thousands of Å^2)
Coverage, ML
α
β
γ
δ
(a)
Island Density (x10^{-5}/Å^2)
Time, Minutes
(c)
Normalized Island Density
OR
TOT = CD
CD
TOT
(b)
Time, Minutes

set of equations

$$dN_k/dt = (1/2)\,\Sigma_{i+j=k}\, W_{ij} - \Sigma_i\, W_{ik} \qquad (1)$$

The collision rate, W_{ik}, for clusters of size i and k is traditionally chosen as $W_{ik} \approx DN_kN_i$, for size-independent D. However, Eq. (1)--and its recent refinements [17, 18]--fail to account for the θ dependence between, for instance, points α and β in Figure 2a. This is because Eq. (1) does not take into account the effective size or edge-separation of the clusters. In order to correct this, we write the collision rate as $W_{ik} \sim P_k\, N_i/\tau$, where τ is the time for the i-cluster to diffuse to a neighboring cluster, and $P_k = N_k/N$ is the probability that a neighboring cluster is of type k. The relative motion of clusters i and k is described by a space-filling random walk with diffusion coefficient 2*D, and for them to meet, this walk must scan $\sim L_e^2$ sites. This takes a time [19] $\tau \sim (L_e^2/\pi)\ln(L_e^2/\pi)/2D$, yielding $W_{ik} \sim DN_iN_k/(1-\theta^{1/2})^2$, neglecting ln-corrections.

These equations, with the measured average value of $D \approx 2\times10^{-17}$ cm^2 s^{-1} and the measured initial island size distribution as input, provide a parameter-free determination of the time-evolution of . The solid lines in Figure 2c show results for points α and β. (We do not attempt to fit points γ or δ, since OR is significant there.) The excellent agreement between model and experiment provides additional support for the claim that cluster coalescence is the dominant mechanism of coarsening under these conditions. More importantly, it indicates that knowledge of D leads to reliable, quantitative predictions of

coarsening kinetics.

The data do not display the asymptotic decay, $N \sim 1/t$, and exponential size distributions predicted by the classic theories [17, 18]. This can be explained in terms of a characteristic time, $t_c = |d \ln N/dt|^{-1}$ (evaluated at t=0), for the coarsening process, which indicates the time for N to decrease by a fixed fraction (by 1/e for exponential decay). t_c can be calculated precisely from Eq. (1) and the initial size distribution, but is given effectively by $t_c \approx (1-\theta^{1/2})^2/DN$ which varies from ~7 hours for point α to ~30 hours for point β. This is comparable to the duration of experimental observation, explaining why asymptotic behavior has not yet appeared.

We have also monitored the evolution of the full island size distribution. For OR, one would expect a sharpening of the initial distribution produced by the nucleation process because of a natural evolution toward equal sizes, and a corresponding slow-down in coarsening [7]. Instead, the data, e.g., for point α up to 7 hours, is consistent with evolution to a monotonically (exponentially) decreasing form. Evolution to such a form is predicted by the rate equation theory [17, 18], and is observed by evolving our equations for longer times (e.g. 20-40 hours for point α). (While the experiment could have been continued longer, statistics of the island distribution become progressively poorer.) The feature that CD produces much broader size distributions than OR can be important if one wishes to use coarsening to tailor the size distribution.

One might expect a mirror-symmetry in the coarsening mechanism and kinetics between, say, adatom islands at $\theta \approx 0.1$ and vacancy islands at $\theta \approx 0.9$. Thus, we also

examine the **high-θ regime**, which extends above ca. 0.80 ML. Here, deposition produces adatom islands sharing so many borders that the film percolates, i.e., it produces a contiguous adlayer pockmarked by isolated vacancy regions. The vacancies are mostly compact, and roughly square (Figure1c). (Although the vacancies formed during deposition are more irregular [6], most of them must restructure quickly between the end of deposition and the start of imaging.) At these θ, a few second-layer adatom islands are usually observable also after deposition. With time, the second-layer islands disappear and partially fill in the vacancies [20], leaving a surface layer consisting of isolated vacancy islands. This we take as the starting point to examine coarsening of the vacancies, as shown in Figure 1c.

This examination reveals two related asymmetries between the low-θ and high-θ regimes. First, the vacancy islands diffuse more slowly than do their mirror-image adatom islands. This is borne out by a quantitative evaluation of D for vacancy islands at 300 K, which is an order of magnitude lower than for the adatom islands, i.e. 3×10^{-18} cm^2 s^{-1}. This value varies little as a function of size in a range of 350 to 3800 atomic vacancies [20]. The second asymmetry is in the coarsening mechanism. Given that D is so much smaller, cluster diffusion would be expected to play a much less important role in coarsening than at lower θ. This is borne out by the data of Figure 3, showing the decrease in the vacancy island density as a function of time at $\theta = 0.87$. CD is simply never observed. Coarsening is due solely to OR of the vacancies. This "particle-hole" inequivalence between coverages θ and 1-θ reflects an asymmetry in associated microscopic activation barriers [20].

Finally, the **transition between the regimes of adatom islands and vacancy**

islands extends from about 0.65 ML to 0.80 ML. In this regime, extensive linkage of adatom islands during deposition leads to a ramified network which percolates at about 0.8 ML. This "continuum percolation" threshold is elevated above the typical value of 0.7 ML due to an effective long-range repulsion between islands formed during deposition, which inhibits percolation.[6] Below about 0.65 ML, we have observed that any small ramified clusters of islands restructure to compact forms, thus moving the adlayer "away from percolation", and the analogous behavior occurs for vacancy regions above 0.80 ML. However in the crossover regime of 0.65-0.80 ML, the ramified network of filled regions is preserved and slowly coarsens over several hours (Figure 1b). It is believed that a near-percolating structure such as this is necessary to support coarsening via edge-running [8]. Ernst et al. reported this effect at 0.5 ML for Cu/Cu(100) [8], in contrast to our observation of 0.65-0.80 ML. However they used low-temperature deposition producing a quasi-random "initial" adlayer state (rather than one with large, compact islands). At 0.5 ML, this quasi-random state is much closer to the random "lattice percolation" value of about 0.6 ML, and contains clusters which are more-highly ramified than does the initial state of our system at the same θ.

In summary, we have provided a comprehensive view of coarsening of Ag/Ag(100) adlayers. In particular, we find a surprising dominance of CD over OR in the coarsening of adatom islands for θ up to 0.65 ML, and accurately model the kinetics using the known value of D. We also observe dramatic asymmetry between the diffusion and coarsening of

Figure 3. N (t) for vacancy clusters at coverage = 0.87 ML, $N_o = 1.5 \times 10^{-5}$ Å^{-2}.

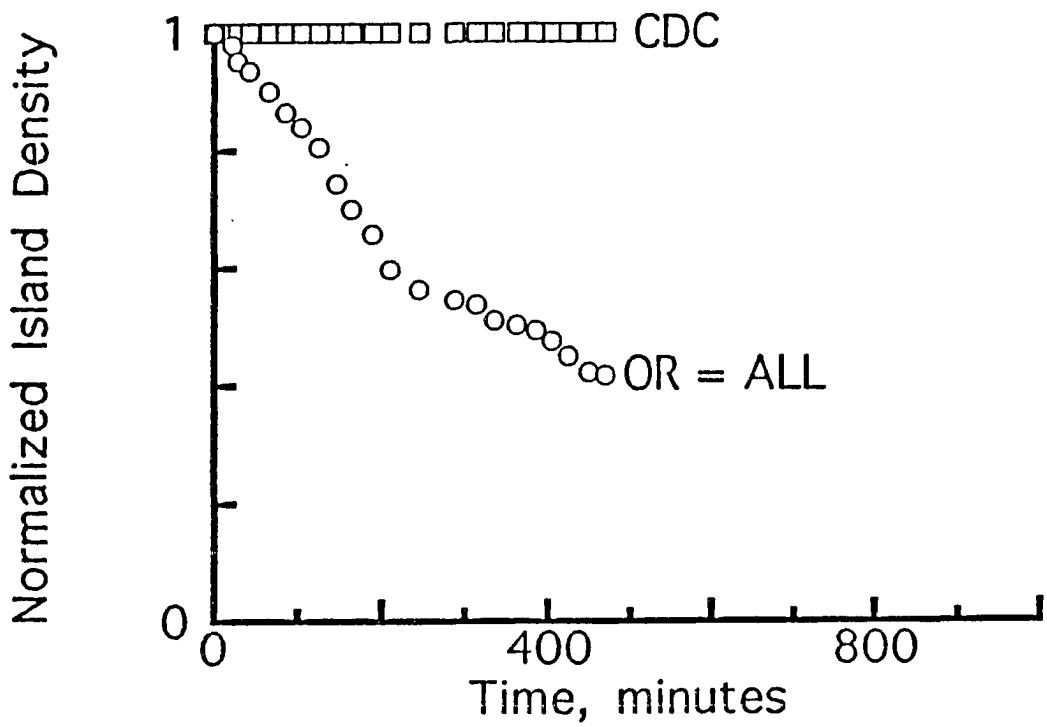
Normalized Island Density
1
0
CDC
OR = ALL
0
400
800
Time, minutes

vacancy islands at high θ, and of adatom islands at low θ. The location of the transition region between these two regimes at 0.65-0.80 ML, characterized by interconnected networks, is explained via concepts from correlated percolation theory.

Acknowledgments

This work is supported by NSF Grants No. CHE-9317660 and GER-9024358. Some equipment and all facilities are provided by the Ames Laboratory, which is operated for the U.S. Department of Energy by Iowa State University.

References

1. C. Günther, et al., Ber. Bunsenges. Phys. Chem. 97 (1993) 522.

2. H. Röder, et al., Nature 366 (1993) 141.

3. S.-L. Chang and P. A. Thiel, CRC Crit. Rev. Surf. Chem. 3 (1994) 239.

4. T. L. Einstein, in Chemistry and Physics of Solid Surfaces 4, R. Vanselow, and R. Howe, Eds. (Springer, Berlin, 1982) 251.

5. J. A. Venables, Phil. Mag. 27 (1973) 697; and references therein.

6. M. C. Bartelt and J. W. Evans, Surf. Sci. 298 (1993) 421; MRS Proceedings 312 (1993) 255; J. Vac. Sci. Technol. A12 (1994) 1800.

7. M. Zinke-Allmang, L. C. Feldman and M. H. Grabow, Surf. Sci. Rep. 16 (1992) 377.

8. H.-J. Ernst, F. Fabre and J. Lapujoulade, Phys. Rev. Lett. 69 (1992) 458.

9. I. M. Lifshitz and V. V. Slyosov, J. Phys. Chem. Sol. 19 (1961) 35.

10. J. D. Gunton, M. S. Miguel and P. S. Sahni, in Phase Transitions and Critical Phenomena 8, C. Domb, and J. L. Lebowitz, Eds. (Academic Press, New York, 1983) 267.

11. C. Chapon and C. R. Henry, Surf. Sci. 106 (1981) 152.

12. S. Stoyanov and D. Kashchiev, in Current Topics in Materials Science 7, E. Kaldis, Ed. (North Holland, Amsterdam, 1981) 71; and references therein.

13. I. C. Oppenheim, et al., Science 254 (1991) 687.

14. J. de la Figuera, et al., Sol. State Comm. 89 (1994) 815.

15. J.-M. Wen, et al., Phys. Rev. Letters 73 (1994) 2591.

16. M. V. Smoluchowski, Phys. Z. 17 (1916) 585.

17. E. Ruckenstein and B. Pulvermacher, J. Catal. 29 (1973) 225.

18. F. Leyvraz, in On Growth and Form H. E. Stanley, and M. Ostrowsky, Eds. (Nijhoff, Boston, 1986).

19. M. N. Barber and B. W. Ninham, Random and Restricted Walks, (Gordon and Breach, New York, 1970).

20. J.-M. Wen and P. A. Thiel, (1995) in preparation.

CHAPTER 4

DIFFUSION OF LARGE METAL VACANCY CLUSTERS ON AG(100)

A paper to be submitted to Surface Science

J.-M. Wen, J. Evans and P. Thiel

1. Introduction

The growth of thin metal films has attracted considerable attention recently. Among the many interactions that control film properties, surface diffusion is one of the most important. The study of the diffusion of surface structures can provide us with valuable information about both surface topography and adatom/surface interactions and, therefore, the energetic aspects of film growth.

The concept of surface diffusion is very broad in scope. Surface diffusion can include movement of surface features such as adatoms clusters and vacancy clusters, as well as other surface phenomena, such as cluster shape changing and step flowing. Many experimental [1-3] and theoretical [4-6] investigations have attempted to understand the epitaxial growth of thin metal films on an atomic scale. From previous studies, adatoms and other nanometer size metal structures, such as vacancy clusters and adatom clusters can diffuse on metal substrates and contribute to film morphology and film evolution [7-13].

Scanning tunneling microscopy (STM) is an ideal experimental probe for

investigating nanometer size structures due to its ability to track local surface structures [3,9].

Some experimental STM data are already available concerning vacancy metal cluster diffusion on metal substrates. Basically, these experiments study the diffusion on triangular lattice fcc metal surfaces [14-16]. Fcc(111) surfaces supposedly have atomically smooth terraces, and, therefore low diffusion barriers. The method used to form large vacancy clusters is to remove atoms from the substrate terraces by such methods as sputtering [14] and STM tip picking [15]. An STM study by de la Figuera *et al.* [15] showed that artificially created (with the STM tip) two-dimensional Cu vacancy clusters on clean Cu(111) are immobile, but on a Co-modified Cu(111) surface, these vacancy clusters undergo surface diffusion. The presence of Co on the Cu surface is needed to lower the surface diffusion barriers. The motion of clusters was considered as Brownian motion. The kink displacement along the internal edge of vacancy clusters is suggested as the atomic motion contributing to cluster diffusion. Another recent STM study of Ag/Ag(111), Comsa [14] showed that the Ag vacancies created by short Ar+ sputtering pulses have fast motion, and the diffusion coefficient is inversely proportional to the cluster size. This relationship suggests that atoms running across vacancy clusters are the cause of cluster migration.

In this paper, we report that on a clean square lattice, the Ag(100), large two-dimensional Ag vacancy clusters undergo measurable diffusion. The vacancies are formed by depositing Ag films at coverages slightly less than 1 ML so that isolated holes can be formed before the film has completed the first layer. The diffusion coefficient we obtained

from STM data is on the order of 10^{-18} cm^2s^{-1} ($2\text{-}6x10^{-18}$ cm^2s^{-1}). The mechanism of vacancy cluster diffusion we suggest, based on STM measurements, is that vacancy monomers leaving and reattaching to the edge of vacancy clusters dominate cluster motion.

2. Experimental

The experimental methods and data analysis used here are documented elsewhere [17]. Briefly, the STM experiments are performed in a UHV system with a base pressure of less than $8x10^{-11}$ Torr. The Ag sample is cleaned by repeated sputter and anneal cycles and the Ag film is evaporated by resistive heating. The vacancy clusters are created by controlling the film coverage and flux, enabling us to create variable sizes of vacancy clusters (images with clusters of 30 to 3800 missing atoms are used here). Since small vacancies have a short lifetime, we exclude vacancies smaller than 350 missing atoms in our diffusion coefficient estimates. We evaporate the Ag films to a coverage of 0.8-0.92 monolayer (ML) at relative low flux (0.15ML/min) to give the film time to develop a layered structure and to avoid forming a large number of second layer clusters. In this coverage range, the film features a well defined two-dimensional (2D) flat film with isolated 2D vacancy clusters of monolayer deep, vacancy clusters. We monitor the movement of these vacancy clusters as a function of time. The time interval between recorded images is 10-15 min. The typical tunneling current is 1-3 nA. The typical gap voltage is 0.1-1.1V. Scan rate depends upon image size and data acquisition rate, and varies from 196 Å/sec to 245 Å/sec.

3. Results and Discussion

Figure 1 shows typical film morphology changes and vacancy formation as coverage increases. At low coverage, the isolated adatom clusters distribute across the surface. At moderate submonolayer coverages, the film forms an interconnected network. At 0.8-0.9 ML, the film changes from a heavily interpenetrating 2D structure to a well defined 2D flat film with isolated 2D vacancy clusters. Low deposition flux is necessary to avoid second layer islands at high submonolayer coverage (second layer islands can also be reduced by a time-anneal at room temperature). The layer-by-layer growth of Ag/Ag (100) at a low deposition rate yields a single layer film at high submonolayer coverages which gives us a control over the formation of vacancy clusters.

The growth mode for Ag on Ag(100) has been demonstrated by other techniques. For example, the observed RHEED intensity oscillation by Suzuki [18] has suggested a layer-by-layer growth mode. Our STM images confirm this.

Figure 2 shows the typical STM images of Ag vacancy clusters. The clusters are one atomic layer deep with an approximately square shape, although rounded corners are common. Some clusters do have a rectanglar shape, but this is not the most stable configuration since significant shape change can be observed [27]. The most stable shape is square because of the adlayer which follows the substrate geometry. This shape change will be discussed in next chapter. The vacancy clusters in Figure 2 range from 350 to 3800 atoms. Our results indicate that the size of clusters changed throughout the observation time. Figure 3 shows a plot of some clusters' size change as a function of time

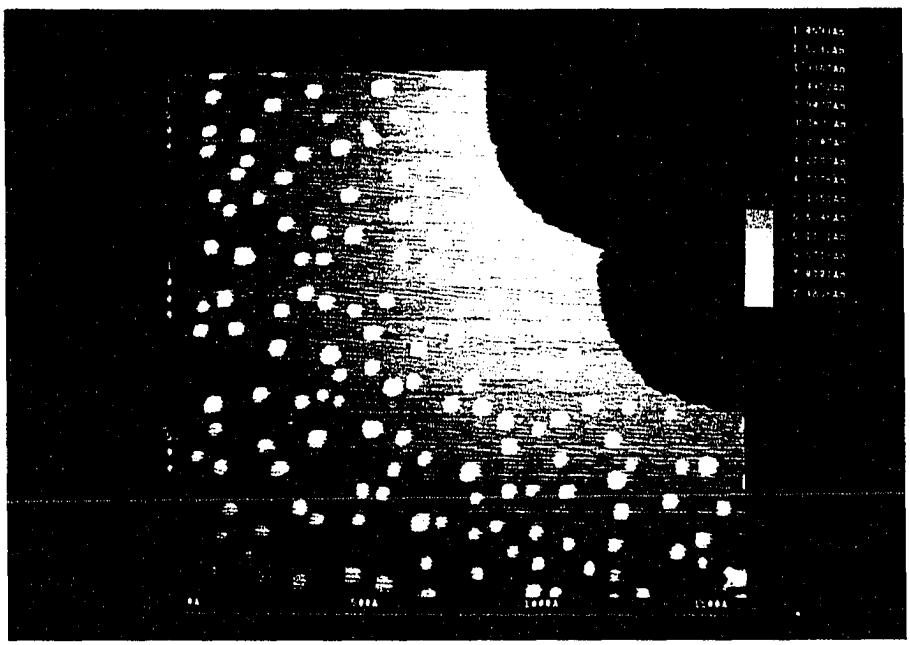

(1)

Figure 1. STM images show a typical film morphology change and vacancy formation as the coverage is increased. (1) coverage = 0.16 ML; (2) coverage =0.63 ML; (3) coverage = 0.89 Ml.

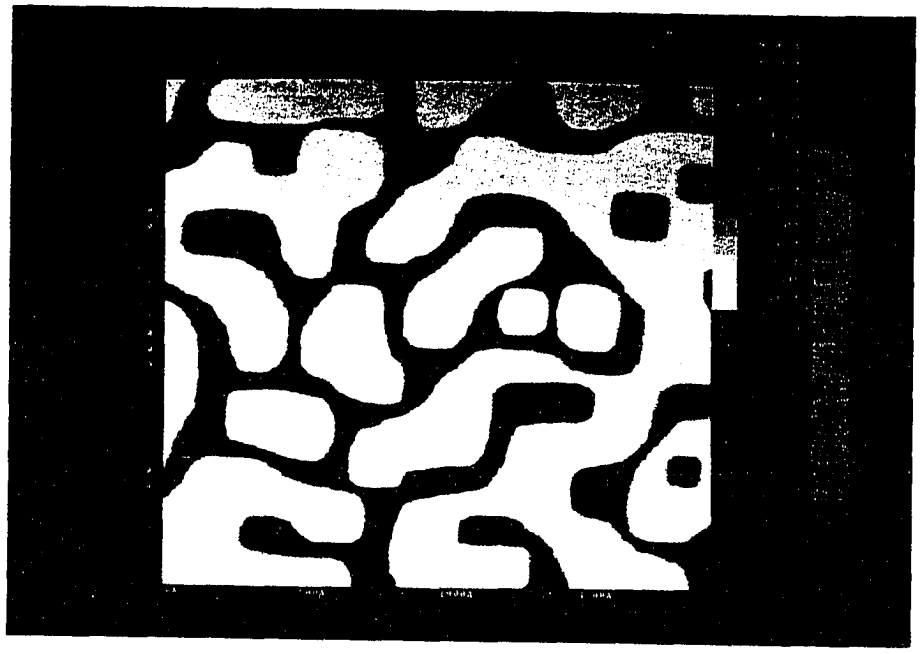

(2)

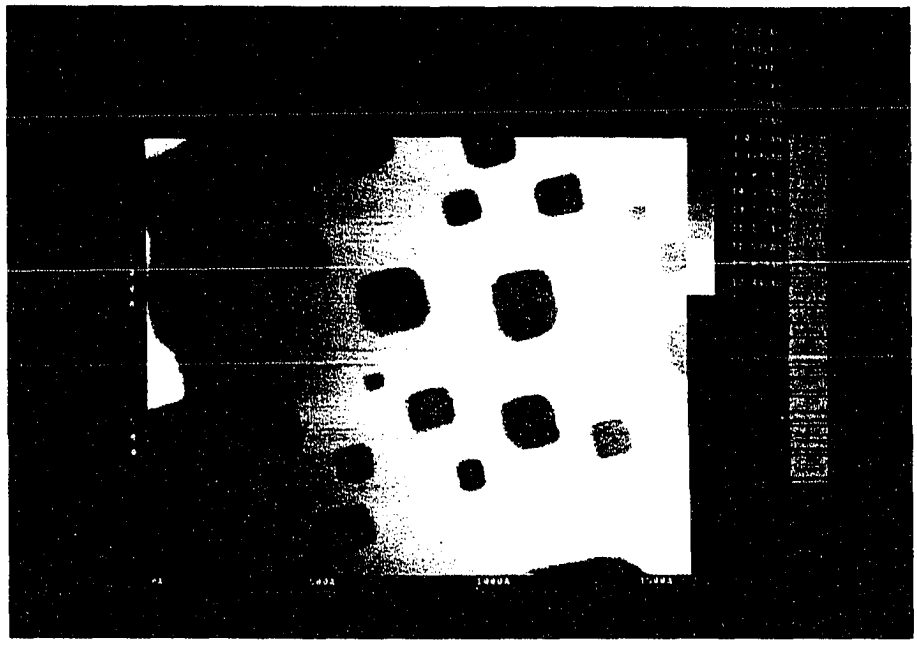

(3)

Figure 1. cont.

Figure 2. STM images of Ag vacancy clusters with a coverage of 0.87 ML. The clusters are all one atomic layer deep with an approximately square/rectangular shape, although rounded corners are common. $t_0 = 0$ hr, $t_f = 6$ hr.

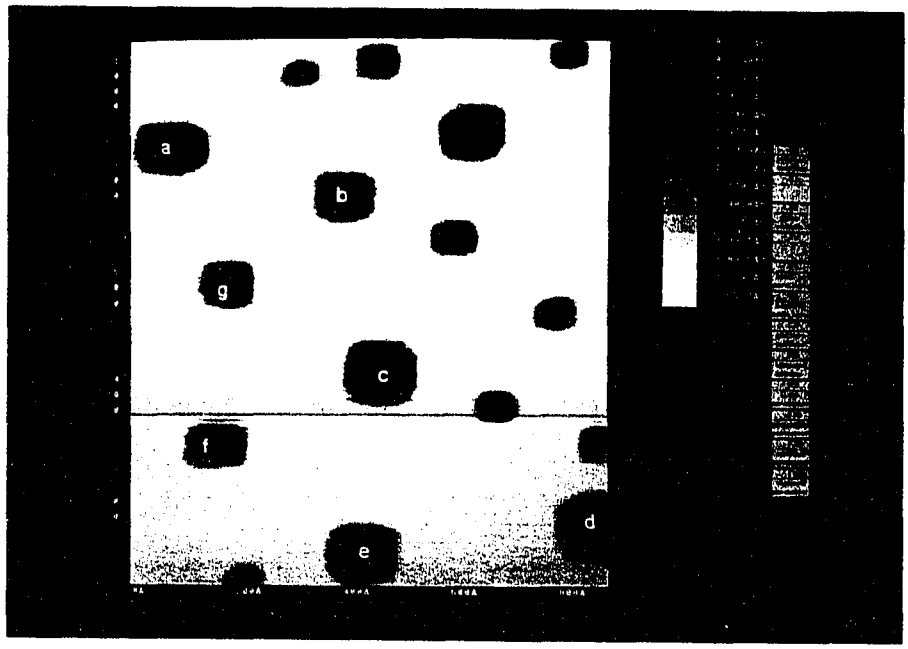

(1) t = 0

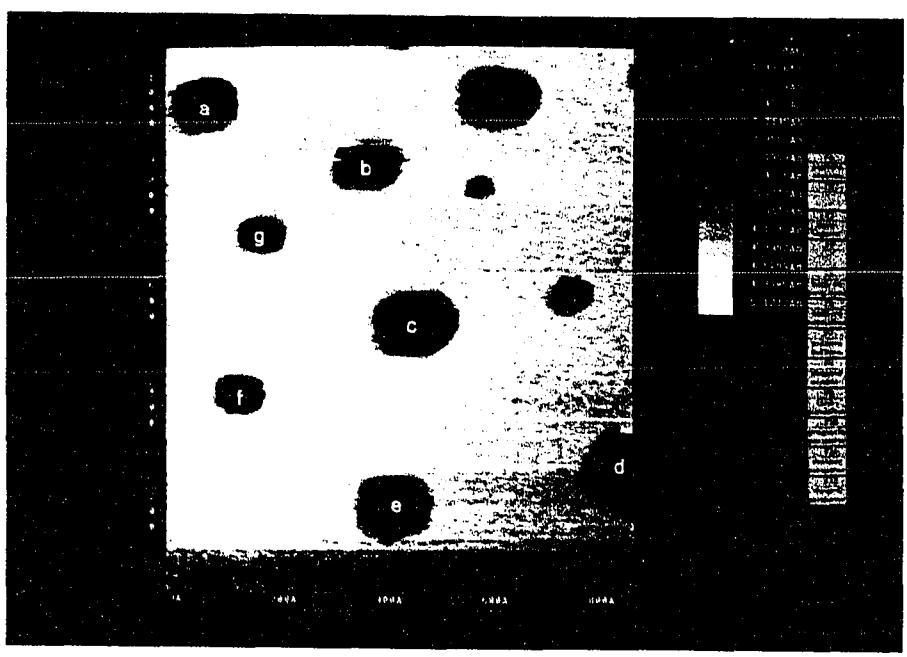

(2) t= t_f

Figure 3. Some clusters' size change as a function of time after stopping deposition. The decay rate of the cluster size is faster for smaller clusters than for larger ones. And the lifetime of small clusters are short.

Size (missing atoms)
0
1000
2000
3000
4000
t (min)
0
100
200
300
400
500

following deposition. The decay rate of the cluster size is faster for smaller clusters than for larger ones, and the lifetime of smaller clusters is shorter.

Figure 4 shows the quantity $<d^2/t>$ where d is the displacement of the cluster's center-of-mass, as a function of the mean time interval between observations, <t>, for two different sized clusters. The trajectories of two differently-sized clusters are illustrated in Figure 5. The net displacement is around 30-50 Å over a period of several hours. The method used to extract the diffusion coefficients (D) is published elsewhere [17]. Using this method we calculate diffusion coefficients which are on the order of 10^{-18} cm^2s^{-1}. Both the distance of vacancy clusters traveling on the surface and their diffusion coefficients are smaller than that of adatom clusters.

A vacancy cluster can be viewed as the opposite of an adatom cluster in surface structure analysis, thus the three existing mechanisms used to describe adatom clusters can be adopted in characterizing vacancy cluster diffusion. As illustrated in Figure 6, the three, non-exclusive, mechanisms which could facilitate vacancy cluster diffusion are: (1) perimeter diffusion (PD) (i.e. vacancy monomers moving along the internal edge of a vacancy cluster); (2) evaporation-condensation of adatom monomers within the vacancy, (i.e., atoms evaporating from an internal edge and condensing on another internal edge); and (3) evaporation-condensation of vacancy monomers over the entire surface (i.e., large vacancy structures and vacancy monomers existing a quasiequilibrium). Comparison of these models with experimental data focuses two things. First, the cluster size's time dependence, (only the third mechanism predicts the cluster's size is a function of the time),

Figure 4. These plots show the quantity $\langle d^2/t \rangle$ where d is the displacement between the cluster's center-of-mass location, as a function of the mean time interval between observation, $\langle t \rangle$, for two different sized clusters.

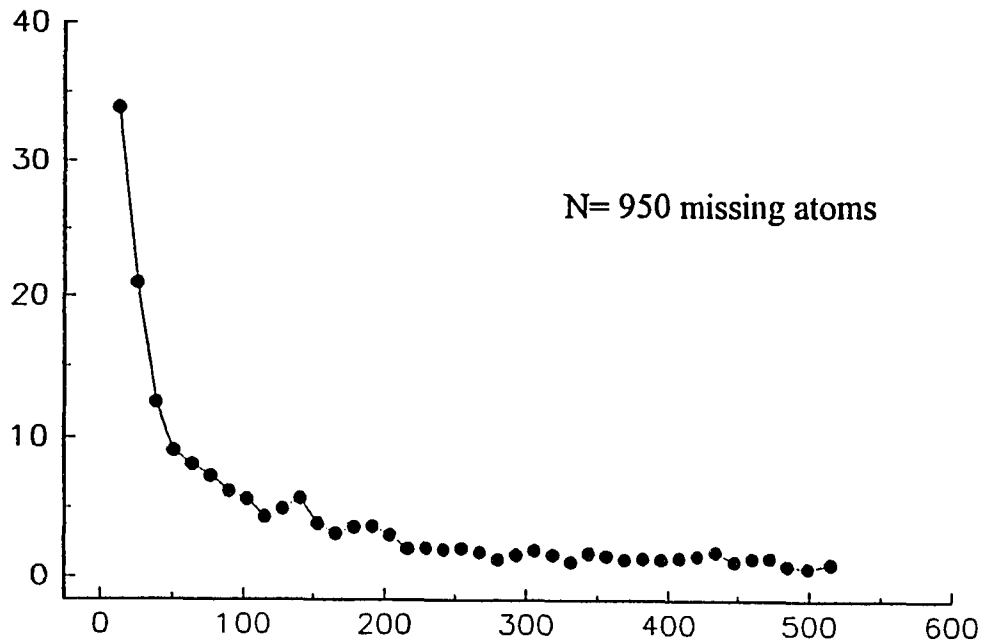
40
30
20
10
0
0
100
200
300
400
500
600
N= 950 missing atoms

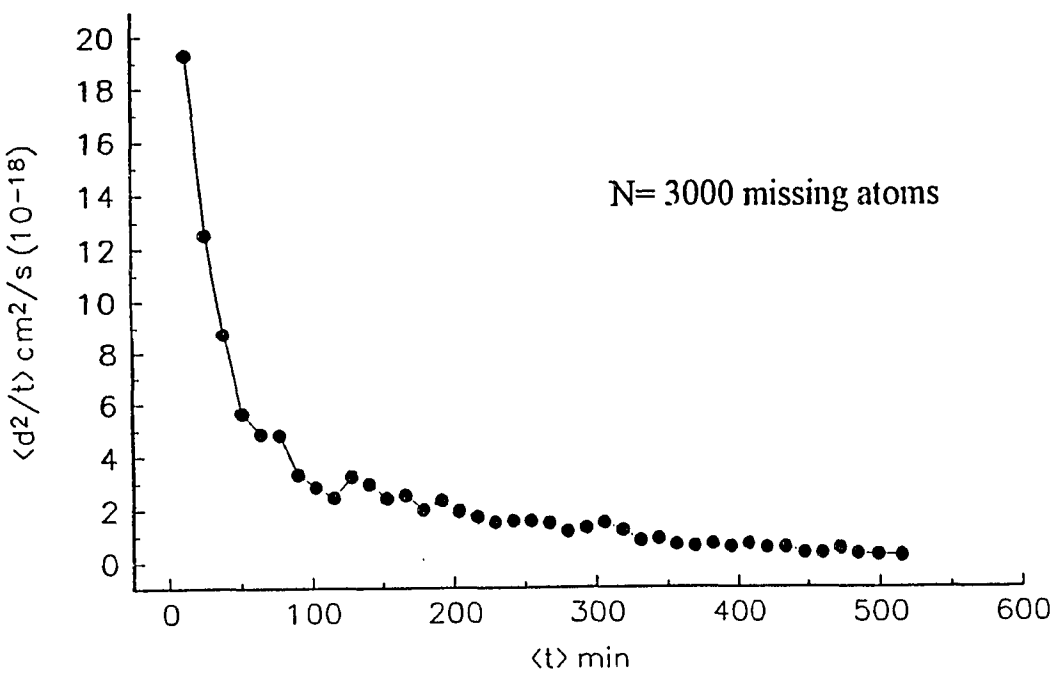
20
18
16
14
12
10
8
6
4
2
0
0
100
200
300
400
500
600
⟨d²/t⟩ cm²/s (10⁻¹⁸)
⟨t⟩ min
N= 3000 missing atoms

Figure 5. The trajectories of two differently-sized clusters.

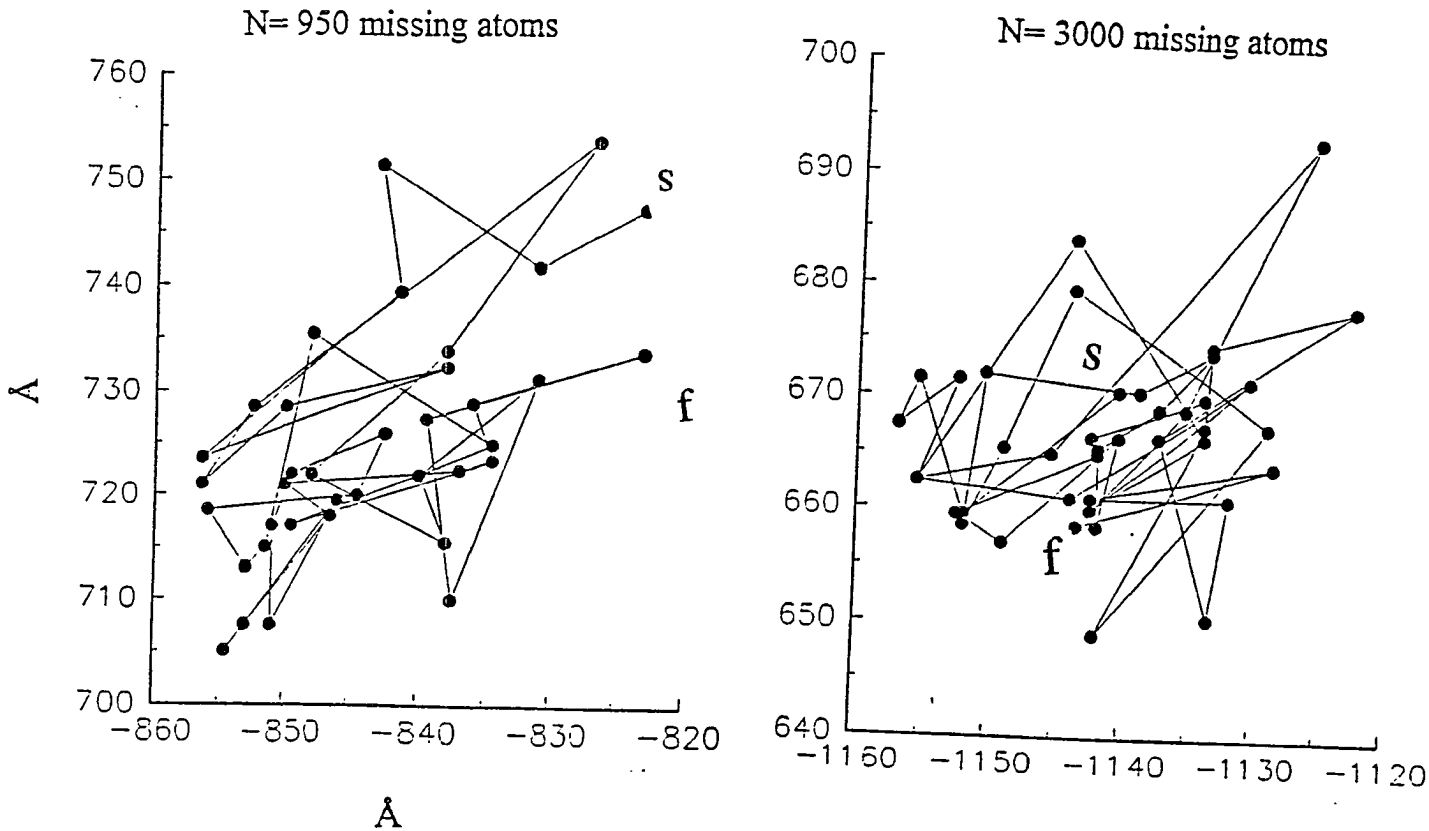
N= 950 missing atoms
760
750
740
730
720
710
700
Å
−860
−850
−840
−830
−820
Å
s
f
N= 3000 missing atoms
700
690
680
670
660
650
640
−1160
−1150
−1140
−1130
−1120
s
f

Figure 6. Three possible mechanisms for vacancy cluster diffusion. The center of the cluster will move when any of the three takes place, but only (3) can affect the size of the cluster.

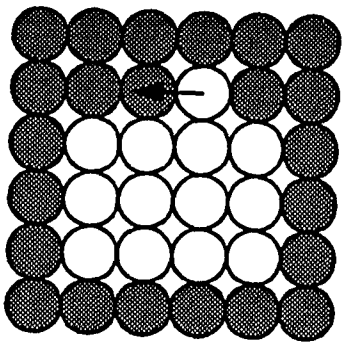

(1)
Vacancy monomer diffuses along an edge

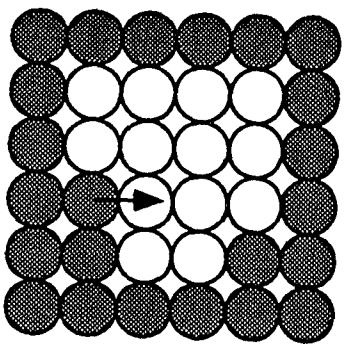

(2)
Atom diffuses across a vacancy cluster

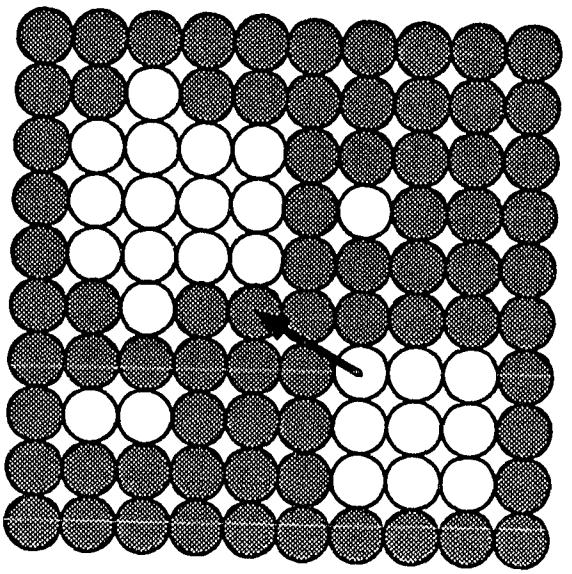

(3)
Vacancy monomer moves toward a large cluster from a small one

○ Vacancy ◍ Substate

second, the prediction of the scaling relationship between diffusion coefficient, D, and cluster size, N. The generally accepted form of the relationship is $D \propto N^{-\alpha}$. Different α values are associated with different mechanisms. We examine the value of D as a function of cluster size (N) for our system. Figure 7 shows the STM data and three modelling predictions in the plot of Log D vs N.

First, we consider perimeter diffusion (PD). An analysis of the barrier associated with atomic motion around clusters can provide a better understanding of the diffusion mechanism. We can divide the motions into fast and slow processes [17]. First we analyze adatom clusters. For large Ag adatom clusters, an atom is expected to have fast motion along its edge due to a small energy barrier [21]. The result of this fast motion can only cause slight displacement of the center of the cluster. To actually move the center of the cluster over long distances, core breakup is required. The core breakup can be considered as a process in which an edge atom leaves the edge. This process needs to overcome a very high energy barrier and therefore is a slow process.

A corresponding mechanism holds for large vacancy clusters. In order to have long-range diffusion, vacancy clusters need to exceed a high energy. An analysis of the energetic diagram calculated using the embedded atom method (EAM) [21] is helpful when considering the different energetics involved in cluster diffusion between vacancy and adatom clusters. The activation energies calculated using the EAM show that energy barriers for both vacancy and adatom cluster core-breakup are 22 kcal/mol and 22.3 kcal/mol, respectively as shown in Figures 8 and 9. These high barriers make core-breakup

Figure 7. STM data and three simulation predictions in the plot of Log D vs N.
The STM data are from a film with coverage = 0.87 ML (file Ag-05-31-94, filled squares), and a film with coverage = 1.1 ML (file Ag-0609-94, black dots)

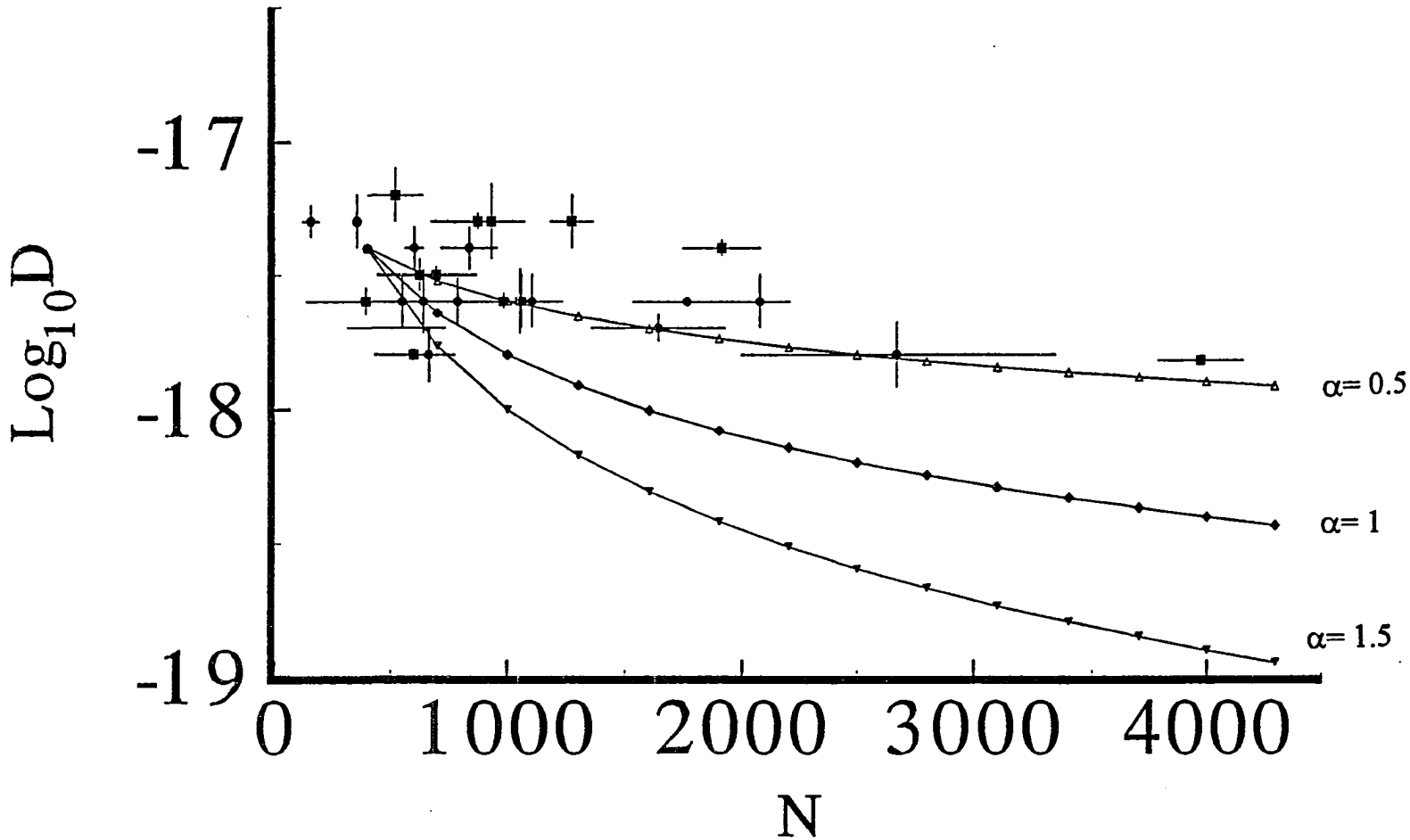
-17
-18
-19
$Log_{10}D$
0
1000
2000
3000
4000
N
α= 0.5
α= 1
α= 1.5

Figure 8. Activation barriers for adatom monomer diffusing in three different cases.

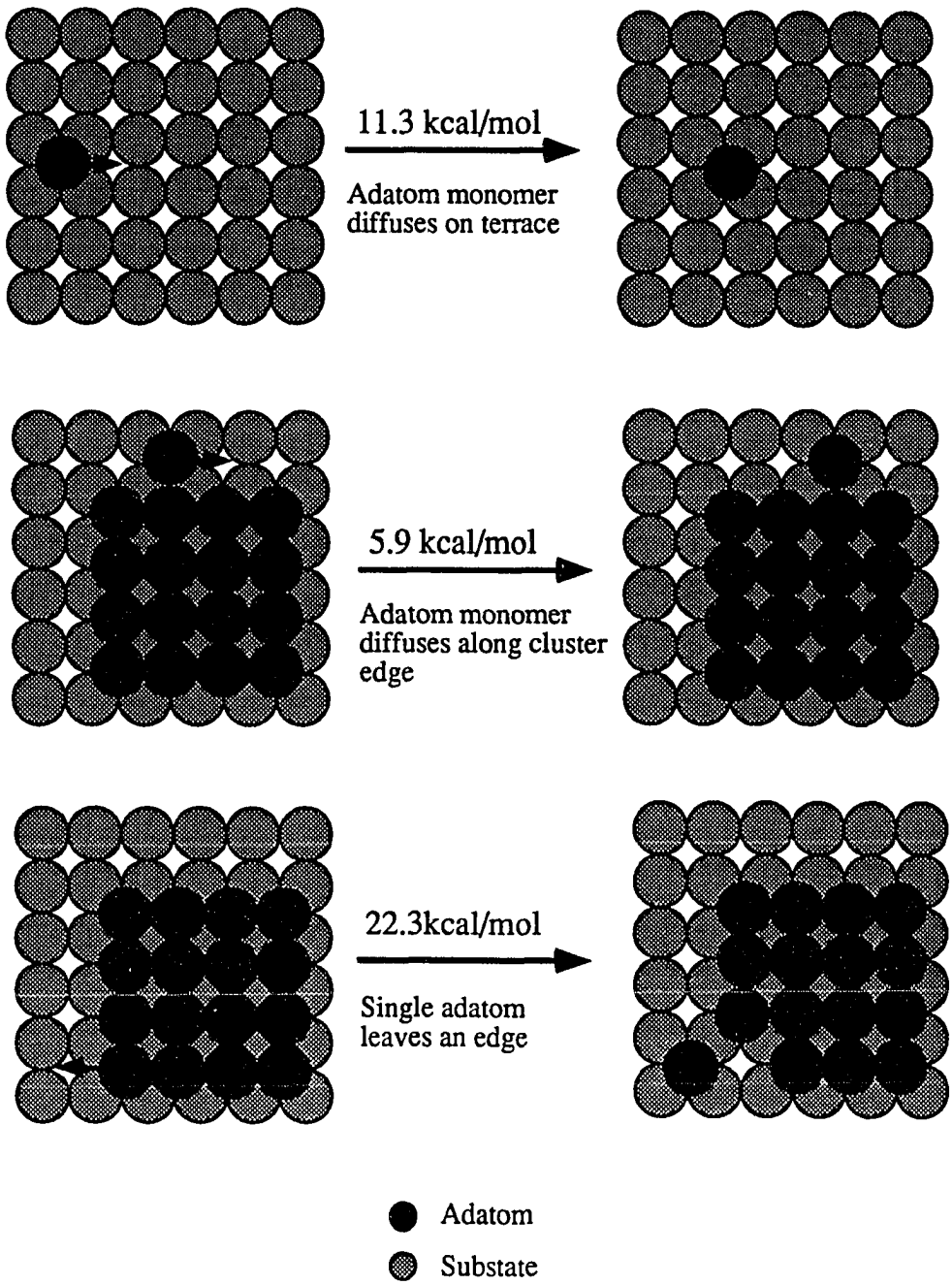
11.3 kcal/mol
Adatom monomer diffuses on terrace
5.9 kcal/mol
Adatom monomer diffuses along cluster edge
22.3kcal/mol
Single adatom leaves an edge
Adatom
Substate

Figure 9. Activation barriers for vacancy monomer diffusing in three different cases.

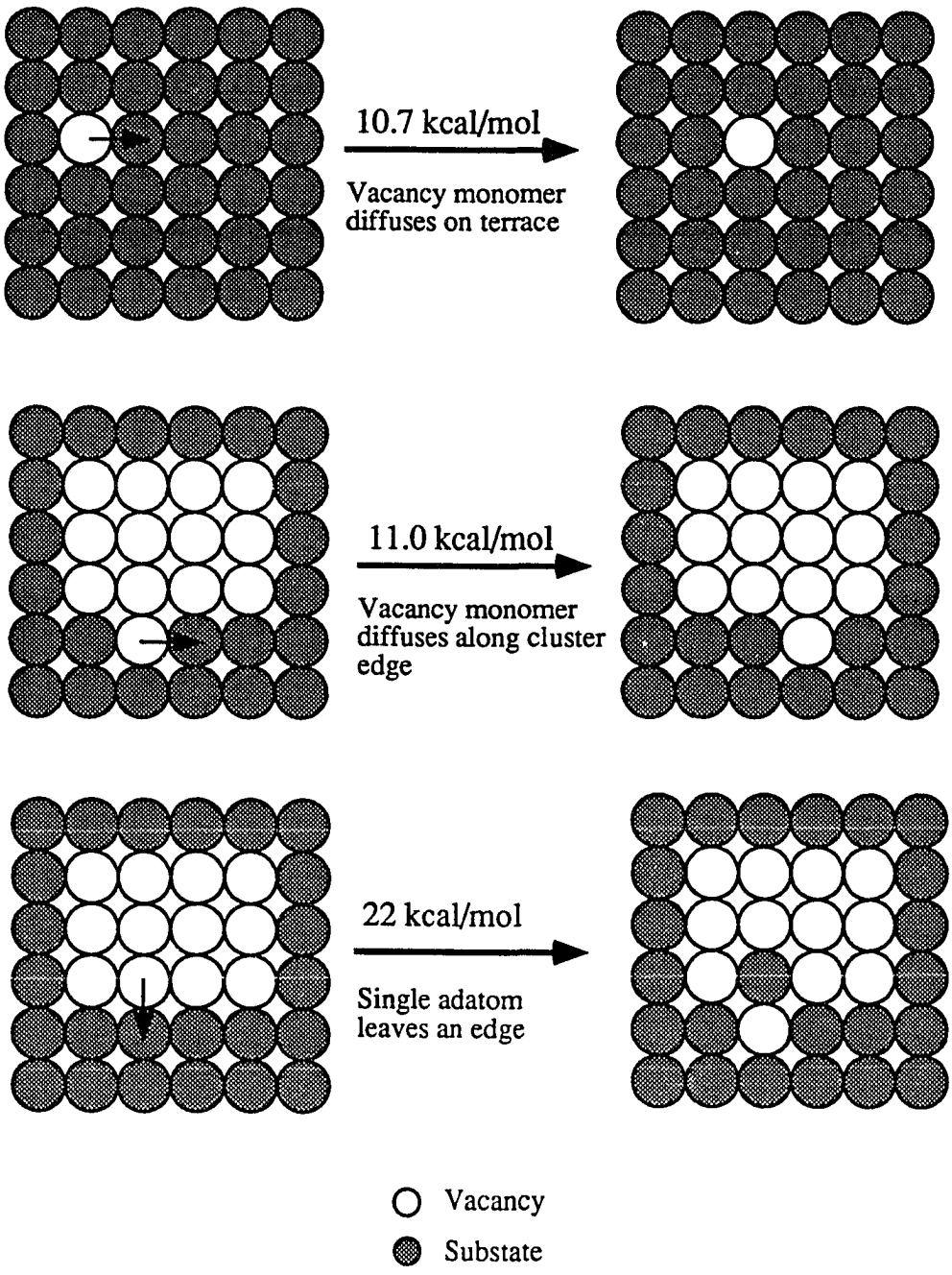
10.7 kcal/mol
Vacancy monomer diffuses on terrace
11.0 kcal/mol
Vacancy monomer diffuses along cluster edge
22 kcal/mol
Single adatom leaves an edge
Vacancy
Substate

equally difficult for both cluster types. On the other hand, when the barriers for single atom and vacancy site movements along a cluster edge are compared (5.9 kcal/mol and 11 kcal/mol, respectively) then it is easy to conclude that a single atom migratioin along cluster edges is much easier than in single vacancy site migration. The general explanation of small adatom cluster short-range diffusion is that adatom diffusion along the cluster edge makes the center of the cluster move [21]. The considerably higher energy required for vacancy movement makes vacancy site edge-running less significant and, therefore, less likely to be a mechanism for vacancy cluster migration. Moreover, when we compare the activation energy needed for a vacancy monomer to migrate on the terrace (10.7 kcal/mol) with the activation energy of a vacancy monomer to run along the vacancy cluster edge (11 kcal/mol), we find that a little difference makes the single vacancy diffusion on the terrace a more favorable motion than that in the adatom case. Several theoretical predictions show $2>\alpha \gg 1.5$ [19-22]. This is represented by the dashed line in Figure 7. From Figure 6, it is clear that the strong dependence of D on N in the PD simulation is incompatible with the experimental results. We examined the cluster size as a function of time during the diffusion process. Under this PD, each vacancy cluster should have a constant size throughout the measurement. But the experimental results show that the mass of a cluster is not conserved. That the vacancy cluster changes its size indicates that mass exchange occurs between the clusters and the film layer, and that the exchange rates among clusters are not the same. So, practically, the film itself is used as a medium by vacancy clusters to transport mass between vacancy clusters. Consequently, some clusters grow at the expense of others. Thus the mass

center of a cluster vacancy will move under the influence of vacancy monomers. Therefore we rule out PD as the dominating mechanism in vacancy diffusion. This is an important point because it helps to explain the feasibility of the vacancy cluster evaporation-condensation mechanism.

The second model that may contribute to an understanding of the diffusion of vacancy clusters shows atoms from the internal edges of the vacancy running across the vacancy cluster. This motion can also result in vacancy cluster diffusion. The modeling [22] has indicated a scaling factor of α=1 [25], i.e., the diffusion coefficient of the cluster shall be inversely proportional to the cluster size. Morgenstern *et al.* [24] also provided a simple theoretical treatment which gave rise to α=1. A modeling done by Soler [23] indicated this mechanism is the least significant mechanism in cluster diffusion on a triangular lattice, However, Morgenstern *et al.* [14], in an STM experiment, showed that this mechanism reflects the vacancy cluster diffusion for the Ag/Ag(111) system. The difference between Ag(111) and Ag(100) is far more than a difference in surface orientation. For example, while the homoepitaxy of Ag/Ag(100) is layer-by-layer [18], Ag/Ag(111) is not [26]. For the Ag/Ag(100) system, we compare our STM data with the α=1 curve (Figure 7). It is clear that the STM data does not fit the calculated α=1 curve. Furthermore, as in the PD mechanism, this mechanism cannot explain the observed vacancy size change behavior.

For the third mechanism, i.e., evaporation-condensation of vacancy monomers (EC), we view the vacancy clusters as being in a quasiequilibrium with a dilute 2D gas of vacancy monomers within the film. Vacancy monomers leaving and re-attaching to the vacancy

cluster's internal edge can result in large displacement of the cluster. This model predicts a scaling factor of α=0.5 [22]. This relatively weak dependence on the size of the cluster, N, is roughly consistent with the STM data (Figure 7). This fact, as well as the fact that vacancy clusters change their size support the idea that EC dominates the diffusion of vacancy clusters. Thus the picture of the diffusion process is that: (1) the vacancy cluster is composed of a number of vacancy monomers, (2) the film (the filled area) contains some vacancy monomers (film vacancy monomer) which are distributed within the film, (3) a quasiequilibrium of vacancy monomers exists between vacancy clusters and film vacancy monomers.

It is easy to explain vacancy clusters' size change with the EC mechanism. The different barriers associated with various atomic configuration cluster edges may give rise to differences in the rates at which vacancy monomers leave and reattach to the internal edges of a large vacancy. The different rates therefore would result in cluster size change.

In the vacancy cluster diffusion process, long range mass transport is involved. The many different atomic motions associated with the vacancy cluster diffusion process and, therefore, with the above three mechanisms are not mutually exclusive. Although based on the scaling factor, we conclude that the EC mechanism dominates the diffusion process, it may be that the other two mechanisms contribute to the process as well.

The Ag /Ag(100) serves as a very good example for comparing the diffusivities of adatom clusters and vacancy clusters. Adatom cluster diffusion is weakly size-dependent in the size range 100-720 atoms with diffusion coefficient (D) on the order of 10^{-17} cm^2s^{-1}

[17]. The vacancy cluster diffusion also has weak size-dependence in the size range 350-3800 atoms with D in the range between 2 to 6 x 10^{-18} cm^2s^{-1} and an average value of 4 x 10^{-18} cm^2s^{-1}. Thus, vacancy clusters have lower diffusion coefficients than adatom clusters. This is supported by the fact that vacancy clusters have little coalescence in the cluster density range where adatom clusters do coalesce [27]. The clusters with faster motion will have a better chance to meet each other and, therefore, to coalesce. de la Figuera and coworkers [15] show that Cu vacancy clusters have diffusion coefficients on the order of 10^{-16} cm^2s^{-1}, two orders of magnitude higher than Ag/Ag(100) , and Cu vacancy clusters do coalesce. In the case of Ag/Ag(111), the diffusion coefficients are even larger ($4x10^{-15}$-$5x10^{-16}$ cm^2s^{-1}) and vacancy coalescence is also observed. Although we can view vacancy clusters as the reverse of adatom clusters, it is not necessary that they have the same diffusion coefficient. The observed difference in diffusivities of vacancy and adatom clusters for Ag/Ag(100) reflects energetic differences in the atomic motions involved in the two different processes.

4. Conclusion

In summary, we used STM to study vacancy cluster diffusion on a clean square lattice. The vacancies were formed by controlling the deposition flux and film coverage. The method is simple and offers similar advantages to the sputtering method. The diffusion coefficient is on the order of 10^{-18} cm^2s^{-1}, smaller than that of adatom clusters, and has a scaling factor α roughly close to 0.5 in $D \propto N^{-\alpha}$. The evaporation-condensation of vacancy

monomers is proposed to dominate the vacancy cluster diffusion process is suggested.

5. Acknowledgments

This work is supported by NSF Grant No. CHE-9317660. Some equipment and all facilities are provided by the Ames Laboratory. Ames Laboratory is operated by Iowa State University under Contract No. W-7405-Eng-82.

References

1. G. Kellogg, Appl. Surf. Sci. 67 (1993) 134.

2. S.-C. Wang and G. Ehrlich, Surf. Sci. 239 (1990) 301; G. L. Kellogg, Phys. Rev. Lett. 73 (1994) 1833.

3. D. D. Chambliss, R. J. Wilson, and S. Chiang, Phys. Rev. Lett. 66 (1991) 1721; R. Q. Hwang, C. Gunther, J. Schroder, S. Gunther, E. Kopatzki, and R. J. Behm, J. Vac. Sci. Technol. A 10 (1992) 1970; D. D. Chambliss, R. J. Wilson, and S. Chiang, J. Vac. Sci. Technol B 9 (1991) 933;R. Q. Hwang and R. J. Behm, J. Vac. Sci. Technol. B 10 (1992) 256.

4. J. C. Hamilton et al., submitted to Phys. Rev. Lett. (1994).

5. C. Massobrio, P. Blandin, Phys. Rev. B 47 (1993) 13687.

6. C.-L. Liu and James B. Adams, Surf. Sci. 268 (1992) 73.

7. J.A. Venables, G.D.T. Spiller, and M. Hanbuecken, Rep. Prog. Phys. 47 (1984) 399 and references therein.

8. C.-L. Liu, Surf. Sci. 316 (1994) 294.

9. S.-L. Chang and P. A. Thiel, CRC Crit. Rev. Sur.Chem. 3 (1994) 239.

10. M. Zinke-Allmang et al.,Surf. Sci. Reports 16 (1992) 377.

11. K.-N. Tu, et al., Electronic Thin Film Science for Electrical Engineers and Materials Scientists, Macmillan Publishing Co. new York, 1991.

12. Z. Zhou and B. Joos, Surf. Sci. 323 (1995) 311.

13. B. Joos and M. S. Duesbery, Phys. Rev. Lett. 70 (1993) 2754; 72 (1994) 3744E.

14. K. Morgenstern, G. Rosenfeld, B. Poelsema, and G. Comsa, Phys. Rev. Lett. 74 (1995) 2058.

15. J. de la Figuera, J. E. Prieto, C. Ocal and R. Miranda, Solid State Communications, 89 (1994) 815.

16. J. de la Figuera, J. E. Prieto, C. Ocal and R. Miranda, Surf. Sci. 307 (1994) 538.
J. S. Ozcomert et al., Surf. Sci. 293 (1993) 183.

17. J.-M. Wen, S.-L. Chang, J. W. Burnett, J. W. Evans, and P.A. Thiel, Phys. Rev. Lett. 73 (1994) 2591.

18. Y. Suzuki, H. Kikuchi and N. Koshizuka, Jap. J. Appli. Phys. 27 (1988) L1175.

19. H. C. Kang, P.A. Thiel and J. W. Evans, J. Chem. Phys. 93 (1990) 9018.

20. A. F. Voter, Phys. Rev. B 34 (1986) 6819.

21. A. F. Voter, SPIE Modeling of Optical Thin Films 821 (1987) 214.

22. K. Binder and M. H. Kalos, J. Stat. Phys. 22 (1980) 363.

23. J. M. Soler, Phys. Rev. B 50 (1994) 5578.

24. The difference in binding energy and diffusion barrier between FCC(100) and FCC(111) can cause different surface dynamics. M. Breeman, et al., Surf. Sci. 323 (1995) 71.

25. In his modeling, Soler has concluded a=3/2.

26. H. A. van der Vegt, H. M. Van pinxteren, m. Lohmeier, and E. Vlieg, Phys. Rev. Lett. 68 (1992) 3335.

27. For Ag/Ag(100), at low coverage (5%-27%ML), the adatom clusters coalesce dominate the coarsening process.

CHAPTER 5

SURFACE DYNAMICAL PHENOMENA

A paper to be submitted to Surface Science

J.-M. Wen, J. Evans and P. Thiel

1. Introduction

The growth of thin metal films has been studied for several decades and has received renewed attention recently with the improvement of film preparation methods, such as molecular beam epitaxy (MBE). Thin films have been used in many different areas due to their unique chemical, structural and electronic properties. Applications include optics, microelectronic devices, and magnetic recording media. The film properties are directly related to their atomic-level structure and morphology. Therefore it is necessary to obtain information about the development of films at an atomic scale. Area-averaged techniques, such as He-scattering and high-resolution low energy electron diffraction, are valuable in measuring the evolution of the film during and after deposition [1-2]. However, these are indirect methods, and information obtained in these ways lacks local structure and morphology information.

Due to its ability to track local surface morphology changes, scanning tunneling microscopy (STM) has also been used to investigate film growth. So far, many STM studies

have been carried out at room temperature and have dealt with the early stages of growth, such as nucleation and film structure [3-6]. These studies obtain information by analyzing the post-deposition film. The direct observation of diffusion processes and film structure change is limited to materials which have high enough diffusitivity at room temperature [7-8]. Although in principle variable-temperature STM can provide better understanding of thin film growth processes, the difficulty of taking actual measurements limits it at present.

The post-deposition stage of film growth is a very important aspect. It can involve individual atom diffusion as well as cluster diffusion. The films are normally in a non-equilibrium condition and evolve toward equilibrium. When thermally induced diffusion is activated, the system will be driven toward equilibrium. During this dynamic process the film structure can change dramatically [9]. In this study, STM investigations of Ag adlayer dynamics on Ag(100) are presented. The dynamics of Ag films are addressed in three related aspects: the interaction between film clusters and surface steps, coalescence between film clusters, and contamination effects on film evolution.

2. Experimental

The experiments are performed in an ultrahigh vacuum (UHV) chamber equipped with standard surface science techniques, such as low energy electron diffraction (LEED) and Auger electron spectroscopy, as well as an Omicron scanning tunneling microscopy (STM). The Ag sample is cleaned by cycles of Ar ion bombardment (1kV) and annealing at 1000K for 20 min. Ag is evaporated onto an Ag(100) using a resistively heated source.

During deposition, the sample is held at room temperature, and the pressure inside the chamber is kept between $3x10^{-10}$ to $8x10^{-11}$. Deposition flux is calibrated by measuring submonolayer coverages with STM. After deposition, the samples are transported into the STM. The images are recorded in a constant-current mode and presented in gray scale with top views. The typical tunneling current is 2-3.5 nA. The typical gap voltage is 0.4-1.1 V. Typically, the time between the end of deposition and the beginning of data acquisition with the STM is from 10 min to 90 min. Scan rate depends upon image size and data acquisition rate, and varies from 196Å/sec to 245Å/sec.

3. Results and Discussion

a. Cluster dynamics near a step edge

Steps play a very important role in film growth. The interaction between a step and an adatom can be divided into the three types as shown in Figure 1: (1) the atom approaches an ascending step edge and then is trapped at the step; (2) the atom approaches a descending step edge and incorporates into the step edge; and (3) an atom approaches a descending step edge but is reflected back before falling over the step edge. During deposition, adatom clusters form following nucleation. In this section, STM data is presented to show the interaction between adatom clusters and step edges. The examination of the interaction between adatom clusters and steps is important not only in revealing the atom/step interaction but also in providing information about the pathway of change in the film structure and morphology.

In this section, five different coalescence phenomena are discussed: (1) a cluster and a straight step; (2) a cluster and a step with a protrusion; (3) a cluster and the internal edge of a vacancy; (4) mass flow between first and second layer clusters; and (5) the depletion zone along the step on the lower terrace.

(1) a cluster and a straight step

As shown in Chapter 2, large Ag adatom clusters can diffuse on large Ag (100) terraces at room temperature in a random manner. Figure 2.1, however, shows STM images taken near a stepped area. In this figure, one sees that a narrow step allow only a few clusters to stay in the center part of the terrace. For even narrower terraces no cluster can form. A step can influence a nearby cluster's diffusion, therefore the cluster undergoes biased motion rather than a random motion. This motion is illustrated in a series of images (Figure 2.2) which shows that the cluster migrates toward the step and then collides with the step. The terrace width under examination in Figure 2.2 is about 280Å. Since the terrace width is so narrow, the clusters close to the step (<~30Å) will interact with the step. We characterize the coalescence process between a cluster and a step by dividing it into three different phases. Phase 1 is approach, where the cluster migrates toward a step while the step, basically, stays stationary. Phase 2 is collision between the cluster and the step, where the cluster and step edge physically touch each other on a short time scale. Phase 3 is rearrangement of the step edge.

In Figure 2.2, the cluster labeled **a** moves toward a step edge as a function of time. A bump is then formed on the step when the cluster touches the step edge. This bump

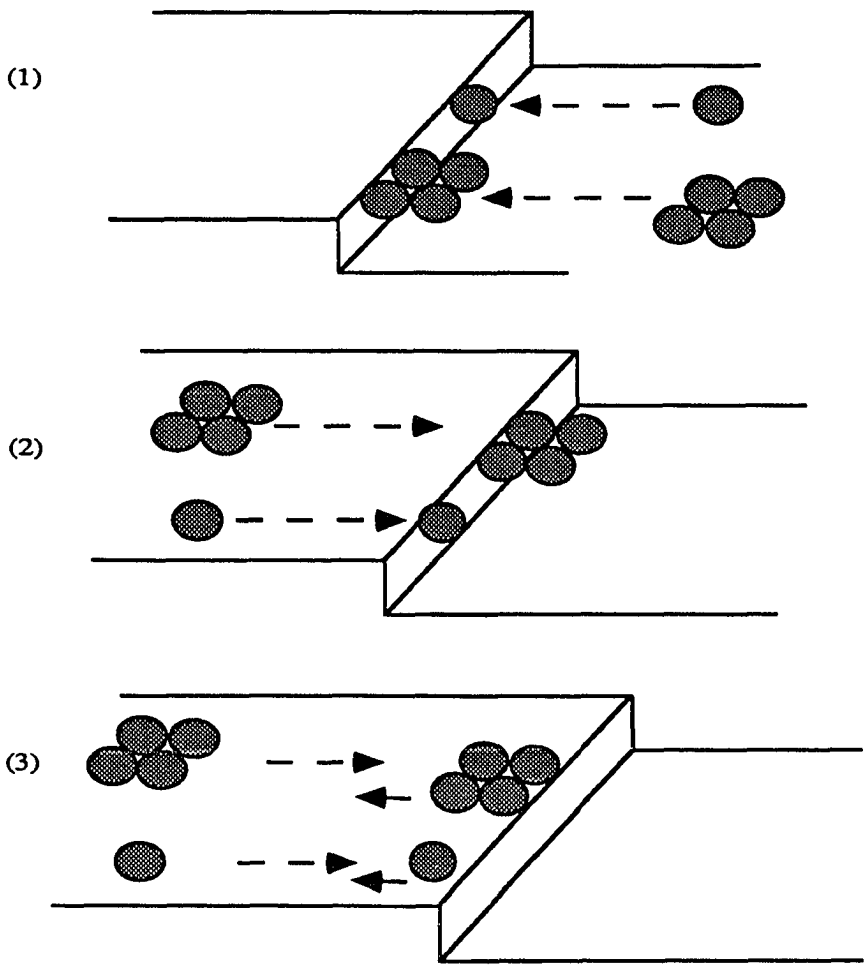

Figure 1. The interaction between a step and a cluster/ atom. (1) an atom/cluster approaches an ascending step edge and then is trapped at the step; (2) an atom/cluster approaches a descending step edge and incorporates into the step edge; (3) an atom/cluster approaches a descending step edge but is reflected back before falling over the step edge.

gradually disappears and the step edge relaxes back into its original shape. In this cluster-step edge case, Phase 1 and 2 are fast motion. Therefore, a short image interval is needed to capture the details of the first two phases. We find that once the separation between the step edge and the cluster edge reaches a minimum distance, the coalescence (collision) occurs in a very short time period. The minimum distance is defined as the smallest observed spacing between the cluster and the step before coalescence takes place. This spacing is found to be around 10Å. After the coalescence, the step starts to rearrange its edge back to a straight edge. It is the third phase. The time needed for the step edge to fully relax is a function of the bump size. As shown in Figure 3, when a smaller cluster collides with a step, it takes less time for the step to change back to its initial shape compared with Figure 2.2. Pimpinelli [10] has estimated the time needed for a bump to form on a step due to thermal excitation. This can be seen as the reverse process of the cases we described above in Figure 2.2. In their estimation, the bump size is related to the time needed to create that bump, and the general trend is that a larger bump needs a longer time to be created. Step relaxation can be viewed as dispersion of bump atoms along the step edge. We use w and h to characterize the shape of the bump, where w is along the step, and h is perpendicular to the step. Figure 4 shows the plot of w and h vs. time, t, for the cluster in Figure 3.1. The increase in w and decrease in h over t indicate that atoms relocate along the step.

The above examples are cases where the clusters interact with [110] step edges (the cluster edges are parallel to the step edges). That the cluster edge interacts with a [100]

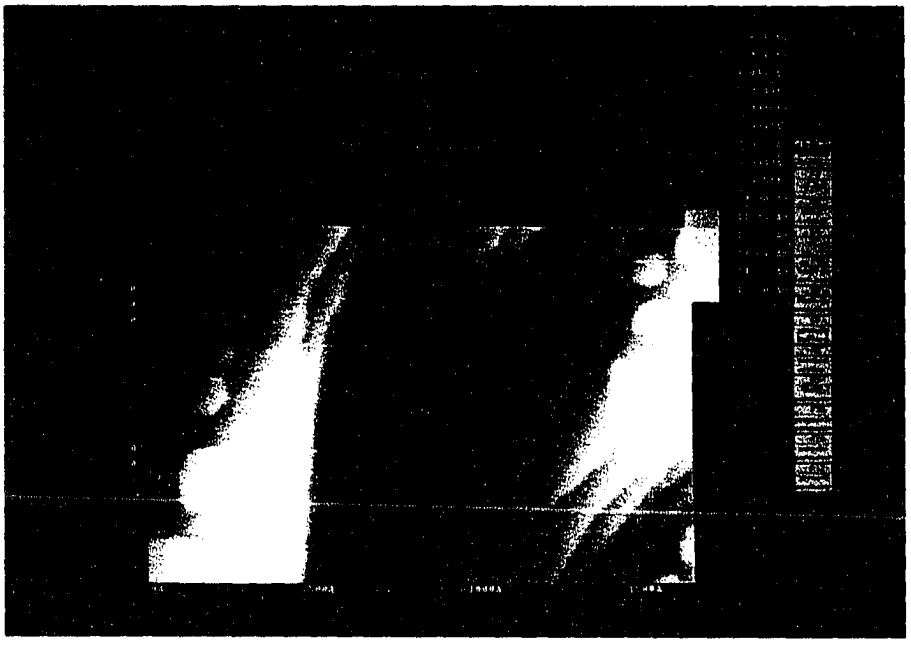

Figure 2.1. The deposited clusters on narrow terraces. Clusters only exist on terraces with certain width.

Figure 2.2. A series of images show that a cluster (75 x 75 $Å^2$) labeled **a** moves toward a step edge (not a straight edge) and then collides with the step. The images are 600 Å x 600 Å. The time interval between images is (1) t = 0; (2) t = 3 min; (3) t =6 min ; (4) t = 95 min. The data is under file name Ag_08-23-93. The file numbers are 6, 7, 8 and 19.

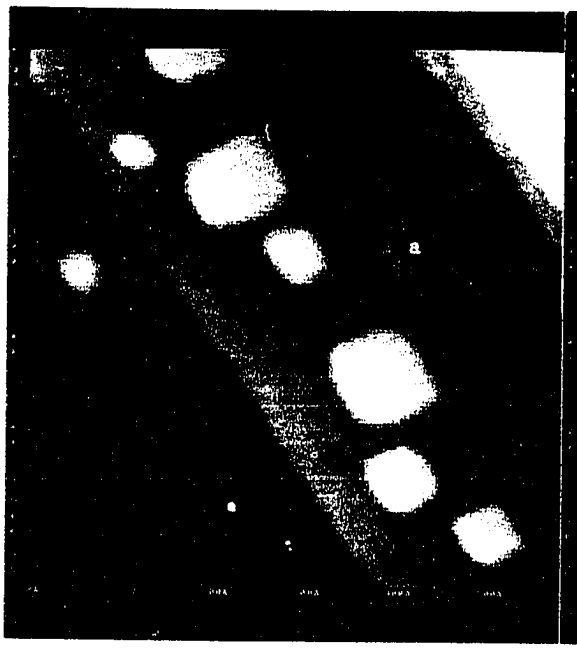

(1)

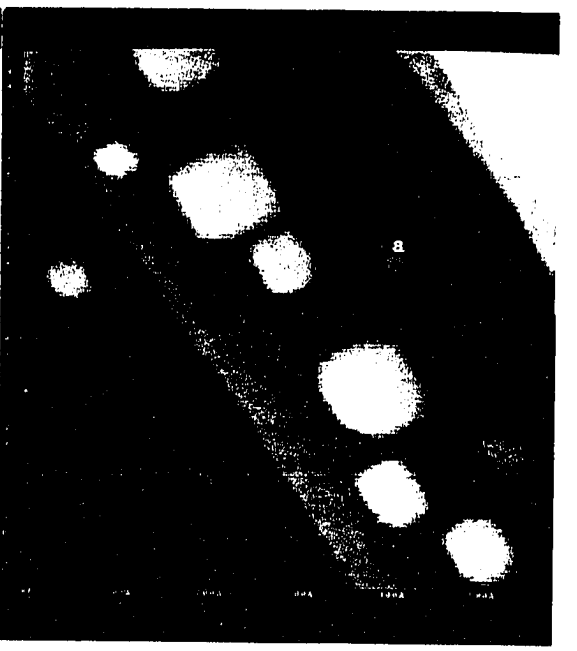

(2)

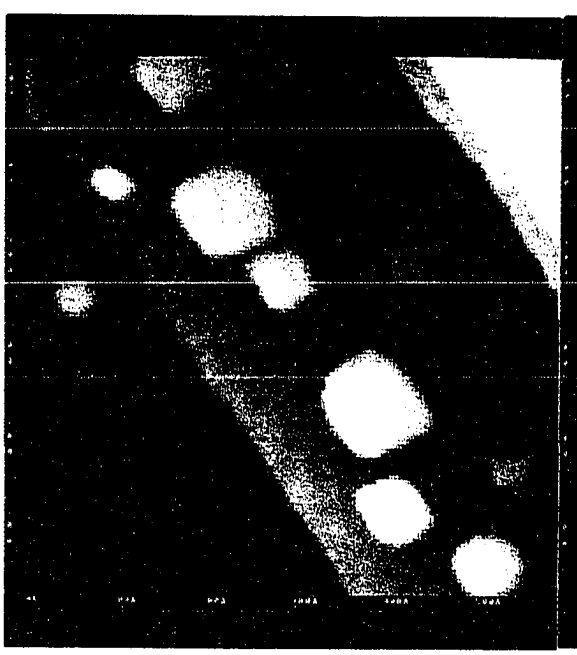

(3)

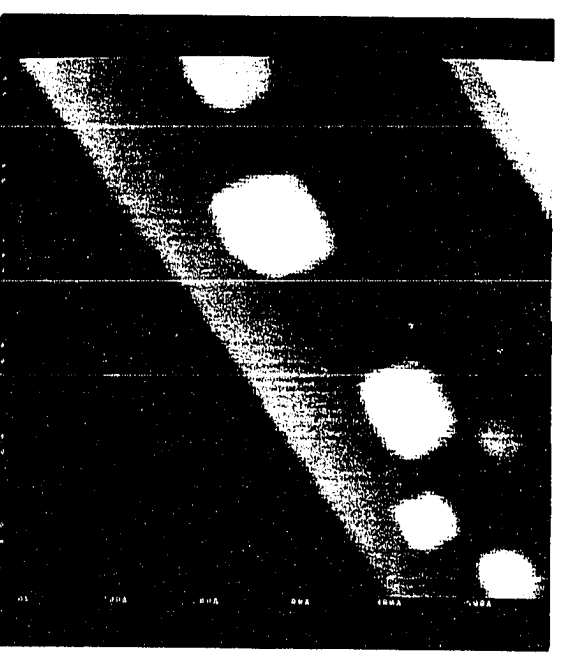

(4)

Figure 3.1. A series of images show that a cluster (55 x 45 $Å^2$) labeled **a** moves toward a step edge (not a straight edge) and then collides with the step. The images are 600 Å x 600 Å. The time interval between images is (1) t = 0; (2) t = 17 min; (3) t =21 min ; (4) t = 25 min. The data is under file name Ag_08-23-93. The file numbers are 23, 24, 25 and 26.

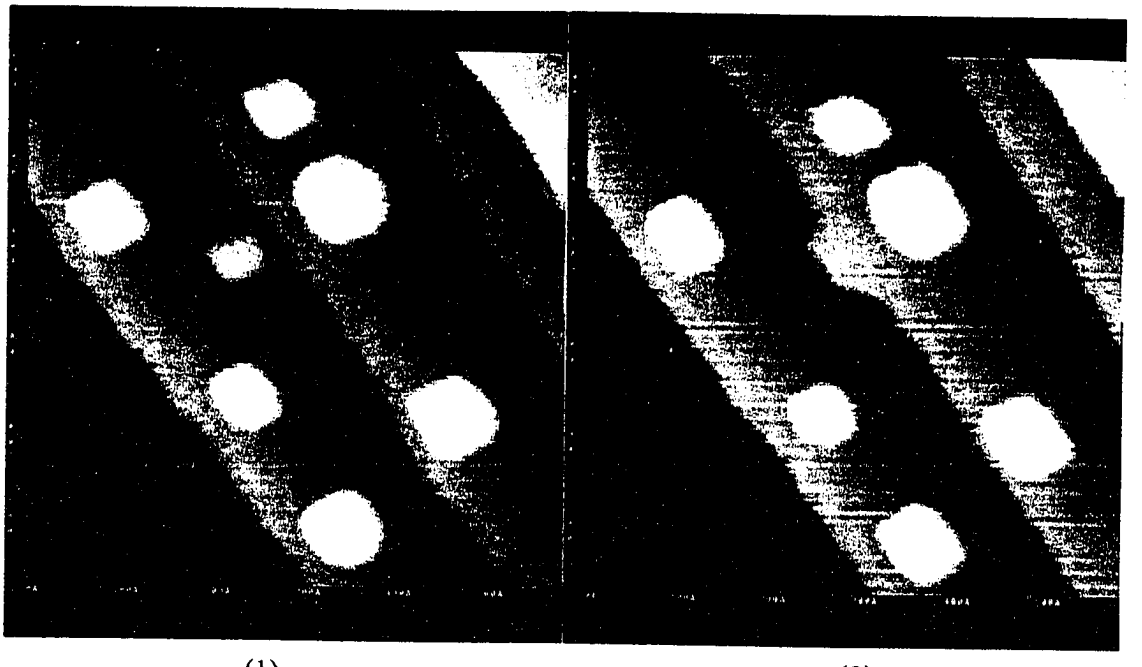

(1) (2)

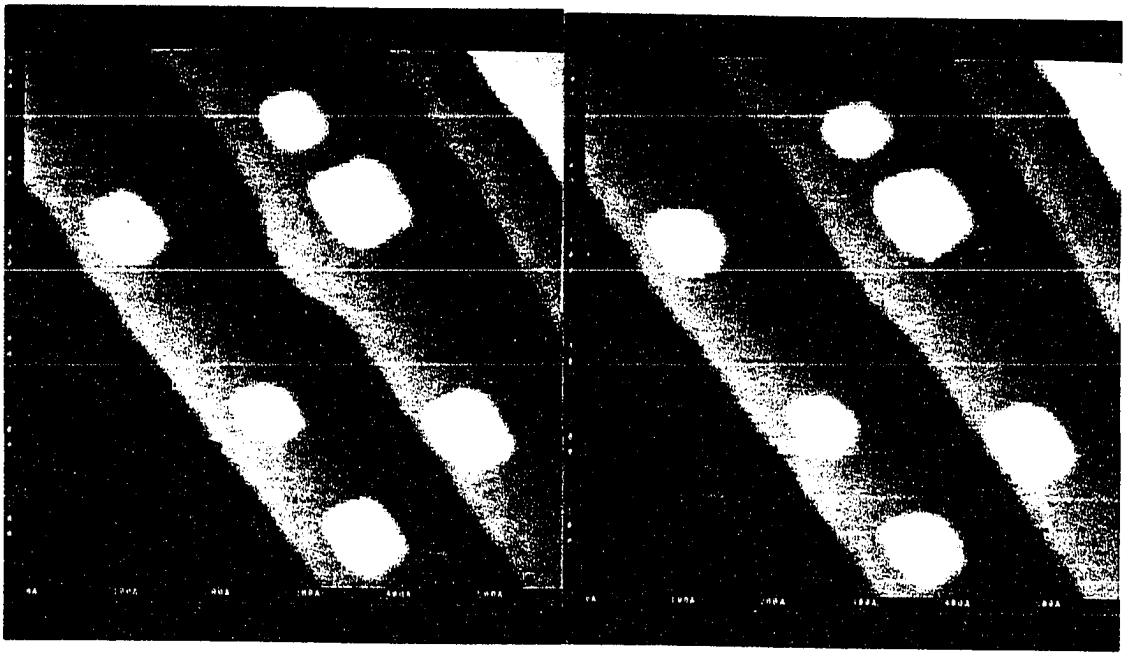

(3) (4)

Figure 3.2. A series of images show that a cluster (55 x 50 $Å^2$) labeled a moves toward a step edge (not a straight edge) and then collides with the step. The images are 600 Å x 600 Å. The time interval between images is (1) t = 0; (2) t = 7 min; (3) t =22 min ; (4) t = 43 min. The data is under file name Ag_08-23-93. The file numbers are 28, 29, 30 and 31.

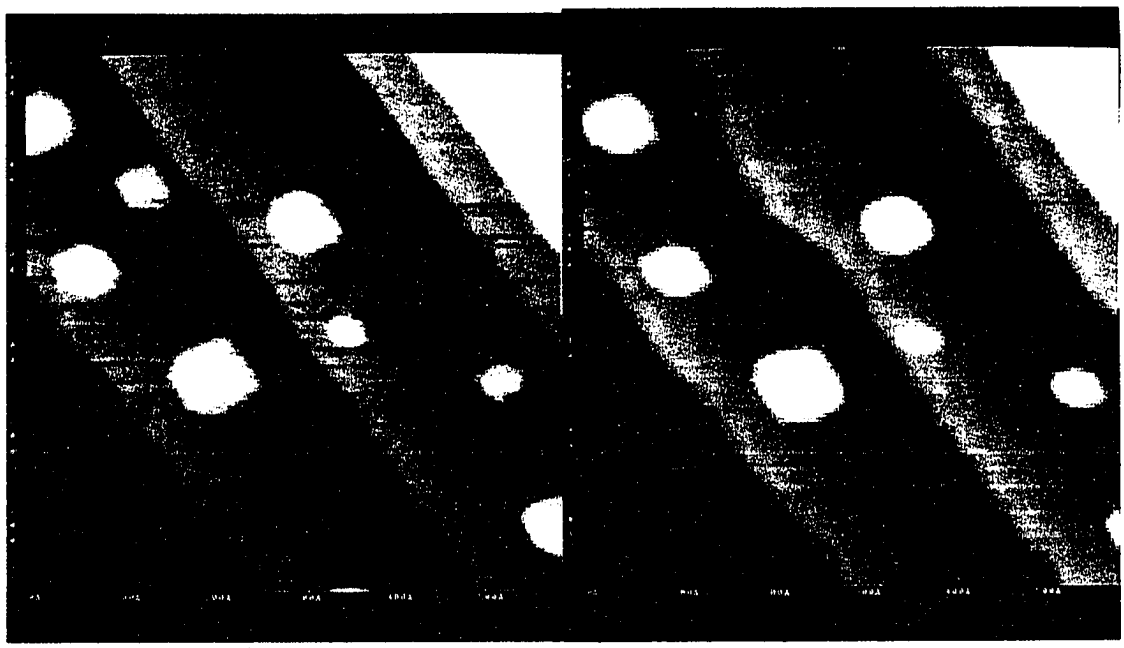

(1) (2)

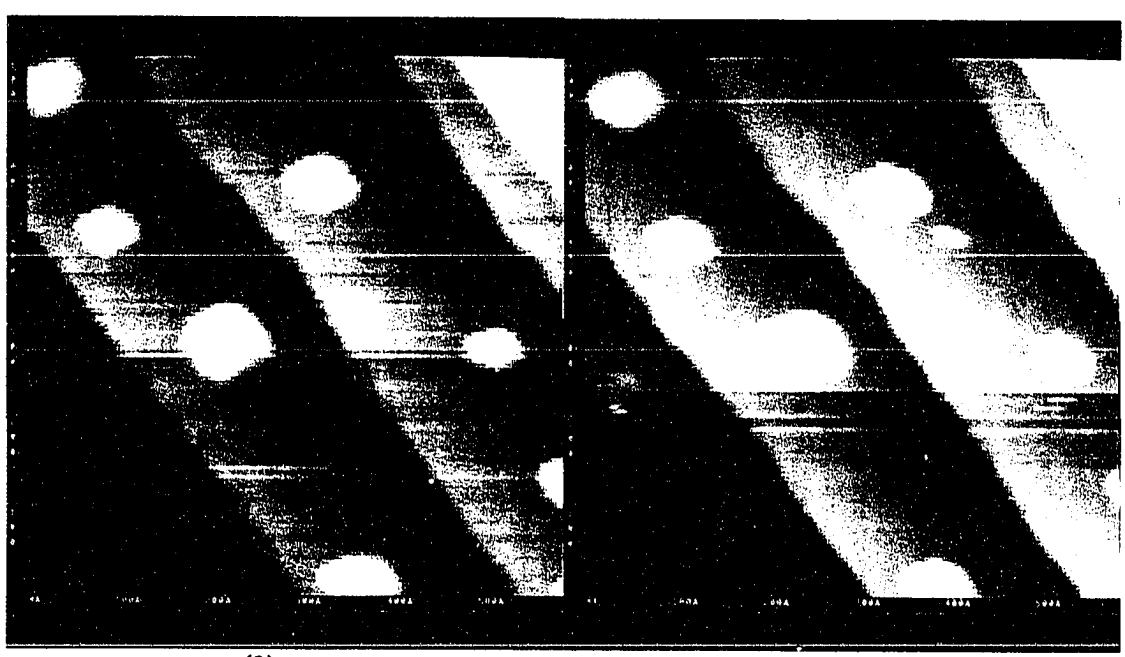

(3) (4)

step edge is also observed, as shown in Figure 5. The plot of h vs. t is shown in Figure 6. Compared to Figure 4, the time needed to reduce h is much longer. Since the step orientations are different in these two cases, it can be seen that there are different dynamics for [100] and [110] steps. Figure 7 shows the atomistic pictures of the two cases. From Figure 7, a slower course to disperse atoms along [100] edge is expected. We have noticed that during the dispersion, the initial stage is to widen the coalescence point. It is a slow process in terms of h value reduction.(For the [110] edge case, no such stage exists).

The overall coalescence shows that a step edge can be a sink not only for adatoms but also for clusters, although the mechanisms may differ. In the adatom case, the fact that adatoms get trapped at step edges can be explained by the lower coordination number in step edges which makes them an energetically favored place to trap adatoms. However, it is difficult to use the same argument to explain cluster trapping at a step edge, since a cluster contains many atoms (10^2 -10^3 atoms).

In the collision of a step edge and a cluster, one of the basic questions that needs to be answered is whether or not the collision occurs in a random manner. Does the cluster migrate randomly before the coalescence takes place? Or does the step capture the cluster when it moves close to the step (capture below a critical separation)?. Our observations are consistent with the latter. Although the actual atomic processes involved in the coalescence are not yet known, we provide three possible mechanisms to explain the step/cluster coalescence.

Figure 4. The plot of w and h vs. t for the cluster in Figure 3.1. The starting time is estimated at t = 14 min.

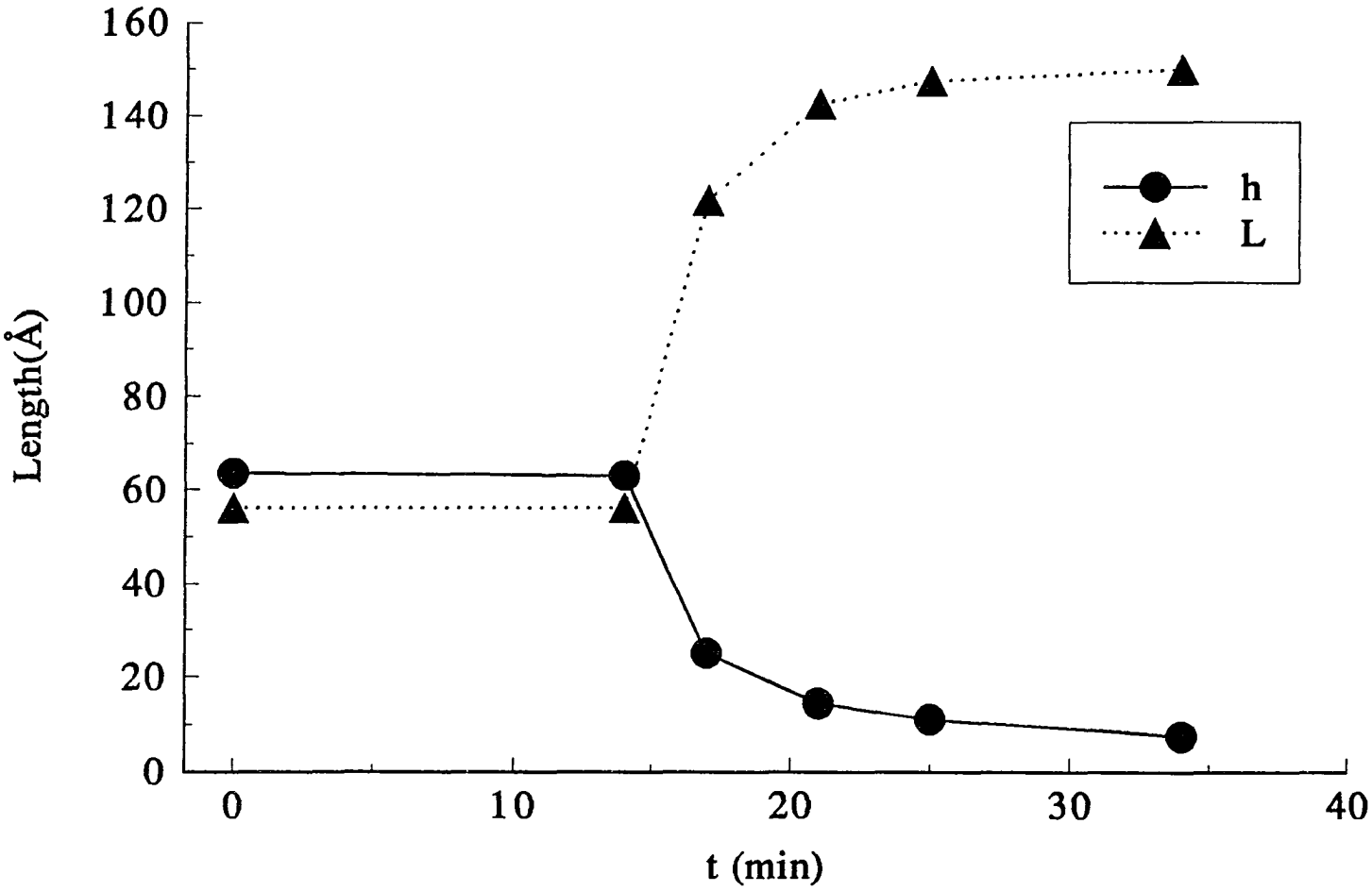
160
140
120
100
80
60
40
20
0
Length(Å)
0
10
20
30
40
t (min)
h
L

Figure 5. A series of images showing that a cluster labeled **a** moves toward a step edge (a straight edge with [100] orientation) and then collides with the step. The images are 1000 Å x 1000 Å. The time interval is (1) 0 min; (2) 29 min; (3) 53 min; (4) 73 min; (5) 122 min; (6) 151 min.; (7) 222 min.; (8) 268 min. The data is under file name Ag-05-28-94.

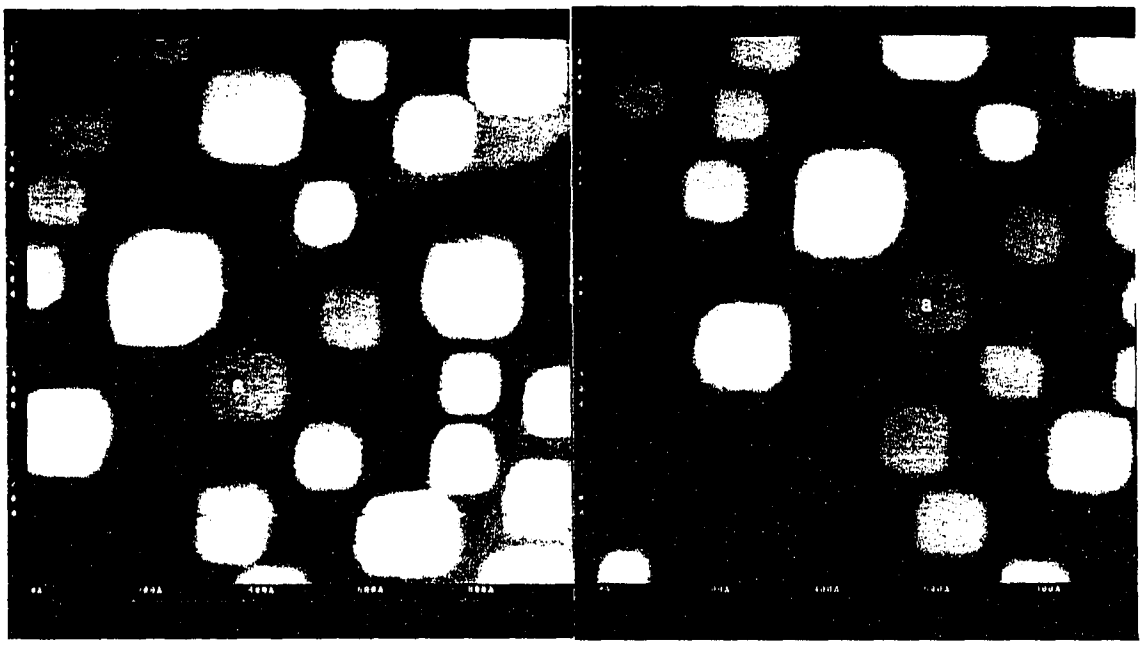

(1) (2)

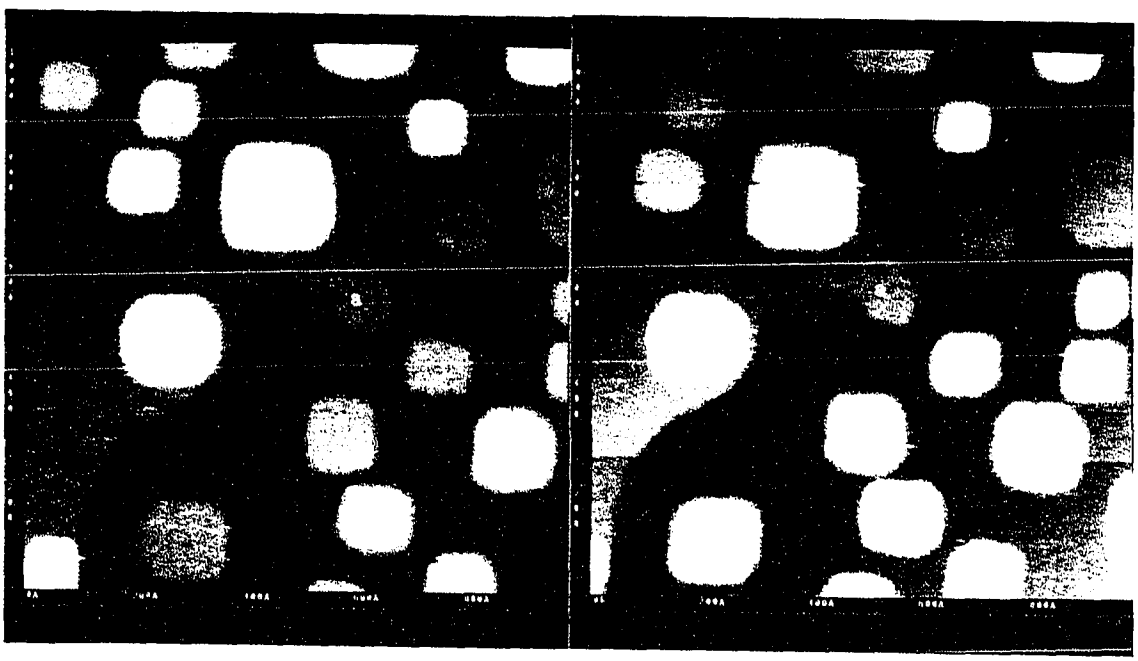

(3) (4)

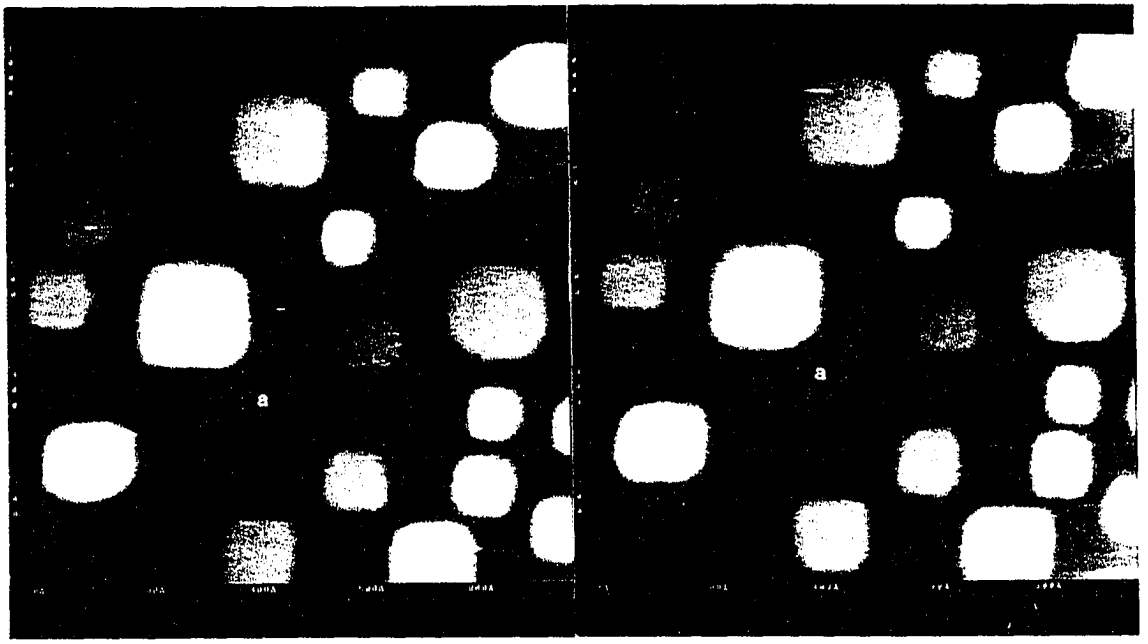

(5) (6)

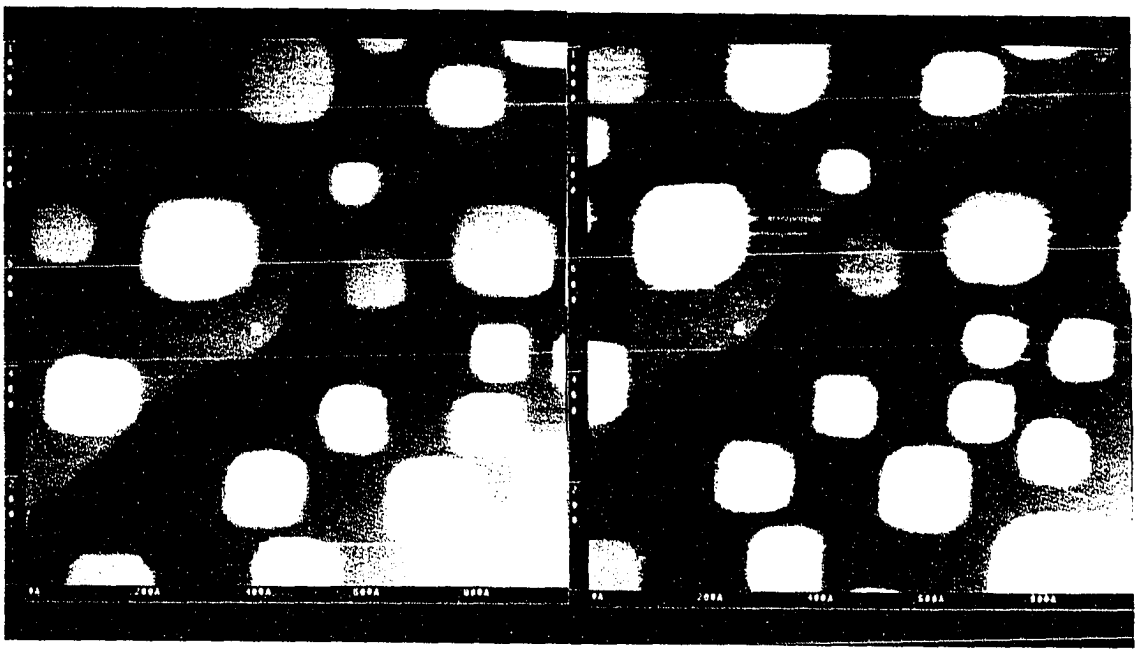

(7) (8)

Figure 5. cont.

Figure 6. h vs. t and Log h vs. Log t for the cluster in Figure 5.
The Log-Log plot shows a difference of h reducing rates between first half and second half.

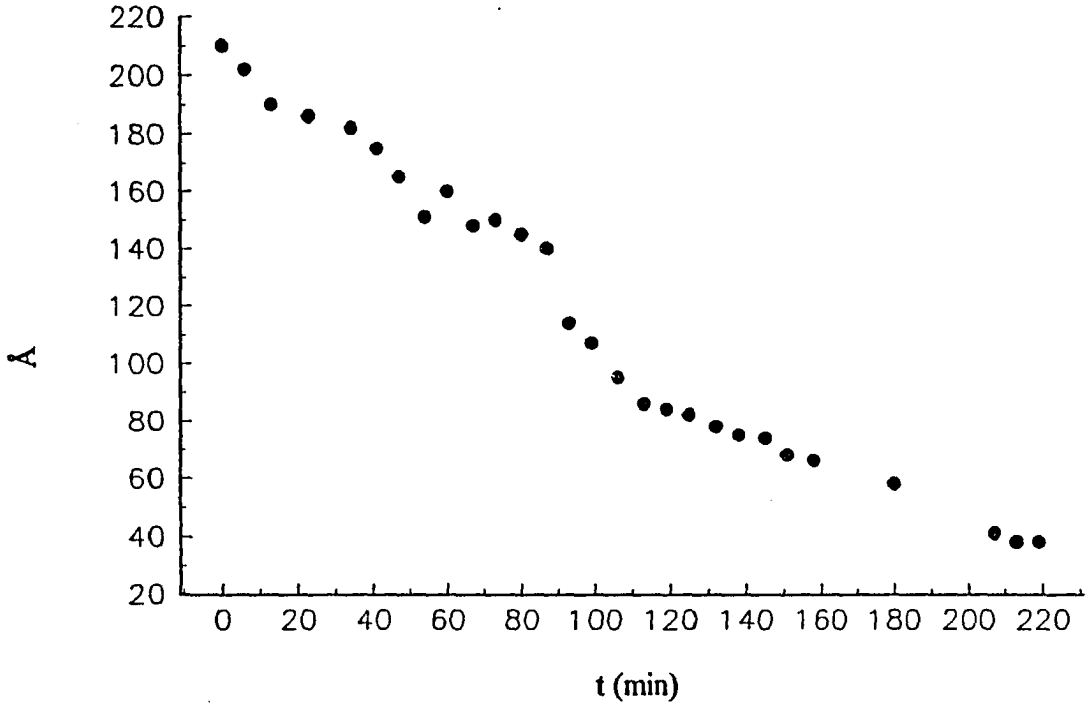
220
200
180
160
140
120
100
80
60
40
20
A
0 20 40 60 80 100 120 140 160 180 200 220
t (min)

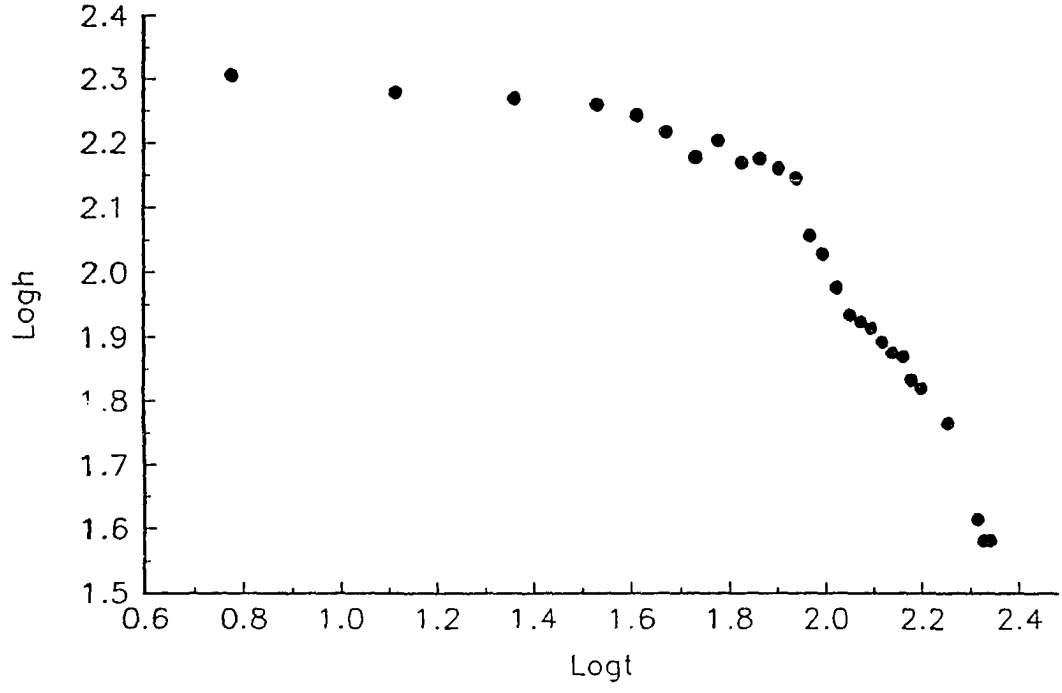
2.4
2.3
2.2
2.1
2.0
1.9
1.8
1.7
1.6
1.5
Logh
0.6 0.8 1.0 1.2 1.4 1.6 1.8 2.0 2.2 2.4
Logt

Figure 7. A simple atomistic illustration of cluster/step coalescence for two different step orientations ([100] and [110] step orientations). The energy barriers used in the picture are from ref. 21 of Chapter 4. Two factors affect the slower the rate of reducing h in [100] step edge case. (1) The widening process for the coalescence point contributes little to the reduction of h value; and (2) Higherbarrier atomic motions are more involving in the [100] case.

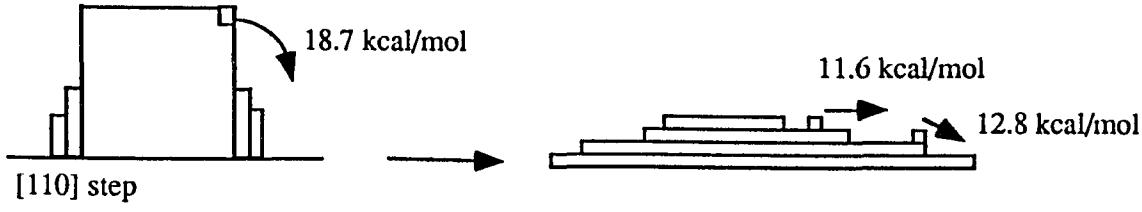
18.7 kcal/mol
11.6 kcal/mol
12.8 kcal/mol
[110] step

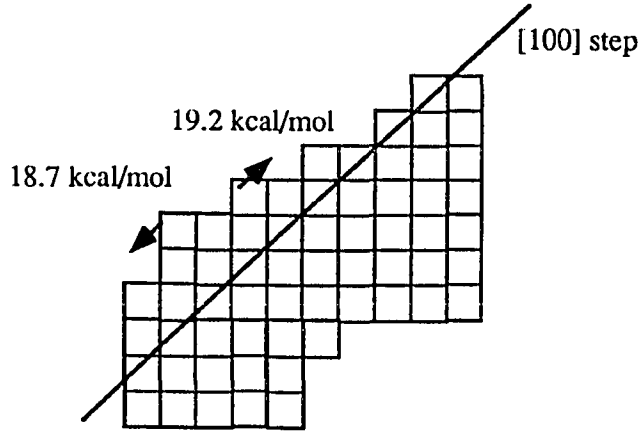
[100] step
19.2 kcal/mol
18.7 kcal/mol

(i) Concentration model

In this model, the adatom concentration builds up between the cluster and the step, and results in coalescence.

We adopt the concept of ripening to model the coalescence between clusters and steps in this system. In ripening, a 2D dilute gas phase is assumed on terraces and around clusters. The partial pressures of adatoms at various surface locations are different. The relationship between the partial pressure of adatoms and a cluster's curvature is governed by the Gibbs-Thomson equation [11]:

$$P_{(r)} \propto P_{(0)} * \mathrm{Exp}(1/r)$$

where $P_{(0)}$ is the equilibrium partial pressure associated with a straight step edge, and $P_{(r)}$ is the equilibrium partial pressure near the edge of a cluster with a radius, r. Here a cluster is assumed to be circular and any irregularities in shape are neglected. Thus, the concentration of adatoms is considered to be evenly distributed around the cluster.

When $r \rightarrow \infty$, the equilibrium partial pressure of a cluster edge decreases to the value of a straight step edge. This relationship indicates that a small cluster has a larger adatom equilibrium partial pressure around its periphery. Since partial pressure is directly related to adatom concentration, the above relationship can also be interpreted in terms of adatom concentration.

Thus the following picture of adatom distribution develops: a dilute 2D adatom gas exists on the terrace, with a higher concentration of adatoms near the straight step edges, an even higher concentration of adatoms around large clusters, and the highest concentration

of adatoms around the smallest clusters. Thus, the concentration around a cluster is inversely proportional to the size of the cluster (cluster curvature.), i.e., the smaller a cluster is, the higher is the concentration around it. Near a straight step edge, the very small curvature indicates a very small 2D gas concentration. When a cluster is far from a step edge the interaction between the atoms around the cluster and the step is weak and, therefore, a random diffusion is observed. When the cluster approaches a step edge and the separation between the cluster and the step is small enough, the adatoms around the cluster will have a tendency to move toward the step, since the the step is a good sink for adatoms. Therefore, the distribution of the concentration of adatoms around the cluster starts to deform. The concentration on the side close to the step edge is then higher than on the other side. And the adatom gas concentration in the area between the cluster and the step edge increases as the cluster moves closer to the step edge. The collision will take place when this concentration reaches a value equal to the atom density of the cluster. After collision, the cluster appears as a bump on the step edge at the location of the collision. The bump atoms rearrange themselves mainly via migration along the step edge. The result is that the bump starts to grow along the step (labeled as w previously) and to shrink in the direction perpendicular to the step (labeled as h previously). This rearrangement process will continue until the step becomes uniform again. The driving force for the bump to smooth out can be considered as: (a) The partial pressure gradient along the step edge. By lowering the curvature at the bump site, the gradient will be reduced. (b) The higher line tension (the 1D analogue of surface tension) associated with higher the curvature site. The

system will reduce the line tension by smoothing out the high curvature sites. The above picture is illustrated in Figure 8.

(ii) Isthmus model

In this model, a narrow bridge is built between the cluster and the step causes the coalescence to occur (Figure 9).

This explanation is also based on the frame work of adatom concentration distribution on different surface features. As stated above, atoms flow from a cluster to a step. When atoms condensing on the step can nucleate new 1D layers, which do not completely disperse on the time scale of evaporation from the cluster, a bump will be built up on the step edge due to the new 1D layer increase in size. When the bump comes in contact with the cluster, in other words, a narrow bridge builds up, and the coalescence starts. Then, after the bridge is formed, edge diffusion dominates mass flow and results in complete coalescence.

(iii) Fluctuation model

In this model, the fluctuation of step and cluster edges results in coalescence when the separation between the cluster and the step is small enough (Figure 10). Neither the step edge nor the cluster edge is stationary in atomic terms. The edge configuration changes are governed by the rates at which individual atoms migrate from site to site along or near edges, as well as the driving force for mass transport. Step motions have been demonstrated by a number of authors [12-15]. Ibach and coworkers [12] showed that frizzled step edges on Ag (111) were due to step motion. Basically, at moderate temperature, two types of step

Figure 8. A simple atomistic illustration of cluster/step coalescence for concentration model.

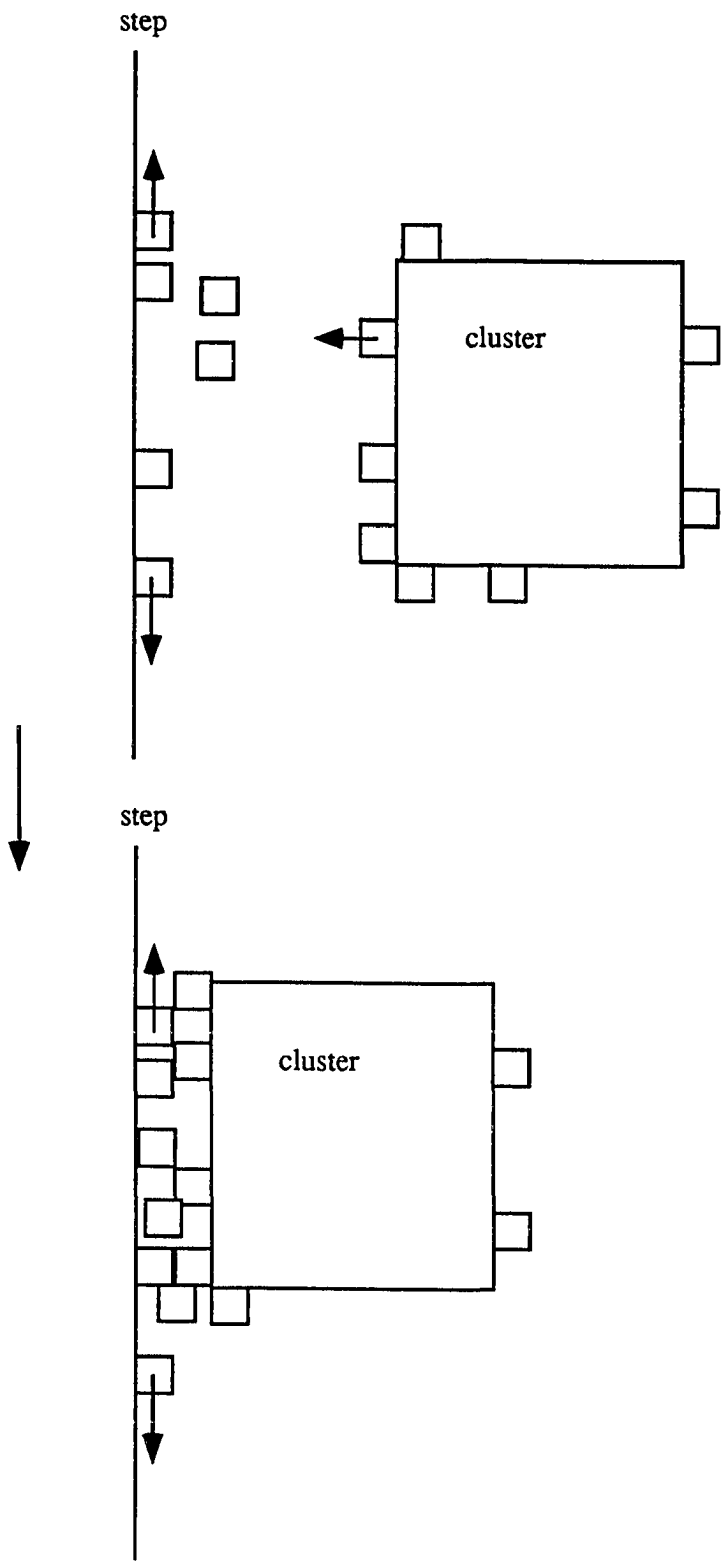
step
cluster
step
cluster

Figure 9. A simple atomistic illustration of cluster/step coalescence for isthmus model. A bridge can be built between the cluster and the step if the dispersion rate along the step edge is smaller than the evaporation rate of the cluster.

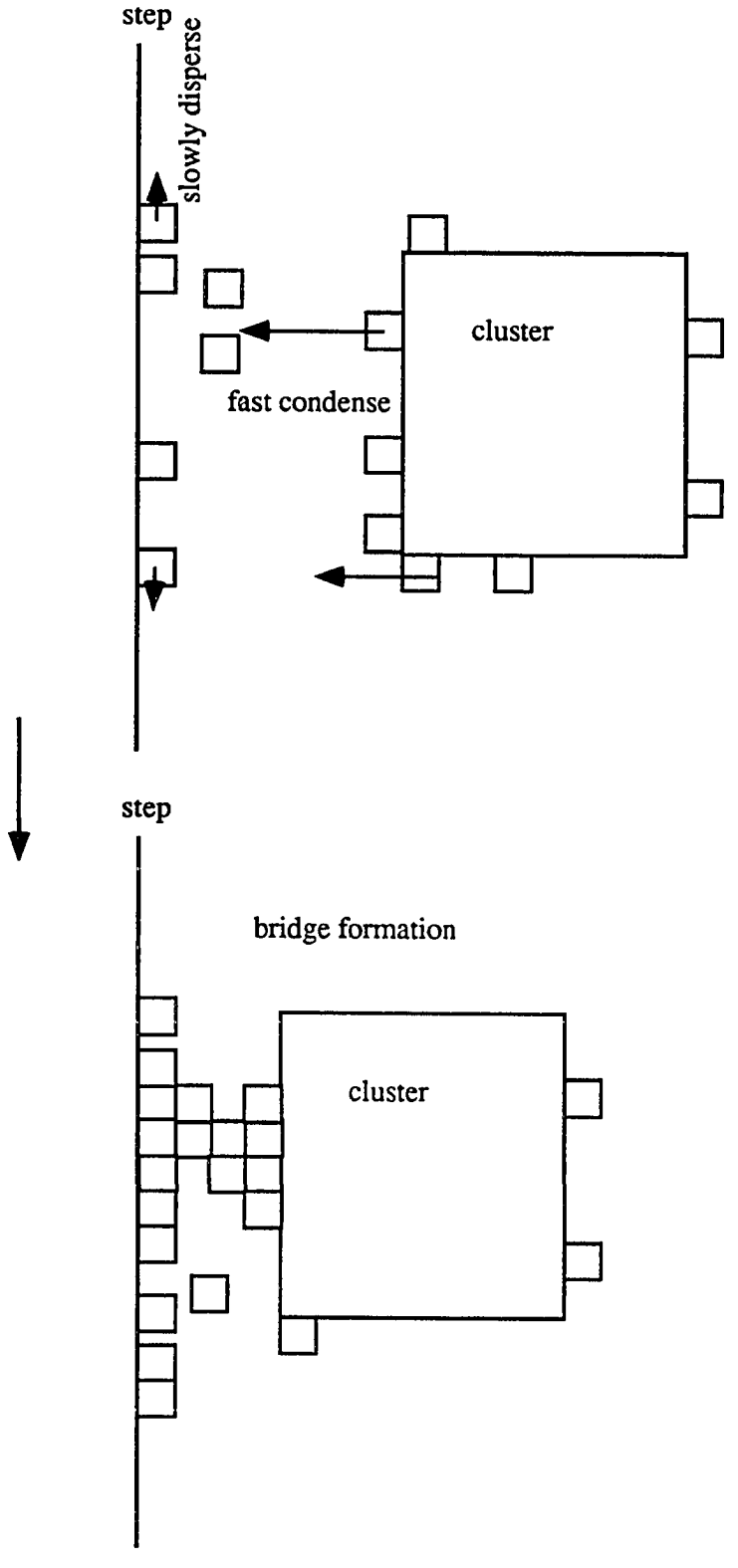
step
slowly disperse
cluster
fast condense
step
bridge formation
cluster

motions are possible. The first type is kink diffusion (or perimeter diffusion). Because kink diffusion requires less energy than removal of atoms from a step edge, such motions are expected at relatively low temperature. The step fluctuations are, therefore, controlled by atoms' motions along the step edges. The second type of step edge motion that needs to be considered is step/terrace atom exchange at high temperature. When the atoms' detachment from step edges are significant, the step fluctuations are controlled by the atom exchange rate between the step and terrace. In this case, the activation energy for an atom to hop off a step edge is overcome by a higher temperature. For both types of step motion, the amplitude and other characteristics depend on the step orientation, as well ws the size/geometry of the local step configuration.

The general trend for coalescence is that the bigger the fluctuation is, the faster the coalescence.

(2) a cluster and a step with a protrusion

As shown in Figure 11, a cluster approaches a linear step edge with a bump (protrusion) at the location where the cluster is approaching. (The protrusion usually results from the incorporation of a cluster into the step prior to observation). In this case, the protrusion will reduce its size by relocating atoms along the step. The rate at which a protrusion reduces its size is faster than the speed of the cluster approaching. Consequently, the gap between the approaching cluster and the protrusion gets larger and coalescence is unable to take place. This observation supports the idea that the atoms within the bump move mainly along the edge. If those atoms move toward the coming cluster and build onto

Figure 10. A simple atomistic illustration of cluster/step coalescence for fluctuation model. The fluctuations of a step edge and a cluster edge can result in coalescence of these two when the separation between them is small enough.

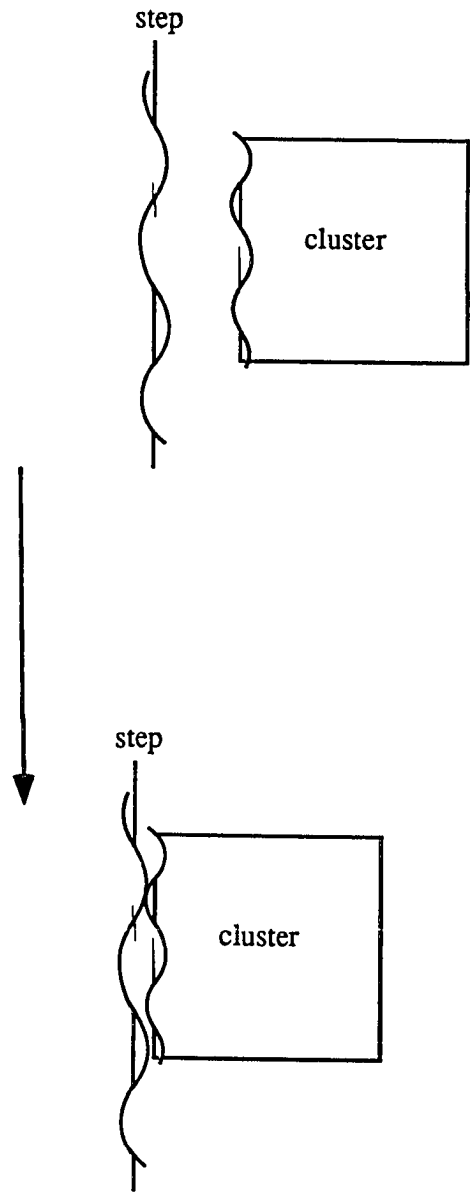
step
cluster
step
cluster

the cluster, then the gap between the cluster and the step should not increase and the size of the cluster should increase.

(3) the internal edge of a vacancy

The relocation of atoms can also be found in vacancy cluster evolution. As shown in Figure 12, a very small gap between a protrusion on one side of the vacancy and the opposite side of the same vacancy makes coalescence very likely to occur, and therefore, create two separated vacancies from the old one. However, the opposite occurs. Due to the reduction in the protrusion size, the gap becomes larger and larger. And the irregular vacancy even changes its shape to a rectangular one finally. Analogously, this observation can be explained as the system reducing its line tension by changing its shape.

(4) the interactions between vacancy clusters and adatom clusters

We will now consider the interaction between the vacancy clusters and adatom clusters which coexist as second layer. We deposit the film at a slightly higher coverage, ca. 0.9-1.2ML. In this coverage range, we can typically obtain both vacancy and adatom clusters at the same time as shown in Figure 13. We will analyze the coverage change as a function of time. The film in Figure 13 has a total coverage of 0.97 ML. The second layer (adatom cluster) coverage is 0.034ML, and the first layer coverage is 0.94 ML (corresponding to a vacancy cluster coverage of 0.065ML). For the case in Figure 13, after 6 hrs, the total area of all adatom clusters (the second layer) in a selected portion of the image was reduced by 72% of it original value and the total area of vacancy clusters was reduced by 49% of its original value. So the adatom cluster (the second layer) coverage

Figure 11. STM images showing that the separation between a cluster and a step with a bump is increased due to the dispersion rate along the step edge being larger than the approaching rate of cluster. Coalescence does not occur. The time interval is: (1) t = 0 min; (2) t= 71 min; (3) t= 160 min; (4) t=270 min. The data is under file name Ag-09-01-94. The file numbers are 44, 68, 89 and 106.

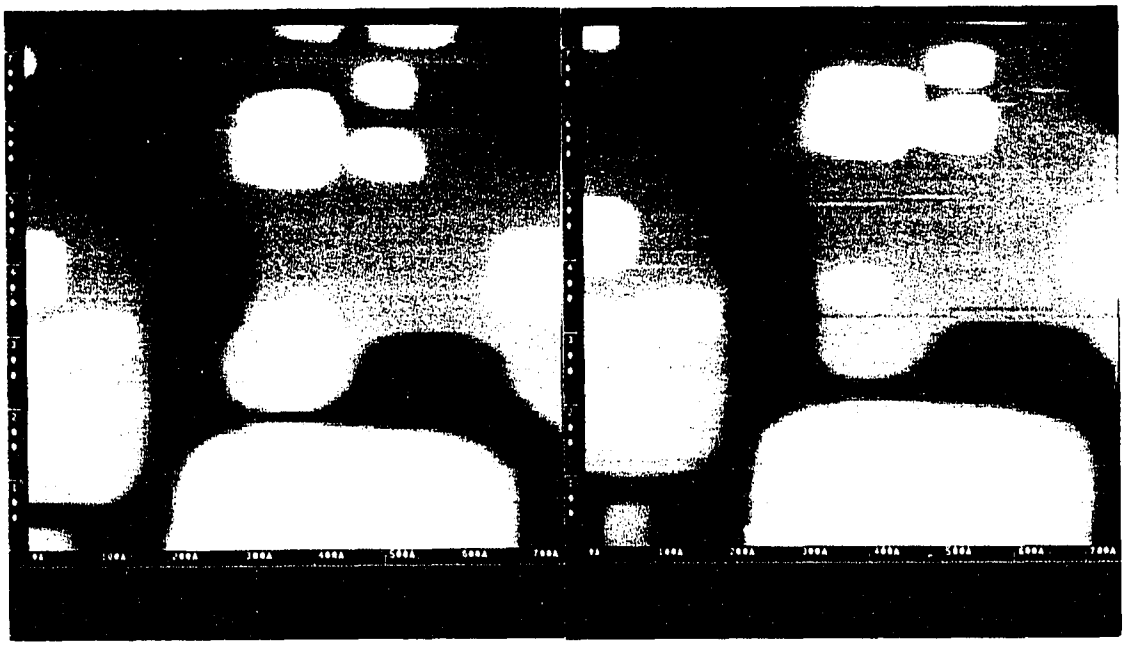

(1) (2)

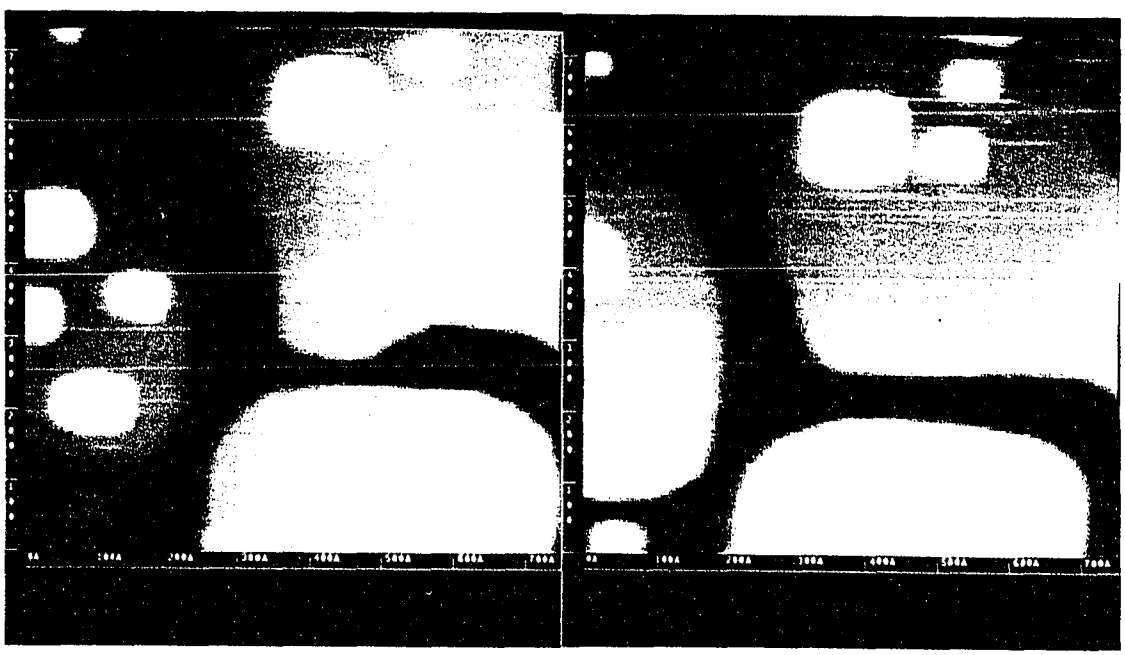

(3) (4)

Figure 12. STM images showing that the vacancy clusters' coalescence. The time interval: (1) t= 0; (2) t=33 min; (3) t= 66 min; (4) t =208. The size at beginning: gap = 31 Å (cluster a), 22 Å (cluster b); respectively; length = 444 Å (cluster a), 502 Å (cluster b); respectively. The data is under file name Ag-06-02-94-A. The file numbers are 5, 7, 9 and 25.

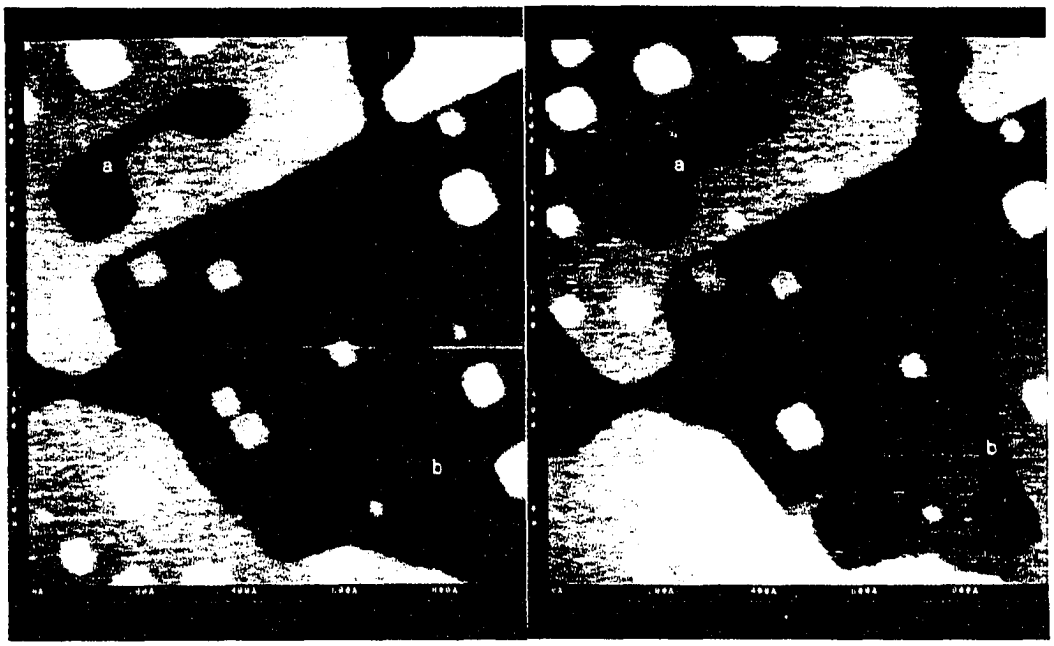

(1) (2)

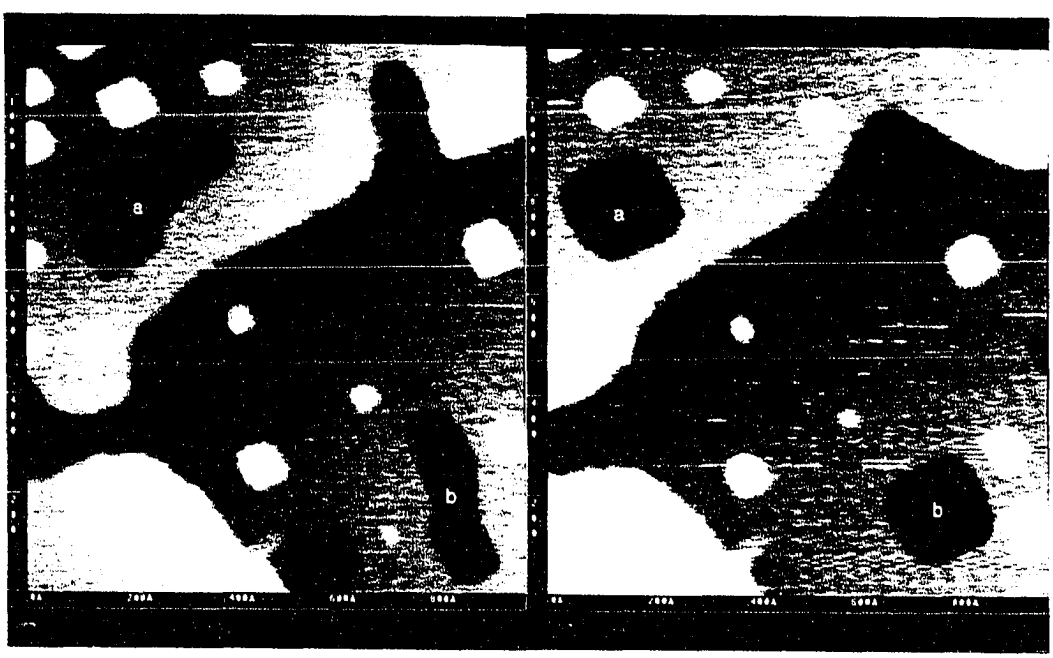

(3) (4)

now is 0.024ML and vacancy cluster coverage is 0.033ML. However, for vacancy only cases, the total vacancy area has little change, for instance, the data shown in Figure 2 of Chapter 4 have only 4% change after 6 hrs.

Clearly a one-way atom flow exists. Atoms fall from those coexisting adatom clusters into the vacancy clusters, but atoms cannot move in the opposite direction. This indicates that a 2D adatom gas does exist and a weak/zero step barrier near the step edge does not prevent atoms from falling into the lower terrace. The existing depletion zone near the descending step supports this weak/no step barrier argument [16]. STM data show that this atom-flow has little effect on the diffusion coefficients of vacancy clusters. The diffusion coefficients we measured from this type of film are of the same order of magnitude as those we mentioned earlier. There is no notable change in diffusion trajectories of vacancy clusters is seen compared with those shown in Figure 4 of Chapter 4. On the other hand, coexisting vacancy clusters do have a significant impact on the behavior of the adatom clusters. The adatom clusters alone have larger diffusion coefficient and longer displacement [8], and in the high cluster density cases clusters undergo coalescence [17]. For the 2D adatom gas, the coexisting vacancy clusters act as strong atom sinks (Figure 14). In addition to the steps and adatom cluster edges, they strongly interrupt the quasiequilibrium between adatoms and adatom clusters, and therefore reduce the diffusivity of adatom clusters. This is evidenced by smaller displacement and diffusion coefficients, faster dissolution and, consequently, little chance for coalescence to occur. For example, the data shown in Figure 13 have an initial adatom cluster number density $=1\times10^{-5}$ with a

Figure 13. STM images of both adatom and vacancy clusters. The time interval between the two is 6 hrs. The white clusters are adatom clusters. The dark clusters are vacancy clusters. The total adatom cluster area decreases and the total vacancy cluster area increases. The data is under file name Ag-06-09-94. The file numbers are 27, 66.

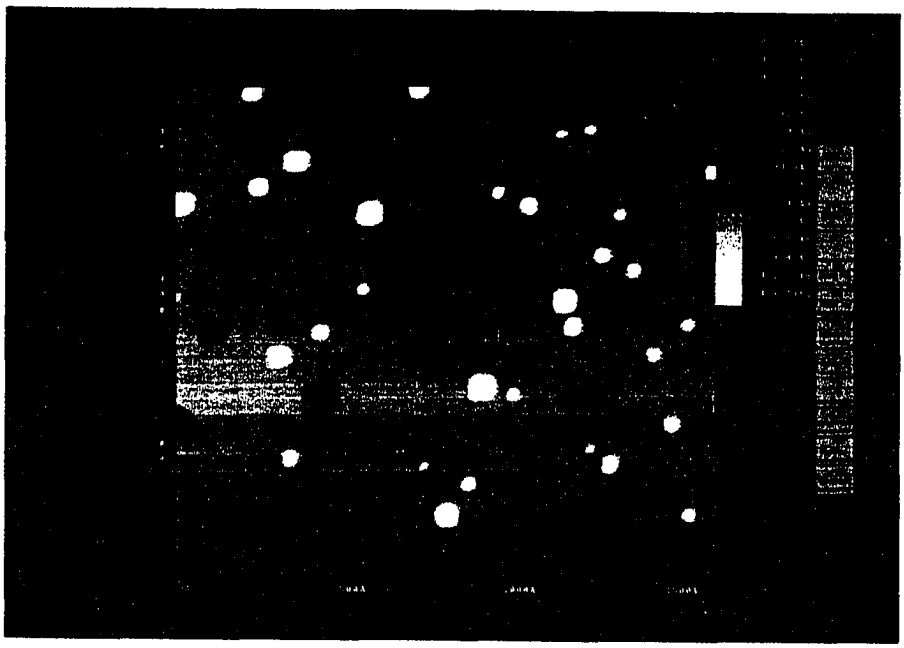

(1)

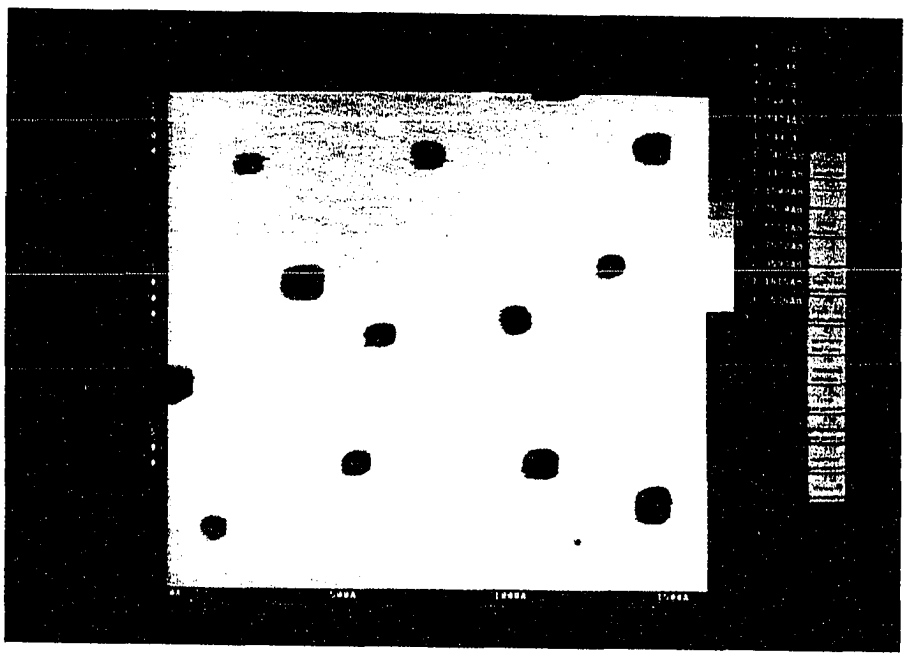

(2)

coverage of 0.034ML. This is within the regime where adatom cluster coalescence can take place [18]. However, throughout the observation time of 6 hrs, no coalescence is seen.

As illustrated above, the second layer cluster will dissolve and move across the descending steps to fill in first layer vacancies. Here, more details are given. In Figure 15.1, a new film is deposited onto an old film which has coarsened into large clusters. We select an isolated area where the second layer adatoms and clusters can not disappear other than by jumping into the first layer. These images eliminate the possibility of incorporating into a step edge. In Figure 15.2, the area changes for both layers as a function of time is plotted. The total area in the second layer decreases as a function of time. However, the first layer cluster does not increase in size, but rather decreases slightly. This indicates that atoms from the second layer clusters are not localized on the edge of the first layer cluster. Since other larger first layer clusters exist near the selected area, it is expected that the selected first layer cluster will lose its atoms to its large neighbors under the Gibbs-Thomson equation.

(5) depletion zone along the step on the lower terrace

Step edges are generally considered as adatom sinks. Atoms landing on the lower terrace near a step edge may be captured by the step before they can nucleate on the terrace. Therefore, a small regime near a step is free of adatom clusters after deposition, i.e. there is a depletion zone. At higher submonolayer coverages some evidence for a depletion zone near the step is still seen. As shown in Figure 16, an irregular shape vacancy is formed along the ascending step at a coverage of 0.85 ML. The orientation of this irregular vacancy follows the step shape. It may be that atoms landing near a step edge can either go to the

step and be captured, or migrate out toward the terrance and nucleate new islands, leaving a depletion zone (long vacancy) at the front of the step edge. As these clusters grow, they coalesce and tend to form a long vacancy along the step edge.

b. Cluster-cluster coalescence

Clusters are important in film growth. Many studies have provided valuable information about film structures and morphology through analyzing cluster characteristics, such as cluster size distribution, spatial distribution and mobility. The study of cluster dynamics is therefore helpful in order to evaluate the roles clusters play in film structure formation and morphology changes. In this section, cluster coalescence under different conditions is discussed.

Two types of coalescence are possible. Static cluster coalescence (coalescence via growth) refers to two clusters meeting and becoming one during deposition while the centers of both clusters are immobile. Dynamic cluster coalescence (coalescence via diffusion) refers to clusters running into each other. This can occur during or after deposition. Dynamic coalescence has been observed at room temperature in some systems. Bassett [19] reported at 250-300°C clusters of Au and Ag in the size range 100-200 Å can coalesce on MoS_2 and C. When they coalesce, their behavior is likened to liquid droplets. Both translation and rotation movements were observed. Pashley [20] suggested that the mass transfer was due to capillary effects between clusters and that surface diffusion is the rate determining step. Chu and Ruckenstein [21], in their study of Pt on C, found that Pt

Figure 14. Illustration of the interaction between adatom and vacancy clusters. The vacancy cluster is an adatom sink which traps adatoms from both large and small adatom clusters. The arrows around two adatom clusters represent the tendency of cluster dissociation. Longer and darker ones indicate higher dissociation rate. Adatom (a) will fill in the vacancy, while adatom (b) has two choices, filling in the vacancy or going into large adatom cluster, since a large cluster is nearby. As a result, vacancy area will decrease and adatom cluster size will decrease also.

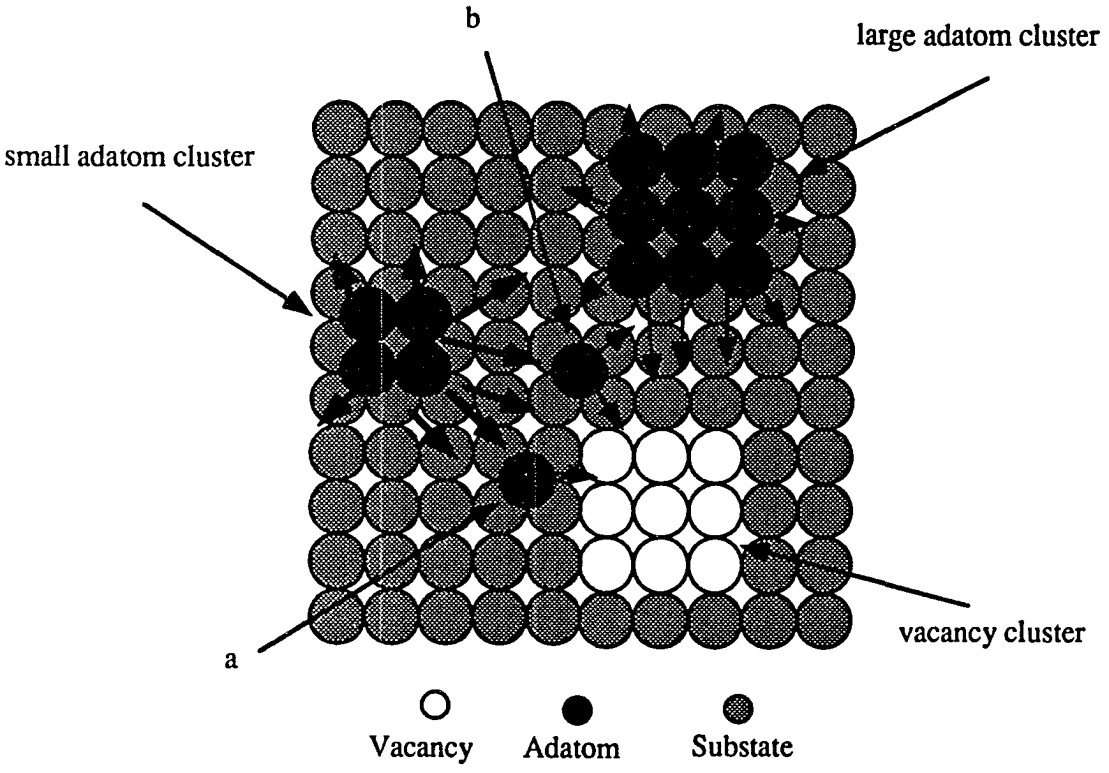
b
large adatom cluster
small adatom cluster
a
vacancy cluster
Vacancy
Adatom
Substate

Figure 15.1. Images showing that the total area of the large isolated cluster in the center of the image and the total area of all the small clusters on that isolated large cluster change as a function of time. The time interval is: (1) t= 0; (2) t= 71 min; (3) t= 231 min; (4) t= 385 min. The data is under the file name Ag-09-01-94. The file numbers are 44, 68, 101 and 120.

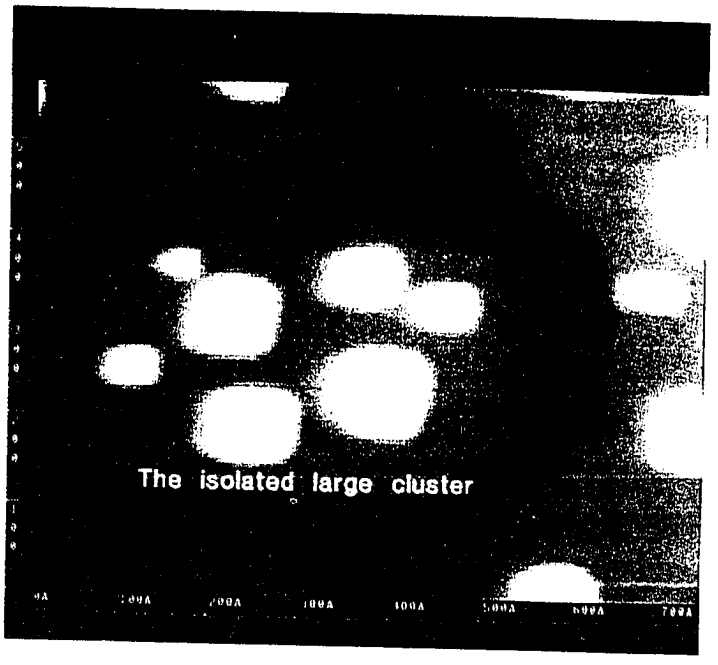

(1)

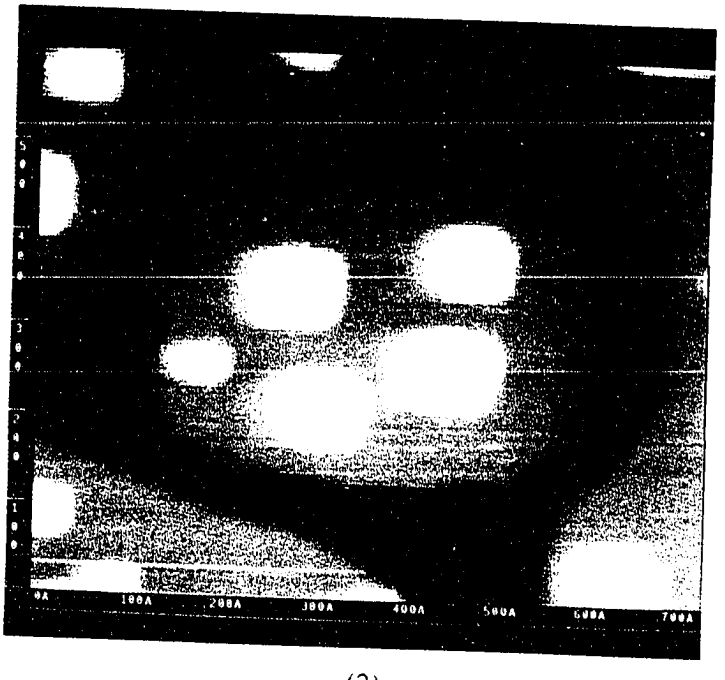

(2)

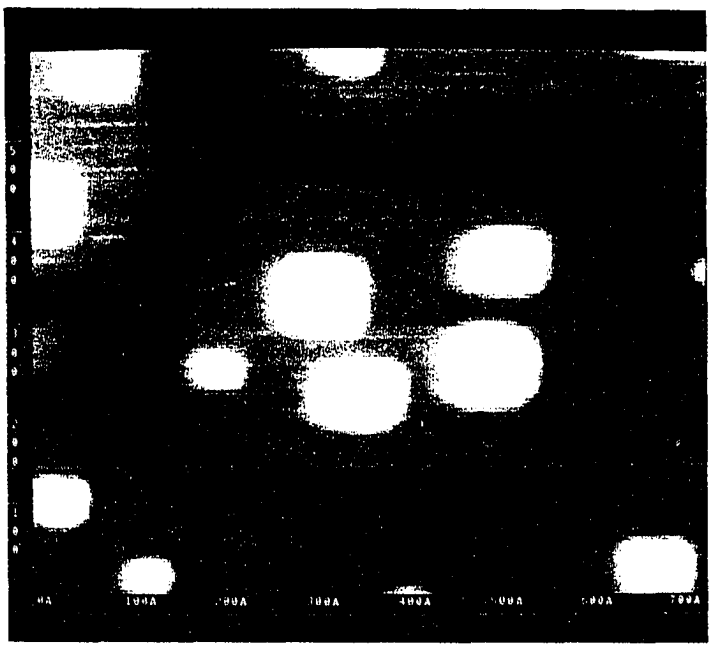

(3)

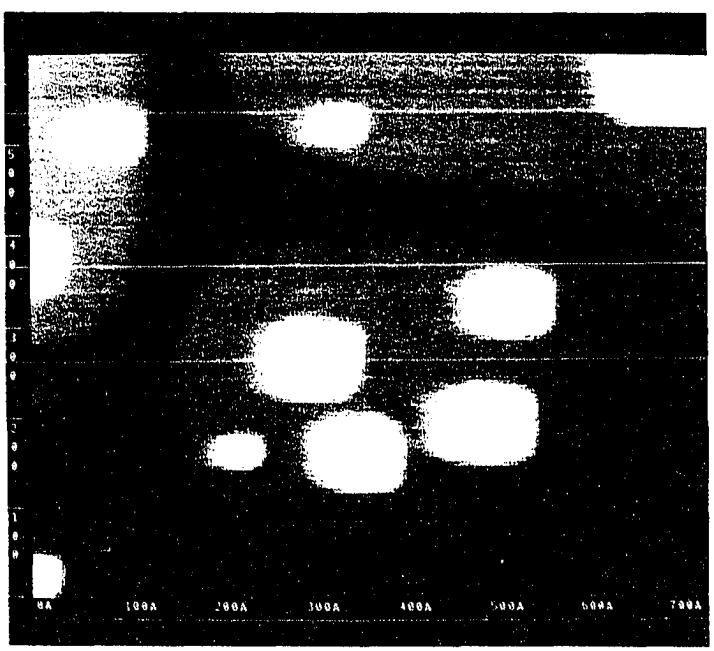

(4)

Figure 15.1 cont.

Figure 15.2. Analysis of the images of Figure 15.1, showing the total area of the large isolated cluster in the center of the image and the total area of all the small clusters on that isolated large cluster as a function of time.

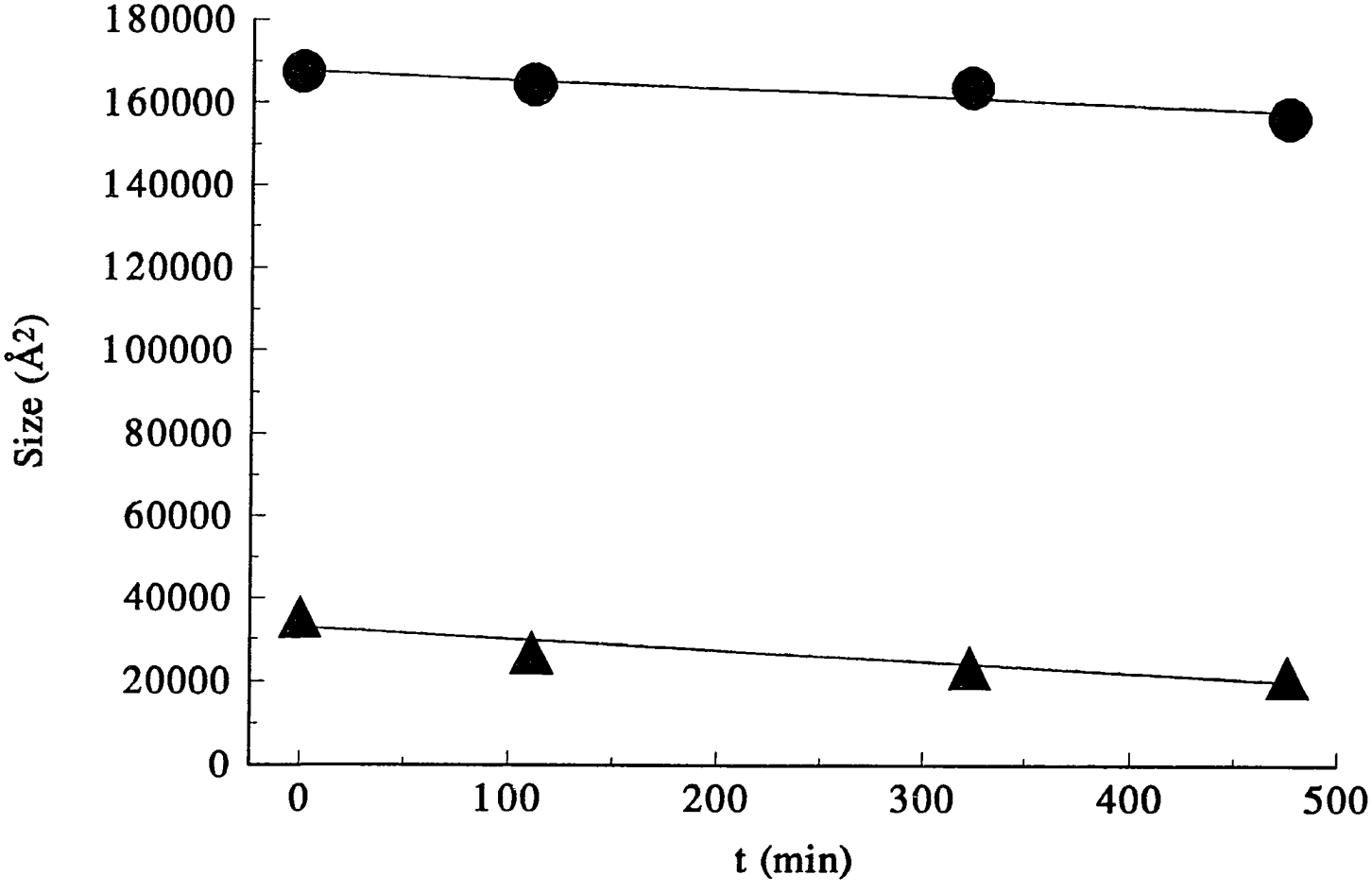
180000
160000
140000
120000
100000
80000
60000
40000
20000
0
Size (Å2)
0
100
200
300
400
500
t (min)

clusters can migrate on C surfaces and coalesce with each other after a heat treatment at 500°C.

For metal-on-metal systems, dynamic coalescence of large Ag clusters on Ag (100) has been reported [8]. In this section, we analyze in detail post-deposition coalescence between Ag clusters at room temperature. We focus on the effects of relative cluster orientation and size. The following are the five cases of coalescence we address: (1) two clusters with a corner to corner orientation; (2) one cluster's corner located at another cluster's [100] edge; (3) both clusters with their [110] edges towards each other; (4) large to small clusters; (5) two clusters with similar size. All cases are illustrated in Figure 17.

Our STM data show that under similar conditions, cases (1) and (2) can have coalescence earlier than case (3), and case (4) can have coalescence earlier than case (5). From examples shown in Figure 17, the initial separations for all five cases are 28 Å , 49 Å, 130 Å, 16 Å and 14 Å, for cases (1), (2), (3), (4), and (5), respectively. And the time needed for coalescence to occur in case (1) is 134 min, in case (2) is 66 min and in case (3) is 165 min. For case (4) and (5), the times are 191 min and 259 min, respectively.

We will use the argument introduced for step/cluster interactions to qualitatively explain the observation. When the Gibbs-Thomson equation is considered, the clusters are assumed to have circular shapes regardless of the real geometry. This assumption gives a uniform distribution of adatom concentration around the clusters and is valid for the purpose of establishing the concept of adatom concentration differences for long straight steps and clusters with finite size.It is necessary that the clusters' shapes be taken

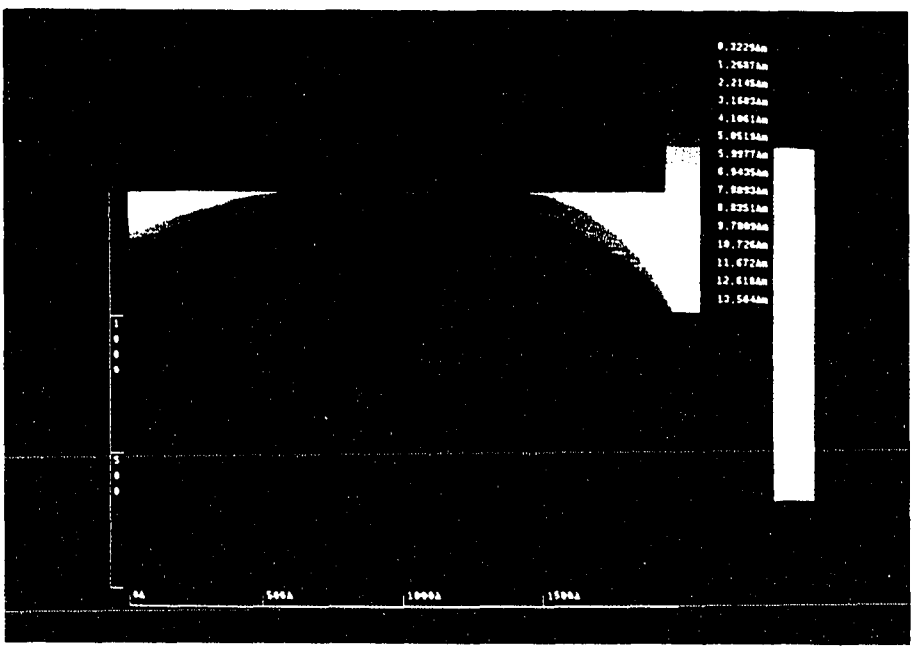

Figure 16. An image (1800 Åx 2000 Å) to show the depletion zone along the step on the lower terrace near a step edge. The data is from file Ag-06-03-94. The file number is 7.

Figure 17. Five cases of coalescence (The data is from Ag-08-31-83):

Case (1) two clusters with a corner to corner orientation. The gap between clusters a and b is 38 Å. The gap between clusters b and c is 28 Å. The sizes of the clusters are: 160Å x180 Å (a) ; 174 Å x 178 Å (b); 130 Å x 136 Å (c). Cluster d is a reference.

(2) one cluster's corner located at another irregular cluster's [100] edge. The gap between the cluster and the edge is 49 Å. The cluster size is 161 Å x 245 Å. The two clusters which coalesce are labelled a and b.

(3) both clusters, aand b, with their [110] edges paralleland adjacent to each other. The gap is 16 Å. The cluster size is 130 Å x196 Å.

(4) large to small cluster. The gap is 16 Å. The clusters' sizes are 87 Å x 65 Å and 125 Å x135 Å.

(5) two clusters with similar size. The gap is 14 Å. The clusters' sizes are 142Å x143 Å and 127 Å x 135 Å.

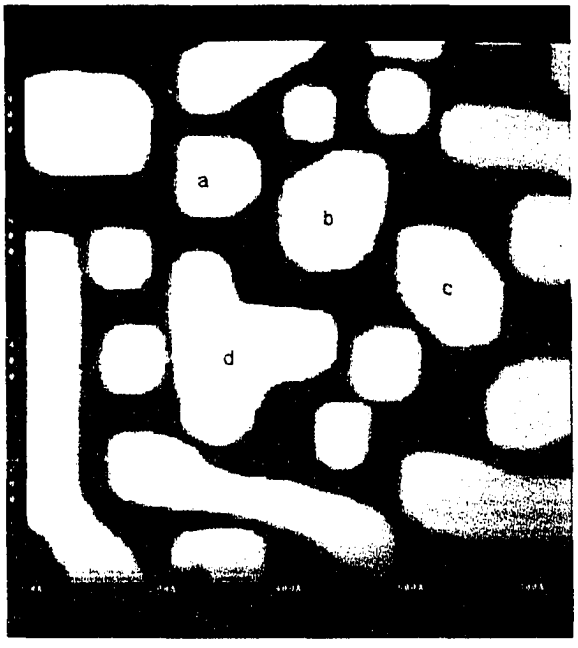

(1)

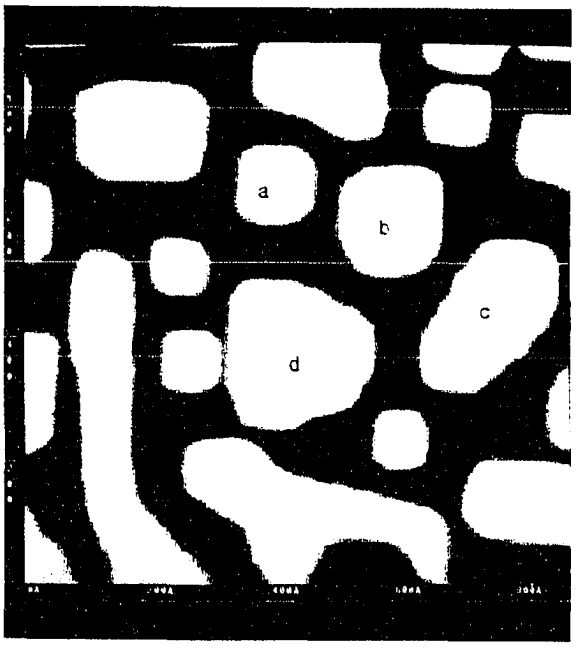

(2)

case (1)

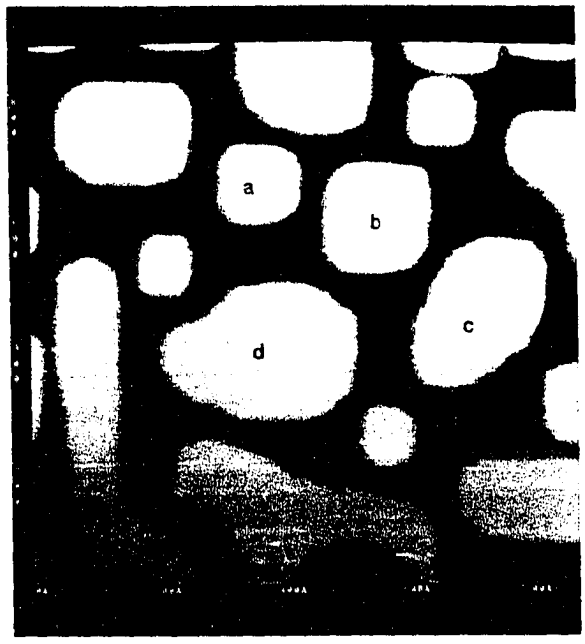

(3)

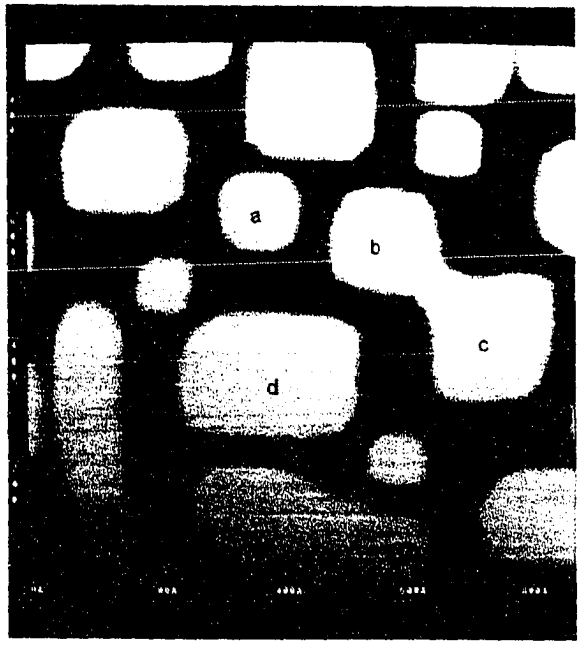

(4)

Figure 17. cont. case (1)

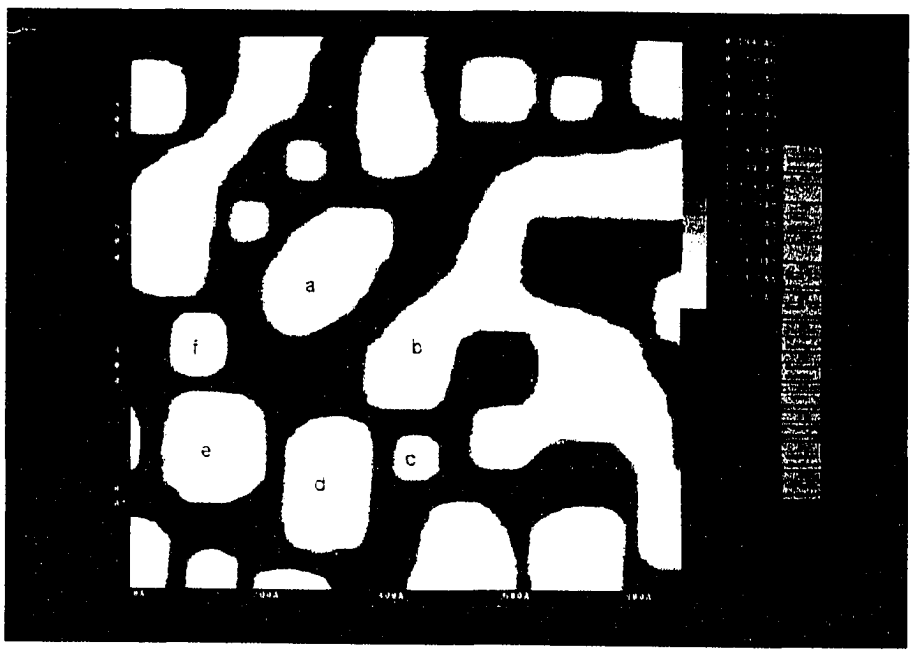

(1)

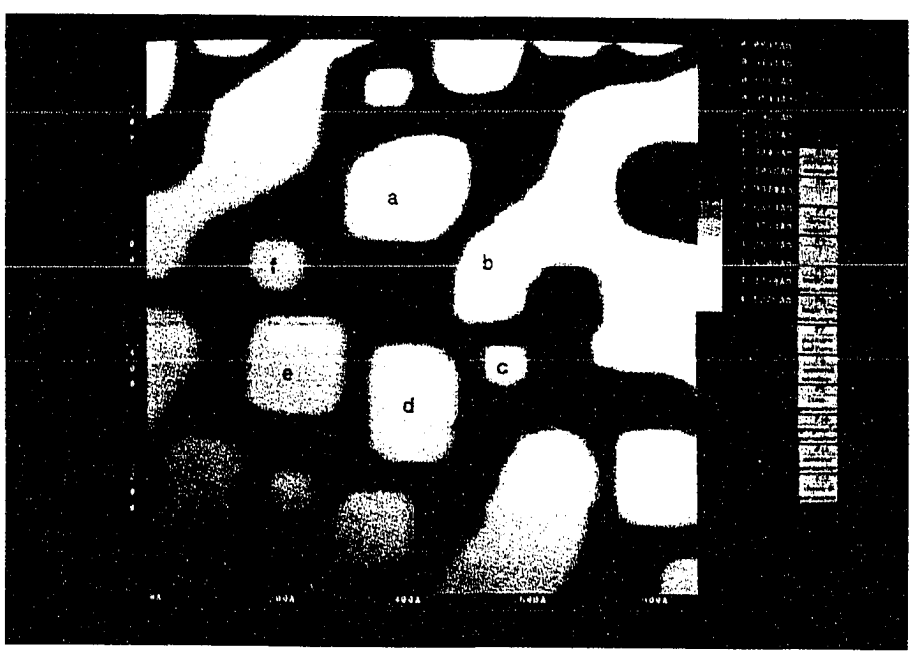

(2)

Figure 17. cont. case (2)

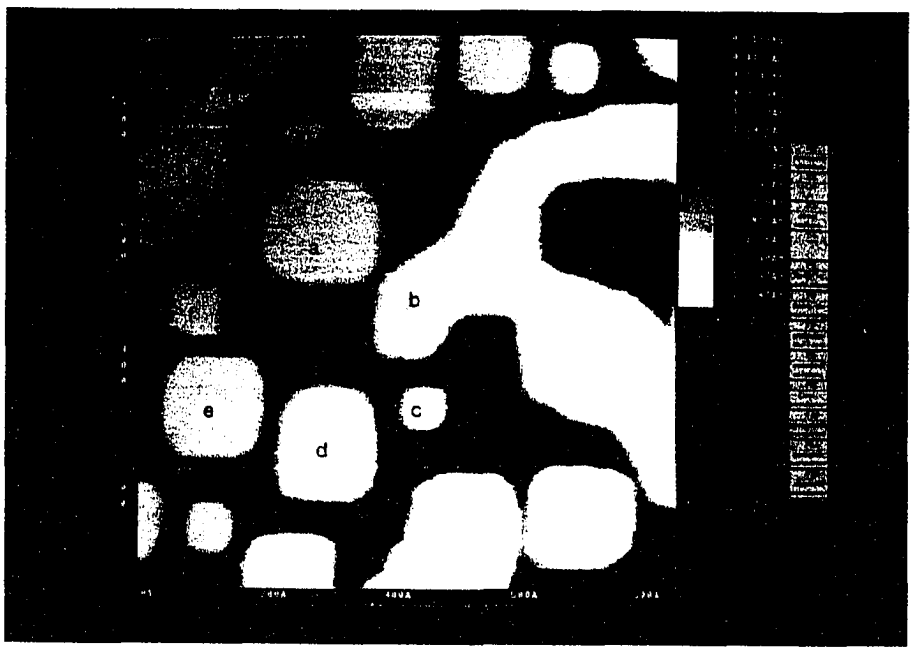

(3)

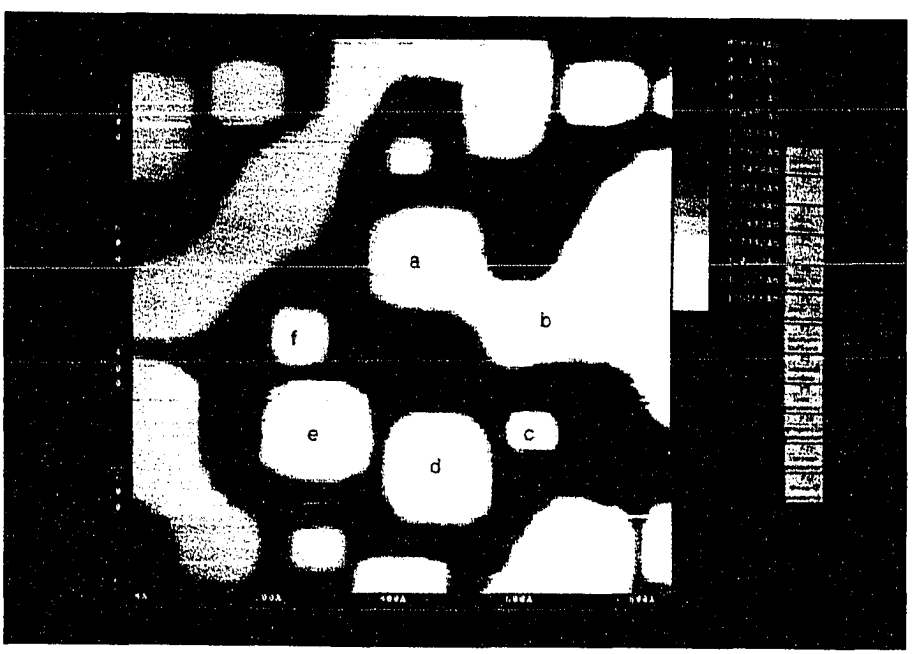

(4)

Figure 17. cont. case (2)

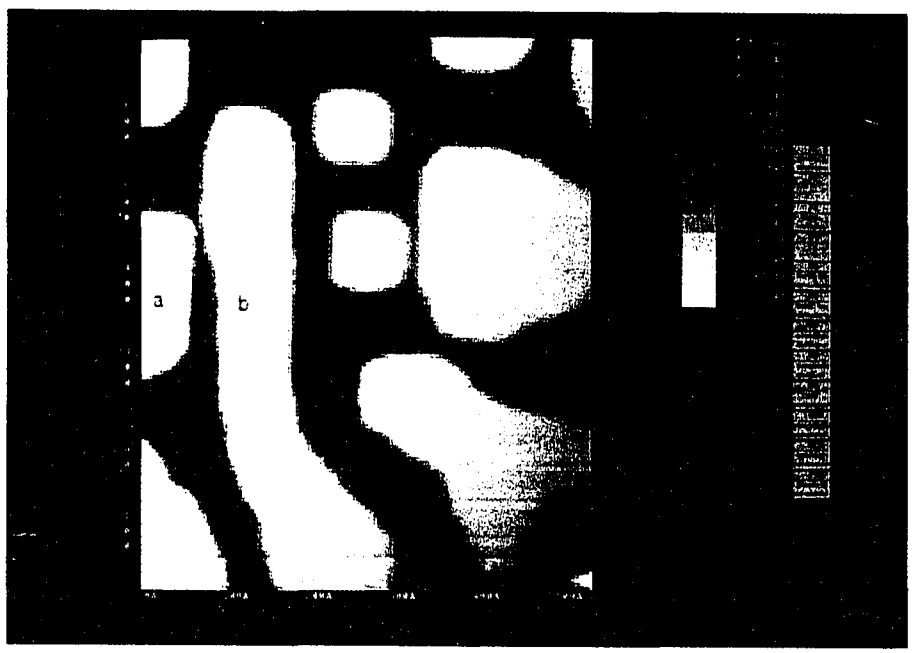

(1)

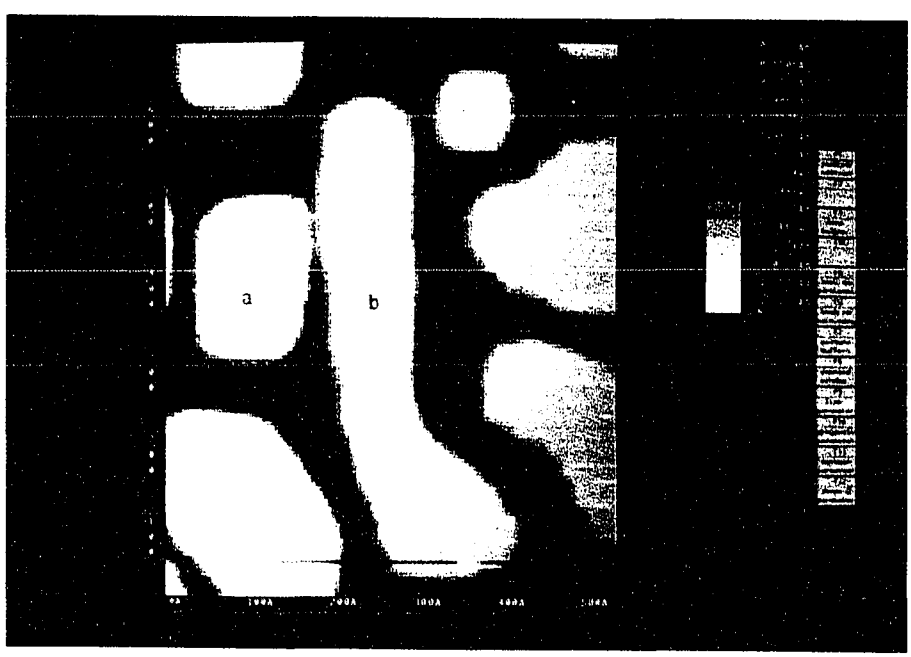

(2)

Figure 17. cont. case (3)

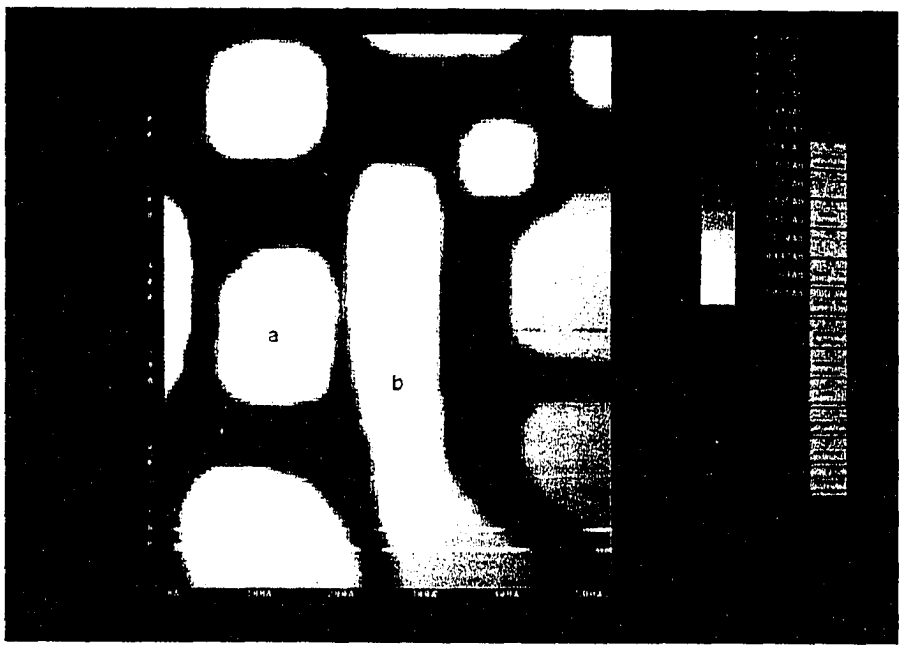

(3)

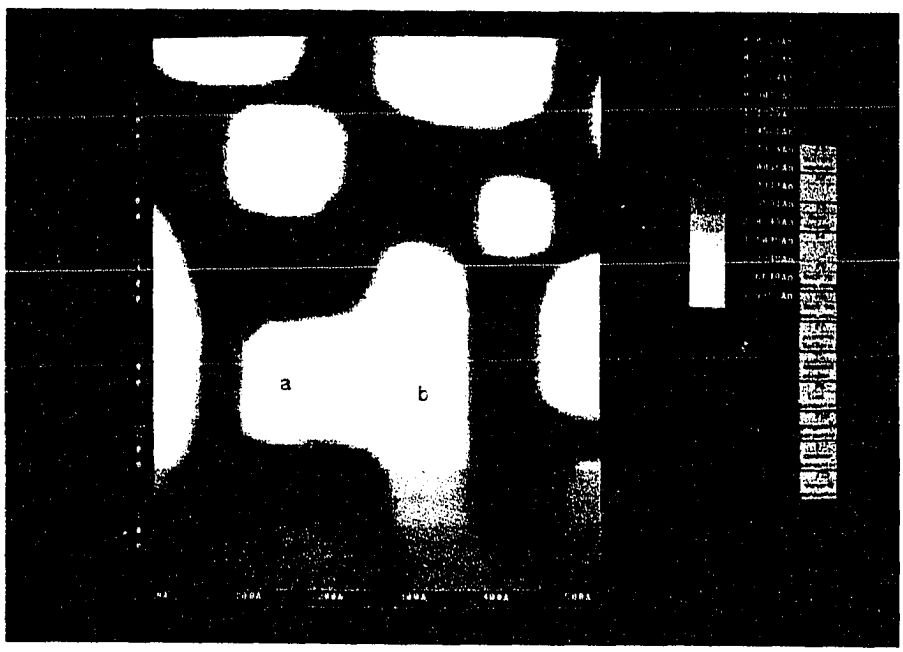

(4)

Figure 17. cont. case (3)

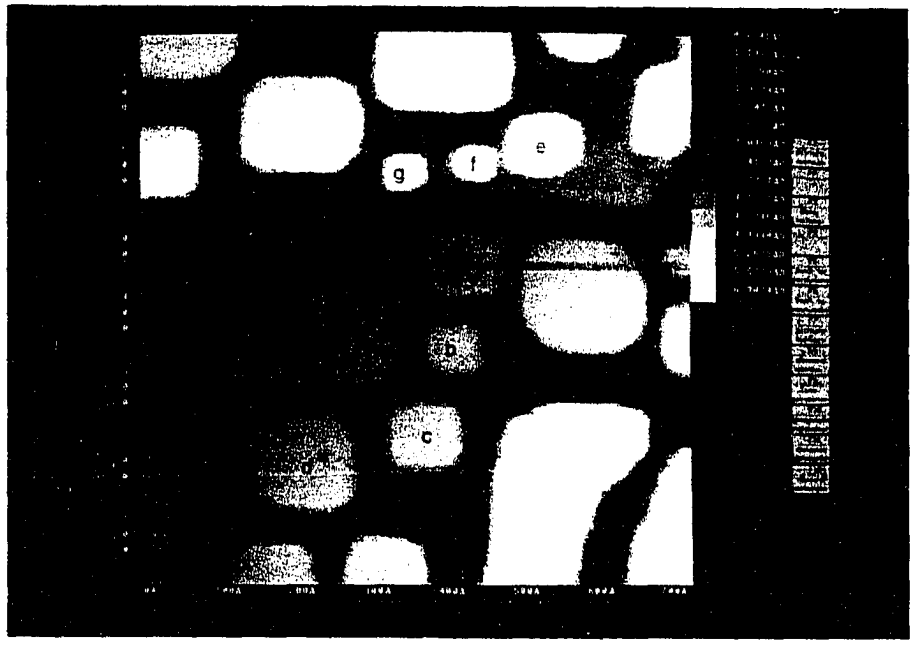

(1)

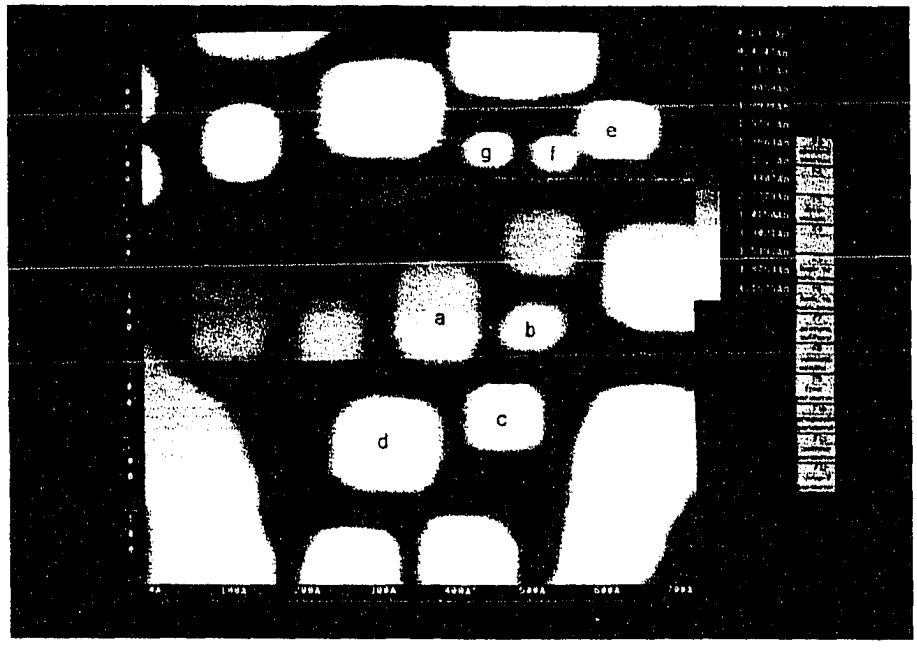

(2)

Figure 17. cont. case (4)

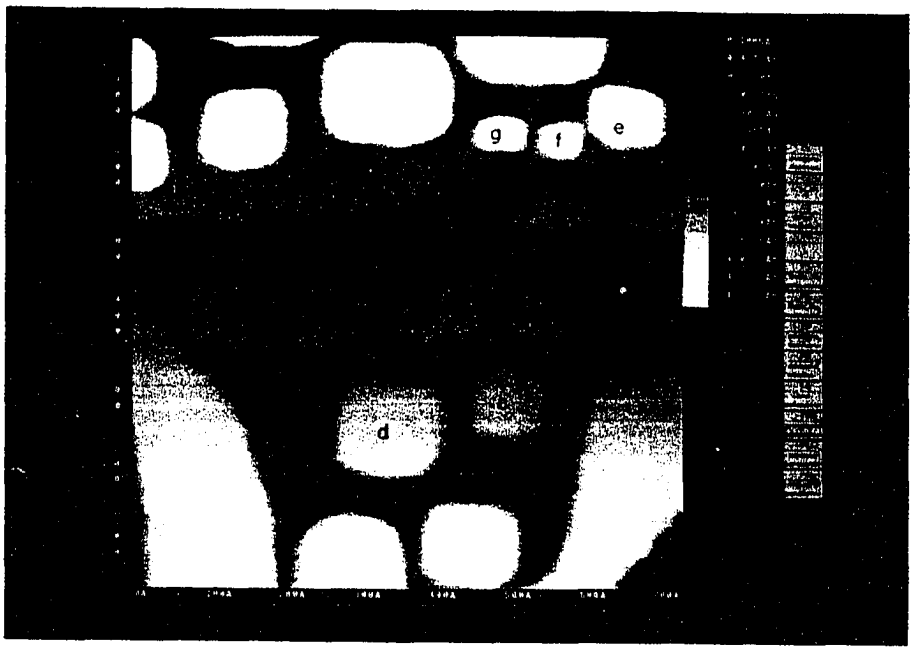

(3)

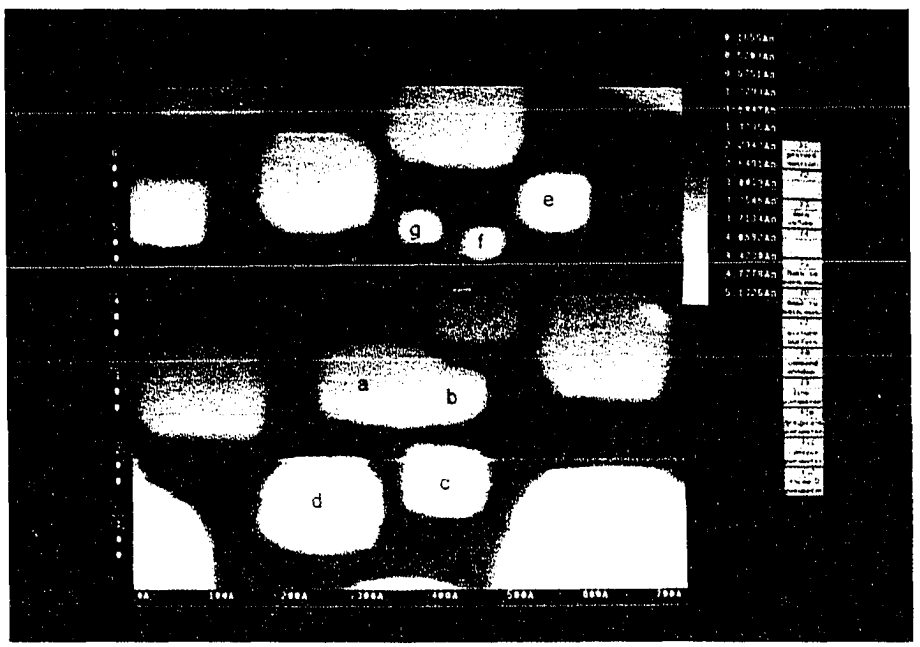

(4)

Figure 17. cont. case (4)

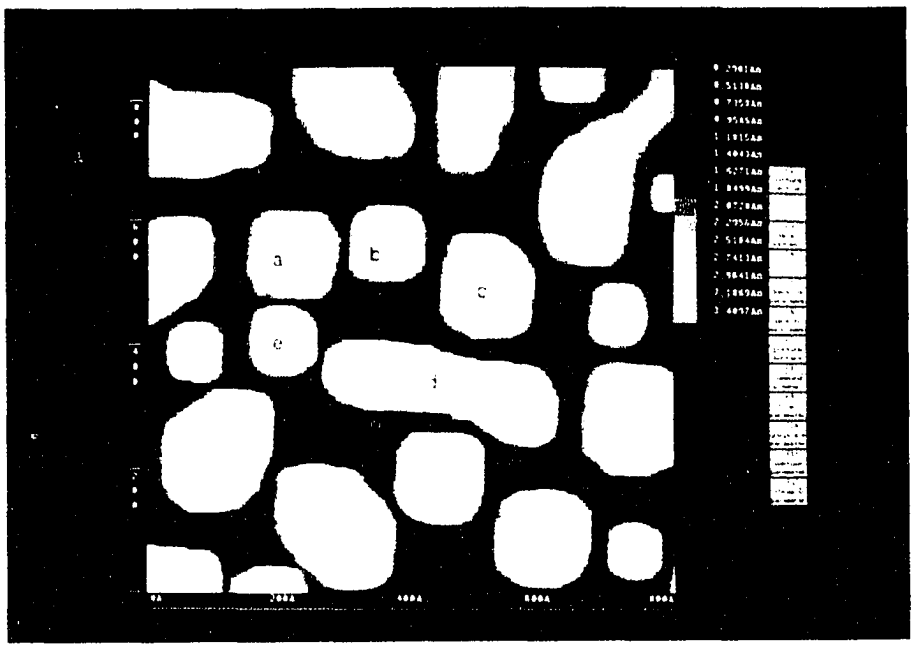

(1)

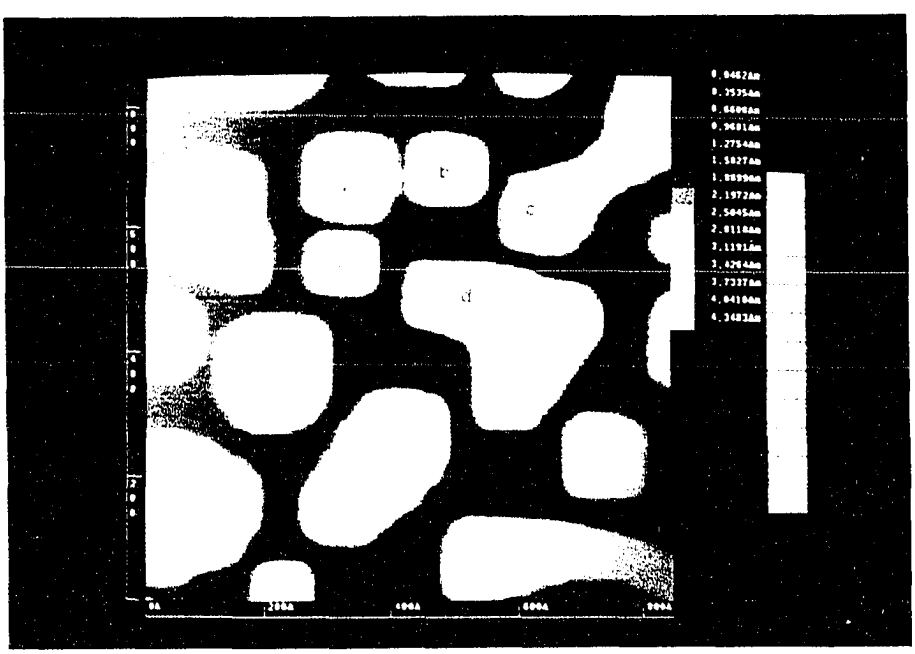

(2)

Figure 17. cont. case (5)

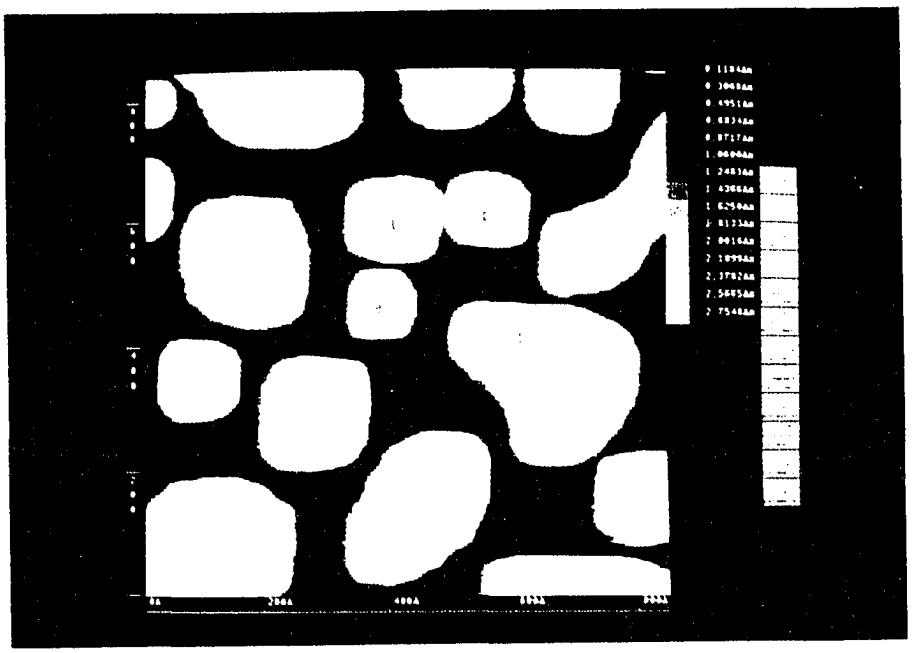

(3)

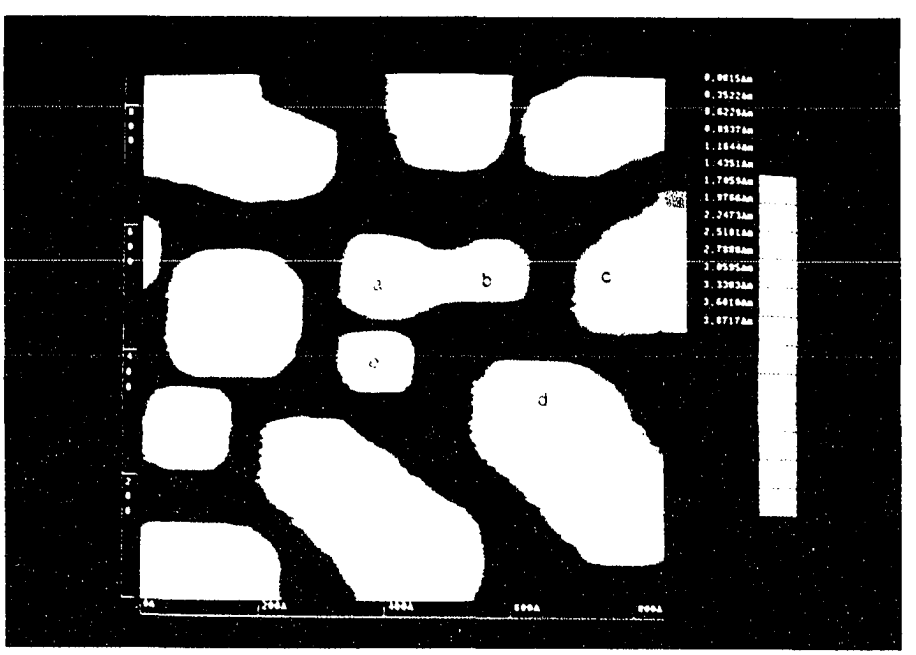

(4)

Figure 17. cont. case (5)

into account in this section, since the length scales of the clusters' involved have little difference (Figure 17 also shows the sizes of the clusters).

Ag clusters on an Ag (100) surface, before coalescence takes place, should have square shapes because clusters will follow the substrate geometry and the square is the most energetically favored shape. However, due to thermal fluctuations, clusters with rectangular shapes also exist. The clusters with non-circular shape, consequently, have a non uniform distribution of adatom concentration around the clusters. Corners, because of their small curvature, will have larger adatom concentrations. Edges, although not perfectly linear due to peripheral atom diffusion and kinks, will still have smaller adatom concentrations. For case (1), when two clusters approach each other in corner-to-corner fashion, the concentration of adatoms in the regime between them will quickly increase. When the concentration reaches the density of clusters, coalescence takes place. This process will take less time than case (3), where clusters approach each other with their [110] edges. For case (2), corner-to-[100] edge, the [100] direction step edge may have a low atom concentration based on the Gibbs-Thomson equation, but due to the nature of [100], less bond-breaking is required for atoms at this edge to leave. So they can make the detachment from the edge easier than atoms at the [110]edge. This less-bond-breaking situation may enhance the adatom concentration; therefore, coalescence can take place more quickly.

The same argument can also be used to explain the cases of different or similarly sized clusters. Comparing cases (4) and (5), the coalescence time is related to the relative cluster sizes. The former is faster than the latter. Here the cluster geometry factor is not

important. Only the cluster curvatures, and therefore cluster sizes, need to be taken into consideration. For two similarly sized clusters (case 5), the curvatures are similar. Therefore the adatom concentrations around the clusters are about the same. When two similarly sized clusters such as these two approach each other, neither side of the adatoms will see the concentration gradient between them. Thus, the distribution of adatoms basically remains unchanged for both clusters. So the coalescence process takes longer. In case (4), where one cluster is larger than the other, the smaller cluster with higher adatom concentration approaches the larger cluster. The concentration gradient makes the adatoms around the smaller cluster move toward the gap between the two clusters. This results in an increase of adatom concentration in the gap. When the concentration increases up to the cluster density, collision occurs and the gap between the two clusters disappears.

c. The influence of contamination on film evolution

(1) Background gas effect

Under ultrahigh vacuum (UHV) conditions, background gases have a minimal effect on film growth and the film evolution process. Therefore, film contamination is generally neglected. But at medium vacuum conditions, background gases can strongly affect film evolution. Sears and Hudson [22] studied Ag crystallite migration over graphite and MoS_2 surfaces at 10^{-5} Torr O_2. They suggested that the motion of Ag crystallites take place on an O_2 layer other than on the bare substrate. Chu and Ruckenstein [21] carried out a study of Pt crystallites on carbon substrates in 10^{-5} -10^{-4} Torr O_2 and water. They found that under

the influence of these environments, Pt crystallites can migrate. Cooper and coworkers [23] reported that Au cluster evolution on Au (111) in air results in significant changes in the size of Au clusters under the influence of background gases. Mass flow is a few hundred times faster in air than in a high vacuum environment. This adsorbate-induced mass flow is explained by reduction of the energy barrier of detaching atoms from steps [23].

Here we present a study of Ag film evolution in the high vacuum regime (Figure 18). We observe a fast decrease in cluster number for a large average cluster size film in $1x10^{-7}$ Torr of air. The film is deposited under UHV conditions. The chamber is then backfilled with air by turning all the pumps off with the gate valve closed. The pressure in the chamber was rises to $1x10^{-7}$ Torr in 20 min. The interval between images averages 80 sec. The clusters disintegrate faster than those under UHV conditions (In our UHV cases, typically the pressure is from $6x10^{-11}$ to $3x10^{-10}$ Torr). Under UHV conditions both cluster ripening and cluster diffusion are observed and cluster diffusion dominates the evolution. The general characteristics of the evolution process are long and slow. However, under high vacuum clusters vanish at very large size ($1x10^{3}$ $Å^{2}$) compared to those under UHV. All clusters disappear after 4 hrs. The diffusion of the clusters is minimal, if any. It is difficult to determine whether there is cluster diffusion because the observation time is limited by fast decay of clusters and therefore no diffusion is estimated. High vacuum can be a problem to resolution during imaging. Sometimes the tip or tunneling junction can even be destroyed.

During cluster ripening, two energy barriers need to be considered. The first is an energy barrier that atoms need to overcome in order to leave clusters, i.e., the core-break

Figure 18. Under high vacuum ($1x10^{-7}$ torr), clusters disappear at faster rate than in UHV condition. All clusters disappear within 4 hrs. The time intervals are: (1) t = 0; (2) t = 3 min; (3) t = 8 min; (4) t = 13 min, (5) t = 18 min; (6) t = 23 min; (7) t = 29 min; (8) t = 35 min; (9) t = 63 min; (10) t=78 min. The data is in file Ag-08-28-93

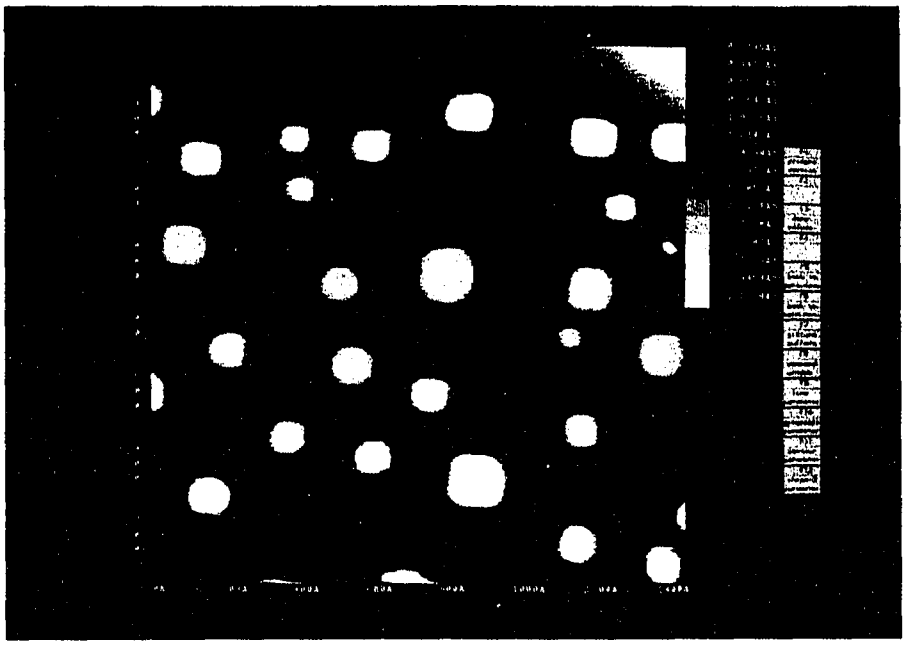

(1)

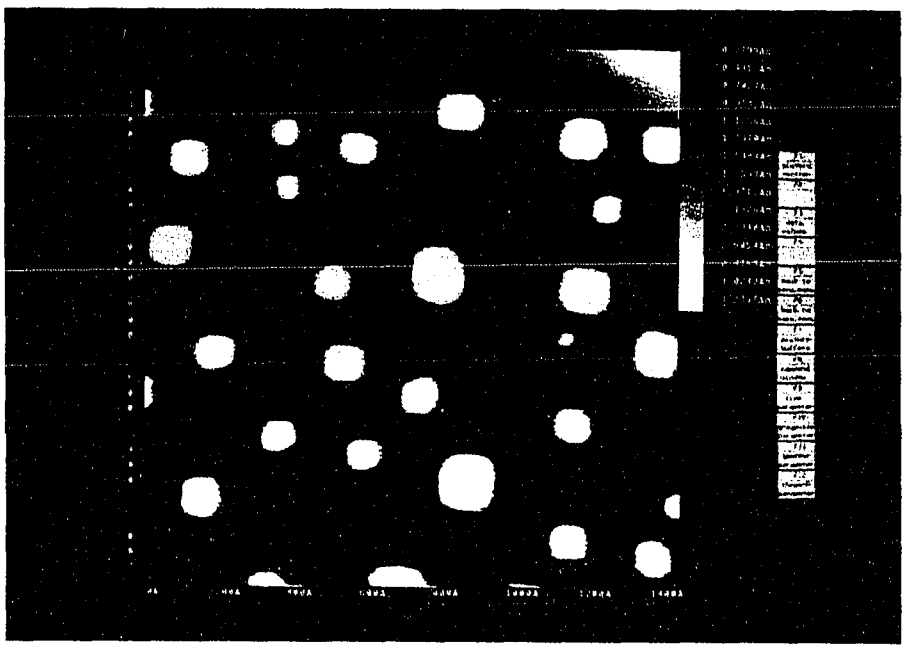

(2)

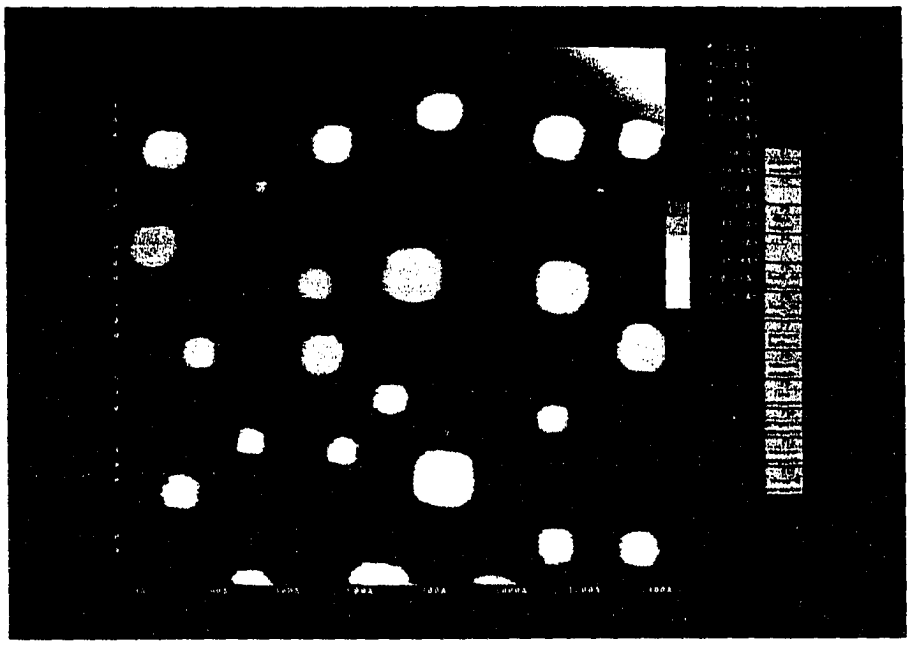

(3)

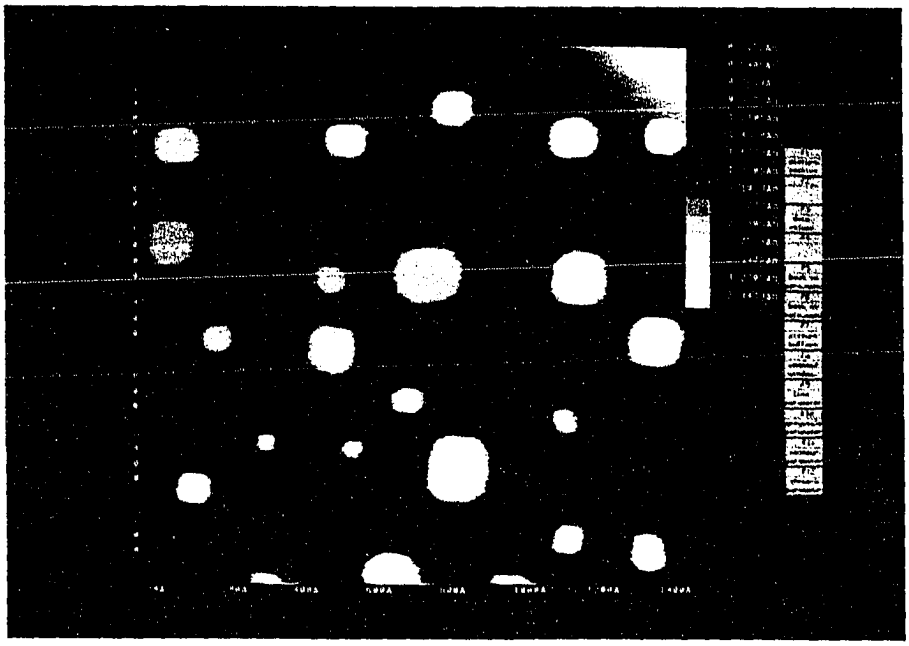

(4)

Figure 18. cont.

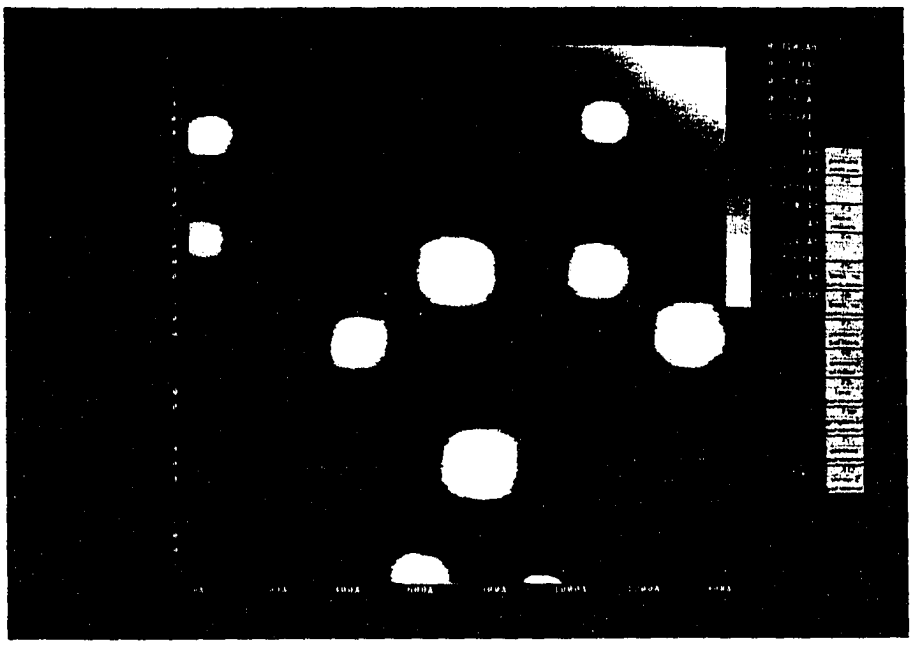

(5)

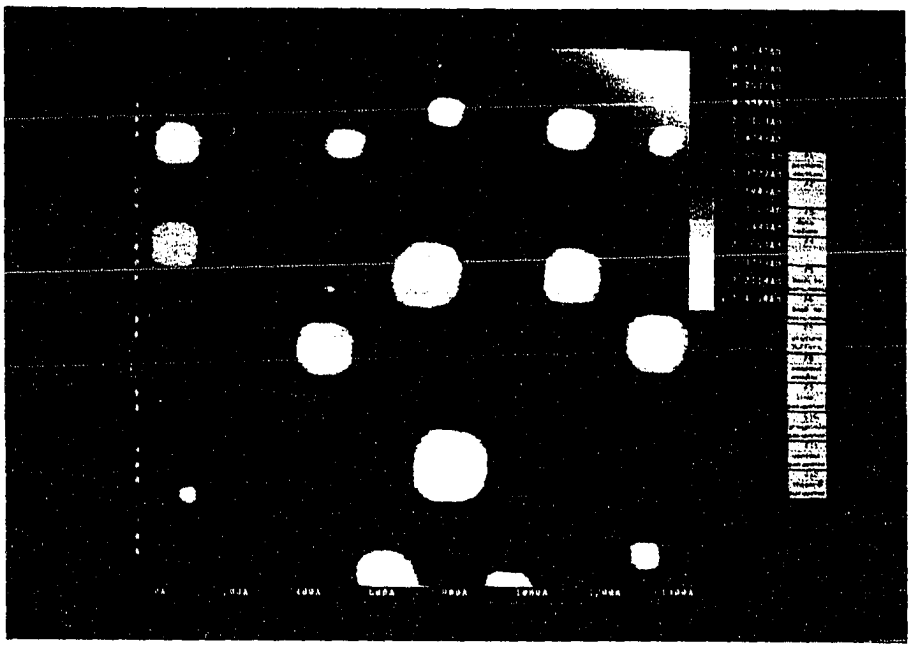

(6)

Figure 18. cont.

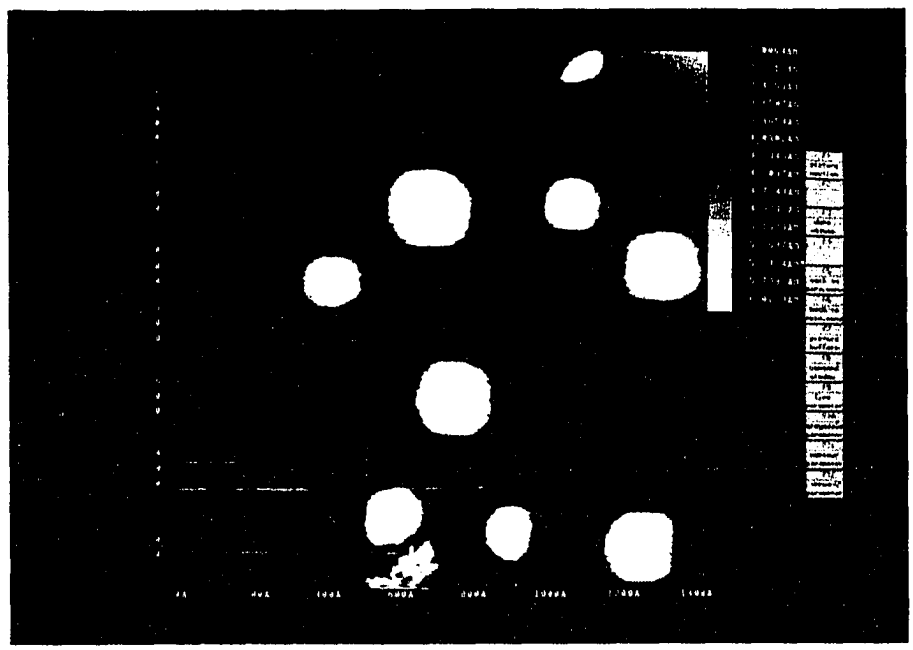

(7)

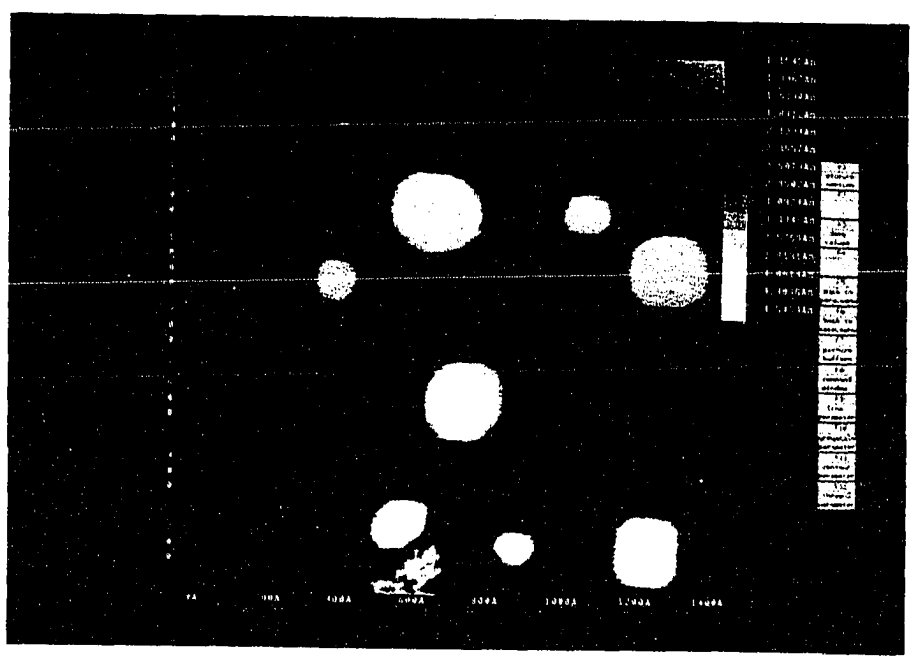

(8)

Figure 18. cont.

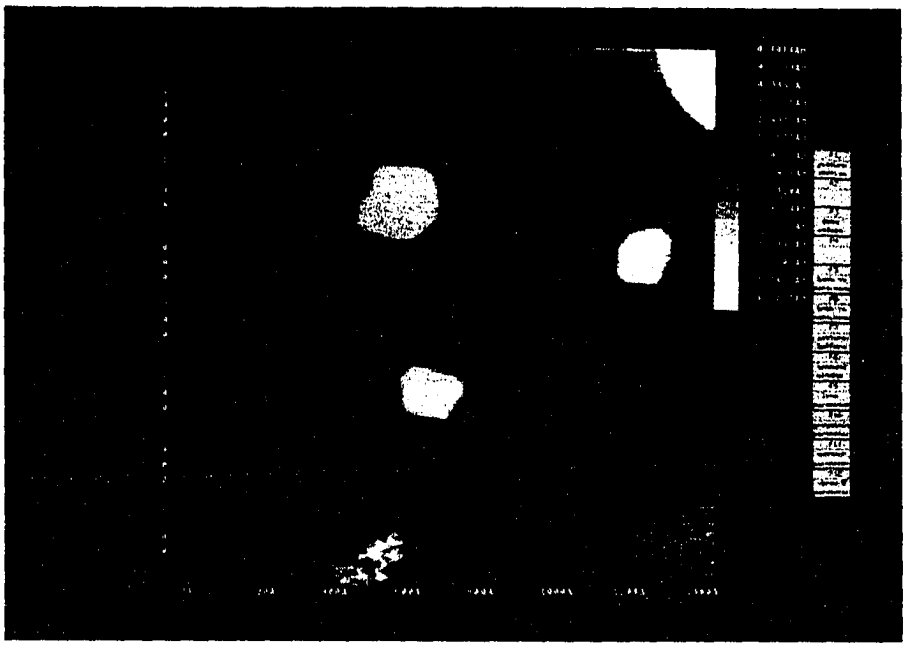

(9)

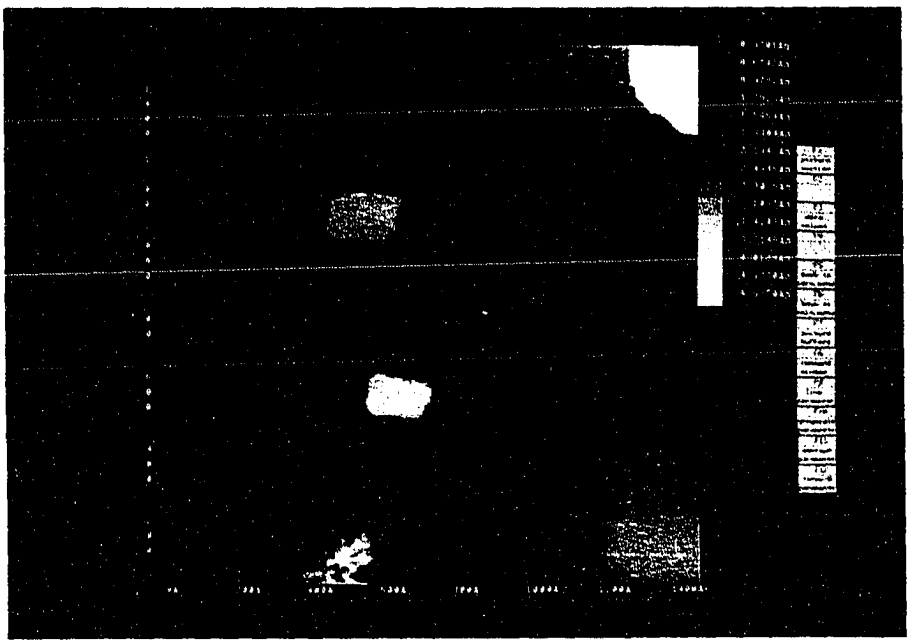

(10)

Figure 18. cont.

barrier. The second is an energy barrier that atoms need to overcome in order to diffuse on the terrace. In the Ag/Ag (100) system, the core-break energy is much higher than that of the diffusion barrier. Therefore, the former is the rate-controlling step. Since clusters change their sizes mainly due to atoms leaving from and reattaching to clusters, we consider that the increased cluster vanishing rate is due, at least partially, to the reduction of the core-break barrier by the background gas.

(2) Visible contamination effect

In this section, we show that contamination on the cluster edge can change film evolution. Figure 19 shows a Ag film at a coverage of 0.69 Ml under UHV conditions. In this figure, we demonstrate that the influence of contamination can affect atomic flow along the film edge. The film is in the regime where the deposited material forms large patches with unfilled channels and holes. Visible contamination is apparent 10 hrs after deposition. The shape of each of these impurities is similar to that of the others. They appear as round dots with a size of order 10^2 Å^2 and a height of 3 Å. Their appearance is different from the contamination leftover on the surface after cleaning. These contamination appear as spires with a size of $1x10^3$ to $1x10^4$ Å^2 and a height of 5 Å and above. These round dots preferentically occupy are step edges or film edges (which are essentially equivalent to step edges). Other positions such as on terrances, are also occupied. The number of impurities increases during the observation time (extending to 28 hrs after deposition). Some impurity sites enlarge themselves slightly over this time period but most remain essentically the same. A notable change in the series of images is the part connecting

Figure 19. Under UHV conditions, STM images show the influence of contamination sites on atom flow. Coverage is 0.69 ML. A bridge area is examined. The presence of contaminations on the edge of the bridge prevents the bridge from breaking or re-shaping. The data is in file Ag-03-22-95.

(1)

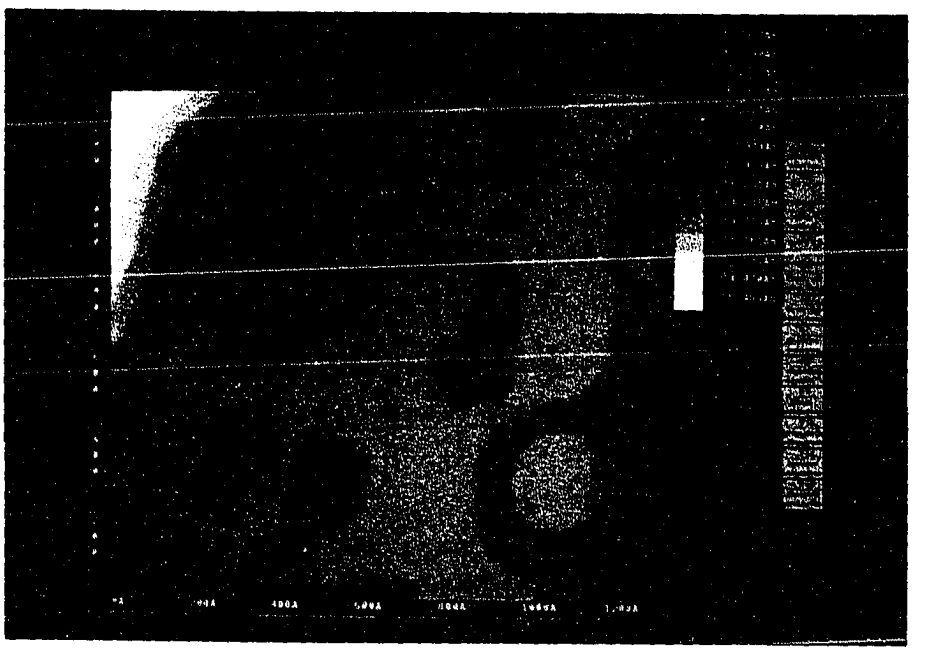

(2)

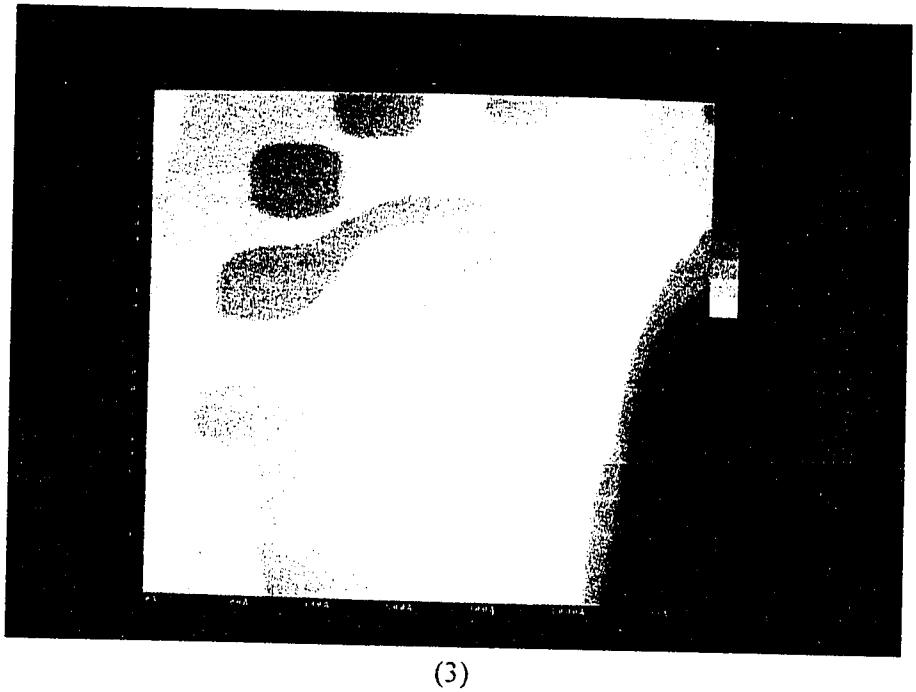

(3)

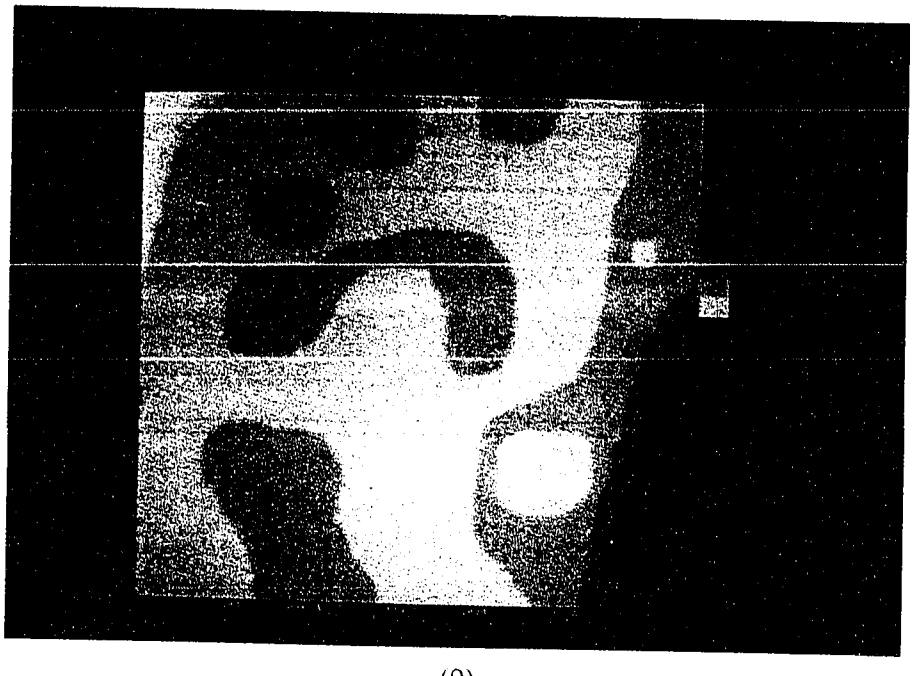

(9)

Figure 19. cont.

the two pieces of clusters. The width of this narrow bridge oscillated over time, as shown in Figure 20. This reflects a mass flow change around that area due to the presence of contamination. Before the contamination builds up, atoms migrate along the film edge and may even leave the edge.

From the images, it can be seen that the film is composed of a network with some isolated adatom clusters at this coverage, and the film edges have many different orientations. Film edges with direction close to [010] have a higher rate of atom loss during the atom relocation. For example, the bridge area marked in Figure 19, oriented near the [010] direction, loses atoms faster than bridges oriented along the [110] direction. Therefore, the local edge starts caving in. A simple picture to explain this is atoms on [010] edge have lower coordination. When this bridge area loses more and more atoms, it gets thinner and thinner and may break. However, if there is a mechanism that can stop the loss of atoms from this place then the connection can be kept. The contamination occupying the film edges can be viewed as providing the necessary means to keep the connection.

Studies have indicated that contamination can pin step edges and the pinning points can stabilize the local step, thus resulting in the reduction of local step atom motion or further establishing a local equilibrium [24-26]. In a study of pinning sites on Ag (110), Ozcomert *et al.* [26] show that impurities pin steps to cause step bunching. Impurities, formed due to surface aggregation, having a spire shape with size of ~ 50 $Å^2$, can pin multiple steps and restrict step mobility.

In our case, the impurities are gradually built up from background gas. The

Figure 20. The bridge width as a function of time. The change is due to contamination sites developing on the edge of the bridge.

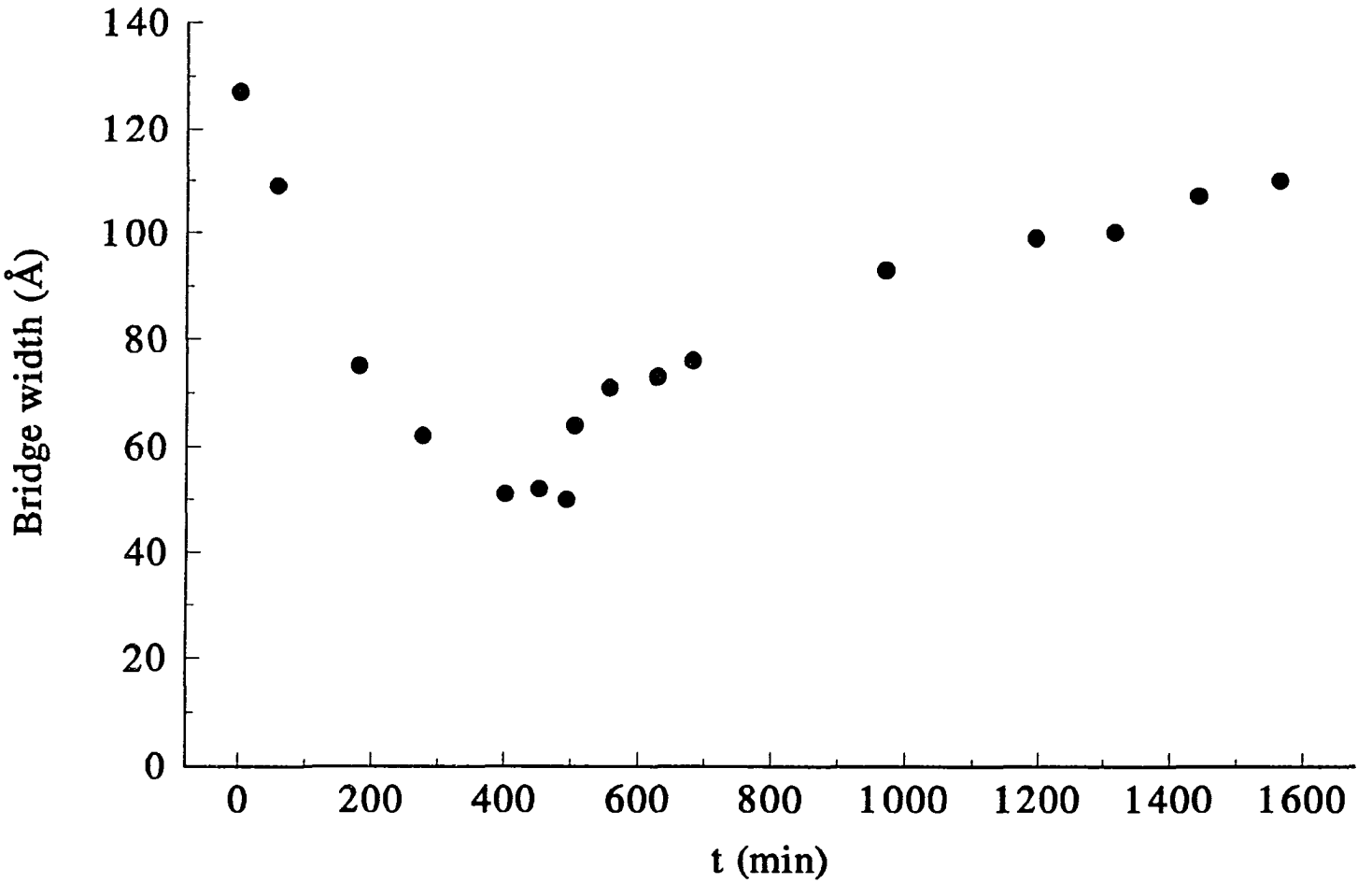
Bridge width (Å)
140
120
100
80
60
40
20
0
0
200
400
600
800
1000
1200
1400
1600
t (min)

coverage (density and size) of these impurities is small and therefore their chemical identities are unknown. The result of pinning can be detected by measuring the width of the bridge area. After the contamination shows up on the terrace or aother part of the bridge location, the bridge area still follows the trend to lose atoms. However, when contamination pins on one edge of the bridge, the width of the bridge stops decreasing and starts to increase. When both sides of the bridge are pinned, the width of the bridge increases even more. This can be explained by the fact that mass flow around the bridge location is turned in an opposite direction. Thus the pinned location must attract atoms, due to presence of the contamination.

4. Summary

We have presented a number of observations of dynamical phenomena of Ag clusters on Ag (100) with UHV-STM. Ag clusters on Ag (100) at room temperature are mobile. The interaction between clusters and between clusters and surface steps is mediated via a 2D dilute adatom gas on the terrace and different adatom concentrations around clusters and steps. Background gases and accumulated impurities on cluster edges can strongly affect the film coarsening processes. The former can enhance clusters dissolution, but the latter can stabilize the local structure and geometry of the Ag film.

5. References

1. C. T. Campbell, Annu. Rev. Phys. Chem. 41 (1990) 775, G. E. Reed, Contemp. Phys. 24 (1983) 535.

2. H. J. Hrnst, F. Fabre. R. Folkerts, and J. Lapujoulade, J. Vac. Sci. Technol. A 12 (1994) 1809.

3. J. A. Stroscio, D. T. Pierce, R. A. Dragoset, P. N. First, J. Vac. Sci. Technol. A 10 (1992) 1993.

4. R. Q. Hwang, C. Gunther, J. Schroder, S. Gunther, E. Kopatzki, and R. J. Behm, J. Vac. Sci. Technol. A 10 (1992) 1970.

5. J. De la Figuera, J. E. Pristo, O. Ocal, and R. Miranda, Solid State Commun. 89 (1994) 815.

6. R. Q. Hwang and R. J. Behm, J. Vac. Sci. Technol. B 10 (1992) 256.

7.G. Ehrlich and K. Stolt, Ann. Rev. Phys. Chem. 31 (1980) 603.

8. J.-M. Wen, S.-L. Chang, J. W. Burnett, J. W. Evans, and P.A. Thiel, Phys. Rev. Lett. 73 (1994) 2591.

9. C. Domb and J. L.Lebowitz eds., Phase Transitions and Critical Phenomena, Vol 8, Academic Press, New York, 1983.

10. A. Pimpinelli, J. Villain, D. E. Wolf, J. J. Metois, J. C. Heyraud, I. Elkinani, and G. Uimin, Surf. Sci. 295 (1993) 143.

11. K.-N. Tu, J. W. Mayer, and L. C. Feldman, in Electronic Thin Film Science for Electrical Engineers and Materials Scientists, P 105, Macmillan Publishing Company, New York, 1989.

12. M. Poensgen, J. F. Wolf, J. Frohn, M. Giesen, and H. Ibach, Surf. Sci. 274 (1992) 430.

13. F. M. Ross and J. M. Gibson, Phys. Rev. Lett. 68 (1992) 1782.

14. A. V. Latyshev, A. L. Aseev, A. B. Krasilnikov, and S. I. Stenin, Surf. Sci. 213 (1989) 15.

15. C. Alfonso, J. M. Bermond, J. C. Heyraud, and J. J. Metois, Surf. Sci. 262 (1992) 371.

16. STM data shows that adatom clusters do not settle near descending step.

17. B. Lewis and J. C. Anderson, in: Nucleation and Growth of Thin Films, Academic

press, New York, 1978.

18. For Ag/Ag(100), at low coverage (5%-27%ML), the adatom clusters coalesce dominate the coarsening process.

19. G. A. Bassett, in: Condensation and Evaporation of Solid, eds. E. Rutner, P. Goldfinger and J. P. Hirth, Gordon and Breach, New York, 1964.

20. M. J. Paesley, J. Phys. D 3 (1970) 707.

21. Y. F. Chu and E. Ruckenstein, Surf. Sci. 67 (1977) 517.

22. G. W. Sears and J. B. Hudson, J. Chem. Phys. 39 (1963) 2380.

23. D. R. Peale and B. H. Cooper, J. Vac. Sci. Technol. A 10 (1992) 2210.

24. M. Mundshau, E. Bauer, W. Telieps, and W. Swiech, Surf. Sci. 223 (1989) 413.

25. B. Van der Hoek, J. P. Van der Eeden, and P. Bennema, J. Cryst. Growth. 56 (1982) 108.

26. J. S. Ozcomert, W. W. Pai, N. C. Bartelt, and J. E. Reutt-Robey, Surf. Sci. 293 (1993) 183.

CHAPTER 6

CONCLUSION

During film growth, adatoms are continuously deposited onto the substrate at a certain rate. The adatoms that land on the substrate will have a certain lifetime to migrate on the surface and interact with the surface atoms as well as with each other. In some cases, these interactions may cause growth of substrate steps, intermixing of deposited atoms and substrate atoms, and alteration of further film growth. These interactions result in nucleation on the surface, two-dimensional (2D) condensation of adatoms into islands and their subsequent growth, and the continuous growth from 2D to 3D cluster.

Growth kinetics depend on the fundamental surface processes of surface adsorption, desorption, and diffusion. Often the thermodynamically favored film states are 2D islands and 3D clusters on the substrate rather than a random distribution of adatoms. Film growth is a non-equilibrium process where surface phase separation occurs and growth kinetics plays an essential role. In this work, the cluster mobility are studied extensively.

From the results summarized below a better understanding of thin film growth process is achieved. The information of the metal cluster mobility on metal surface can be used to get information of surface diffusion energy barriers which in turn can help people to understand the fundamental interaction involved in the film growth for other systems.

In summary, we used STM to study metal thin film growth processes. The main conclusions are:

1. Large metal cluster diffuse on Ag(100) surface. The metal-metal system large adatom cluster diffusion is reported for the first time. The evaporation-condensation of adatoms dominating the vacancy cluster diffusion process is suggested. The diffusion coefficients is on the order of 10^{-18} cm^2s^{-1} .

2. Metal film evolution behaviors at different coverage regime are examined. At low coverage, cluster diffusion dominates the coarsening process. At high submonolayer coverage, vacancy cluster repining dominates the process. At moderate coverage, edge-running dominates the process.

3. The vacancy cluster diffusion is also observed. The vacancy were formed by controlling the deposition flux and film coverage. The method is simple and offers similar advantages of the sputtering method. The diffusion coefficients is on the order of 10^{-18} cm^2s^{-1}, is smaller than that of adatom clusters, and has a scaling factor α roughly close to 0.5 in $D \propto N^{-\alpha}$. The evaporation-condensation of vacancy monomers dominating the vacancy cluster diffusion process is suggested.

4. We have presented a number of observations of dynamical phenomena of Ag cluster on Ag (100) with UHV-STM. Ag cluster on Ag (100) at room temperature are mobile. The interaction between clusters and between clusters and surface steps are mediated via 2D dilute adatom gas on the terrace and different adatom concentrations around clusters and steps. Background gases and impurities on cluster edges can strongly

affect film coarsening process. The former can enhance clusters dissolution, but the latter can stabilize the local structure and geometry of the Ag film.

Additional work can be done in the following areas. First, the temperature dependence of clusters' mobility is useful to get information about diffusion barriers. Second, similar measurements for different orientations of Ag substrates are useful to compare the impact of substrates on film growth process.

REFERENCES

1. J. D. Doll and A. Voter, Ann. Rev. Phys. Chem. 38 (1987) 413.

2. S. Wang and G. Ehrlich, Surf. Sci. 206 (1988) 451.

3. D. W. Bassett and M. J. Paesley, J. Phys. D 3 (1970) 707.

4. R. T. Tung and W. R. Graham, Surf. Sci. 97 (1980) 73.

5 G. Ayrault and G. Ehrlich, J. Phys. Chem. 60 (1974) 281.

6. C. L. Chen and T. T. Tsong, Phys. Rev. Lett. 66 (1991) 1610.

7. D. W. Bassett and P. R. Webber, Surf. Sci. 70 (1978) 520.

8. J. D. Wrigley and G. Ehrlich, Phys. Rev. Lett. 44 (1980) 661.

9. G. L. Kellogg, Phys. Rev. Lett. 67 (1991) 216.

10. P. J. Feibelman, Phys. Rev. Lett. 65 (1990) 729.

11. G. L. Kellogg and P. J. Feibelman, Phys. Rev. Lett. 64 (1990) 3143.

12. C. L. Chen and T. T. Tsong, Phys. Rev. Lett. 64 (1990) 3147.

13. G. L. Kellogg, A. F. Wright, and M. S. Daw, J. Vac. Sci. Technol. A 9 (1991) 1757.

14. G. L. Kellogg, Surf. Sci. 266 (1992) 18.

15 .K. Stolt, W. R. Graham, and G. J. Ehrlich, J. Chem. Phys. 65 (1976) 3206.

16. W. R. Graham, and G. J. Ehrlich, J. Phys.: Metal Phys. F 4 (1974) L212.

17. T. T. Tsong and R. Gasanova, Phys. Rev. B 22 (1980) 4632.

18. D. W. Bassett, J. Phys. C 9 (1976) 2491.

19. P. Cowan and T. T. Tsong, Phys. Rev. A 53 (1975) 943.

20. V. R. Dhanak and D. W. Bassett, Surf. Sci. 238 (1990) 289.

21. P. J. Feibelman, Phys. Rev. Lett. 58 (1987) 2766.

22. U. M. Titulear and J. M. Deutsch, 77 (1982) 472.

23. U. Landman and M. F. Shlesinger, Phys. Rev. B 16 (1977) 3389.

24. G. Ehrlich and K. Stolt, Ann. Rev. Phys. Chem. 31 (1980) 603.

25. G. L. Kellogg, Appl. Surf. Sci. 67 (1993) 134.

26. S. C. Wang and G. Ehrlich, Surf. Sci. 239 (1990) 301.

27. S. C. Wang and G. Ehrlich, J. Chem. Phys. 91 (1989) 6535.

28. G. L. Kellogg, Phys. Rev. Lett. 73 (1994) 1833.

29. G. L. Kellogg and A. F. Voter, Phys. Rev. Lett. 67 (1991) 622.

30. H. J. Hrnst, F. Fabre. R. Folkerts, and J. Lapujoulade, J. Vac. Sci. Technol. A 12 (1994) 1809.

31. D. D. Chambliss, R. J. Wilson, and S. Chiang, Phys. Rev. Lett. 66 (1991) 1721.

32. R. Q. Hwang, C. Gunther, J. Schroder, S. Gunther, E. Kopatzki, and R. J. Behm, J. Vac. Sci. Technol. A 10 (1992) 1970.

33. D. D. Chambliss, R. J. Wilson, and S. Chiang, J. Vac. Sci. Technol B 9 (1991) 933.

34. R. Q. Hwang and R. J. Behm, J. Vac. Sci. Technol. B 10 (1992) 256.

35. E. Kopatzki, S. Gunther, W. Nichtl-Pecher, and R. J. Behm, Surf. Sci. 248 (1992) 154.

36. S. Rousset, S. Chiang, D. E. Flower, and D. D. Chambliss, Phys. Rev. Lett.69 91992) 3200.

37. J. A. Stroscio, D. T. Pierce, R. A. Dragoset, P. N. First, J. Vac. Sci. Technol. A 10 (1992) 1993.

38. I. Gane, Phys. Rev. Lett. 68 (1992) 156.

39. Y. W. Mo, Phys. Rev. Lett. 71 (1993) 2926.

40. Stroscio, Phys. Rev. Lett. 70 (1992) 156.

41. Y. W. Mo, Phys. Rev. Lett. 71 (1993) 2923.

42. R. M. J. Cotterill, M. Doyoma, J. J. Jackson and M. Meshii, Eds., Lattice Defects in Quenched Metals (Academic Press, New York, 1965).

43. R. W. Balluffi, J. Nucl. Mater. 69-70 (1978) 240.

44. D. P. Lahiri, T. R. Ramachandra and A. K. Jena, J. Mater. Sci. 11 (1976) 471.

45. A. Parthasarathi and H. L. Fraser, Philos. Mag. A 50 (1984) 89.

46. A. Parthasarathi and H. L. Fraser, Philos. Mag. A 50 (1984) 101.

47. J. de la Figuera, J. E. Pristo, O. Ocal, and R. Miranda, Solid State Commun. 89 (1994) 815.

48. K. Morgenstern, G. Rosenfeld, B. Poelsema, and G. Comsa, Phys. Rev. Lett 74 (19950 2058.

49. W. Ostwald, Z. Phys. Chem. (Leipzig) 34 (1900) 495.

50. I. M. Lifshitz and V. V. Slyozov, J. Phys. Chem. Solid 19 (1961) 35.

51. C. Wagner, Z. Elektrochem. 65 (1961) 581.

52. P. Wynblatt and T. Ahn, Sintering and Catalysis, Ed G. C. Kuczynski (Plenum, New York, 1975).

53. G. Insmeister, Thin Solid Films, 4 (1969) 363.

54. H. Schmeisser, Thin Solid Films 22 (1974) 83.

55. S. Stoyanov and D. Kashchiev, Current Topics in Materials Science Vol.7, Ed E. Kalidis (North-Holland, New York, 1981).

56. M. Zinke-Allmang, L. C. Feldman, S. Nakagara and B. A. Davidson, Phys. Rev. B 39 (1989) 7848.

57. M. Futamoto, M. Hanbucken, C. J. Harland, G. W. Jones and J. A. Venables, Surf. Sci. 150 (1985) 430.

58. M.A. Listvan, Surf. Sci. 173 (1986) 294.

59. E. Bauer, M. Mundschau, W. Swiech and W. Telieps, Ultramicroscopy 31 (1989) 49.

60. M. G. Lagally, Y. W. Mo, R. Kaiotis, B. S. Swartzentruber and M. B. Webb, in Kinetics and Ordering and Growth at Surfaces, Ed. M. G. Lagally (Plenum, New York, 1990).

61. Y. M. Mo, R. Kaiotis, B. S. Swartzentruber, M. B. Webb and M. G. Lagally, J. Vac. Sci. Technol. A 8 (1990) 201.

62. K. Hartig, A. P. Janssen and J. A. Venables, Surf. Sci. 74 (1978) 69.

63. G. W. Jones, J. M. Norskov and J. A. Venables, Phys. Rev. Lett. 65 (1990) 3317.

64. J. A. Venables, J. Vac. Sci. Technol. B 4 (1986) 870.

65. T. M. Ahn, S. Purushothaman and J. K. Tien, J. Phys. Chem. Solids 37 (1976) 777.

66. G. Binnig, H. Rohrer, C. Gerber and E. Weibel, Appl. Phys. Lett. 40 (1982) 178.

67. G. Binnig, H. Rohrer, C. Gerber and E. Weibel, Phys. Rev. Lett. 49 (1982) 57.

68. "Proceeding of the Fourth International Conference on Scanning Tunneling Microscopy/Spectroscopy" J. Vac. Sci. Technol. A 8 1990.

69. J. Tersoff and D. R. Hamann, Phys. Rev. Lett. 50 (1983) 1998; Phys. Rev. B 32 (1985) 805.

70. C. J. Chen, J. Vac. Sci. Technol. A 6 (1988) 319; Phys. Rev. Lett. 65 (1990) 448.

71. N. D. Lang, Phys. Rev. Lett. 58 (1987) 45.

72. S. Ciraci, A. Baratoff and I. P. Batra, Phys. Rev. B 41 (1990) 2763.

73. G. Doyen and D. Drakova, Surf. Sci 178 (1986) 375.

74. C. J. Chen, "In troduction to Scanning Tunneling Microscopy", Oxford University Press, New York, 1993.

ACKNOWLEDGMENTS

First, I am greatly indebted to my research advisor, Professor Patricia Thiel, for her guidance and support during my graduate study in Iowa State University.

I thank all members of the Thiel group. I am very grateful to Dr. Joe Burnett for teaching me the principles of surface science and ultra-high vacuum technology. The appendix IV is done by Dr. Joe Burnett. With his permission, I include it in this thesis to show the viberation isolation characterics of our STM. I thank Drs. Cynthia Jenks and Mark Jensen for all the assistance they provided. Their help are greatly appreciated.

I thank Professor James Evans and Dr. M. Bartelt for teaching me the basic theories of thin film growth.

Finally, I thank my wife and my parents for all their support and love. This dissertation is dedicated to them to express my great gratitude.

This work was performed at Ames Laboratory under Contract N. W-7405-Eng-82 with U.S. Department of Energy. The United States government has assigned the DOE Report number IS-T 1762 to this dissertation.

APPENDIX I

THE CONSTRUCTION OF THE VACUUM CHAMBER

The vacuum we used to carry out all experiments is composed of two parts. The upper part is used to house all the equipment, including STM, sample transfer arm, evaporation source, etc. It includes two levels. The lower part is used to house all the pumps. The entire chamber (excluding two mechanical pumps) sits on a metal table, which is supported by a servo controlled air suspension unit. The unit provides vibration isolation.

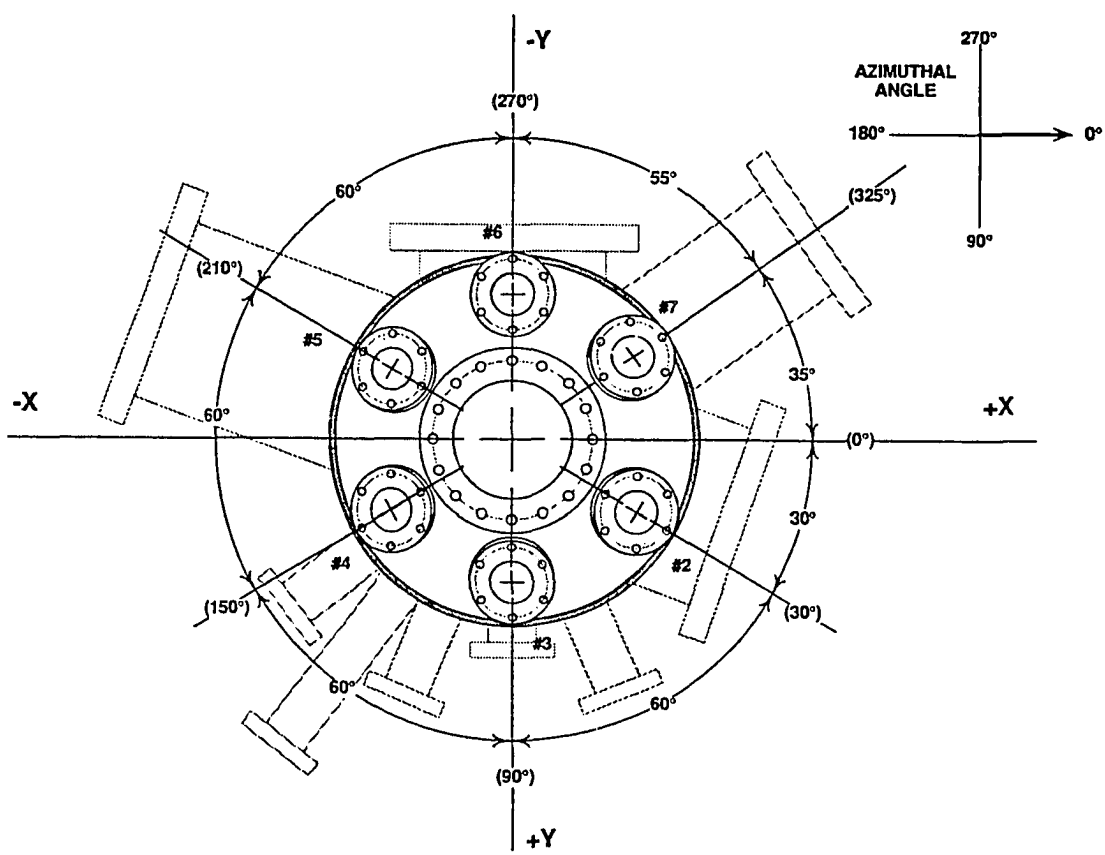

Figure 1. Vacuum chamber upper part, first level ports

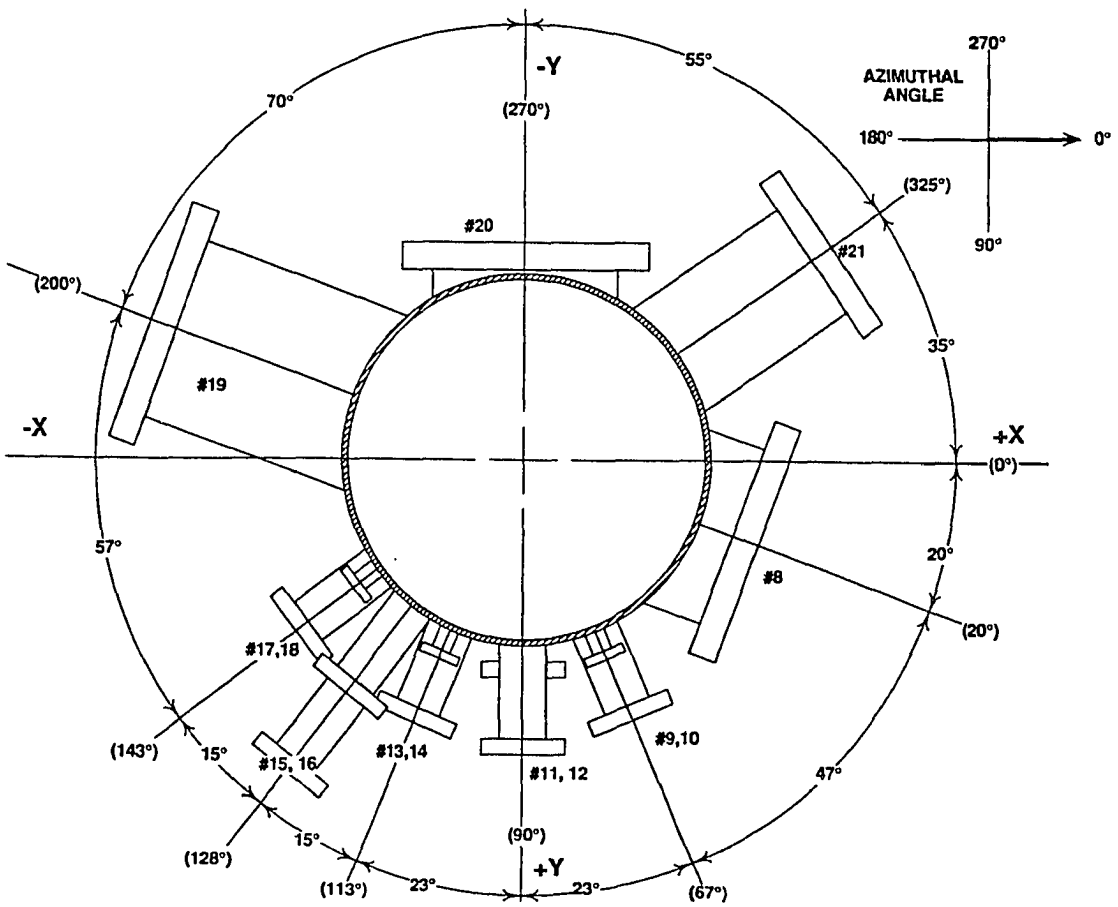

Figure 2. The vacuum chamber upper part second level ports

port # 8: view port; port #12: sample transfer arm; port #18: evaporation source
port # 20: STM

Table 1. Port configurations

PORT #	FLANGE	PORT LENGTH INCHES	FOCAL POINT			ELEVATION ANGLE	AZIMUTHAL ANGLE	TUBE DIAM. INCHES	AZIMUTHAL ANGLE OF FOCAL POINT	RADIUS OF FOCAL POINT
			X	Y	Z					
FIRST LEVEL										
1	6" O.D. ROTATABLE CONFLAT	21.15"	0	0	0	90	0	4	0	3
2	2 3/4" O.D. TAPPED NONROTATABLE CF	6.1"	2.598	1.500	13.5	72	30	1.51	30	3
3	2 3/4" O.D. TAPPED NONROTATABLE CF	6.1"	0	3.000	13.5	72	90	1.51	90	3
4	2 3/4" O.D. TAPPED ROTATABLE CF	6.1"	-2.598	1.500	13.5	72	150	1.51	150	3
5	2 3/4" O.D. TAPPED NONROTATABLE CF	6.1"	-2.598	-1.500	13.5	72	210	1.51	210	3
6	2 3/4" O.D. TAPPED ROTATABLE CF	19.62"	0	-4.700	0	90	270	1.51	270	4.7
7	2 3/4" O.D. TAPPED NONROTATABLE CF	6.1"	2.457	-1.725	13.5	72	325	1.51	325	
SECOND LEVEL										
8	8" O.D. NONROTATABLE CONFLAT	8"	0	0.00	13.5	0	20	6		
9	1 1/3" O.D. NONROTATABLE CONFLAT	7"	0	0.00	16.5	0	67	0.75		
10	2 3/4" O.D. ROTATABLE CONFLAT	9"	0	0.00	13.5	0	67	1.51		
11	2 3/4" O.D. TAPPED NONROTATABLE CF	6.5"	0	3.00	13.5	40	90	1.51	90	3
12	2 3/4" O.D. TAPPED ROTATABLE CF	9.5"	0	0.00	13.5	0	90	1.51		
13	1 1/3" O.D. NONROTATABLE CONFLAT	7"	0	0.00	16.5	0	113	0.75		
14	2 3/4" O.D. ROTATABLE CONFLAT	9.3"	0	0.00	13	0	113	1.51		
15	2 3/4" O.D. TAPPED ROTATABLE CF	7"	-1.847	2.36	13.5	42	128	1.51	128	3
16	2 3/4" O.D. ROTATABLE CONFLAT	12.5"	0	0.00	14	0	128	1.51		
17	1 1/3" O.D. NONROTATABLE CONFLAT	7"	0	0.00	16.5	0	143	0.75		
18	2 3/4" O.D. ROTATABLE CONFLAT	9.3"	0	0.00	13	0	143	1.51		
19	8" O.D. ROTATABLE CONFLAT	13"	0	0.00	13.5	0	200	6		
20	8" O.D. ROTATABLE CONFLAT, TAPPED	7"	0	0.00	13.5	0	270	6		
21	6" O.D. ROTATABLE CONFLAT	12"	0	0.00	13.5	0	325	4		

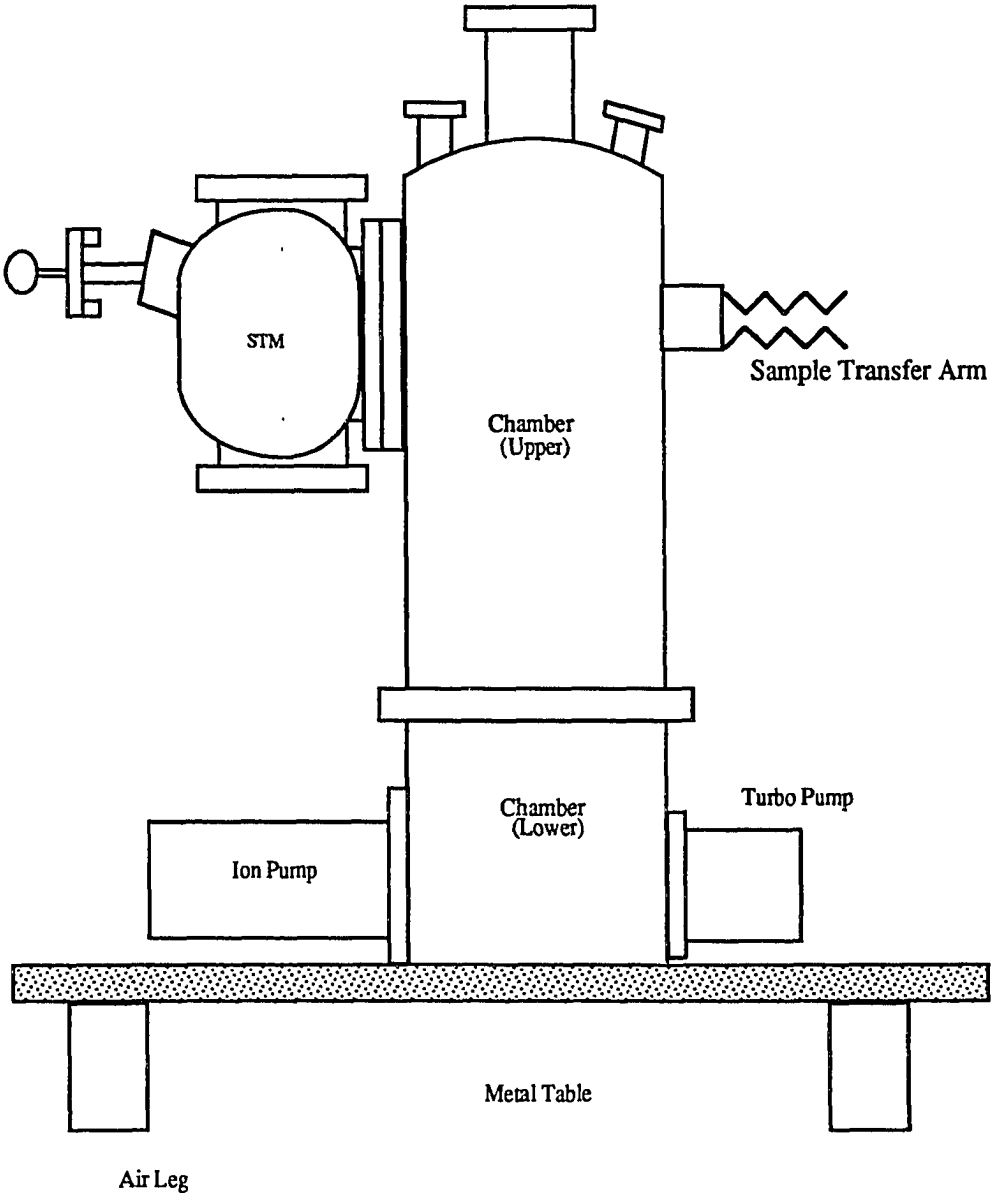

Figure 3. The side view of the chamber

APPENDIX II

PREPARATION OF SCANNING TUNNELING MICROSCOPY TIP

In recent years interest in ultrasharp tips has been greatly enhanced by their role in scanning tunneling microscopy (STM). The quality of STM tips is one of the important factors which affect the resolution of the STM images. The procedures to produce sharp tips can be classified into three categories: (1) mechanical method; (2) physical method; and (3) chemical method [1].

Mechanical methods generally involve simple mechanical operations, such as cutting or grading a metal wire made of W, Pt-Ir, Pt-Rh [2,3]. A sharp tip is formed based on the assumption that a single atom or a cluster of atoms must protrude at the cut end and therefore provide the atomic sharpness needed in STM measurements.

Physical methods involve modification of the tips end, such as coating [4], ion sputtering [5], and field evaporation [6].

Chemical method is basically etching a metal wire electrochemically. This method has been used extensively to sharpening metal tips to a very small apex radius [7]. Both ac and dc current are used. Tip preparation setup is simple. The following is a general description of etching process. A metal wire (used as tip material), such as W wire, is placed in an electrolyte (1-2N KOH or NaOH) with only a portion of the wire inside the solution. Another electrode (Pt, Au) is also placed inside the electrolyte. The etching process starts when an ac or dc power supply is connected to the two electrodes. The metal

wire is etched until it breaks into two parts. The broken ends are used as tips.

We use electrochemical etching to make STM tips. The setup is shown in Figure 1. We use W wire (0.25 mm diameter) as tip material. And Au is used as the second electrode. A gold wire about 1mm in diameter is bent as a circular shape with diameter 0.5 inch. The W wire is placed in the center of the Au ring. A 2N KOH solution is used as electrolyte. We use KOH solution to rinse the Au ring to form a thin liquid film on the Au ring after installing the W wire. Then a dc power supply is connected to the two electrodes. We use 5-7V voltage which gives a current of 2-3 mA. The etching process takes about 1 hour. In order to get a smooth etched tip, the position of W wire is adjusted to make sure the etching point constant during the course of etching. The resultant W tips are examined with a scanning electron microscopy (SEM), as shown in Figure 2.

References:

1. M. Fotino, Rev. Sci. Instrum, 64 (1993) 159.

2. S. Chiang and R. J. Wilson, IBM J. Res. Develop., 30 (1986) 515.

3. V. Elings and F. Wudl, J. Vac. Sci. Technol., A 6 (1988) 412.

4. T. S. Ravi, R. B. Marcus, T. Gmitter, H. H. Busta, and J. T. Niccum, J. Appl. Phys. Lett. 57 (1990) 1413.

5. J. A. Kubby, and B. M. Siegel, J. Vac. Sci. Technol., B 4 (1986) 120.

6. J. K. Gimzewski, E. Stoll, and R. R. Schlittler, Surf. Sci., 181 (1987) 267.

7. A. F. Melmed, J. Vac. Sci. Technol., B 9 (1991) 601.

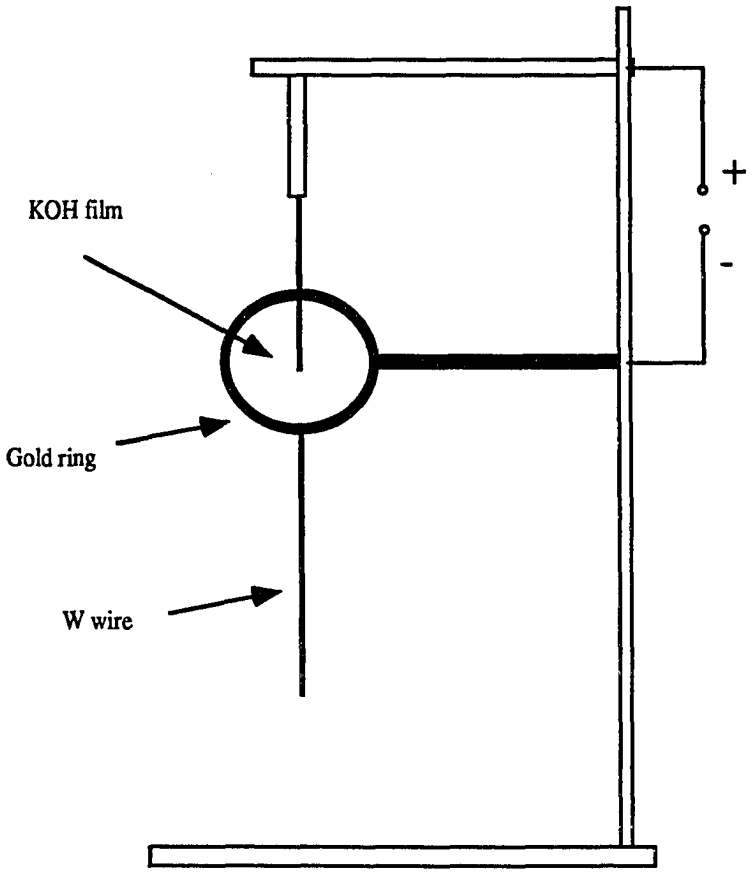

Figure 1.1. Schematic of tip preparation set-up

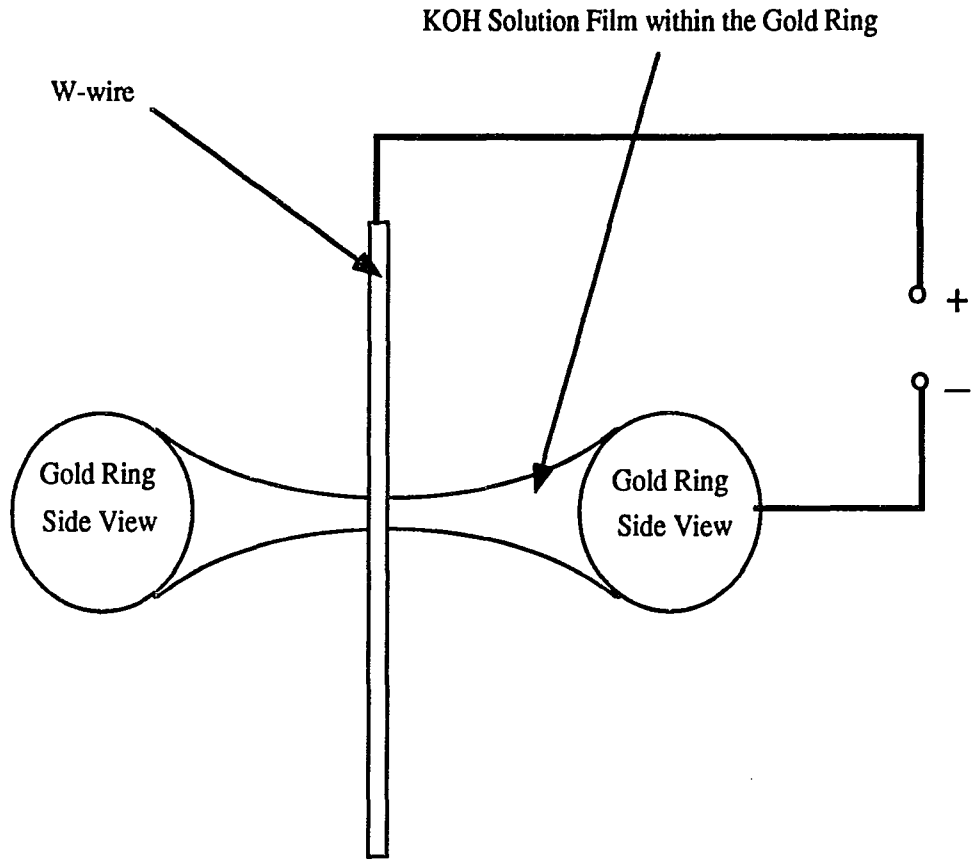

Figure 1.2. Schematic of aqueous KOH solution film and gold ring

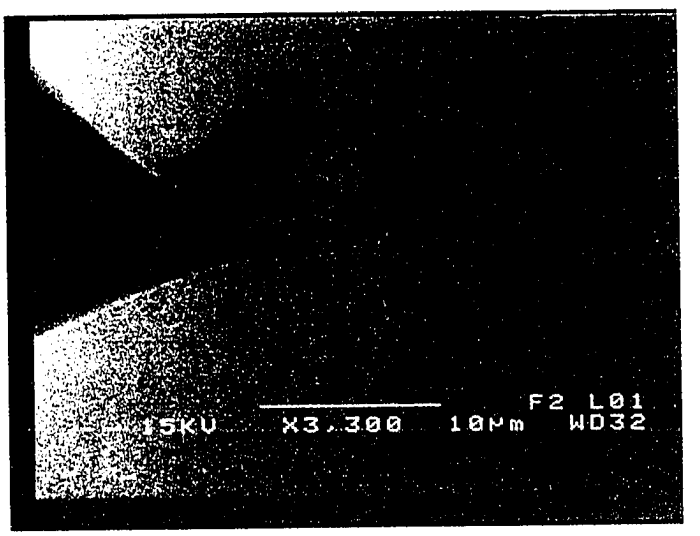

(1)

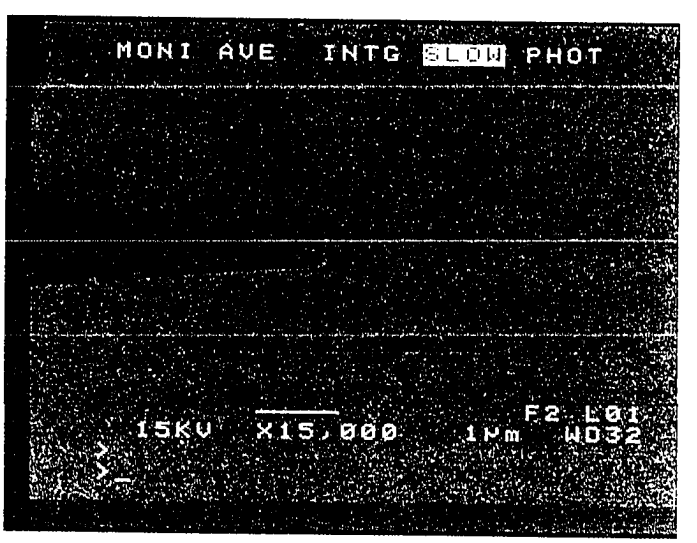

(2)

Figure 3. SEM pictures of a W tip with different magnifications

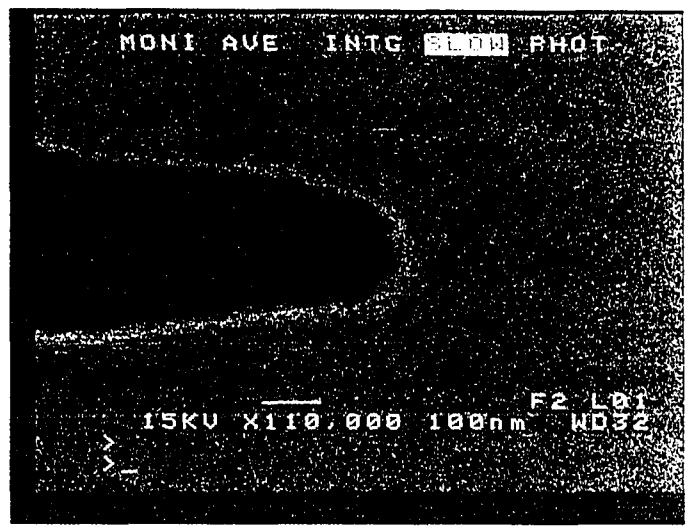

(3)

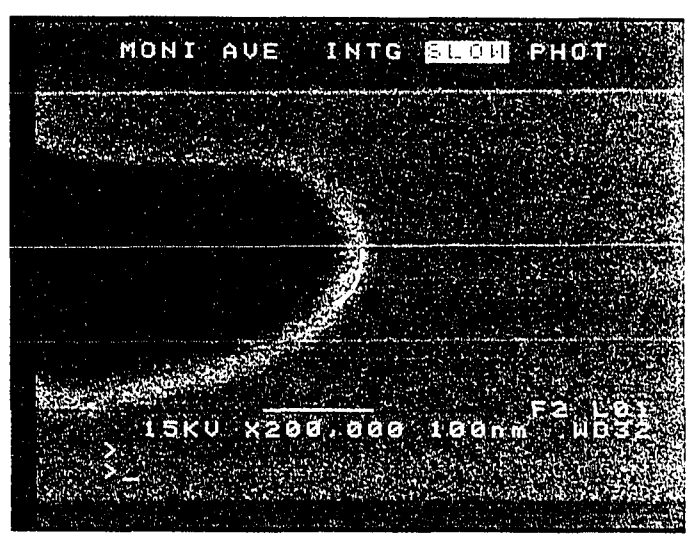

(4)

Figure 3. cont.

APPENDIX III

THE MAJOR STM DATABASE

Table 1. STM data

File Name	Flux(ML/Min)	Coverage (ML)	Cluster Density x 10-5(Å2)	Time Length (min)	
#040793	1.8	0.03	1.5	n/a	
#0412	1.98	0.23	5.6	n/a	
#0412a	2.1	0.35	6	n/a	
#0413	4.8	0.16	6.5	n/a	
#0429	1.6	0.16	5	n/a	
#0503	2.8	0.23	7.4	n/a	
#0823	n/a	n/a		600	steps
#0828	1.68	0.28	1.1	192	high vac
#0831	7.2	0.65		1200	
#0901	9	1.4		1361	2nd evp
#0908	0.18	0.015	0.99	1244	
#0913	0.24	0.007	0.26	1540	
#1221	n/a	n/a		524	steps
#1224	0.56	0.228		300	
#1224a	0.56	1.12		100	
#1227	1.08	0.09	3.1	1705	
#1229	1.08	0.09		396	from 1227
#1230	1.08	0.09		330	from 1227
#010794	0.23	0.015	2	200	
#0110	0.6	0.09	0.52	500	
#0519	n/a	n/a		200	steps
#0528	0.36	0.36	2.2	708	
#0531	0.36	0.9	n/a	1100	
#0602	0.3	0.68	n/a	180	
#0602a	0.3	0.95	n/a	990	
#0603	0.3	1.8	n/a	200	
#0606	0.3	2.2	n/a	30	

Table 1. cont.

#0607	0.3	3.5	n/a	300	
#0608	0.3	0.36	n/a	300	
#0609	0.3	1.1	n/a	1320	
#0610	0.3	8.8	n/a	50	
#0614	1.26	0.57	n/a	110	
#0615	1.26	0.28	n/a	156	
#0617	1.26	1.2	5.9	354	
#0619a	1.26	0.89	n/a	300	
#0620			n/a	n/a	3 times evp
#0621		0.75	n/a	n/a	two layers
#0707	0.28	0.07	2.6	550	
#0711	5.4	0.27	6.9	600	
#0712	0.48	0.05	5.4	1300	
#0715	0.48	0.03	3.8	340	
#032095	0.11	0.69	n/a		
#0322	0.11	0.68	n/a		

APPENDIX IV

SUMMARY OF VIBRATION ISOLATION MEASUREMENTS AND ESTIMATE OF VIBRATIONAL NOISE REACHING THE TIP-SAMPLE JUNCTION

1. Introduction

In order to resolve atoms using scanning tunneling microscopy (STM), it is necessary to minimize vibrational displacements between the scanning tip and the sample surface. Because atomic corrugations on metal surfaces are typically on the order of 0.1Å, vibrational amplitude displacements between the tip and the surface should be less than 0.01Å. Thus *the vibration goal of the system is on the order of 1 pm or 0.01* Å along the tip axis. For our instrument, this corresponds to the horizontal direction. Interatomic spacings are in general larger than the corrugations, therefore the demands upon the vibration isolation in the direction perpendicular to the tip axis (vertical direction for our instrument) are relaxed. Vibration isolation is especially challenging when STM is carried out under ultra-high-vacuum (UHV) conditions.

This report is intended to provide a functional description of methods used for vibration isolation in UHV-STM work. For a rigorous discussion and presentation of the theory of vibration isolation, the reader is referred to refs. 1-6. The vibration findings for the STM laboratory are summarized and presented here. In addition, methods of predicting the

vibration amplitudes transmitted to the STM junction are presented here.

Two major factors contribute to the stability of the tip-sample junction. The first is the rigidity of the STM scanner-sample holder assembly itself; a rigid system transmits smaller vibration amplitudes than does a soft system. (In other words, a greater force is required to deform a rigid assembly.) Such rigidity is built into the STM design and for commercial systems is generally beyond the control of the user. The second factor to be considered is the reduction of environmental vibrations reaching the STM stage. It is this aspect of the vibration isolation system over which the user has considerable control, and is therefore emphasized in this report.

Fig. 1. is a schematic diagram illustrating the principal components of a vibration isolation system for an STM. In Fig. 1a, a single-stage vibration isolation system is employed, while Fig. 1b depicts a 2-stage vibration isolation system. In this figure, a single stage of the vibration isolation system is represented by a damped spring. In practice, the actual vibration isolation stages utilized vary considerably from system to system, but generally consist of one (or more) of the following:

(a) a series of viton pads

(b) bungee cord suspension of the STM

(c) a soft spring suspension of the STM stage with eddy current damping

(d) pneumatic vibration isolation legs

Each of these vibration isolation methods may be characterized by a resonance frequency, μ_o, and a damping ratio, ξ.

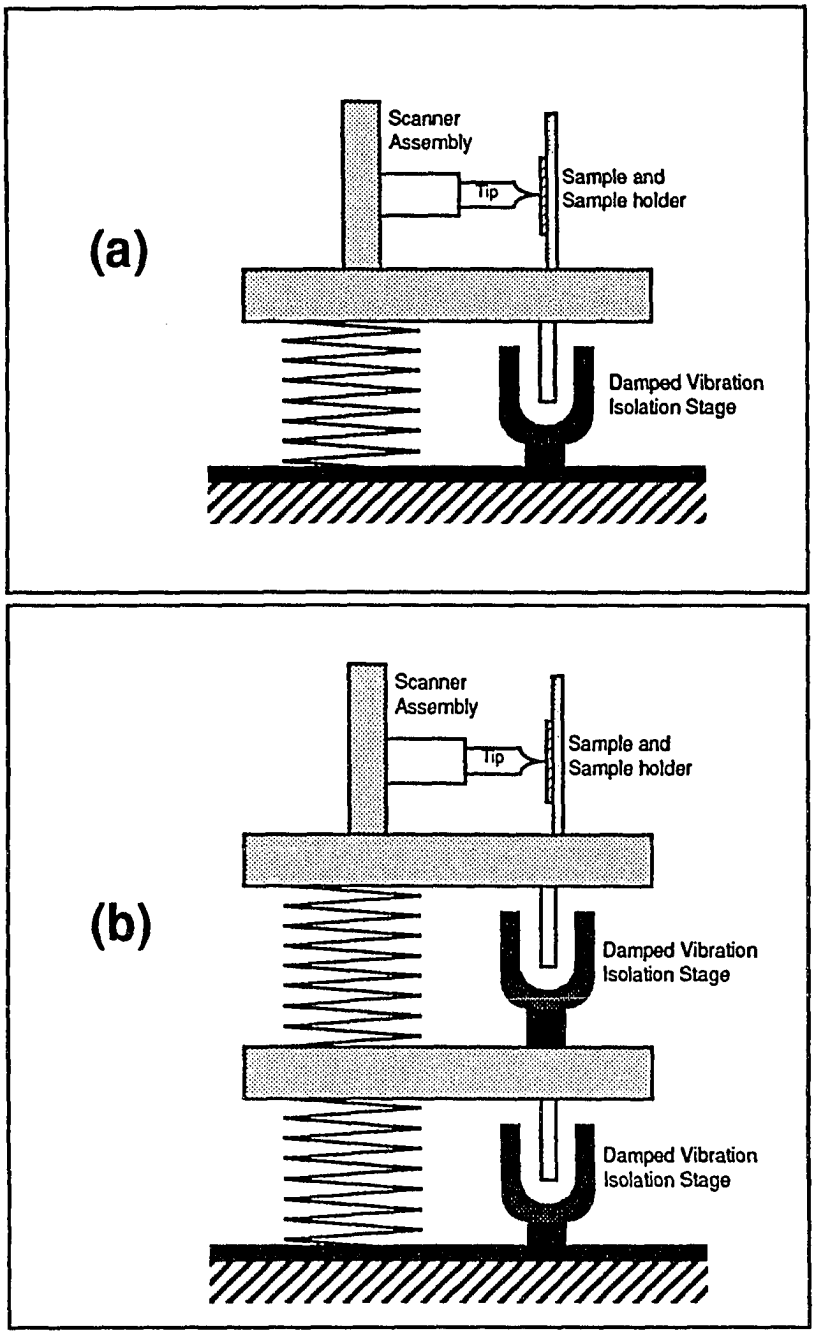

Figure 1. (a) STM assembly with a single stage of damped vibration isolation. (b) STM assembly with two stages of vibration isolation. Each stage of the vibration isolation system may be characterized by its resonance frequency and its damping coefficient.

2. External Vibrations:

The primary sources of vibration external to the STM stage are:

(i) Building vibrations

(ii) Pumps vibrations

(iii) Chamber vibrations

Buildings generally vibrate at frequencies from 1 - 100 Hz [3-5]. Lower floors exhibit vibrations in the 1-10 Hz range while upper floors have resonance frequencies in the 15-25 Hz range. In addition, ventilation ducts, motors, and transformers give rise to vibrations at the line voltage frequency and its harmonics [6].

The mechanical pumps on a vacuum chamber can introduce vibrations to the STM, typically at the line frequency and its harmonics (30, 60, 120 Hz). Turbomolecular pumps can introduce high frequency vibrations. In order to minimize pump vibrations, the mechanical and turbomolecular pumps are connected to the chamber via soft bellows. (It is not clear at this time whether bellows provide sufficient isolation.)

The chamber does not in and of itself cause vibrations, but may transmit and even amplify external vibrations. For example, the large viewports may be excited acoustically and oscillations in the tunneling current may be observed. Long lever arms, such as the sample transfer arm and the sample holder may also contribute to low frequency vibrations. To minimize the chamber amplification and transmittance of vibrations, the chamber has been constructed of heavyweight stainless steel and a support structure for the transfer arm has been designed. (Note that the approach outlined here has been to *increase* the rigidity of

the chamber.)

In Fig. 2, vibrational amplitude displacements are plotted as a function of frequency for our laboratory. Measurements were carried out on the floor, the support table, and the STM using an accelerometer (from Ames Lab Facilities). These data are for vertical displacements; similar measurements were carried out in the horizontal direction and are presented in the appendix. It may be seen that vibration amplitudes on the order of tens of thousands of Ångstroms occur at low frequencies. The data in Fig. 2a were collected with all of the pumps on, while measurements for Fig. 2b were carried out with all pumps turned off.

3. External Vibration Isolation

As mentioned earlier, spring suspension systems, pneumatic legs, bungee cords, and viton pads are common methods of external vibration isolation. Each of these may be considered in terms of a damped harmonic oscillator. (Such a model is appropriate for these systems in the limit displacements where the spring restoration force is linear with displacement [$F = - k x$]. For coil springs, bungee cords, and pneumatic legs this criteria is met for larger displacements than for viton pad vibrations. Nonetheless, for small displacements, such a model is appropriate for viton pads [5].) The equation of motion for a damped harmonic oscillator is given by [4]:

$$m\frac{dx^2}{dt^2} + b(\frac{dx}{dt} - \frac{dx'}{dt}) + k(x - x') = 0 \qquad (1)$$

where m is the mass supported by the spring (the STM assembly), b is the damping factor, k is the spring constant, and x and x' refer to the displacements from equilibrium positions of the mass and the spring support , respectively. Eqn. 1 reduces to Hook's law in the absence of damping (b=0). The damping force in Eqn. 1 is proportional to the relative velocities between the spring support and the supported mass, m. These variables are shown in Fig. 3. For a sinusoidal displacement, x'(t), of the spring support, with an amplitude given by x_o' (where $x'(t) = x_o' e^{i2\pi\nu t}$), the amplitude transmitted by the spring, x_o, to the supported mass may be referenced to x_o' to yield:

$$\left|\frac{x_o}{x_o'}\right| = \sqrt{\frac{1+\left(\frac{\xi\nu}{\nu_o}\right)^2}{\left(1-\left(\frac{\nu}{\nu_o}\right)^2\right)^2 + \left(\frac{2\xi\nu}{\nu_o}\right)^2}} \qquad (2)$$

This function, the amplitude transfer function, is plotted in Fig. 4 for several values of ξ, the damping ratio for the system. The resonance or natural frequency of the spring (also called the eigenfrequency), ν_o, is given by:

$$\nu_o = \frac{\sqrt{k/m}}{2\pi} \qquad (3)$$

where k is the spring constant and m is the mass. The damping ratio, ξ, is the ratio of the damping coefficient, to the critical damping coefficient:

$$\xi = \frac{\gamma}{\gamma_c} \tag{4}$$

The damping coefficient, γ, and the critical damping coefficient, γ_c, are given by:

$$\gamma = \frac{b}{2m} \quad \text{and} \quad \gamma_c = 4m\pi\nu_o \tag{5}$$

where, b is the damping factor (from Eqn. 1). (For magnetic damping, $\gamma = 9.69 \times 10^{-9}$ B *l* *S*/ρ, where B is the magnetic field in Gauss, l is the thickness of the conductor in the direction of B, S is the cross sectional area, and ρ is the resistivity of the conductor.)

In Fig. 4, it may be seen that an undamped spring ($\xi = 0$) offers significant vibration isolation at frequencies above the resonant frequency of the spring. Displacements with characteristic frequencies of greater than 100 Hz are reduced by more than 4 orders of magnitude, while disturbances with frequencies of 10 - 100 Hz result in less than 1% transmission. For disturbances occurring at the spring resonance frequency, amplification of the disturbance occurs. The spring offers no vibration isolation at frequencies below the resonance frequency. The effect of damping the spring is to decrease the amplification of disturbances occurring at or near the natural spring frequency, albeit at the expense of amplitude reduction at higher frequencies. Overdamping of the system considerably reduces the vibration isolation of the spring. It may be seen that at low frequencies (1-100 Hz), vibrational displacements of the laboratory floor of a few thousand Ångstroms would result in the transmittance of displacements of more than 10 Å, regardless of damping. From a

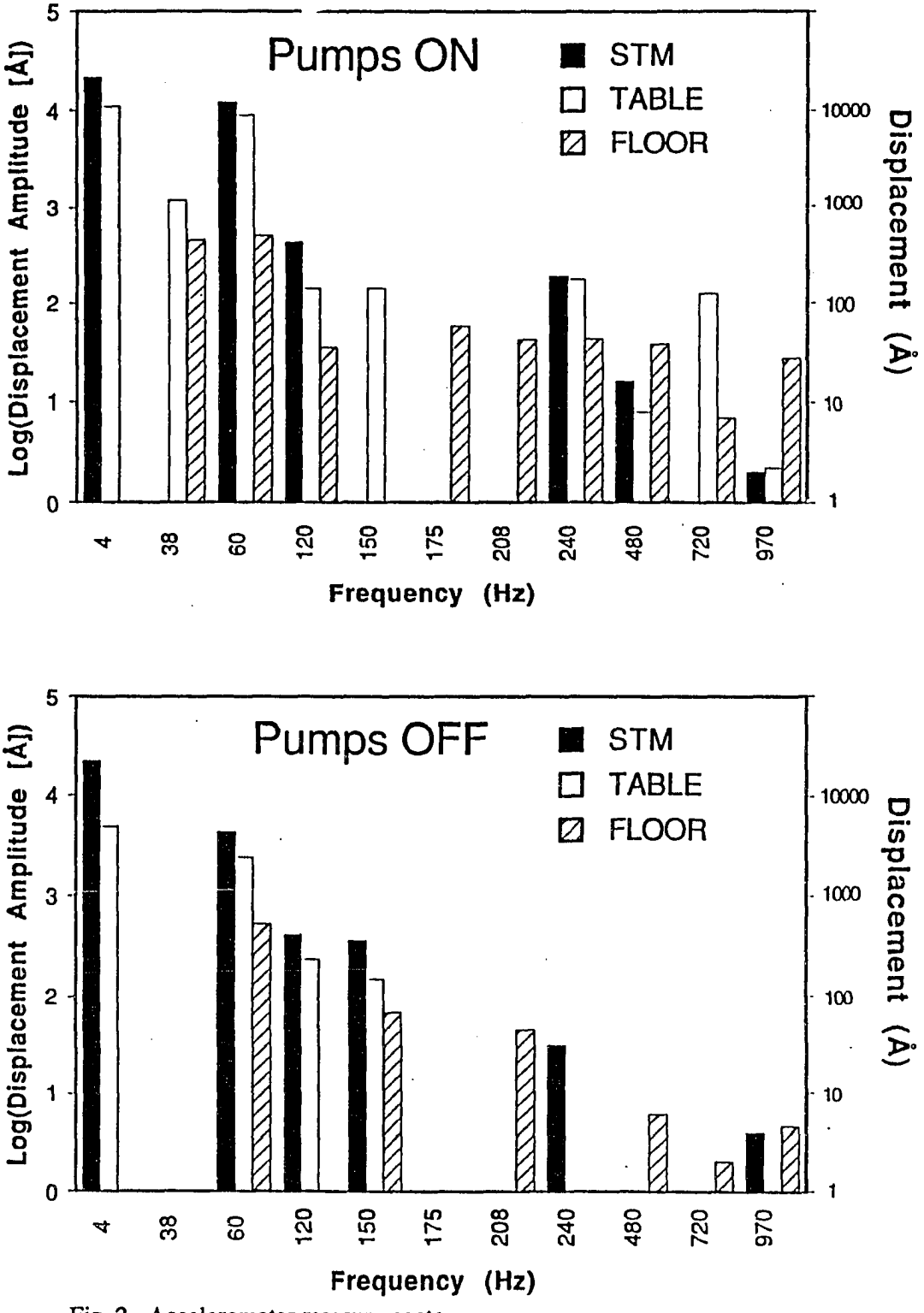

Fig. 2. Accelerometer measurements.

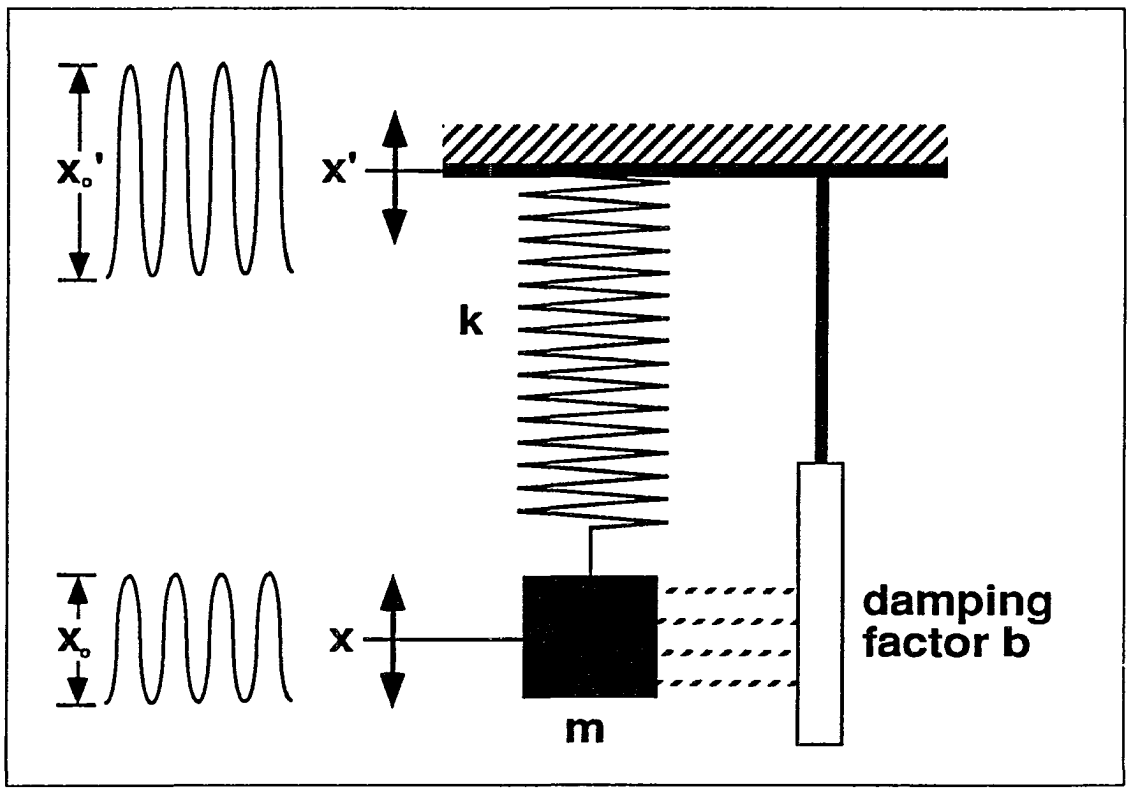

Figure 3. Illustration of variables used in Eqn. 1.

design viewpoint, it is desirable to utilize a spring with a resonance frequency far removed from any vibration frequencies and to incorporate only minimal damping. In other words, a very soft spring (small value of k and therefore small resonance frequency, ν_0) with minimal damping should be used. In general, the longer the spring, the lower the resonance frequency [2]:

$$\nu_o \cong \frac{1}{2\pi}\sqrt{\frac{g}{l}} \tag{6}$$

where l is the relaxed length of the spring and g is the earth acceleration constant. (For example, resonances of 1 and 0.3 Hz would be expected for 25 and 250 cm elongations, respectively. The Omicron STM has 4 springs that are approximately 10 cm in length, with a natural resonance of 1 Hz; the resonance frequency of the Burleigh instrument is 3 Hz while the Park instrument has a double-stage spring system with a resonance frequency of 2 Hz.)

Installation of double-stage vibration isolation systems has been found to provide additional vibration isolation [4-6]. The overall amplitude transfer function for double-stage vibration isolation is given by the product of the two individual suspension systems:

$$\left|\frac{x_o}{x_o'}\right| = \left|\frac{x_1}{x_1'}\right| \times \left|\frac{x_2}{x_2'}\right| = \left|\frac{x_1}{x_1'}\right| \times \left|\frac{x_2}{x_1}\right| = \left|\frac{x_2}{x_1'}\right| \tag{7}$$

where x_i and x_i' refer to the transmitted displacement and the external displacement, respectively. The displacement passing through the first stage of the vibration isolation system, x_1, is the source of displacement for the second stage, x_2', thus $x_1 = x_2'$. This method of determining the overall transmission function of the vibration isolation system is

appropriate for systems using either multiple spring suspension or a vibration isolation system consisting of spring suspension coupled with bungee cords and/or pneumatic legs. (It is also used for a series of stacked viton pads, separated by metal plates [5]) In Fig. 5, the amplitude transfer function for a double-spring suspension system with identical damping and resonance frequencies is shown along with the amplitude transfer function for one of the suspension systems (ν_o = 1 Hz and ξ = .10). Again, it is desirable to minimize the overall resonance frequency of the suspension system and to use minimal damping. Utilization of springs with slightly different resonance frequencies reduces the amplification of the system for disturbances at and near resonances and therefore allows smaller damping ratios to be utilized.

4. The rigidity of the STM scanner assembly

In section 3, the reduction of vibrations reaching the STM stage (isolation of the STM stage from environmental vibrations) was discussed. In this section, the transfer of vibrations between the tip and sample, caused by vibrations which have reached the STM stage, will be considered. It should be pointed out that, if the STM stage were absolutely rigid, that is, if no displacement between the tip and the sample can occur, then there would be no need for the spring isolation discussed in the previous section. Thus, the rigidity of the STM is of primary concern in eliminating vibrations between the tip and the sample. The rigidity of the STM assembly is characterized by its resonance frequency, ν'_o, and the quality factor, Q', of the tip-sample junction. The more rigid the structure, the larger the resonance frequency. The quality factor, Q', is inversely proportional to the damping ratio

for the rigid body; a larger quality factor is associated with a more rigid assembly.

STM piezo scanners typically have resonance frequencies of 10 - 100 KHz. Tripod scanners generally have lower resonant frequencies than do single-tube scanners. (The Omicron STM tripod scanner assembly has a resonance frequency of 20 KHz and that of the Park instruments is 15 KHz. The Burleigh instrument utilizes a single-tube scanner resulting in a resonance frequency of 30 KHz.) The overall resonance frequency of the scanner-tip assembly is generally reduced to 1 - 5 KHz. This decrease in rigidity is caused by joints, junctions, supports, the coarse motion stage, and connectors. We have observed a tip-sample resonance of 5 KHz with the Omicron STM.

The amplitude transfer function (also known as the stiffness or, alternatively, the damping transfer function) for a rigid STM assembly is given by [3,4]:

$$\left|\frac{z_o}{z_o'}\right| = 1 - \sqrt{\frac{1+\left(\frac{\nu}{\nu_o' Q'}\right)^2}{\left(1-\left(\frac{\nu}{\nu_o'}\right)^2\right)^2 + \left(\frac{\nu}{\nu_o' Q'}\right)^2}} \qquad (8)$$

where z_0' is the amplitude of the vibration of the STM stage (due to external vibrations), z_0 is the resultant amplitude displacement of the tip-sample junction, ν is the frequency of the z_0 displacement, ν'_0 is the resonance frequency of the tip-sample assembly, and Q' is the quality factor of the tip-sample junction. (This function is for a sinusoidal displacement, z'(t), of the tip-sample junction, with an amplitude given by z_0', where $z'(t) = z_0' e^{i2\pi\nu t}$, analogous to the amplitude transfer function for a soft spring, given by Eqn. 2.) The

amplitude transfer function is plotted in Fig. 6, for resonance frequencies of 1 and 5 KHz (and with a typical Q' value of 30 [3,4]). The rigidity of the STM scanner assembly results in very effective isolation from low frequency vibrations. Fig. 6 shows that increasing the rigidity (higher resonance frequency) drastically improves vibration isolation. The curve associated with the 5 KHz resonance is representative of our instrument. Vibrations of several thousand Ångstroms at frequencies of less than 10 Hz result in tip-sample displacements of less than a few hundredths of an Ångstrom.

5. Combination of soft suspension with the rigid STM scanner assembly

It has been shown that soft suspension systems effectively reduce high frequency vibrations, while the rigidity of the STM isolates efficiently against low frequency vibrations. The overall transmission of external vibrations to the tip-sample junction is given by the product of the transmission functions of the soft suspension system and the rigid STM assembly (Eqns. 2 and 8 or for multiple suspension systems, Eqns. 7 and 8):

$$\left|\frac{x_o}{z_o'}\right| = \sqrt{\frac{1+\left(\frac{\xi\nu}{\nu_o}\right)^2}{\left(1-\left(\frac{\nu}{\nu_o}\right)^2\right)^2+\left(\frac{2\xi\nu}{\nu_o}\right)^2}}\left[1-\sqrt{\frac{1+\left(\frac{\nu}{\nu_o'Q'}\right)^2}{\left(1-\left(\frac{\nu}{\nu_o'}\right)^2\right)^2+\left(\frac{\nu}{\nu_o'Q'}\right)^2}}\right] \qquad (9)$$

The overall transfer function is shown in Fig. 7 (ν_O = 1 Hz, ξ = .10, ν_O' = 5000 Hz, and Q' = 30) for both a single-spring and double-spring suspension system. For a single-stage vibration isolation system, displacements at the tip-sample junction will be on the

order of 0.01 Å for external vibrational amplitudes with characteristic frequencies of less than 1000 Hz (corresponding to the region where the amplitude transfer is less than 10^{-5}). At higher frequencies, between 1000 and 5000 Hz, external vibration amplitudes can not exceed 10 Å in order to meet a tip-sample amplitude of less than 0.01 Å. The addition of a second spring-suspension system significantly relaxes this restriction, reducing the overall amplitude transmission to less than 10^{-8} for the entire frequency range from a few Hz to 10 KHz. At the resonance frequency of the soft spring, the overall amplitude transmission function has a local maximum of approximately 10^{-6}; thus external vibration amplitudes occurring at or near this frequency must be held to less than 10,000 Å to keep the tip-sample displacement amplitude to less than 0.01 Å.

6. Estimate of actual noise transferred to the tip-sample assembly

The actual amplitude of the tip-sample displacement for our instrument can be estimated from the accelerometer data collected for our laboratory (shown in Fig. 2). A model noise spectrum is constructed by adding the accelerometer data to an arbitrary $1/f$ background [2]. This is shown in Fig. 8. The accelerometer data used for this figure corresponds to that measured on the STM with the pumps running. It should be noted that these measurements were carried out in the vertical direction and thus would lead to tip sample displacements parallel to the sample surface (corresponding to the lateral resolution of the STM). Measurements in the horizontal direction were also carried out and are presented in the appendix. All displacements in the horizontal direction were significantly lower than those in the vertical direction and therefore would be expected to result in a

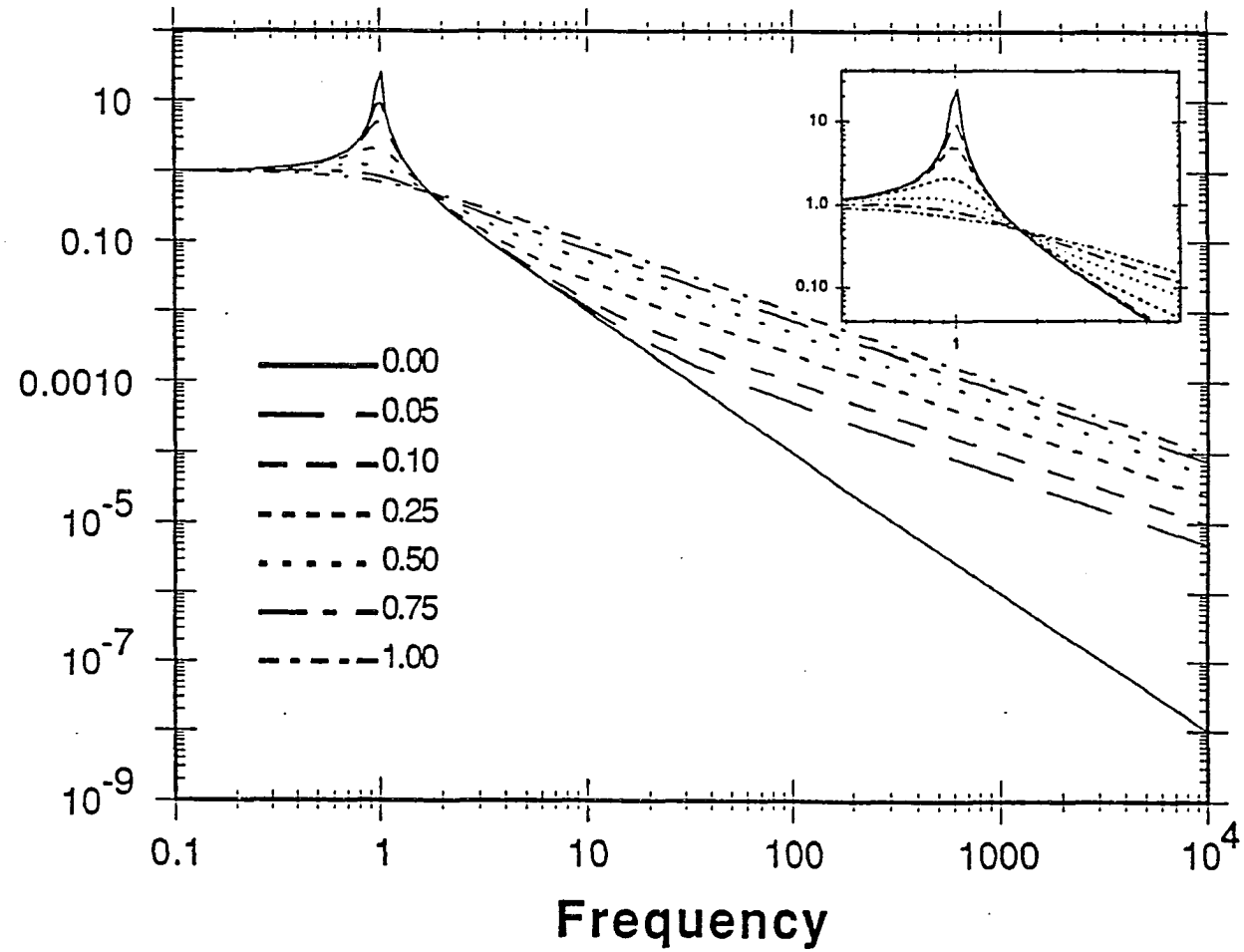

Fig. 4. Amplitude transmission functions are plotted for a variety of damping ratios. The eigenfrequency, ν_o, of the spring is 1 Hz.

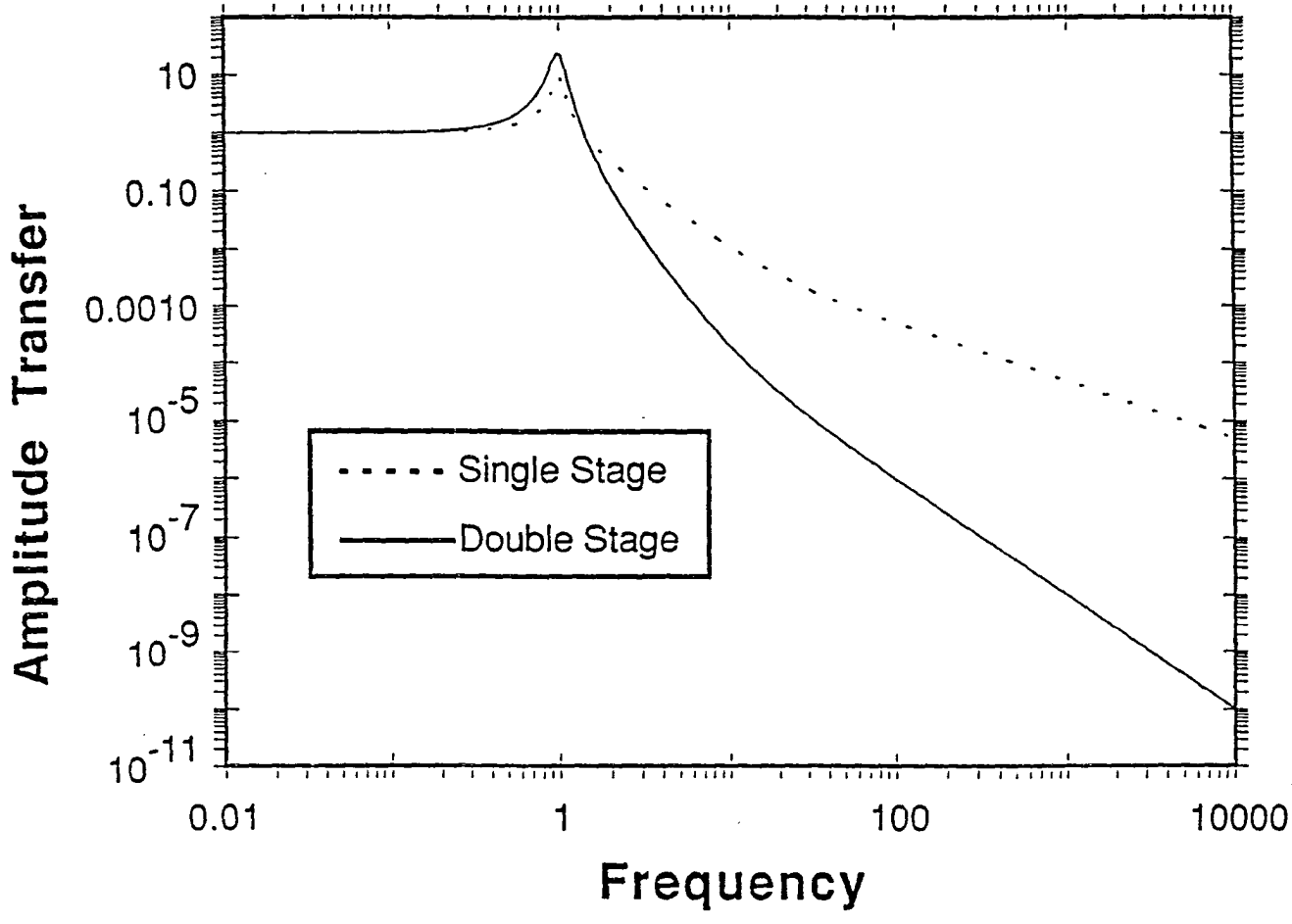

Fig. 5. Plot of the amplitude transfer functions for double- and single-stage vibration isolation systems.

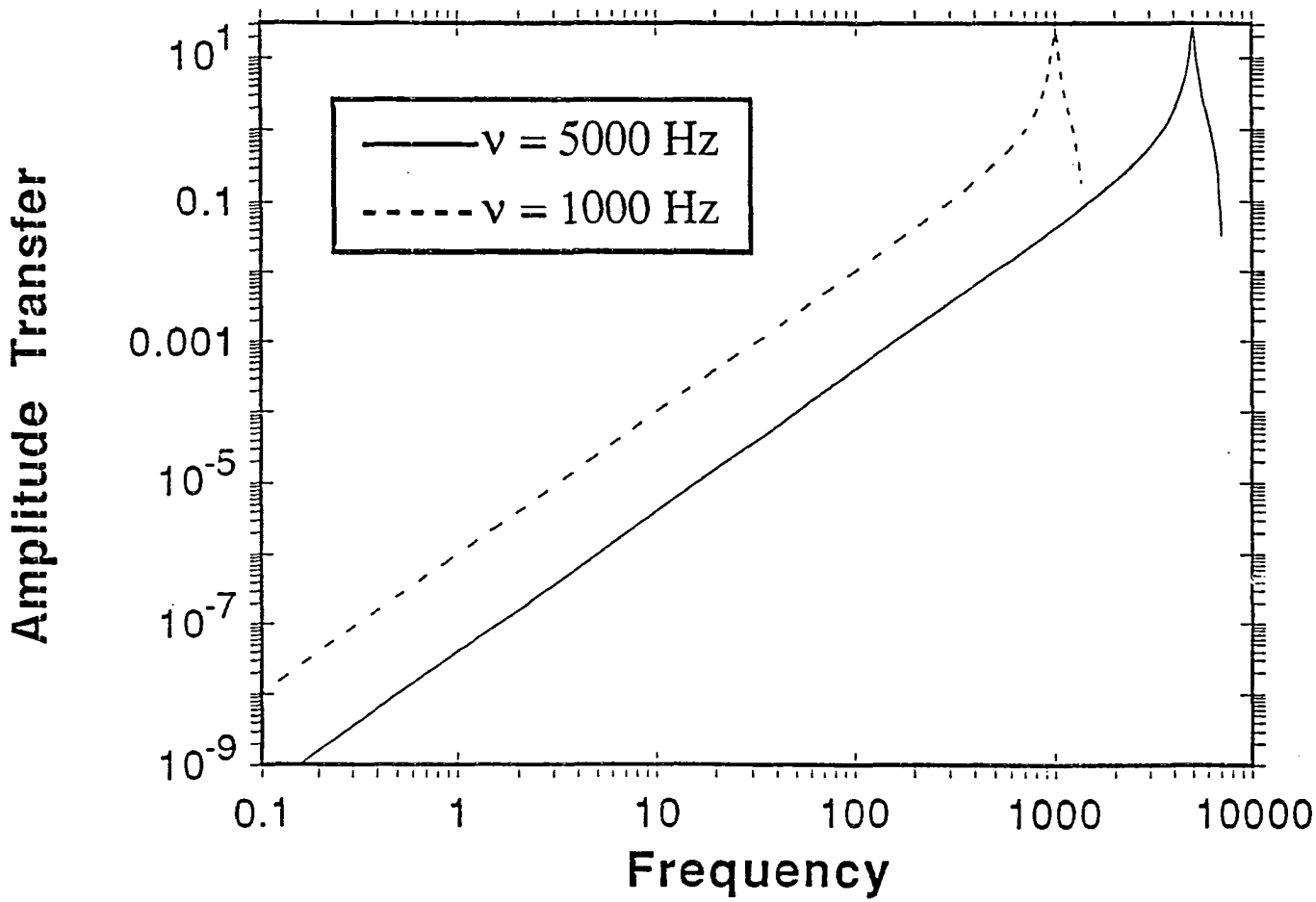

Fig. 6. Amplitude transfer function for a rigid STM assembly.

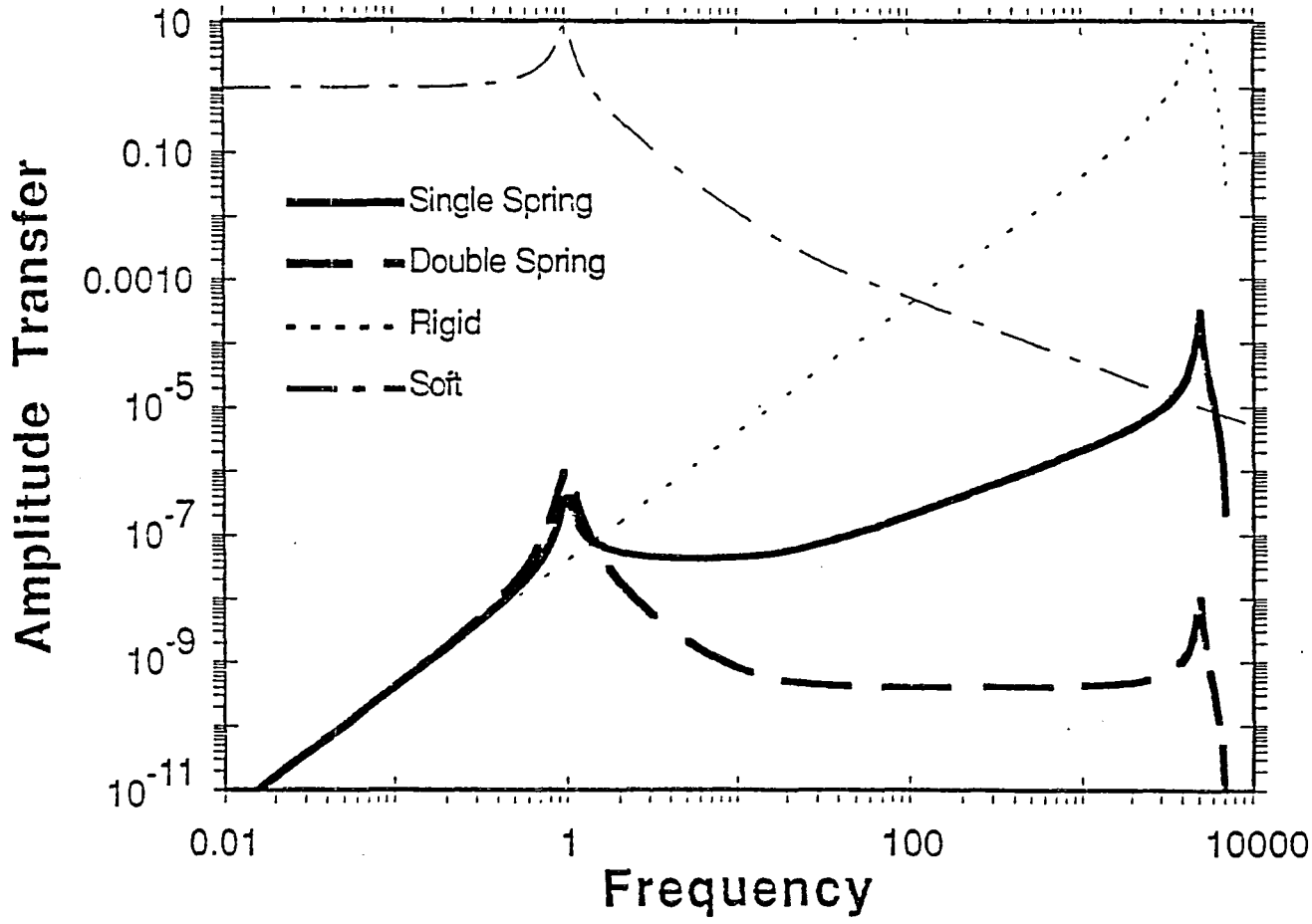

Fig. 7. Overall amplitude transfer functions for a rigid STM supported by both single- and double-spring suspension are shown. For comparison, the transfer functions of the components are also plotted.

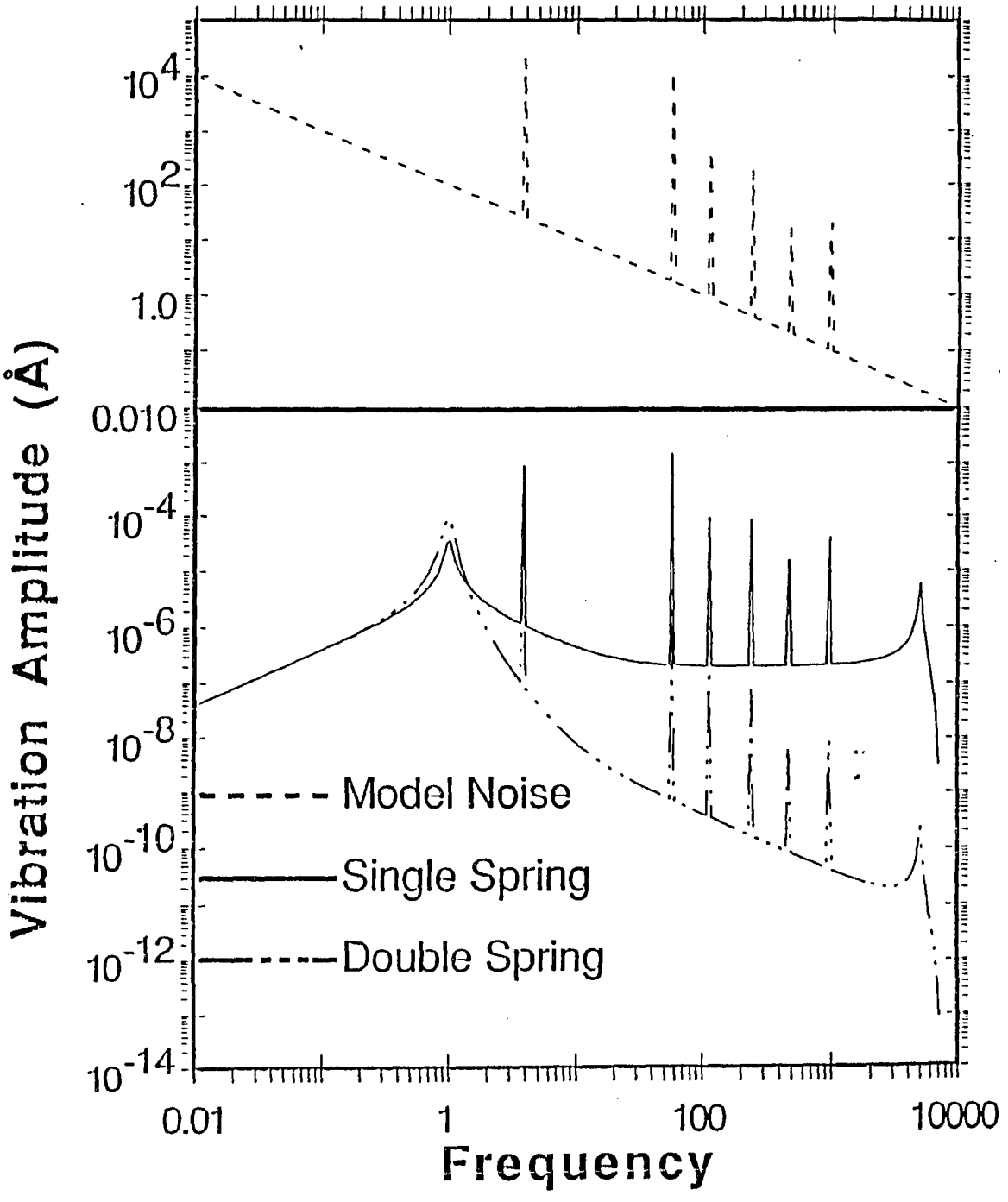

Fig. 8. Transmitted vibrational amplitudes based upon the measured displacements are plotted as a function of disturbance frequency.

smaller displacement of the tip-sample junction perpendicular to the sample surface (vertical resolution of the STM).

To determine the amplitude of the displacement of the tip-sample junction, the model noise spectrum is multiplied by the global amplitude transfer function (Eqn. 9). The results of this transformation are shown in Fig. 8 for for both a single-spring and a double-spring suspension system (as in Fig. 6: $\nu_0 = 1$ Hz, $\xi = .10$, $\nu_0' = 5000$ Hz, and $Q' = 30$). A horizontal line is drawn to show the location of a displacement amplitude of 0.01 Å; the transmitted amplitude is less than 0.01 Å over the entire frequency range for both the single- and double-spring suspension system.

7. Conclusions

Measurements of the vibrational amplitudes in the STM laboratory have been carried out using an accelerometer. These measurements include both horizontal and vertical displacements of the floor, of the support table, and of the STM. Estimates of resultant tip-sample displacements have been calculated for both a single- and double-spring suspension system, which have been used to model the spring suspension system of the Omicron STM and the combination of the Omicron spring suspension system with pneumatic legs, respectively. The results of these calculations indicate that tip-sample vibrations of less than 0.01 Å should be realized.

References:

1. C. M. Harris and C. E. Crede; Shock and Vibration Handbook (McGraw-Hill, New York, 1976).

2. R. W. Little; Elasticity (Prentice-Hall, Englewood Cliffs, New Jersey, 1973).

3. D. W. Pohl, "Some Design Criteria in Scanning Tunneling Microscopy," IBM J. Res. Develop., 30 (1986) 417.

4. S.-I. Park, C. F. Quate, "Theories of the Feedback and Vibration Isolation Systems for the Scanning Tunneling Microscope," Rev. Sci. Instrum., 58 (1987) 2004.

5. M. Okano, K. Kajimura, S. Wakiyama, F. Sakai, W. Mizutani, and M. Ono, "Vibration Isolation for Scanning Tunneling Microscopy," J. Vac. Sci. Technol., Sect. A 5 (1987) 3313.

6. Y. Kuk and P. J. Silverman, "Scanning Tunneling Microscope Instrumentation," Rev. Sci. Instrum., 60 (1989) 165.

Appendix

For the following accelerometer measurements, the displacement, **x** (Å), is related to the acceleration, **a** (g), by:

$$x(Å) = (7.02 \times 10^9)\, a(g)/f^2 \qquad \text{and} \qquad a(g) = (1.42 \times 10^{-10})\, x(Å)\, f^2,$$

where **f** is the frequency (Hz). The acceleration and frequency may be taken straight from the graphs and plugged into the above equation.

The source of the above equation follows:

$a\,(\sin 2\pi ft) = x = d^2(x \sin 2\pi ft)/dx^2$; **a** (Pk to Pk) $= (2\pi^2 x f^2)$;

a (rms) $= 0.707\pi^2 x f^2$